Summer 7-17-2017

TIME AND ENERGY CHARACTERIZATION OF A NEUTRON TIME OF FLIGHT DETECTOR USING A NOVEL COINCIDENCE METHOD FOR CONSTRAINING NEUTRON YIELD, ION TEMPERATURE AND LINER DENSITY MEASUREMENTS FROM MAGLIF EXPERIMENTS

Jedediah Styron
University of New Mexico

Jedediah Daniel Styron

Candidate

Nuclear Engineering

Department

This dissertation is approved, and it is acceptable in quality and form for publication:

Approved by the Dissertation Committee:

Dr. Gary Cooper, UNM Faculty, Chairperson

Dr. Adam Hecht, UNM Faculty

Dr. Mark Gilmore, UNM Faculty

Dr. Carlos Ruiz, Sandia National Laboratories

TIME AND ENERGY CHARACTERIZATION OF A NEUTRON TIME OF FLIGHT DETECTOR USING A NOVEL COINCIDENCE METHOD FOR CONSTRAINING NEUTRON YIELD, ION TEMPERATURE AND LINER DENSITY MEASUREMENTS FROM MAGLIF EXPERIMENTS

by

JEDEDIAH D. STYRON

B.S. NUCLEAR ENGINEERING, SPRING 2013
UNIVERSITY OF NEW MEXICO

M.S. NUCLEAR ENGINEERING, FALL 2014
UNIVERSITY OF NEW MEXICO

DISSERTATION

Submitted in Partial Fulfillment of the
Requirements for the Degree of

Doctor of Philosophy
Engineering

The University of New Mexico
Albuquerque, New Mexico

July, 2017

Acknowledgements

I would like to thank my advisor Dr. Gary Cooper for his patience, support and encouragement throughout this project. I would also like to thank the rest of the team from Org. 1677 at Sandia National Laboratories: Dr. Carlos Ruiz, Dr. Kelly Hahn, Dr. Gordon Chandler, Dr. Brett Jones, and Jose Torres for their support and advice during this work. Others who have offered support are: Dr. Alan Nelson and Bruce McWatters (all from Sandia National Laboratories), Dr. Adam Hecht and Dr. Mark Gilmore for sitting on my committee.

Most of all I would like to thank my wife Theresa and my daughter Cassandra for dealing with the several exceptionally late nights and early mornings. Thanks to all the others I have not mentioned and for your understanding when I couldn't get away. My grandfather, "Papa", provided me with inspiration throughout this journey. Unfortunately, he passed away prior to me receiving my Ph.D., but he always knew I would succeed before I did. Thanks for always believing in me, big guy!

Sandia National Laboratories is a multimission laboratory managed and operated by National Technology and Engineering Solutions of Sandia, LLC., a wholly owned subsidiary of Honeywell International, Inc., for the U.S. Department of Energy's National Nuclear Security Administration under contract DE-NA-0003525.

Abstract

The focus of this work is the characterization of a typical neutron time-of-flight (NTOF) detector that is fielded on inertial confinement fusion (ICF) experiments conducted at the Z-experimental facility with emphasis on the Magnetized Liner Fusion (MagLIF) concept. An NTOF detector consisting of EJ-228 scintillator and two independent photomultiplier tubes (PMTs), a Hamamatsu-mod 5 and Photek-PMT240, has been characterized in terms of the absolute time and energy response. The characterization was done by measuring single, neutron-induced events in the scintillator by measuring the alpha particle and neutron produced from the D-T reaction in kinematic coincidence. The results of these experiments provided the time dependent instrument response function and the detector sensitivity as a function of applied voltage covering the entire dynamic range of the detector. Historically, impulse response functions have been measured using various photon sources as surrogates for a neutron source. Thus, this measurement using a single hit neutron source results in the most accurate measured response function, which will improve the accuracy of impulse response corrections to the NTOF signals.

While this detector has not yet been fielded on any MagLIF experiments, the development of a predictive capability was desired for transferring the measured detector response from the calibration geometry to the more complex Z geometry. As a proof-of-principle, a detailed model of the Z-machine was developed in MCNP6 to correct for geometry issues when transferring the calibration results from a light lab setting to the Z-environment. Representative values for the instrument response function and the sensitivity for the current detectors fielded on MagLIF experiments were convolved with the modeled results. These results were compared with data collected on three previous MagLIF experiments. The comparison shows the model results can be used to constrain three parameters that are relevant for diagnosing the plasma performance and confinement – the plasma ion temperature, the beryllium liner areal density, and the neutron yield – which significantly enhances the information that can be obtained from the Z NTOF signals. The model also clarifies the source of features that have been observed in the NTOF signs that were not well understood before. In addition, this capability and methodology can be used to re-design the source to detector lines-of-sight such that the magnitudes of the required corrections are minimized.

Table of Contents

List of Figures

List of Tables

1 Introduction

1.1 Thermonuclear Fusion

Thermonuclear fusion is the process of two light nuclei interacting to form a single, heavier element and a single nucleon (either a proton or neutron). Elements that fuse to form nuclei having masses less than Fe-56 undergo exothermic reactions that release a significant amount of energy. Thus, there are a number of possible fusion reactions, but the four that have drawn the most interest from the scientific community are shown in equations 1-1 through 1-4.

$$D + T \rightarrow {}_2^4He + n + 17.6\ MeV \qquad [1-1]$$

D+D

$$D + D \xrightarrow{\sim 50\%} {}_2^3He + n + 3.27\ MeV \qquad [1-2]$$

$$D + D \xrightarrow{\sim 50\%} {}_1^3H + H + 4.03\ MeV \qquad [1-3]$$

$$D + {}_2^3He \rightarrow {}_2^4He + H + 18.35\ MeV \qquad [1-4]$$

Fusion reactions have a very high specific energy content, especially if isotopes of hydrogen are fused. This value, for the D-T reaction, as shown in Table I, is very large when compared with the specific energy of a fission reaction and the two fuels commonly used to produce energy today. This property is one of the reasons fusion continues to be an attractive option as a viable and sustainable energy source.

Table I Comparison of specific energy values for fossil fuels, fission, and fusion

Fuel Source	u (MJ/kg)
Bituminous Coal	~30
Methane (Natural Gas)	55
U-235 Fission	82000
D-T Fusion	340000

While fusion is an attractive option, extracting the energy does not come without significant challenges. To initiate a fusion reaction, the two ion species must overcome the repulsive

Coulomb potential of two charged particles with charges of the same sign. For example, to fuse two hydrogen atoms, the ions must have energies of approximately 150 keV to overcome the repulsive Coulomb force. The energy required to fuse two ions increases as a function of charge and this is why lower Z elements, like deuterium and tritium, are more likely to fuse than higher Z elements.

Ideally, the energy distribution of the fusing ions will constitute a Maxwellian distribution and, hence, can be characterized by a temperature and an average ion energy. A majority of the reactions will be the result of the interaction of ions in the high-energy tail of the distribution. As a result of these reactions from the high-energy tail, significant fusion can take place in a plasma with an average ion temperature of only a few keV (~10^8 K). However, to achieve sustainable fusion energy breakeven the product of the fuel ion density and the time the fuel is at that density must exceed a certain value while at the necessary temperature (for deuterium-tritium fuel this product must exceed about 10^{20} sec/m^3 while the temperature is at ~10keV). These conditions have individually been reached in a laboratory setting, but not simultaneously, which is necessary to reach "breakeven". Achieving fusion energy breakeven has eluded researchers for decades and continues to be a very active area of physics and engineering research today.

1.2 Plasma Confinement

There are two main approaches, or confinement schemes, being investigated to produce large scale fusion plasmas: magnetic confinement fusion (MCF) [1] and inertial confinement fusion (ICF) [2]. Magnetic confinement fusion relies on large magnetic fields, ~ 10 Tesla, to confine the plasma within a large volume region, ~800 m^3. For ion densities of $10^{20}/m^3$, Lawson's criterion predicts that the plasma must be confined for a few seconds to produce more energy than was required to produce and confine the plasma. The biggest MCF facility in the world will be the International Thermonuclear Experimental Reactor (ITER) tokamak facility located in the south of France. ITER is still in the construction phase at this time and the first deuterium-tritium plasma experiment is forecasted for the year 2030 [3]. The second method, inertial confinement fusion (ICF), relies on compressing the fuel to the high temperatures and densities required. The inertia of the compressed fuel provides the confinement in this approach. If the fuel can be compressed to densities on the order of $10^{29}/m^3$, the confinement time required to

reach breakeven conditions will be on the order of nanoseconds, which, in turn, is on the same time scale for the fuel mass to disassemble. Currently, within the United States, there are three large scale ICF experimental test facilities – the Z-machine [4], a pulsed power accelerator located at Sandia National Laboratories, and two laser fusion facilities, the National Ignition Facility (NIF) [5] at Lawrence-Livermore National Laboratories, and the Omega laser facility [6] at the University of Rochester Laboratory for Laser Energetics.

The Z-machine is the largest and most powerful pulsed-power generator in the world. The driving force of the Z-machine comes from 36 Marx generators that are capable of producing ~30 MA of current that can be delivered to a target load [4] in less than a hundred nanoseconds. In addition to producing large currents, the Z-Machine is also the most powerful x-ray source in the world, creating > 300 TW of x-ray power [7]. Within the ICF campaign at the Z-Facility there are two different approaches to obtaining fusion. These two approaches both utilize deuterium-deuterium (D-D) fuel at present to avoid the hazards that using tritium would introduce.

The primary experimental campaign is studying the feasibility of the magnetized liner inertial fusion (MagLIF) concept [8] [9]. In the MagLIF concept the fusion "target" is composed of a small cylindrical liner, usually made of beryllium, which contains the deuterium gas fuel. The large current produced by the Z-machine is made to flow through this cylindrical liner. The resulting J x B forces cause the liner to implode, compressing and heating the fuel. The novelty of the MagLIF approach is that an externally applied magnetic field, ~ 10 Tesla, is applied prior to the initiation of the current flow such that the field can diffuse through the liner and into the deuterium gas. As the liner implodes this magnetic field thermally isolates the hot fuel from the cold liner by suppressing electron flow and serves to stabilize, to some degree, the imploding liner Rayleigh-Taylor instabilities. Further, a laser is used to preheat (~ 2.5 kJ) the fuel prior to the completion of the implosion. The laser used in these experiments is provided by the Z-Beamlet [10] facility, which is in close proximity to the Z-machine. A typical MagLIF confinement and an illustrative representation of the MagLIF concept are shown in Figure 1.

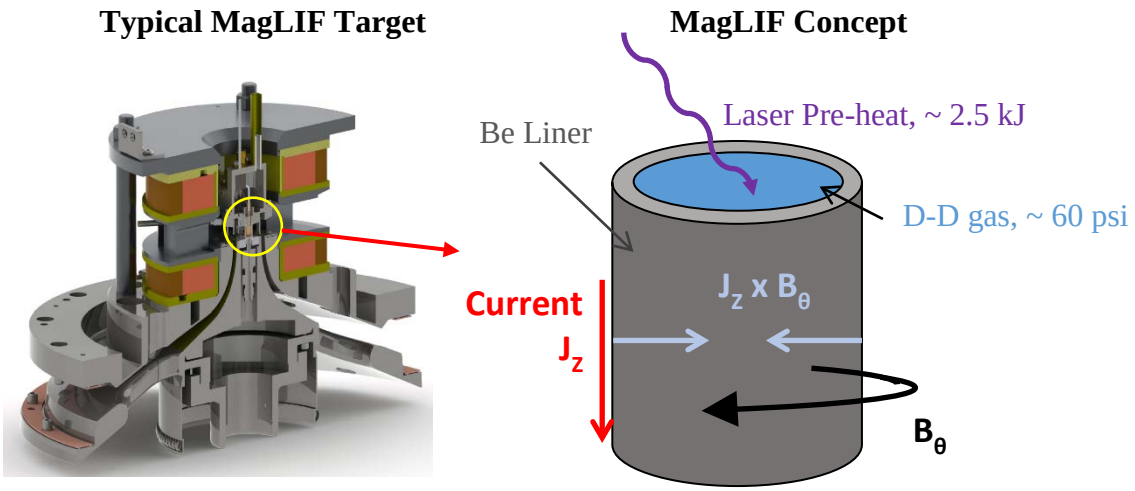

Figure 1 A typical MagLIF confinement and an illustrative view of the MagLIF concept used at Sandia National Laboratories' Z accelerator

The second ICF campaign is the deuterium gas puff platform [11] [12] [13]. In these experiments deuterium gas is pulsed into the target chamber just as the current is applied. Again, the resulting J x B force causes the gas to implode on axis. Gas puffs are comparable to plasmas generated with a dense plasma focus (DPF) and are unique in that the burn time is on the order of tens of nanoseconds, which is large when compared to MagLIF burn times that are less than a few nanoseconds. In the past, wire arrays [7] were used to create x-rays to drive implosions in various geometries including the dynamic hohlraum [14].

The NIF and Omega facilities utilize laser energy to study ICF fusion concepts. Omega is smaller than the NIF in terms of available laser energy with 60 lasers capable of producing energies > 40 kJ while the NIF is far more powerful with 192 lasers that can generate energies >2 MJ. At either facility they can couple energy to the target using either direct [15] [16] or indirect methods [17]. Direct drive fusion is an approach that couples multiple laser beams from various angles directly to the fuel, in most cases a cryogenic mixture of 50/50 deuterium-tritium. The typical cryogenic target is less than a centimeter in diameter with a thin plastic shell, or ablator, which has a tritium vapor core that is encapsulated by a thin deuterium-tritium ice layer. The most popular method for indirect drive utilizes a hohlraum target, which is a hollow cylindrical tube typically made of a high Z material [18]. The laser beams are focused onto the inner walls of the hohlraum, where the laser energy is absorbed and re-emitted in the form of x-rays. The cryogenic target is placed within the center of the hohlraum to promote isotropic

heating of the target. While near isotropic heating is advantageous, it is inefficient because some laser energy is lost as heat in the hohlraum [19].

1.3 Neutron-time-of-flight diagnostics and measurable quantities

Regardless of the experimental platform, experimenters need to infer quantities that provide information about the performance of the ICF implosion. This often requires measuring the reactant products that are emitted in the fusion reaction. The charged particles produced in the reactions (see equation 1-1 through 1-4) can be measured directly, but are usually not energetic enough to escape the confines of the plasma. While this is not useful for diagnostic purposes, this is a desired effect for forming a hot, dense region that is necessary for achieving ignition conditions. Since the two most common fusion reactions, D-D and D-T, emit neutrons in addition to charged particles, information has to be extracted from the neutron measurement. Measuring the neutrons is advantageous since they are free of charge and readily escape the plasma without interaction and they contain valuable information about the ions from which they were produced. Quantities such as the bang time, burn history, ion temperature, fusion energy yield, and the areal density are all inferred from neutron measurements. Alternatively, quantities relevant to the electrons, such as electron density and temperature, can be inferred from x-ray diagnostics. The one exception, where a charged particle can be measured directly, is the D – ^{3}He reaction shown in equation 1-4, which produces a 14.7 MeV proton. This reaction has been studied at the OMEGA facility as a surrogate to the D-T plasma [20]. A more comprehensive review of ICF plasma diagnostics that are in use at multiple facilities can be found in references [21], [22] and [23].

In ICF experiments the most common and widely used neutron detection system is the neutron time-of-flight (NTOF) detector. In fact, every ICF facility in the country employs several NTOF detectors on nearly every experiment [23] [24] [25]. The NTOF is a simple system that has a scintillator material, often an organic plastic, coupled to a photomultiplier tube (PMT) that is powered by a high-voltage power-supply (HVPS). The signal from the PMT can be used for single event counting, but for time-of-flight measurements the signal is current integrated and analyzed using a digitizer. The measured signal from the digitizer or oscilloscope is a differential voltage spectrum with respect to time, which is a direct measure of the time dependent energy deposition within the scintillator. The first ever reported use of NTOF detectors in the literature

was in 1955 by Cranberg and Levin [26] and the first reported NTOF use for neutron spectral measurements was by Bogdanov et al in 1956 [27]. Representative data from a typical NTOF measurement and the various parameters that can be inferred from typical MagLIF deuterium-deuterium plasmas are shown in Figure 2. These quantities will be further defined in the following section.

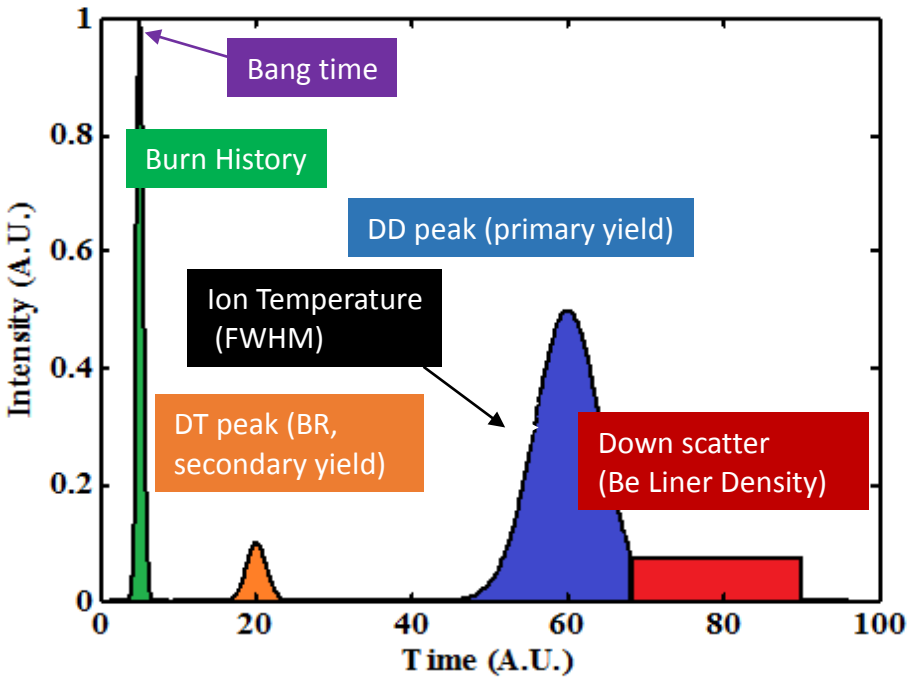

Figure 2 Representative data from a typical NTOF measurement. Shown are the expected features and inferred parameters from a typical MagLIF experiment.

1.3.1 Neutron energy spectra from time-of-flight diagnostics

The neutron energy spectra can be determined from the NTOF differential time signal by knowing the relationship between energy and velocity, or the distance traveled per unit time as shown in equation 1-5 [28].

$$E = \frac{1}{2}Mv^2 = \frac{1}{2}M\left(\frac{d^2}{t^2}\right) \qquad (1-5)$$

The transformation from dN/dt, which is extracted from the time-of-flight signal, can be converted to the differential energy spectrum, dN/dE by using the following chain rule expansion, where the mass is in energy units of MeV.

$$\frac{dN}{dE} = \frac{dN}{dt}\frac{dt}{dE} = \left(\frac{M^{0.5}d}{2c\sqrt{2E^{1.5}}}\right)\frac{dN}{dt} \qquad (1-6)$$

Using the same formulation, the resulting energy resolution for a specific, neutron-energy at a given time resolution from an NTOF measurement can be calculated using the expression for dE/dt.

$$\delta E = \frac{2c\sqrt{2E^{1.5}}}{M^{0.5}d}\,\delta t \qquad (1-7)$$

Being able to resolve the neutron energy spectra became much more significant in 1973 when Brysk [29] proposed that the width of the neutron energy spectrum can be used to infer the ion temperature of either a D-D or D-T fusion plasma. His derivation assumed the following: the ion distributions within the plasma can be described by a Maxwellian distribution, there is negligible non-thermal ion motion, the reaction rate can be described by a delta function, and the fusion cross-section can be predicted using semi-classical Gamow theory. The results of this derivation are given in equations 1-8a and 1-8b, for D-D and D-T neutrons, respectively. Brysk showed the neutron energy distribution will be Gaussian and the full-width-at-half-the-maximum (FWHM), ΔE, is proportional to the ion-temperature, kT_i in keV. The first ever reported ion-temperature measurement that was inferred from NTOF data using this formulism was made by Lerche and company in 1977 [30].

$$\Delta E = 82.5\sqrt{kT_i}\ \ for\ DD\ neutrons \qquad (1-8a)$$

$$\Delta E = 177\sqrt{kT_i}\ for\ DT\ neutrons \qquad (1-8b)$$

A similar formulation presented by Lerche and Remington a few years later describe the relationship between the FWHM, in nanoseconds, to the ion temperature, in keV, for a given source to detector distance d [31]. This relationship was shown graphically in Figure 2 as the width of the blue Gaussian D-D peak.

$$\Delta t = 0.778\left[\frac{ns}{m\sqrt{keV}}\right] d\sqrt{kT_i}\ for\ DD\ neutrons \qquad (1-9a)$$

$$\Delta t = 0.122\left[\frac{ns}{m\sqrt{keV}}\right] d\sqrt{kT_i}\ for\ DT\ neutrons \qquad (1-9b)$$

In more recent work it was shown that the assumption of negligible non-thermal ion populations is not valid in some plasmas. In these cases, the FWHM of the neutron distribution will have a power law contribution from the supra-thermal ion population in addition to the thermal broadening contribution of the ion temperature [32]. The relationship between the neutron energy distribution and the ion-temperature is continually evolving and still remains a very active area of research today.

1.3.2 Neutron yield, ion ratio and areal density

In addition to knowing the neutron energy spectrum, other quantities can be extracted from integrating the timing signal. The typical NTOF signal will nominally have two parts – the Gaussian portion that corresponds to the primary, un-scattered source neutrons and a secondary tail from neutrons that have been reduced in energy from interactions within the plasma or target material. This is represented in Figure 2 as the blue and red regions, respectively. The integral quantity of the primary Gaussian signal can be used to infer the neutron yield [33], or the total number of neutrons produced in either the D-D or D-T reaction of interest. The neutron yield is an important metric in determining the success of an implosion since the amount of fusion energy produced is proportional to the product of the neutron yield and the amount of energy released per reaction. If an isotropic source is assumed, the neutron yield can be calculated if the total charge, q, the detection sensitivity, ϵ, and the solid angle subtended by the detector, Ω_{SA}, are known.

$$Y_n = \frac{4\pi}{\Omega_{SA}} \frac{q}{\epsilon} \qquad (1-10)$$

The total measured charge, q, can be found by integrating the NTOF signal as shown in equation 1-11, where H is the differential amplitude in volts, and Ω_{imp} is the signal cable impedance in units of ohms. The units of this equation are coulombs, which is analogous to integrating Ohms Law with respect to time, where the current I (t) = V(t)/R.

$$q\,[C] = \frac{1}{\Omega_{\text{imp}}} \int H(t)dt = \int I(t)dt \qquad (1-11)$$

The integral quantity of the secondary tail gives the total number of neutrons that have undergone at least one interaction. If the scattering contribution within the neutron spectrum is

from the plasma ions or other material relevant to the target, the ratio of the scattered neutron yield to the total neutron yield is a direct measure of the areal density in g/cm^2. In laser driven fusion [34] this is a measure of the ablator and fuel areal density and in MagLIF experiments this is an indicator of the beryllium liner density at stagnation [35].

An integral neutron measurement that is very specific to MagLIF is the effective magnetic field within the plasma column. This measurement is possible only for pure deuterium plasmas, which MagLIF employs exclusively. For reacting D-D plasmas there are two possible reaction channels that will produce neutrons. The primary reactions will be D-D, where ~50% of the reactions will produce 2.45 MeV neutrons (equation 1-2) and the other ~50% will produce a tritium particle (equation 1-3), which, in turn, can interact with the deuterium fuel to produce 14.1 MeV neutrons (equation 1-1). The ratio of these two yields gives information about the ion densities within the plasma. In addition, the effective magnetic field achieved within the plasma column at stagnation [36] will cause an observable spectral shift in the axial direction from the magnetized tritium ions within the fuel. In addition to magnetization, information can be obtained about the isotropy of the reacting ions if several neutron integral measurements are taken at various locations with respect to the source. This is an indicator as to whether the neutrons were produced by a thermal plasma or generated through the streaming of ions (beams) in a preferential direction.

1.3.3 Bang time and burn history

Two other very important measurements, the bang time and the burn history, are related to the stagnation point and the confinement time of the plasma. The bang time refers to the moment in time where the ion species in the plasma start to interact, and if the pressure and temperatures are high enough, fuse [37]. This value is typically inferred from the prompt gamma emission that always precedes the neutrons in arrival time at the detector given the difference in particle velocities. This is represented in Figure 2 by the peak gamma emission denoted by the purple region. The burn history or burn width refers to the duration in time when the ions continue to fuse and emit neutrons [38] [39]. The measurement of the burn width is an important metric in determining ignition conditions [40] and is strongly dependent on the type of plasma. In MCF the width could be a few seconds, while for direct and in-direct drive ICF plasmas the width can be sub-nanosecond and for Z-pinch MagLIF and gas puff plasmas the width can vary from a few

nanoseconds to tens of nanoseconds. In ICF plasmas this measurement requires using an NTOF or solid-state detector placed in close proximity to the source to eliminate the temporal broadening from the neutron energy spectra. This type of measurement also requires the use of a detector with an inherent time response less than the expected burn width of the source. This measurement was shown previously in Figure 2 and is denoted by the width of the green region.

2 Background for This Work

2.1 Instrument Response Function and NTOF Sensitivity

The inference of the ion temperature, bang time, and burn width are all dependent on the neutron detection time history. Extracting these quantities from the time history measurement appears to be straightforward, but there are several time dependent processes that can contribute to the observed signal from an NTOF system. The absolute timing of a measurement is a strong function of the neutron transit time, which depends on the burn width, source to detector distance, the scintillator thickness, and the energy of the particle. There is additional timing inherent to the detector that includes the scintillation photon transit time from birth to the photocathode and the photoelectron transit time from the photocathode to the anode. Additional delay is added by the cable length from the PMT to the digitizer. Some of these parameters are fixed variables, like the source to detector distance, cable length and digitizer noise, but others are statistical processes such as the production of visible light in the scintillator, photoelectron emission from the photocathode, and secondary electron emissions from the dynodes within the PMT.

The statistical processes inherent to the scintillator and PMT of an NTOF system can be described mathematically by an instrument response function (IRF). In most cases the IRF is represented by an exponentially modified Gaussian distribution to reflect the scintillator decay and the PMT response [41]. It is important to note that this function does not capture the transit times, or the throughput delay of the scintillator, light guide, and PMT. The IRF can be theorized, but since the IRF is representative of a detector system it is usually obtained experimentally. In most cases this involves illuminating the scintillator with a short pulse laser, or with an intense beam of photons and measuring the resulting signal [42] [43]. In the event neither of these methods are available, the response function can be obtained by measuring cosmic events using a coincidence system [44]. To measure the response for neutrons directly is

a difficult task. Single event neutron sources that emit mono-energetic neutrons in a short burst generally do not exist. However, this type of source can be approximated if a neutron detector is placed at a distance very far from the source where the probability of detecting multiple neutrons is minimized. Klir et al recently reported on this type of measurement using a dense plasma focus and Z-pinch device [33]. Single neutron sources can also be approximated through the use of a coincident technique and an accelerator [45] [46].

Thus, the acquired NTOF signal, mathematically, is the convolution of the true signal, which contains primary and scattered neutrons, along with prompt photons, and the instrument response function (IRF). There are two ways to go about extracting the true signal – either by de-convolving the IRF from the total signal or convolving a neutron spectrum at a known ion-temperature with the IRF to re-create the total signal. De-convolution or unfolding methods remove the IRF from the measured differential spectrum, which in principal should leave the unadulterated neutron time distribution [47]. This is often done using fast Fourier transforms or with analytical Fourier transforms if a functional dependence is assumed. When there are poor statistics, or the instrument response function is a large fraction of the measured signal, this method often fails. In a convolution or forward-fit technique, an analytical representation of the IRF is convolved with a neutron spectrum that is varied by changing the ion-temperature. The variable result is then compared to the experimental data to determine the conditions of the experiment within a specified uncertainty. This method is advantageous over de-convolution methods in that the solution can be found using integral parameters [48].

The detection efficiency or the detector sensitivity, required to calculate the neutron yield (equation 1-10), is another useful metric that relates the detector response in terms of signal amplitude to the average energy deposited within the detector. This parameter must be known absolutely to accurately infer the neutron yield from neutron time-of-flight data. Much like the IRF, this parameter can be theorized, but since it is strongly dependent on the system it is typically found experimentally. The preferred method for obtaining the detector sensitivity is to infer the value from cross-calibration with a known diagnostic [49] [50]. For example, the NTOF detectors used at the Z-Machine are cross-calibrated in situ with the primary D-D neutron yield diagnostic: indium activation [51]. The NTOF detectors used at the NIF and OMEGA facilities are calibrated in situ at the OMEGA facility by means of cross-calibration to neutron

yields calculated from Cr-39 analysis [52]. Independent and ex situ calibrations can be done with a known neutron source or with a yield monitor, such as an activation diagnostic [53], and an accelerator. Once these parameters are determined they can be used with a neutron transport model to provide a predictive capability for future experiments using a forward fit analysis.

2.2 NTOF usage at the Z-pulsed power facility

There are presently five NTOF detectors that are fielded on every MagLIF experiment. A diagram showing a cross-section view of the Z-machine and the relative location of each NTOF detector is shown in Figure 3. Each line-of-sight is unique in that each detector views the source through a different geometry.

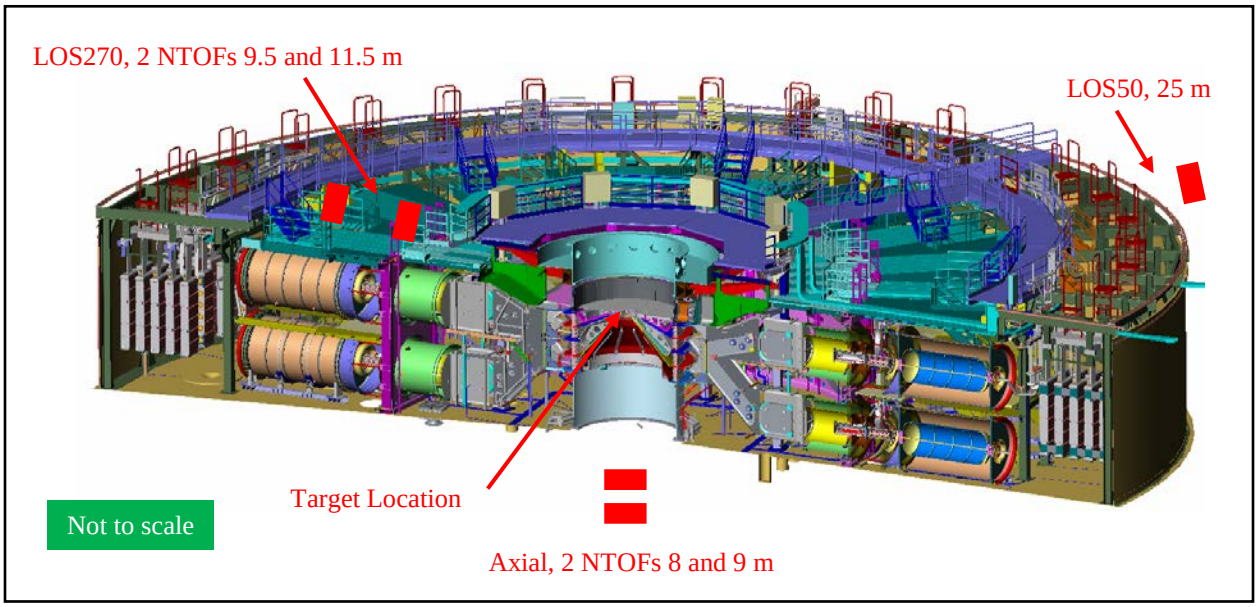

Figure 3 NTOF detector location at the Z-pulsed power facility [4]

For this work, the primary focus will be line-of-sight 270 (LOS270), where presently two of the five NTOF detectors are fielded. The two detectors on LOS270 are located coaxially and are separated by a distance of 2 meters at 9.5 and 11.5 meters, respectively. Both detectors have a cylindrical EJ-228 scintillator that is 2.54 cm thick and a diameter of 7.62 cm. The detector closest to the source is a single PMT design, where the scintillator edge is viewed by a single Hamamatsu mod-4 PMT that is coupled to the scintillator via a Lucite light guide. The detector at 11.5 meters is a dual PMT design, where the scintillator is viewed on edge, equidistant, by two independent PMTs coupled through Lucite light guides. The two PMTs chosen for this design

are a Photek PMT240 and a Hamamatsu mod-5. The use of two PMTs allows the same signal to be viewed with a different dynamic range that is set by the separately applied voltages. The Photek is different from the Hamamatsu in that it has nominally a 3X faster time response and can be gated either on or off. This allows the PMT240 to be gated off prior to the arrival of the neutrons to avoid saturation from the large bremsstrahlung signal that always precedes the neutrons. However, at the cost of having better timing characteristics, the Photek is limited in the amount of charge that can be deposited, nominally < 15 nanocoulombs. These two different detector designs are shown in Figure 4, where the 9.5-meter, single PMT detector is shown on the top and the 11.5-meter dual PMT design is shown in the bottom.

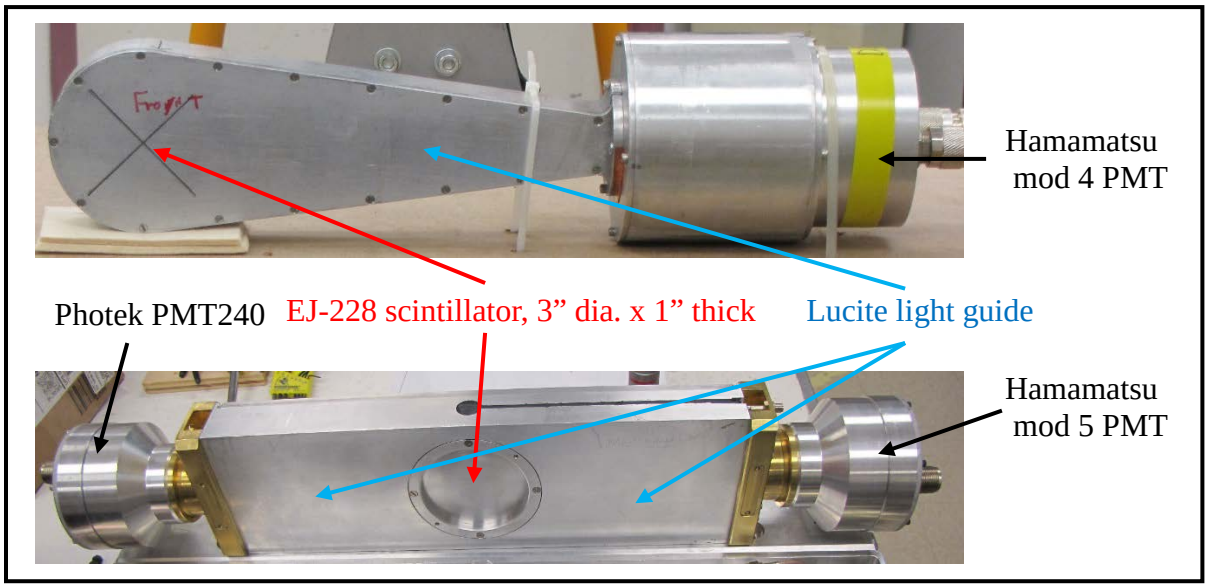

Figure 4 NTOF detectors currently fielded on line-of-sight 270 at the Z-experimental facility. Top figure - 9.5 meter detector, Bottom figure - 11.5 meter detector

These detectors are fielded in an environment where there is a large contribution to the detector signal from neutrons that have undergone at least one scattering event either from structural or shielding material. This poses two different challenges: Firstly, additional scattering material adds structure to the observed NTOF signal that interferes with the inference of the neutron yield, ion temperature and the liner density. Secondly, it is difficult to transfer detector calibrations due to the complexity of the experimental geometry versus the calibration geometry. This is in stark contrast to time-of-flight measurements made at the NIF and OMEGA facilities, where the source to detector lines-of-sight are designed specifically to minimize neutron scattering and are well collimated. Examples of time-of-flight data from a typical MagLIF target

are shown in Figure 5 and Figure 6 to illustrate this point. The data shown in Figure 5 were taken with the Hamamatsu mod 5 PMT at the 11.5-meter location and Figure 6 shows acquired data from the 9.5-meter detector. Shown in each of these figures is the D-D neutron NTOF signal with an idealized Gaussian fit on the left, and the residual of the fit on the right. The residual in each figure shows the inherent structure in the signal where the data departs the most from the idealized Brysk model in the primary peak and the influence of the beryllium liner in the continuum region.

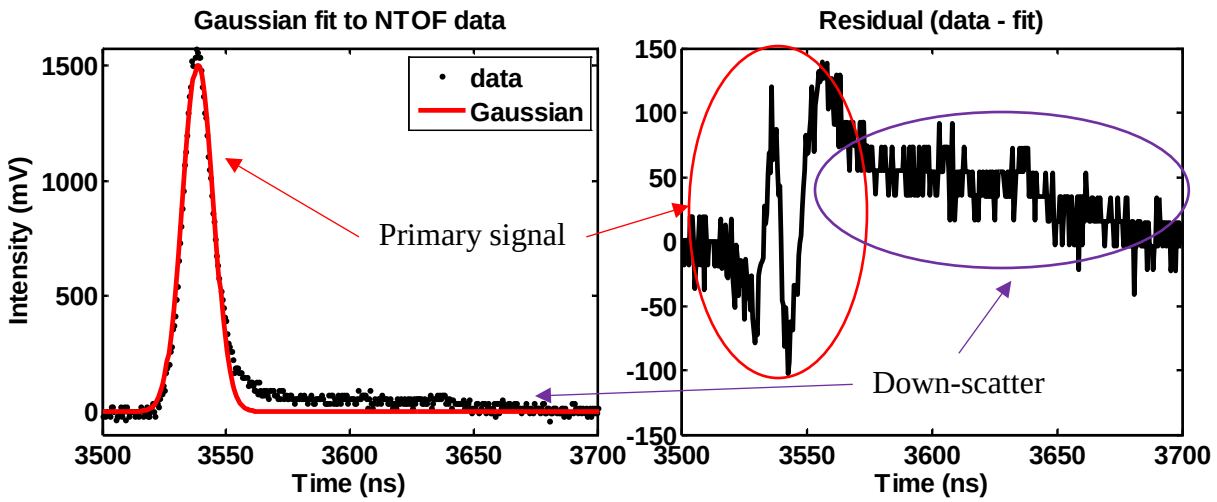

Figure 5 LOS 270 NTOF signal from the Hamamatsu side of the dual PMT, 11.5 meter detector

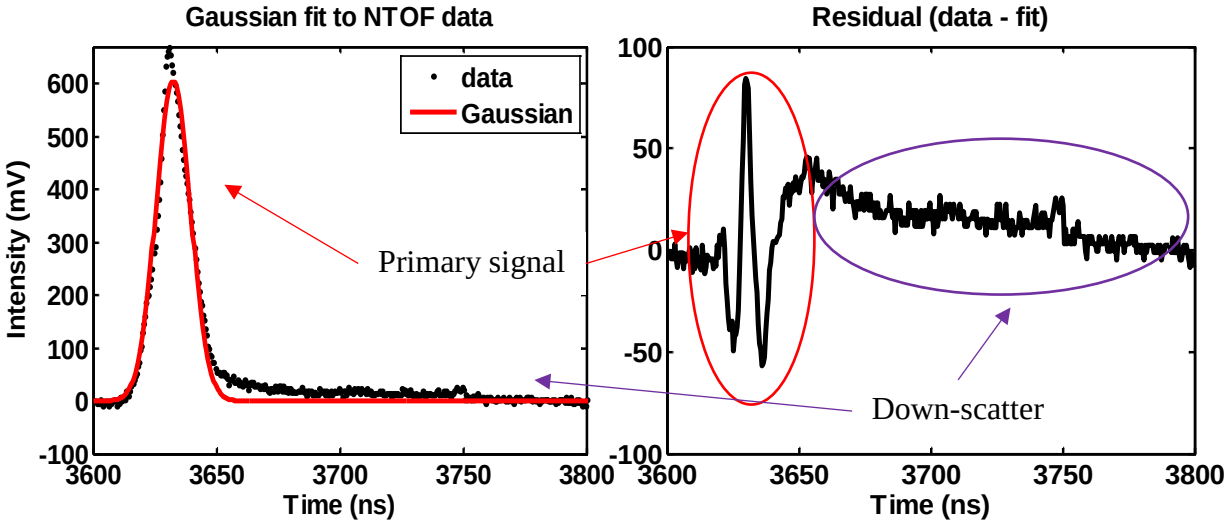

Figure 6 LOS 270 NTOF signal from the Photek side of the dual paddle

However, the biggest challenge with neutron measurements at the Z-facility is the large bremsstrahlung pulse that is present on every experiment. When Z is fired, 20 MA of current converges on the target, which produces a large amount of high-endpoint, energy bremsstrahlung emission from streaming electrons. These photons can have endpoint energies in excess of 10 MeV, which is above the threshold energy for many photon-induced reactions. In fact, the bremsstrahlung directly interferes with the inference of the neutron yield through the primary yield diagnostic: activation analysis of indium [54]. Since the bremsstrahlung can saturate the scintillation detectors, several inches of lead is required directly in the detector line-of-sight to reduce the number of photons incident on the detector. In addition to down-scattered neutrons and the bremsstrahlung, additional shielding material increases the potential for a large prompt gamma-ray background from neutron activation. To complicate things further, the structure seen in the NTOF signals can also be the result of EMP pick-up in the PMT or noise induced by the digitizer used in the acquisition system. Thus, there are many contributions to the measured signal that need to be accounted for prior to determining the ion temperature, yield or liner density.

2.3 Focus of this work

For this work, a dual PMT NTOF detector will be fully characterized by measuring the instrument response function and detector sensitivity using a novel experimental technique. This characterization will be applied to results obtained from a high resolution transport model of the MagLIF geometry, developed using MCNP6. The results of this effort constrain the inferred ion temperature, neutron yield, and beryllium liner density for a specific MagLIF implosion. The rest of this thesis will describe the relevant physics of an NTOF detector, a novel experimental method for extracting the instrument response function and detector sensitivity will be presented along with the results from these measurements. In addition, a proof-of-principle methodology for inferring the ion temperature, yield, and liner density values for past and future MagLIF experiments conducted at the Z-pulsed power facility will be discussed.

3 Theory

3.1 Relevant physics of organic scintillators

The use of organic scintillators provides a number of advantages for measuring pulsed neutron sources, where timing and count rates are of a concern. They are affordable, can be fabricated into any shape, have nanosecond timing characteristics and a relatively high hydrogen to carbon atom ratio of 1.1. Organic scintillators typically come in the form of liquid or plastic media and will be briefly described here. A more complete and thorough discussion of organic scintillators can be found in the seminal work of Birks [55]. Organic scintillator detectors, in general, work by absorbing kinetic energy that is lost from charged particle interaction with the molecular components of the scintillator. The absorption of energy causes the excitation of various molecular states that de-excite back to the ground state and in the process re-emit energy in the form of visible light that is subsequently converted to a measurable current using a PMT. The number of scintillation photons created and the energy each emitted photon carries is a statistical process dependent on the energy level structure of the organic molecules present in the scintillating medium. These values will vary as a function of the charged particle specie interacting and the quantity of kinetic energy that is deposited. Fast electrons in the low MeV range interacting in typical plastic scintillators result in the emission of 8 to10 photons having energies in the range of 3 to 4 eV per photon for every keV absorbed within the scintillator [56]. This value is rather low when compared with sodium iodide crystals, which produce ~ 40 photons per keV absorbed. As a result, sodium iodide crystals, when compared with organic scintillators, have superior energy resolution. The time it takes to create and collect visible light for organics, however, is in the nanosecond range, whereas the time response for sodium iodide crystals is in the microsecond range. This difference makes organic scintillators a superior choice when timing is of a concern.

The timing properties of the scintillator are highly dependent on the molecular electronic states within the scintillator. The de-excitation of the molecular states can be characterized by two different physical phenomena – prompt fluorescence and delayed phosphorescence. Prompt fluorescence occurs with a lifetime in the sub-nanosecond time scale and comes from the direct occupation and de-excitation of singlet molecular states. Delayed phosphorescence occurs from the occupation of the triplet states from mobile excitons that occupy these states through inter-

system crossing. These states de-excite later in time with lifetimes that can vary from a few nanoseconds to hundreds of nanoseconds. Since these processes are defined mathematically with a differential rate equation and a rate constant that defines the lifetime, the solution for the scintillator decay has an exponential form. The number of states available will dictate how many decay components are required in the coupled rate equations [57]. This process is also dictated by the species of the charged particle. Heavier ions create much more damage along the ionization path. These damage sites alter the material properties and allow for the occupation of more triplet states. This larger production of triplet states is what causes the longer scintillator decay times observed with ions when compared with electrons. Thus, more triplet states are occupied as the stopping power is increased. For some applications the population of triplet states is a desired effect since pulse shape discrimination can be employed to distinguish between photon and neutron induced events [56].

The time dependent relationship between light emission and energy deposition for an organic scintillator is best described by Birks formula [55], as shown in equation 3-1.

$$\frac{dL}{dx} = \frac{S\frac{dE}{dx}}{1 + kB\frac{dE}{dx}} \qquad [3-1]$$

In this equation dL/dx is the amount of light produced per unit path length, dE/dx is the energy loss per unit path length, S is the scintillation efficiency, B is the ionization density, and k is the fraction of the ionization density that leads to quenching. In the absence of quenching (k is small) or if dE/dx is comparatively small, Birks formula predicts that the amount of light produced per unit energy loss becomes a constant, S. This is only the case for gammas and fast electrons [56].

$$\frac{dL}{dx} = S\frac{dE}{dx} \quad or \quad \frac{dL}{dE} = S \qquad [3-2]$$

In the case of neutron detection where the protons, alpha particles and heavy ions are the particles of interest, the amount of quenching, represented by k, can become large and thus can no longer be neglected. The quenching parameter is a function of particle charge and mass and is a measure of de-excitation processes that do not result in the emission of light, such as energy

loss in the form of heat or molecular vibration. Particles that are more massive will result in less light output due to saturation along the secondary electron tracks. The same phenomenon will occur as the charge of the particle increases. Since the quenching parameter is specie dependent and the scintillation efficiency is dependent on the properties inherent to the system (type of scintillator material, reflective materials around the scintillator, and the PMT) these values are often determined empirically and represented with a common unit - MeV_{ee} (MeV electron equivalent). MeV_{ee} is a normalization factor relating the amplitude of a measured signal from a charged particle to that of a measured signal created by a 1-MeV electron. Thus, for a particular ion specie and energy deposited, the absolute pulse amplitude can be determined if the signal amplitude from a 1-MeV electron is known. Light output curves measured by Batchelor et al. relating MeV_{ee} to energy deposition for various species of charged particles are shown in Figure 7 [58]. The relationships measured by Batchelor et al. are shown on a semi-log scale to show the relative difference in the order-of-magnitude of the light output as a function of charged particle type.

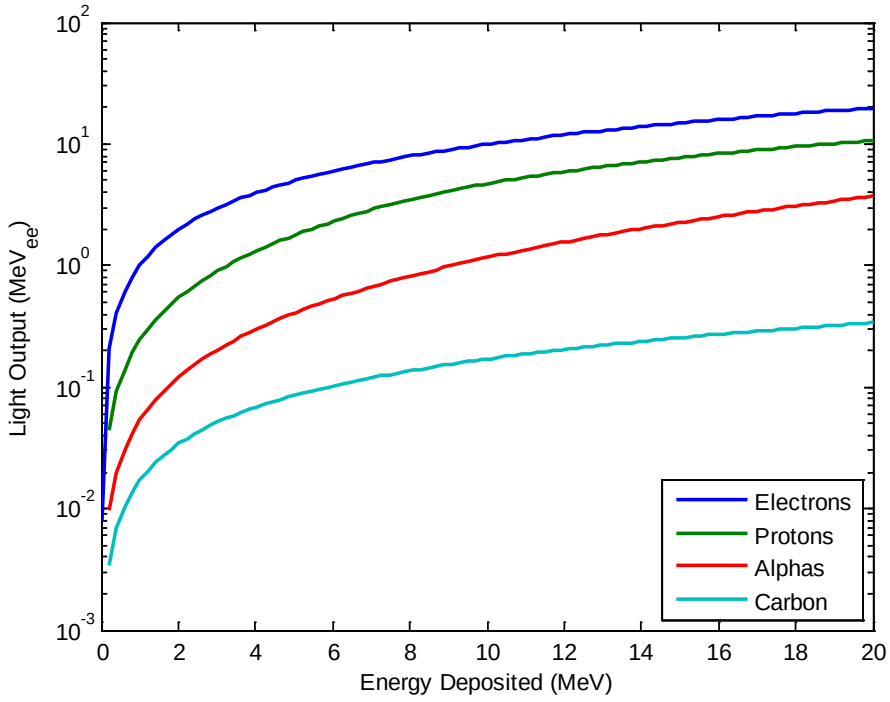

Figure 7 Light output curves, in MeV_{ee} as a function of energy deposition for electrons, protons, alphas, and carbon ions in hydrocarbon scintillators [55]

The light output functions that are of most interest for neutron detection are for elastically scattered protons and carbon ions, and if the energy is high enough, alpha particles are emitted

from the de-excitation of the C-13 nucleus via in-elastic neutron scattering. Shown in Table II are the relevant, charged-particle-producing reactions for neutron energies below 15 MeV in a plastic scintillator with a hydrogen-to-carbon ratio of 1.10 [59]. The microscopic cross-sections used in calculating these values are for ^{1}H and elemental carbon. These values can be found in reference [59]. Also shown in Table II is the Q-value for each reaction, the reaction threshold energy, the mean free path for each reaction channel, and the normalized probability of each occurrence for both D-D and D-T neutron energies. The probability distribution of reactions relevant to D-D neutrons is dominated by elastic scattering with hydrogen, while elastic scattering with carbon provides only a second order contribution.

Table II Reactions of interest for a plastic scintillator at neutron energies below 15 MeV[56]

Reaction	Q-val. (MeV)	E_{Th} (MeV)	$\Sigma_{2.45}$ (cm^{-1})	$P(\Sigma_{2.45})$ (%)	$\Sigma_{14.1}$ (cm^{-1})	$P(\Sigma_{14.1})$ (%)
$^{1}H(n,n)^{1}H$	0.00	------	2.58	64.3	0.683	38.1
$^{12}C(n,n)^{12}C$	0.00	------	1.59	35.7	0.827	41.6
$^{12}C(n,n')^{12}C$ (L1)	-4.40	4.81	------	------	0.210	10.6
$^{12}C(n,n')3\alpha$ (L2)	-7.65	8.30	------	------	1.93e-2	1.0
$^{12}C(n,n')$ 3α (L3)	-9.64	10.4	------	------	6.66e-2	3.4
$^{12}C(n,n')$ 3α (L4)	-10.8	11.7	------	------	2.00e-2	1.0
$^{12}C(n,n')$ 3α (L5)	-11.8	12.8	------	------	1.20e-2	0.6
$^{12}C(n,n')$ 3α (L6)	-12.7	13.8	------	------	6.52e-3	0.3
$^{12}C(n,\alpha)^{9}Be$	-5.70	6.18	------	------	6.99e-2	3.5

However, since the light yield for protons is generally two orders of magnitude greater than that for carbon ions, the detector response to D-D neutrons is almost entirely (> 99%) from elastically scattered protons. Alternatively, for D-T neutrons, the frequency of carbon interactions becomes much more significant and the production of alpha particles from the inelastic scattering channels that exist above 8.3 MeV become relevant. Again, if the magnitude of the light yield is included in the equation the dominant mechanism is still elastically scattered protons (> ~95%).

3.2 Methods for measuring light output relationships for charged particles

Since elastically scattered protons are the most dominate reaction for neutron measurements well below ~ 30 MeV, several groups [60, 61, 53, 58, 62, 63] have measured proton light yield curves for a variety of scintillators utilizing a variety of techniques. Only the time-of-flight and maximum pulse height methods that motivated this work will be briefly presented here. The time-of-flight method relates a measured signal to a discreet neutron energy by utilizing the relationships shown in equations 1-5 and 1-6, which relates the neutron energy to the time it takes the neutron to travel some distance. The maximum pulse height method, on the other hand, relates the value of the measured signal to the maximum proton energy. The maximum proton energy that can be obtained in a single neuron collision is equivalent to the full energy of the incident neutron as described by the kinematics of a two-body problem. Results from these different works are compared in Figure 8 where the scintillator type and the group responsible for the measurement are noted in the legend. It should be noted that the Pozzi et al. curve was only validated up to 6.5 MeV [62].

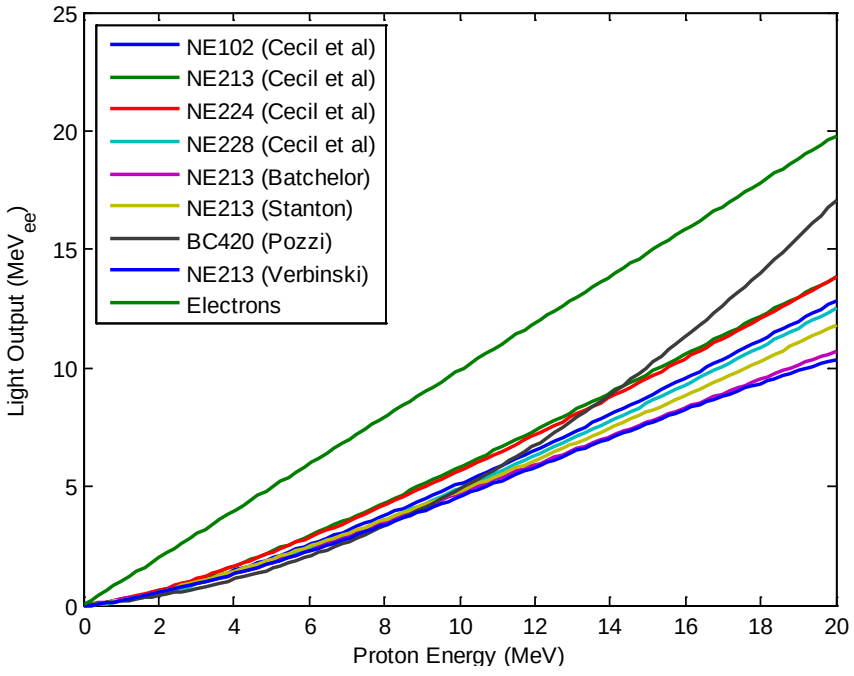

Figure 8 Light output curves in MeV$_{ee}$ for protons and various organic scintillators [64] [58] [65] [62] [66]

In 1961, Batchelor, et al. reported the first measurements of a neutron induced recoil proton response function for the liquid organic scintillator NE-213. Their detector design was similar as to what is used on the Z-machine today, where the scintillator is viewed on either side by two individual, independent photomultiplier tubes [58]. D-D and D-T neutrons were produced using a 6 MV Van de Graaf accelerator. The resulting neutron energies ranged from 2 to 21 MeV. The accelerator was pulsed in 2 nanosecond intervals at a current of 5 MA. The neutron energies were inferred by measuring the two PMT signals in coincidence, where the coincidence signal served as a start signal for the data acquisition and the signal obtained from the accelerator beam stopped the acquisition. The relative time difference in the two signals provided the differential time spectrum. They used these results to approximate a solution to Birks equation for the detector response to recoil carbon ions and alpha particles. These relationships were shown previously in Figure 7. In addition to their experimental work, they developed a Monte Carlo model coupled with their results to predict the performance of other scintillators. A similar set-up was used by Brown et al. to obtain the IRF and the light output correlation for a bi-benzyl crystal [45]. Pozzi et al. [62] also employed the time-of-flight method, but they utilized a time-to-amplitude converter (TAC) to measure the time-of-flight of neutron emissions from a Cf-252 source. The time-of-flight was determined from the coincidence measurement of the prompt gamma emission and corresponding neutron.

J.B. Czirr et al. [60] experimentally obtained light output functions for several types of scintillators to investigate the difference in their response. In their work, they chose to use a maximum pulse height method. In this method, due to poor energy resolution and particle straggling, the maximum recoil proton energy is assumed to occur at the half-height of the maximum amplitude pulse. This same method was used by Verbinski et al. to obtain their light output functions [66]. This method is similar to the Compton edge method for measuring the response to Compton scattered electrons as described in references [67] [68].

3.3 Applying correlations through modeling

The utility of measuring and developing these empirical relationships for instrument and charged particle response functions is to provide a predictive capability for future experiments. The response functions are implemented in a computer code, along with the other relevant physics, to solve a problem using either analytical, deterministic, or statistical (Monte Carlo) methods.

While several groups have developed codes to calculate the detection efficiency of organic scintillators, only a select few that have motivated this work will be discussed here [69] [70] [71] [72] [73] [64].

In 1964 Richard J. Kurz from the University of California at Berkeley conducted some of the earliest research in this area [74]. He developed an analytical code to calculate the detection efficiency (the number of measurable events per incident neutron above some threshold value) for an organic scintillator for various incident neutron energies. This work is unique in that Monte Carlo methods at this time were far more preferential. The number of measurable events that would occur were inferred by calculating the total number of reactions that occurred within some scintillator volume for each relevant reaction channel, which were shown previously in Table II. Based on the differential cross-section values and the relevant kinematics he was able to calculate the energy distributions of the secondary charged particles from primary and secondary neutron interactions. These values were then folded with the appropriate response functions, provided by Gooding and Pugh, to determine the relative amplitude for each event with the assumption that all the particle energy is deposited in the scintillator. This work assumed uniform neutron irradiation, cylindrical symmetry, and no more than two interactions per source neutron. This formalism was validated with some degree of uncertainty up to incident neutron energies of 90 MeV. However, with his simplifications, the method suffered when the scintillator size exceeded that of the incident neutron mean-free-path and when tertiary and higher order neutron interactions become relevant.

In 1971 Noel R. Stanton extended the capabilities of the Kurz code by converting it from an analytical to Monte Carlo formulation [65]. The change in formalism allowed for uniform neutron irradiation on the face of both rectangular and cylindrically shaped scintillators and the neutron energy could be either mono-energetic or sampled from an energy distribution. The biggest improvement was allowing for higher-order neutron interactions, which significantly improved the predictive capability for larger scintillators. Using the Monte Carlo approach allowed for a single neutron to be tracked through the scintillator until it reached an irrelevant energy or escaped. Throughout each neutron track, the reaction type, energy deposited, and time histories were kept. Stanton also improved upon the output of the calculation. In addition to the efficiency calculation, he included a pulse height distribution that could be convolved with a

Gaussian energy broadening function to account for the statistical processes in the scintillator and the PMT. This code was validated up to incident neutron energies of 300 MeV. This version of the code underwent another overhaul in 1979 by Cecil et al. from Kent State University [64]. They included updated differential cross-section data, new light output curves relating MeV_{ee} to energy deposition, relativistic kinematics to account for higher energy neutrons, and range effects to account for charged particle slowing down.

Meanwhile, in 1965 a group from Oak Ridge National Laboratories was developing a general Monte Carlo transport code, O5R [75]. Consequently, this code was written for the CDC-1604A supercomputer that was invented just eight years prior by Seymour Cray. This was the first time a technical code would be processed on a super computer. Unlike Monte Carlo programs of today, where the cross-sections are treated as continuous, this code utilized cross-section groups. The cross-section data were divided into 12 energy super-groups from 7×10^{-5} eV to 77.13 MeV, where each super-group contained 128 sub-groups. Within each super-group 200 to 2000 neutrons were available for transport in a maximum number of 16 regions, with an unlimited number of nuclides in each region. This code was groundbreaking in the size and type of problem it was capable of solving.

In 1968 R.E. Textor and V.V. Verbinski adapted the code O5R to O5S to develop a predictive capability that included detector response [76]. The code assumed mono-energetic neutrons incident on the face of a cylinder or along the curved surface of the cylinder normal to the incident neutron beam. The light output function they used for protons was measured in their experiment and then implemented in the code. To correct for small fluctuations in the response they tailored the output curves for alphas and carbon ions to match the data. This code was experimentally validated up to incident neutron energies of 20 MeV. Much like the Stanton output, the calculation produced a histogram distribution of pulse height spectra that could later be convolved with a Gaussian function to allow for statistical effects.

Twenty years later in 1988 the O5S code was reconfigured by J.K. Dickens and became known as SCINFUL, for Scintillator full response to neutron detection [71]. The code included a point source of neutrons that could be uniformly distributed in energy or with a Maxwellian distribution. In addition, they included a pulse shape discrimination function, much like what is seen experimentally to differentiate between gamma and neutron events. The last feature

includes light attenuation in the scintillator prior to reaching the PMT. This program was validated up to incident neutron energies of up to 80 MeV. The O5S and SCINFUL codes both assume all charged particle energy is deposited locally within the volume of a cylindrical scintillator.

In 2002 another Monte Carlo code, MCNP-PoliMi, which is short for "Politechnico di Milano," where the code was developed from the general Monte Carlo code MCNP4C [72]. This code, unlike its predecessors, is capable of modeling a much more detailed experimental geometry. This was the first code that did not assume a uniform neutron irradiation and could account for neutron scattering from other materials into the scintillator. In addition, MCNP-PoliMi tracks individual reaction types and the energy deposited for each interaction. These results are multiplied by a user defined light output correlation and then summed over a user defined pulse generation time. To date this is the most realistic transport model used to infer detector sensitivities. This code underwent a transformation to MCNPX-PoliMi in 2012, which include the same capabilities as MCNP-Polimi, but with additional features to expand its problem solving capability [77]. MCNPX-Polimi is designed to process individual reactions and is capable of charged particle transport, but the calculation does not do so and still assumes full energy deposition within the scintillator. This code, using the light output functions they measured, was validated up to incident neutron energies of 6.5 MeV, well below the carbon inelastic reaction that produces multiple alpha particles [78].

3.4 Transport in MCNP6

Mathematically, the distribution of neutrons for any problem can be described in space, angle, energy, and time by the linear Boltzmann transport equation as shown in equation 3-3.

$$\frac{1}{v}\frac{\partial\psi(\vec{r},E,\vec{\Omega},t)}{\partial t} = Q(\vec{r},E,\vec{\Omega},t) + \iint \psi(\vec{r},E',\vec{\Omega}',t)\Sigma_s(\vec{r},E'\to E,\vec{\Omega}'\to\vec{\Omega})d\vec{\Omega}'dE' - [\vec{\Omega}\cdot\nabla+\Sigma_T(\vec{r},E)]\cdot\psi(\vec{r},E,\vec{\Omega}',t) \quad [3-3]$$

This equation can be described as a continuity equation, where the gains are equivalent to the losses, in time, energy, and space for the angular dependent neutron flux, ψ. The terms on the right side of this equation, from left to right, are the external source, the scattering term, leakage

term, and the collision operator. When this equation is applied to a MagLIF geometry the external source represents the isotropic emission of fusion neutrons created in the plasma and the multiplication term that is often seen in this equation can be neglected since no fissionable material is present. The constants in this equation, Σ_s and Σ_T are defined for a specific volumetric region of a specified composition at a given neutron energy.

In the general sense this equation is unsolvable and requires significant simplification to make it even somewhat tractable. Often these simplifications, which are made in space, time, or energy, can give a representative solution, and if the geometry is simple enough, a first order solution. In other words, simplification of this equation leads to an exact result to an approximate problem. Monte Carlo methods, on the other hand, provide approximate solutions to exact problems. This characteristic is why Monte Carlo algorithms are usually the best option for obtaining solutions where more complex geometries are present. The downfall of using Monte Carlo methods is a solution can only be obtained if, and only if, each neutron history is independent and identically distributed. To meet this requirement, a sufficient number of neutron histories need to be processed to provide a statistically relevant answer, which can make obtaining a solution computationally expensive. For this work, the Monte Carlo code MCNP6 will be used to solve the transport equation. MCNP6 is a very powerful and well-established tool for modeling radiation transport in complex geometries [54]. The advantage to using this code is that MCNP is maintained by Los Alamos National Laboratories and is continually updated and validated by the larger nuclear community.

MCNP solves the transport equation implicitly by removing the dependence of the angular flux by tracking both primary and secondary neutrons through all angles of incidence and geometric regions. Analytically this reduces equation 3-3 to equation 3-4, which is now in terms of the scalar neutron flux.

$$\frac{1}{v}\frac{\partial \phi(\vec{r},E,t)}{\partial t} = Q(\vec{r},E,t) + \int\int \phi(\vec{r},E',t)\Sigma_s(\vec{r},E' \rightarrow E,\mu)dE'd\mu \qquad [3-4]$$
$$-\nabla \cdot \vec{J}(\vec{r},E,t) + \phi(\vec{r},E,t)\Sigma_T(\vec{r},E)$$

For a given volumetric region, defined by the spatial vector $\vec{r}$, the scalar neutron flux is the product of the neutron density and the neutron velocity.

$$\phi(E,t,r) = \int \psi\left(E,t,\vec{r},\vec{\Omega}\right)d\vec{\Omega} = v(E,t)N(\vec{r}) \qquad [3-5]$$

Even in terms of the scalar neutron flux, analytically equation 3-4 is still unsolvable due to the coupling of the leakage term, which is now in terms of a current (J), the scattering term and the collision operator. Consequently, these three terms are of most interest to this problem. For any region outside the scintillator these terms describe the number of neutrons that are either scattered into the detector or removed by absorption in which case photons could be generated. Within the scintillator the collision operator describes neutron removal from the scintillator through absorption; the leakage term defines the number of neutrons leaving the scintillator without interaction while the scattering term describes the change in angle and energy of the interacting neutrons.

The neutron distribution in space, time, and energy from elastic scattering interactions (right hand side of equation 3-4, first term) is explicitly dependent on the differential neutron scattering cross-section denoted by $\Sigma_s(\vec{r}, E' \rightarrow E, \mu)$. This term describes the probability of a neutron being down-scattered to energy E from an initial energy E' into some scattering angle μ. More importantly, for the purposes of neutron detection, this term also describes the recoil proton production rate within a scintillator volume. The desired relationship for inferring the number of protons produced within a specific volume at a certain time and energy is given by equation 3-6.

$$N_h(t,E) = \iint \phi(E',t)\Sigma_s(E' \rightarrow E,\omega)dE'd\omega \qquad [3-6]$$

The only unknown in equation 3-6 is the differential cross-section that defines the probability of a proton being scattered into an energy E from an interaction with a neutron of energy E' into some angle ω. The proton differential cross-section can be determined using kinematic relationships and the neutron differential cross-section. For convenience the derivation is included in the next section.

3.5 Kinematic relationships and the differential cross-section

The neutron differential cross-section (barns per steradian) that is often used in neutron transport can be defined as the probability of a neutron being emitted into a given center of mass angle after an elastic scattering interaction. These values are well known for many isotopes and can be found in a variety of libraries. For this work, the cross-sections used throughout come from the ENDF7.1 evaluation that is maintained by Brookhaven National Laboratories [59]. The differential neutron cross-section can be transformed from the scattering angle in the center-of-mass frame to a differential of any kinematic variable of either the neutron or proton as long as the functional dependence between the two quantities is known. The solutions to the two-body kinematic equations are well known relationships, but their derivation will be included here for convenience. A description of the reaction kinematics in the center-of-mass and lab frames of reference are shown in Figure 9. In this figure, the energy and mass of the projectile particle (neutron), target nucleus (proton), recoil particle (scattered neutron), and recoil nucleus (scattered proton), are denoted by subscripts 1, 2, 3, and 4 respectively. In interactions involving elastically scattered neutrons, the projectile and recoil particle are the same and the target and recoil nucleus are the same.

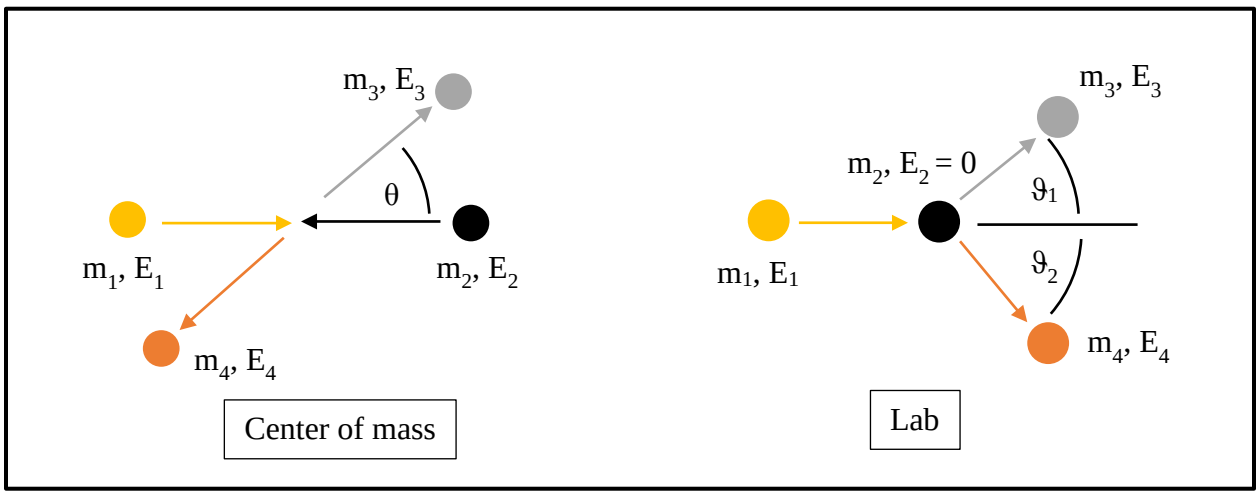

Figure 9 Center of mass and lab kinematic relationships for a two body problem

The kinematic variables in the lab reference frame that are of interest: the angle of emission and the kinetic energy for the recoil particle and nucleus, can be written functionally in terms of the

scattering angle, theta, in the center-of-mass and can be transformed using the following non-relativistic equations, 3-7 through 3-13, for a two-body problem. The following definitions, equations 3-7 to 3-9, make the kinematic equations much more tractable, and thus will be used throughout. Here A is the mass ratio of the projectile and the target nucleus, A' is the mass ratio of the recoil and projectile particles, and μ is the cosine of the scattering angle in the center of mass frame.

$$A = \frac{m_2}{m_1}, A' = \frac{m_3}{m_1}, m_2 = m_4, \mu = \cos(\theta) \qquad [3-7]$$

$$\beta = \left(\frac{A}{A'}(A + 1 - A')\left[1 + \frac{(1+A)}{A}\frac{Q}{E_1}\right]\right)^{1/2} \qquad [3-8]$$

$$\gamma = \frac{\beta A'}{(A + 1 - A')} \qquad [3-9]$$

Using these definitions, the ejected particle (scattered neutron) and the lab angle into which the particle is emitted are given by equations 3-10 and 3-11, respectively.

$$E_3 = \frac{E_1 A'}{(1+A)^2}(\beta^2 + 1 + 2\beta\mu) \qquad [3-10]$$

$$\omega_1 = \cos(\vartheta_1) = \frac{1 + \beta\mu}{\sqrt{(\beta^2 + 1 + 2\beta\mu)}} \qquad [3-11]$$

Similarly, the energy and lab angle of the recoil nucleus can be found using equations 3-12 and 3-13.

$$E_4 = \frac{E_1(A + 1 - A')}{(1+A)^2}(\gamma^2 + 1 - 2\gamma\mu) \qquad [3-12]$$

$$\omega_2 = \cos(\vartheta_2) = \frac{1 - \gamma\mu}{\sqrt{(\gamma^2 + 1 - 2\gamma\mu)}} \qquad [3-13]$$

In an elastic scattering event with a neutron ($A' = 1, Q = 0, \beta = A, and\ \gamma = 1$) equations 3-10 to 3-13 simplify and reduce to the neutron elastic scattering relationships given by equations 3-14 to 3-17.

$$E_3 = \frac{E_1}{(1+A)^2}(A^2 + 1 + 2A\mu) \qquad [3-14]$$

$$\omega_1 = \cos(\vartheta_1) = \frac{1 + A\mu}{\sqrt{(A^2 + 1 + 2A\mu)}} \qquad [3-15]$$

$$E_4 = \frac{2E_1 A}{(1+A)^2}(1-\mu) \qquad [3-16]$$

$$\omega_2 = \cos(\vartheta_2) = \left(\frac{1-\mu}{2}\right)^{1/2} \qquad [3-17]$$

The probability of a recoil particle having an energy, E_4 from an interaction with a neutron with energy E_1 can be found by applying the chain rule to the differential cross-section, as shown in equation 3-18.

$$\sigma_s(E_1 \rightarrow E_4) = \frac{d\sigma}{dE_4} = \frac{d\sigma}{d\mu}\frac{d\mu}{dE_4} \qquad [3-18]$$

In this equation, $\frac{d\sigma}{dE_4}$ is the differential cross-section with respect to the energy of the recoil nucleus in the lab frame, $\frac{d\sigma}{d\mu}$ is the differential cross-section with respect to the cosine of the scattering angle in the center of mass and $\frac{d\mu}{dE_4}$ is the differential cosine of the scattering angle in the center-of-mass frame with respect to the recoil nucleus energy in the lab frame. Since the recoil particle energy is written as a function of the scattering angle cosine in the center of mass, the differentiation is more tractable using an implicit technique as shown in equations 3-19a, b, and c.

$$\frac{d}{dE_4}[E_4] = \frac{d}{dE_4}\left[\frac{E_1(A+1-A')}{(1+A)^2}(\gamma^2+1-2\gamma\mu)\right] \qquad [3-19a]$$

$$1 = \frac{d\mu}{dE_4}\left[\frac{-2\gamma E_1(A+1-A')}{(1+A)^2}\right] \qquad [3-19b]$$

.

$$\frac{d\mu}{dE_4} = \frac{(1+A)^2}{2\gamma E_1(A'-A-1)} \qquad [3-19c]$$

Equation 3-19c can now be substituted into equation 3-18 to calculate the total number of protons produced with energy E, at time t, from an interaction with a neutron of energy E' within a specific volume V.

$$N_h(t,E) = \int \phi(E',t)\Sigma_s(E' \to E)\frac{V(1+A)^2}{2\gamma E'(A'-A-1)}dE' \qquad [3-22]$$

Notice the angular dependence of the secondary particles is no longer in the equation. By applying the chain rule expansion, the angular dependence was implicitly included. Since the solution to the MCNP calculation is the scalar neutron flux that is discretized in N time bins and M energy bins, a more appropriate form for equation 3-22 is a summation. This summation, shown in equation 3-23, gives a matrix solution for the recoil proton distribution in time and energy space.

$$N_h(t_k,E_j) = \frac{V(1+A)^2}{2\gamma(A'-A-1)}\sum_{i=1}^{M}\frac{\phi_i(E_i',t_k)\Sigma_s(E_i' \to E_j)}{E_i'}\Delta E_i' \qquad [3-23]$$

Notice that this equation is only a source description for the number of protons N_h, produced with energy E_j within time t_k from elastic interactions with a neutron of energy E'_i. The loss term in this equation is neglected and all protons are assumed to deposit energy locally and come to rest within the scintillator volume. The other parameters in this equation are as follows: $\phi(E_i,t_j)$ is the energy and time dependent scalar neutron flux in units of neutrons per cm^2 obtained from

the MCNP transport calculation, V is the scintillator volume in units of cm^3, and $\Sigma_s(E_i' \rightarrow E_j)$ is the tabulated differential cross-section in terms of cm^{-1}. It should be noted since the neutron flux is discretized into discreet bins, the mid-point of each bin is the assumed value.

With the recoil proton distribution known in energy and time the associated light output from the recoil protons can be determined. For the protons the Stanton approximation to Birks equation will be used throughout where the light yield, Ly, in MeV_{ee} is produced from a recoil proton with energy, E as shown in equation 3-24.

$$L_y = -10.68 * \left(1 - exp(-0.07E^{0.89})\right) + 0.929E \qquad [3-24]$$

The total solution, shown in equation 3-25, can be found by summing over all possible proton energies. This gives a solution for the time dependent light output, which is equivalent to an experimentally obtained NTOF signal.

$$L_t(t_k)[MeVee] = \frac{V(1+A)^2}{2\gamma(A'-A-1)} \sum_{j=1}^{K} \sum_{i=1}^{M} \frac{\phi_i(E_i', t_k)\Sigma_s(E_i' \rightarrow E_j)}{E_i'} \Delta E' \, \Delta E_j Ly_j(E_j) \qquad [3-25]$$

If this equation is multiplied by the time interval Δt and then summed over all time bins, as shown in equation 34, the solution is in terms of MeV_{ee}-seconds and is equivalent to an integrated NTOF signal, which has units of volt-seconds.

$$S_t[MeVee - sec] = \frac{V(1+A)^2}{2\gamma(A'-A-1)} \sum_{k=1}^{N} L_t(t_k)\Delta t \qquad [3-26]$$

The quantities obtained in equations 3-25 and 3-26 can be convolved with the experimentally obtained IRF using fast Fourier transforms to give an answer that is quantitatively equivalent to the experimentally observed NTOF signal.

4 IRF and Sensitivity Experiment

4.1 Experimental Set-up

The instrument response function and the detector sensitivity for a typical current integrated NTOF detector were obtained by measuring digitized waveforms of single D-T neutron interactions with the plastic scintillator. Neutrons were produced at Sandia National Laboratories' Ion Beam Laboratory (IBL) using a 300 kV Cockroft-Walton generator to accelerate a 2.5-μA beam of 175-keV D^+ ions onto a stationary, 2.6-μm thick, ErT_2 target. The resulting neutron energy spectrum from the D(T,α)n nuclear reaction is found from the kinematic relationships associated with accelerating a D^+ ion of known energy onto a stationary tritium nucleus. Two surface barrier detectors (SBD) at fixed angles of 110 and 165 degrees with respect to the beam were used to measure the corresponding alpha particles that were emitted into these proscribed solid angles. These detectors are at a fixed distance, 30.5 cm, and are collimated such that the solid angle subtended by the source and detector geometry is very well defined - 54 micro-steradians +/- 3 %. The number of alpha particles measured at each specific angle can be used independently to calculate the number of neutrons emitted into any angle using the Associated Particle Method (APM) [51] [79]. The relevant components of the experimental set-up are shown in Figure 10.

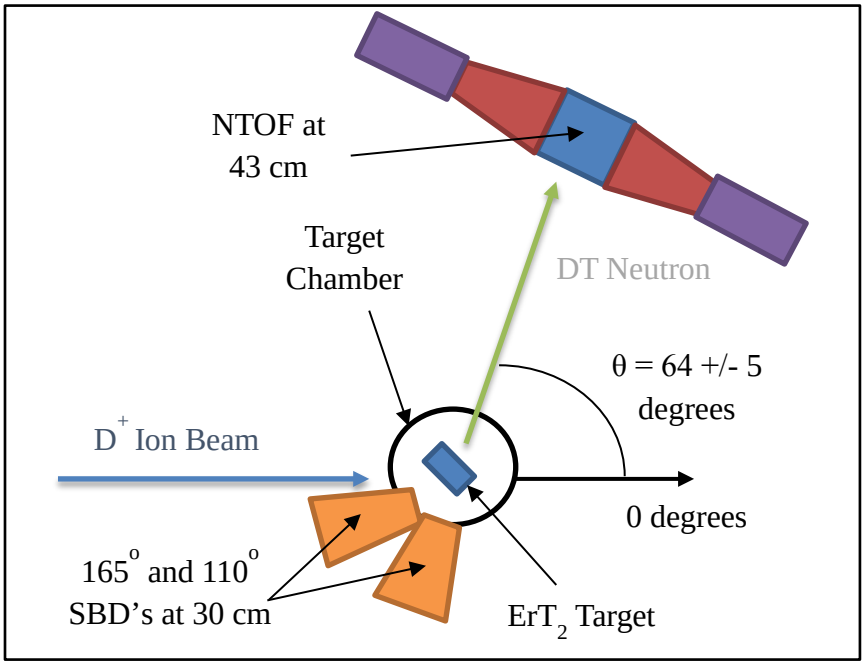

Figure 10 IBL experimental configuration

For these measurements, to ensure the measured signal was from a single neutron, a dual PMT NTOF detector, as described previously in section 2-2, was placed at a specific location such that the 110 degree SBD and the NTOF were in kinematic coincidence. It is important to mention that the coincidence measurement only depends on the emission angle of the D-T reaction products. Since this is a two-body problem the kinematic relationship (see section 3) between the emitted neutron and alpha particle can be calculated exactly. However, the kinematics for this experiment are variable from the dE/dx losses experienced by the D^+ ion in the target. This results in fusion reactions occurring for ion energies ranging from 0 to 175 keV, where 175 keV corresponds to a fusion reaction at the front of the target and 0 keV corresponds to the reaction when the D^+ ion has been fully ranged in the target. These relationships are depicted in Figure 11.

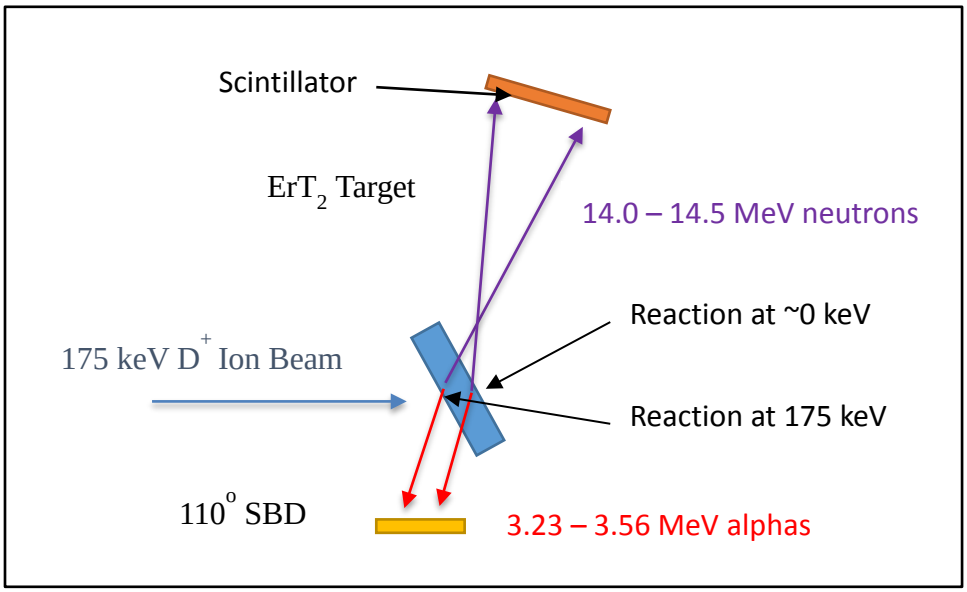

Figure 11 Kinematic relationship that establishes coincidence between the two reactant products

Even though the difference in ion energy is small, this has a significant effect on the kinematics. For a fixed alpha emission into an angle of 110 degrees the neutron emission angle varies between 61 and 70 degrees. This range in angle results in a variation of the incident neutron energy from 14 to 14.5 MeV, where 70 degrees and 14 MeV correspond to fusion at 0 keV. Thus, to establish a coincident measurement with the 110-degree SBD detector, the NTOF needed to be placed at an angle between 61 and 70 degrees with respect to the beam. The optimum neutron emission angle and distance to maximize the number of observed coincident

events was found by weighting the kinematic relationships by the total fusion cross-section at the varying ion energies. This distance is 43.6 cm at an angle of 64 +/- 5 degrees for an acceleration potential of 175 keV. If a more mono-energetic neutron energy is desired, the detector can either be moved further away from the target or collimated to subtend the desired, smaller solid angle.

To establish a coincidence measurement between two independent events, it is necessary to have two similar pulse shapes from the outputs of the two detectors. The challenge with this measurement is that the SBD and NTOF detectors have very different timing and pulse shape characteristics. The timing signal from the SBD pre-amplifier is nominally a 50-ns wide, bi-polar pulse, while the output of a typical PMT is Gaussian in shape and only a few nanoseconds in width. The output signal of each detector was input to an Ortec 584 constant fraction discriminator module to alleviate this difference. The 584 CFD unit has many advantages for this type of measurement. First, the time delay through the constant fraction unit is fixed at nominally 25 ns. Second, there are three available outputs on the CFD module that produce fast, negative signals. Two of these outputs are fixed, Gaussian-shaped, negative-timing pulses with 5 ns widths and amplitudes of 800 mV. The third output, the negative block (BK) output, is a standard, negative-TTL pulse with variable width and a fixed amplitude of 800 mV. The three 584 outputs from each of the two detectors were used to monitor different quantities. The BK outputs were used to monitor individual count rates for both the SBD and NTOF detectors while the two timing outputs were used to establish and monitor the coincidence count rates. A block diagram illustrating the use of the 584 CFD units and other components of the acquisition system are shown in Figure 12.

The coincidence unit chosen for these measurements was the Ortec 4020C logic unit. This unit has a minimum coincidence timing overlap of 3 ns and has less than a 10 ns delay. The positive TTL output from this module was used to trigger the data acquisition by the Tektronix DPO7254 oscilloscope. The fast, negative-timing output from the 4020C was input to a counter to monitor the coincident count rates. The other 584 negative outputs were routed through a time-to-amplitude converter (TAC), where the signal from the SBD 584 served as the start trigger for the TAC acquisition and the time-delayed NTOF 584 output stopped the TAC acquisition. The TAC served primarily as a coincidence monitor and secondarily to observe the relative shift in the PMT throughput delay. The TAC output was routed through a multi-channel analyzer, which

displays the differential time difference between the SBD and NTOF signals. Using both the TAC and the 4020C logic unit provided a redundant monitor of the observed coincident rates. In addition to the coincidence system, other electronics were included to monitor the differential energy spectrum of the alpha particles and was used to infer the number of neutrons emitted into a given angle. A multi-channel scalar was used to monitor the beam current as a function of time. Together these two systems provided information about the target conditions as a function of time.

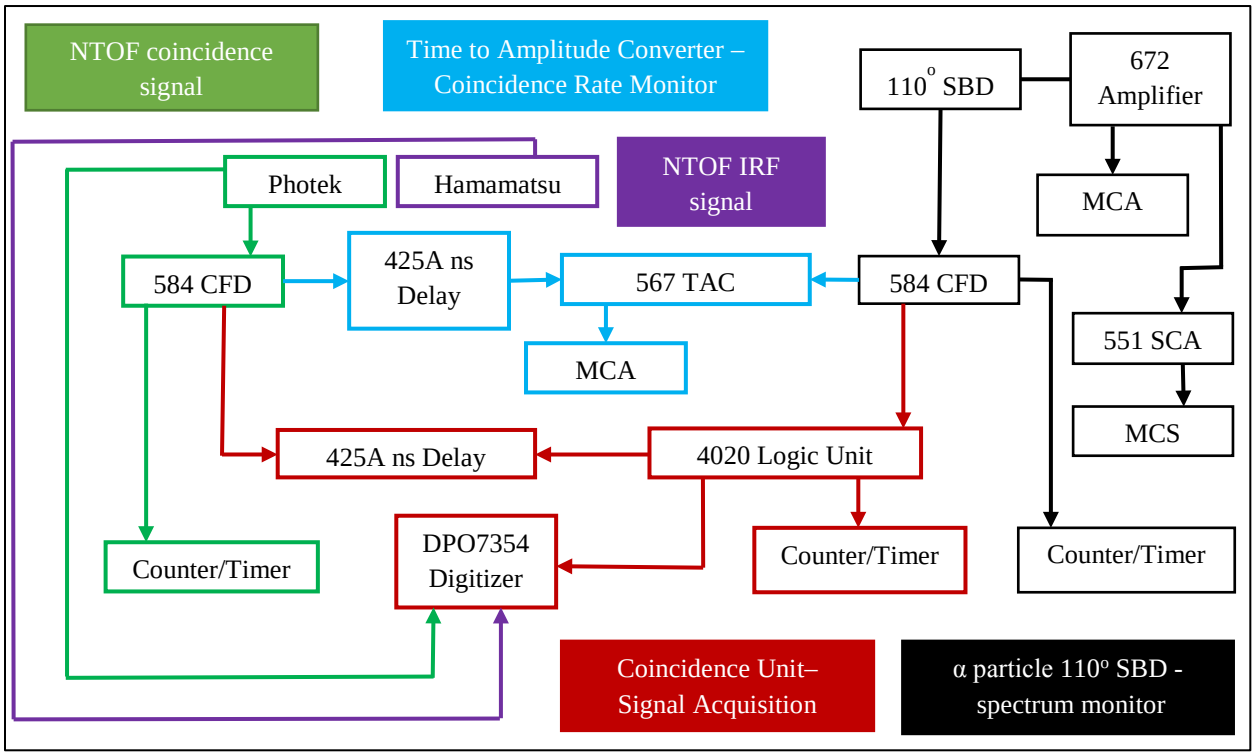

Figure 12 Electronics Configuration for acquiring digital waveforms and various count rates

For each coincident event, the corresponding neutron signals from the Hamamatsu (mod 5) and Photek (PMT240) were collected and saved on a Tektronix DPO7354C digitizer. Viewing both PMT signals at the same time allowed for data to be collected on the non-coincident PMT without adding additional delay or splitting the signal, which can add reflections or structure to the signal of interest by introducing a slight impedance mismatch. The nominal delay to establish coincidence was ~ 54 ns for the mod 5 and ~ 63 ns for the PMT240, which means the PMT240 is faster by 9 ns when compared with the mod 5 PMT. The data for the non-coincident signal were post-processed using the fixed time delay between the tubes to establish whether the signal was

from a coincident neutron or not. The digitizer was set to collect data over an 80-ns interval with 50-ps time resolution at a sampling rate of 2.5 GHz.

The impulse response functions of each PMT were then measured separately as a function of the applied voltage to the PMT of interest. For these measurements the PMT of interest was placed in coincidence with the SBD and one thousand NTOF signal waveforms were collected at each operating point. The applied voltage for the mod 5 was varied from -1.7 to -2.4 kV in 0.1 kV increments and the PMT240 was varied from -3.8 kV to -4.6 kV in 0.1 kV increments. The lower limit on the applied voltage for each tube is where the observed amplitude of the waveform was comparable with the 8-mV minimum discriminator level on the 584 unit. The discriminator level for each bias setting was nominally 25 mV for the PMT if the data allowed and the discriminator level for the SBD was fixed at 15 mV, which corresponds to the lower limit of the alpha energy peak. The alpha energy peak was only observable over a small range of amplitudes. At 25 mV this signal was no longer observable.

The first experiment that was conducted utilized 170 feet of RG-223 standard 50-ohm cable. This cabling was part of an existing infrastructure at IBL for calibrating activation diagnostics, where signal attenuation and dispersion are not of concern. It was realized during the experiment that this particular cabling was too attenuating for the bandwidth of the measured signal to get quality data. As a result, measurements were retaken using a low-loss, 50-ohm, LMR-600 cable. The signal quality was significantly better with the LMR-600, which has an attenuation coefficient at 1-GHz that is approximately a factor of four less than the RG-223. The initial data acquired with the RG-223 cabling were later compensated to correct the cable induced distortions. Details of the compensation correction and analysis of these data are given in Appendix A. The data and analysis presented in the main body of this report are for a D^+ ion acceleration potential of 175 keV and the LMR-600 cable. These experiments were also repeated at a D^+ ion energy of 50 keV. Additional waveforms from experiments conducted at acceleration potentials of 50 keV and 175 keV are presented in Appendices B and C, respectively. Analysis of the 50 keV data is presented in Appendix D and additional analysis for the data taken at 175 keV is presented in Appendix E.

4.2 Experimental Results - Coincidence and Alpha Particle Data Analysis

There are several parameters of interest that can be extracted from the experimental data: the coincident count rate, the relative throughput delay of each PMT, the instrument response function, the detector sensitivity, absolute detection efficiency, and the gain of each PMT. The first experimental observable that will be discussed is the coincidence count rate. Example coincidence curves are shown in Figure 13 for both the Hamamatsu at -2.0 kV (left) and the Photek at -4.2 kV (right).

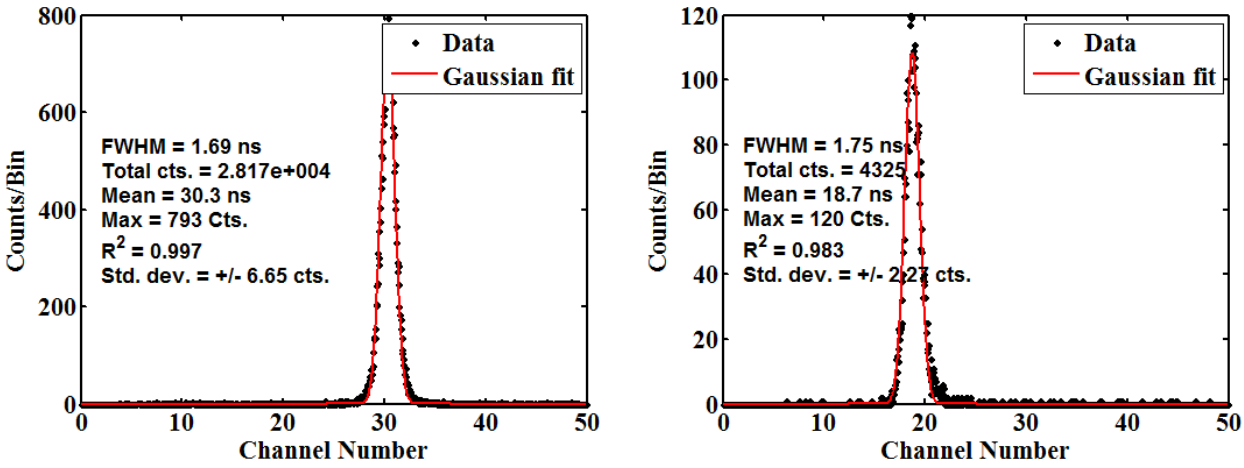

Figure 13 Coincident curves for LMR600 data, Left - Hamamatsu at -2.0 kV, Right – Photek at -4.6 kVThis measurement shows a very precise coincidence between the SBD and NTOF detector.

The coincidence efficiency for a 50-ns interval is 99.2% with an inherent background of random incidentals of 0.8%. This value is inferred by calculating the number of counts in the peak region and the total number of counts within the 50-ns interval. Thus, there is high confidence that these measurements are from neutron interactions and not from prompt photons or cosmic-ray interactions. In addition, the neutron fluence incident on the detector was nominally 10^5 neutrons per second or an average neutron incident rate of one neutron every 10 micro-seconds. Thus detection of multiple neutrons within the 50-ns interval was of minimal concern. Furthermore, when the NTOF detector was placed in anti-coincidence with the SBD detector (at an angle less than 61 degrees or at an angle greater than 70 degrees) a constant count rate comparable to the random incidental rate and no discernible peak region was observed. These anti-coincidence measurement results validate that neutrons were indeed being measured in the coincidence measurements and, hence, validates the overall methodology.

There are two parameters of interest associated with the coincidence curve: the centroid and the FWHM. The coincidence curve is a measure of the relative time difference of the SBD and NTOF signal and therefore the centroid is the mean difference and the FWHM quantifies the distribution. If the SBD detector is held constant and the NTOF bias is varied, then slight changes are observable in in the mean value of the coincidence peak. Thus, this mean value is a relative measure of the PMT throughput delay as a function of applied voltage. This relationship is shown for both PMTs in Figure 14. The relative delay for the Hamamatsu tube decreases as the applied voltage is increased at a rate of 1.5 ns per kV. This rate is consistent with previous experimental results from a previous version of the Hamamatsu tube [44]. The Photek, however, is nominally constant with a change of only 150 ps per kV. The limiting factor in these data that prevents the measure of the absolute throughput delay is the FWHM, or the distribution associated with the coincidence curve, which, to obtain an absolute measurement, would have to approach a delta function. Additional coincidence data and throughput delays are presented in Appendix F.

The FWHM of the coincident signal agrees with the expected timing uncertainties of the measurement. From the variable kinematics there is an uncertainty associated with the time-of-flight for each particle (1.1 ns for the alpha and 0.16 for the neutron) and an uncertainty of 0.46 ns associated with the neutron transit time through the scintillator for a total of 1.72 ns.

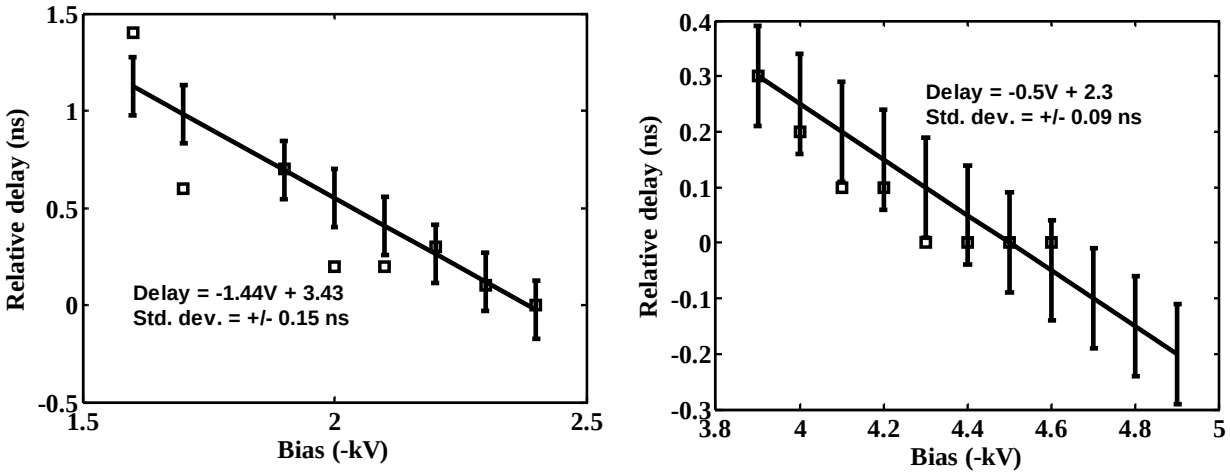

Figure 14 Relative throughput delay for the Hamamatsu (left) and the Photek (right) PMTs

The uncertainty in in the variable kinematics was further observed by reducing the incident D^+ ion energy to 50 keV, which in turn, reduces the range of possible neutron and alpha energies. The expected reduction from the kinematics was observed in the widths of both the alpha energy spectrum, shown in Figure 16, and the FWHM (1.5 ns) of the coincidence curve (Appendix F). In addition, a sharp decrease in the measured neutron rate was observed and the rate appears to scale consistently with the total fusion cross-sections at 175 and 50 keV.

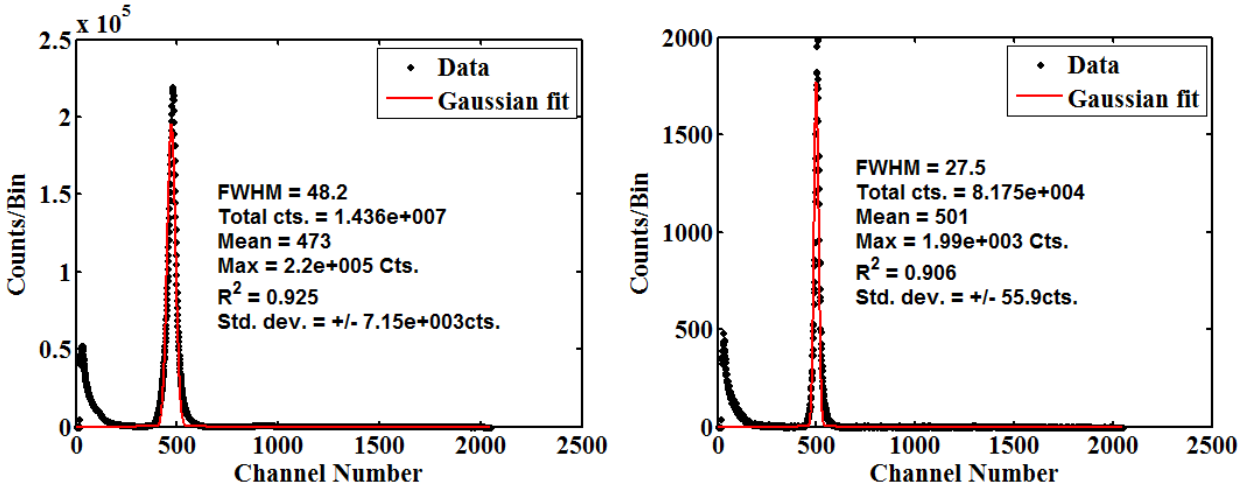

Figure 15 Measured alpha particle energy spectra at 110 degrees for incident D^+ ion energies of 175 keV (left) and 50 keV (right)

Aside from observing kinematic behavior, the true utility of measuring the alpha particle is to both establish the coincidence event and to serve as a neutron yield monitor. Using the associated particle method, as mentioned previously, the number of neutrons emitted into a given solid angle may be inferred from the number of alpha particles measured at any other known angle. Thus, a detection efficiency in terms of observable counts per incident neutron, or in this case, the number of neutrons observed that produce a measured signal greater than 25-mV, the value of the lower-level discriminator. The observed relationships for the efficiency as a function of applied voltage are shown for the Hamamatsu tube (left) and Photek tube (right) in Figure 16. The efficiency, when observed as a function of bias, has a linear trend. This relationship is expected since the differential recoil proton energy distribution is uniformly distributed and therefore, the cumulative integral has a linear relationship. Increasing the bias of the PMT effectively amplifies lower energy proton signals above the discriminator value. This is equivalent to changing the point on the linear curve where the efficiency is measured.

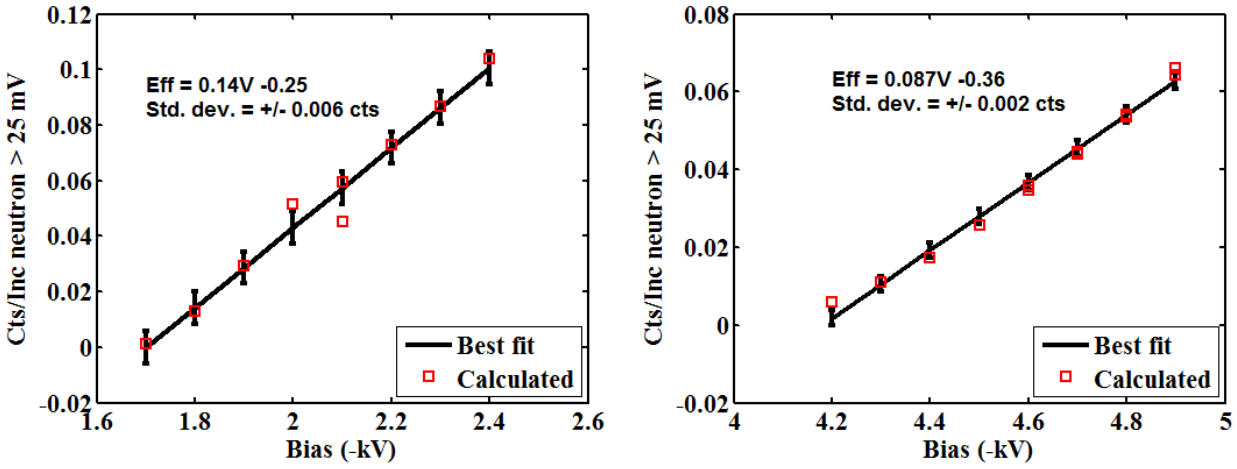

Figure 16 Counting efficiency > 25 mV, Hamamatsu (left), Photek (right)

4.3 Experimental Results – Instrument Response Function

While all the previous data are useful and confirm some of the physics relevant to the experiment, the true purpose of these measurements was to extract the instrument response function. A representative IRF is shown in Figure 17 to illustrate the parameters that define the IRF mathematically and the physical meaning of each. These parameters can be separated into two categories, time and energy, which will be discussed separately. The total width, the Gaussian width, and the decay component are all relative to the time response of the PMT and scintillator, while the maximum amplitude and charge deposition are related to the energy deposition of the recoil proton.

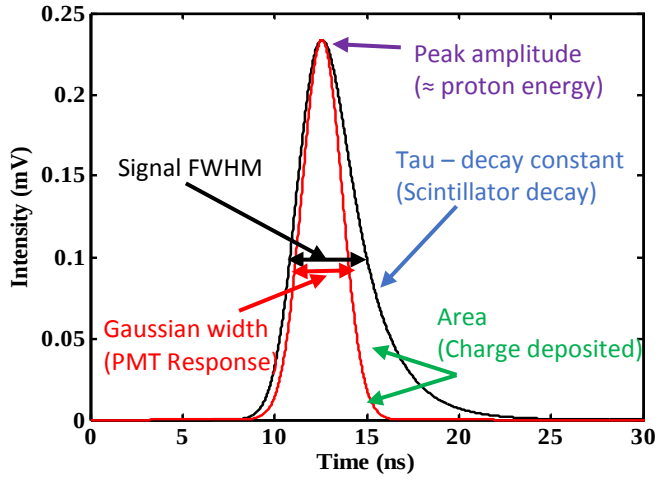

Figure 17 Shown are the parameters of a representative IRF and the physical meaning of each parameter.

Typical waveforms that were acquired for the Hamamatsu mod 5 and the Photek PMT240 are shown in Figure 18 and Figure 19, respectively. In each figure a "well-behaved" pulse shape is shown on the left and a waveform with multiple structures is shown on the right to illustrate the range of data that was acquired. Additional waveforms including functional fits to the signals are presented in Appendix C.

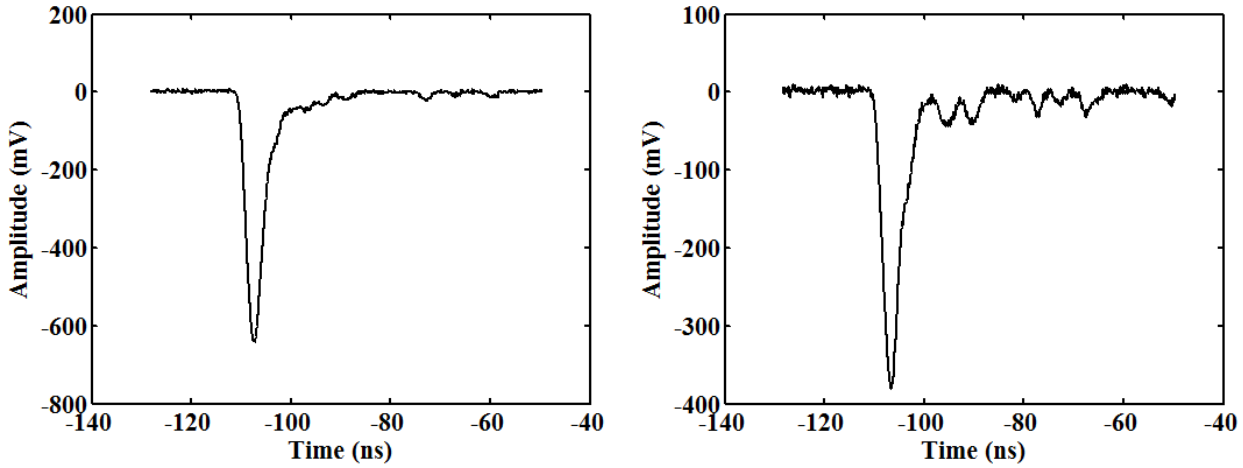

Figure 18 Typical data for the Hamamatsu mod 5 PMT, data shown for -2.4 kV

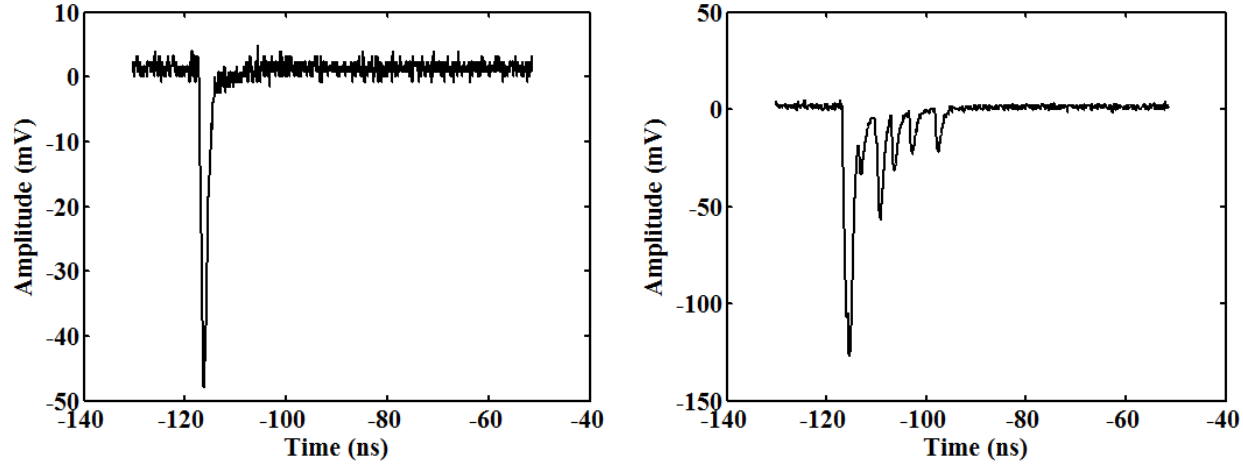

Figure 19 Typical data for the Photek PMT240 PMT, data shown for -4.6 kV

The number of observable "peaks" within a single impulse response waveform were, on average, ~ 3 for the Hamamatsu and ~ 5 for the Photek. In fact, "single peak" waveforms were observed in less than ~ 10% of the acquired waveforms. Given this behavior, the data were analyzed using two different techniques to extract, firstly, the average behavior of several waveforms and

secondly, to extract information relevant to each visible peak structure in terms of location, shape, and frequency.

4.3.1 IRF Analysis – Averaging Technique

The instrument response function was determined firstly by averaging each waveform collected for a particular bias setting. Each waveform was normalized to a fixed value on the leading edge and then averaged point-by-point to calculate the averaged, time-dependent signal. The fixed value on the leading edge was nominally taken as 10% of the maximum net signal (maximum amplitude minus the maximum background). This variable leading edge was employed to account for the change in signal amplitude as a function of bias since a fixed leading edge value may be too large at a lower bias and too small at a higher bias. On average, 99% of the acquired waveforms were used in the average analysis. Data that was not included was rejected for having anomalous behavior, such as an overly large background or visible pre-pulses, reflections, or digitizer clipping. Examples of this analysis are shown in Figure 20 for the Hamamatsu at -2.0 kV on the left and the Photek at -4.2 kV on the right. The blue data are the superimposed, raw data after normalization and the red curve depicts the calculated, average waveform that represents the IRF as defined in this work.

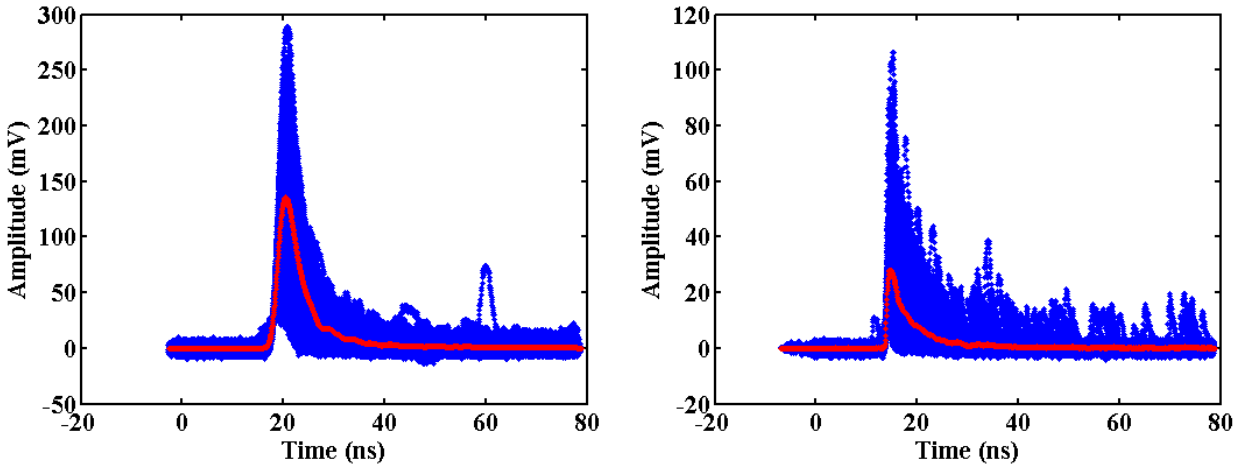

Figure 20 – Average IRF value (red) obtained from 1000 coincident waveforms (blue). Shown on the left – Data taken with the Hamamatsu at -2.0 kV. Shown on the right – Data taken with the Photek at -4.2 kV

Each averaged waveform was fit using a Gaussian function convolved with an exponential decay as shown in equation 4-1.

$$IRF(t,\mu,\tau,\sigma,A) = A * \exp\left(-\frac{t-\mu}{\tau}\right) * \exp\left(\frac{\sigma^2}{2\tau^2}\right) * \left(1 + \operatorname{erf}\left(\frac{t-\mu-\frac{\sigma^2}{\tau}}{\sqrt{2\sigma^2}}\right)\right) \qquad (4-1)$$

Using this particular model, the five values shown previously in Figure 16 were extracted for each PMT bias setting: the FWHM of the signal, the decay component of each waveform (given by τ), the amplitude (given by A), the sensitivity (area under the peak), and the width parameter (related to sigma) of the Gaussian portion of the signal. The uncertainty for this analysis is defined only for the FWHM of the signal. The uncertainty was determined at the one-sigma level from the width of the probability distribution associated with the leading edge time stamp used to normalize the waveforms. This of course assumes Gaussian statistics were applicable to these data. Statistical uncertainties from the averaging were assumed negligible due to the large number of data points that were averaged.

Shown in Figure 21 are the three timing parameters, the total signal width, the Gaussian width of the signal, and the decay coefficient, relevant to the IRF as a function of bias. Also shown is an average IRF that is representative of the results for the Hamamatsu mod-5 PMT (bottom right). The FWHM of the Hamamatsu tube (top left) decreases as the applied voltage increases at a rate of 50 ps per 100 volts. For a bias of -2.0 kV the measured FWHM of the total signal was 4.7 +/- 0.1 ns. This value is in good agreement with the expected trend and previously measured data taken using the linear accelerator at the Idaho State University [44]. For reference, the measured FWHM for the Hamamatsu mod-4 from those experiments at the same bias voltage was 4.5 ns.

The reason for the expected trend of the FWHM versus applied voltage is twofold. As the bias is increased there is a larger applied voltage between the photocathode and anode, which increases the acceleration potential of the emitted photoelectron. As the energy of the photoelectron is increased, the electron multiplication is improved by increasing the secondary electron emission efficiency from the dynode material. With improved efficiency and greater energy there is less dispersion in the collection time of the electrons, thus reducing the signal width [80]. This trend is consistent not only for the overall signal width, but also the width parameter for the Gaussian portion of the waveform (bottom right), implying that the decay constant, τ, is a constant that is independent of bias (top left). Notice that τ only varies by 200 ps over an applied voltage range of 700 V, which is well within the uncertainty of the measurement. This behavior is consistent

with the expected result for a fixed PMT pulse width at a particular bias and a constant scintillator decay.

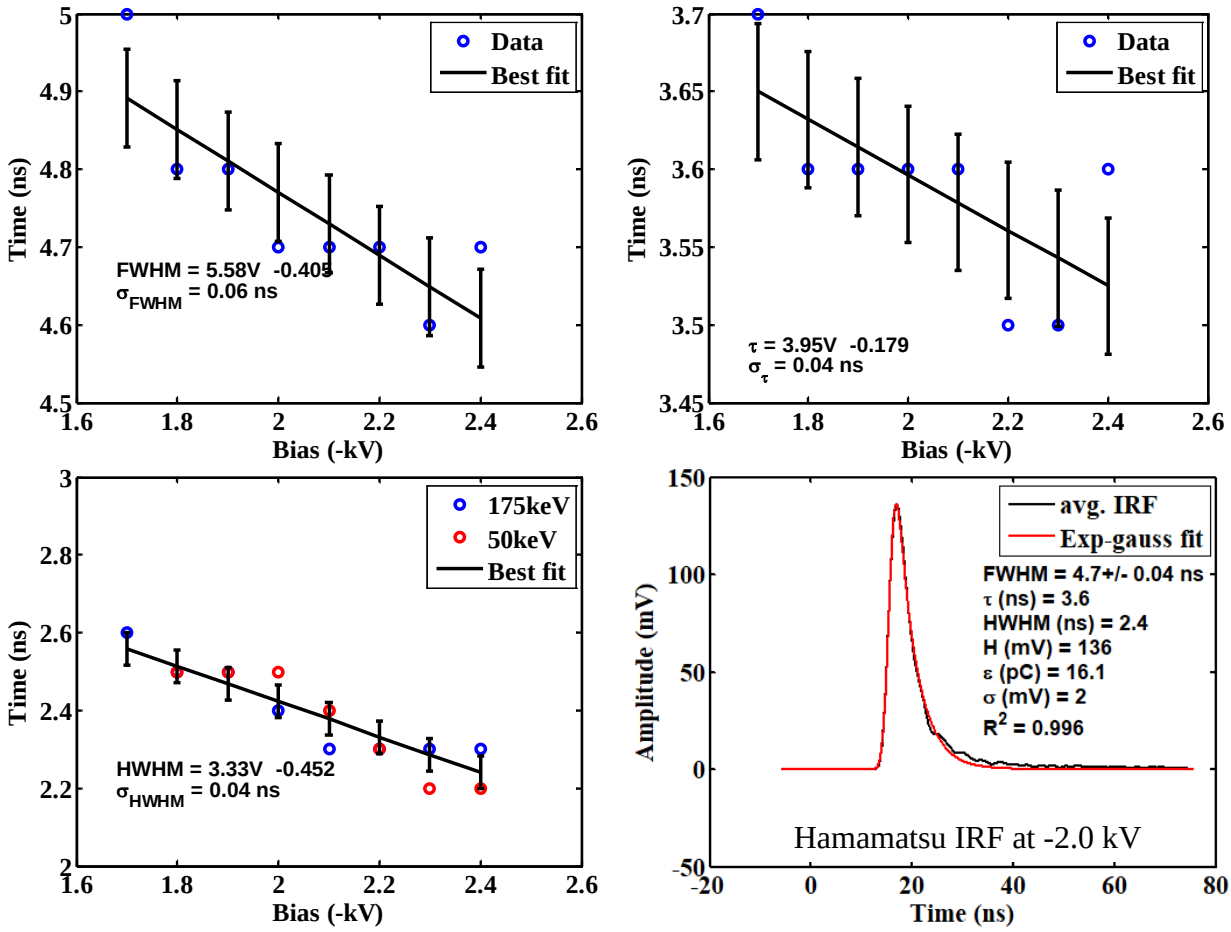

Figure 21 Extracted IRF time parameters from averaged waveforms for the Hamamatsu mod 5 PMT as a function of detector bias

A similar analysis is shown for the Photek PMT240 in Figure 22. The timing characteristics of the Photek are much different than that of the Hamamatsu and the observed values do not follow the same trends (top right). The average width parameter of the Gaussian portion (bottom left) of the fit parameter is ~880 ps, which is representative of the PMT response. This value is in excellent agreement with the 850 ps that is specified by the manufacturer [81]. This behavior is consistent with a micro-channel plate PMT. The variation in electron transit times through this type of PMT is negligible for the range of acceleration potentials given the close proximity of the dynode plates. This structure, which consists of two micro-channel plates, greatly reduces the number of electrons collected at the anode. This does, however, make the Photek very sensitive

to detector bias in terms of charge collected. This fact is largely responsible for the observed increase in the signal width and the decay coefficient as the bias is increased. This increase can be attributed to the gain of the tube. Lower amplitude peaks observed later in time cannot be resolved at lower bias settings. In addition, the measured value for the scintillator decay from the Photek data (top right), while comparable to the Hamamatsu, is slightly higher. This behavior is a result of the better resolution of the Photek, which is able to capture ~ 3 X the number of events of the Hamamatsu tube.

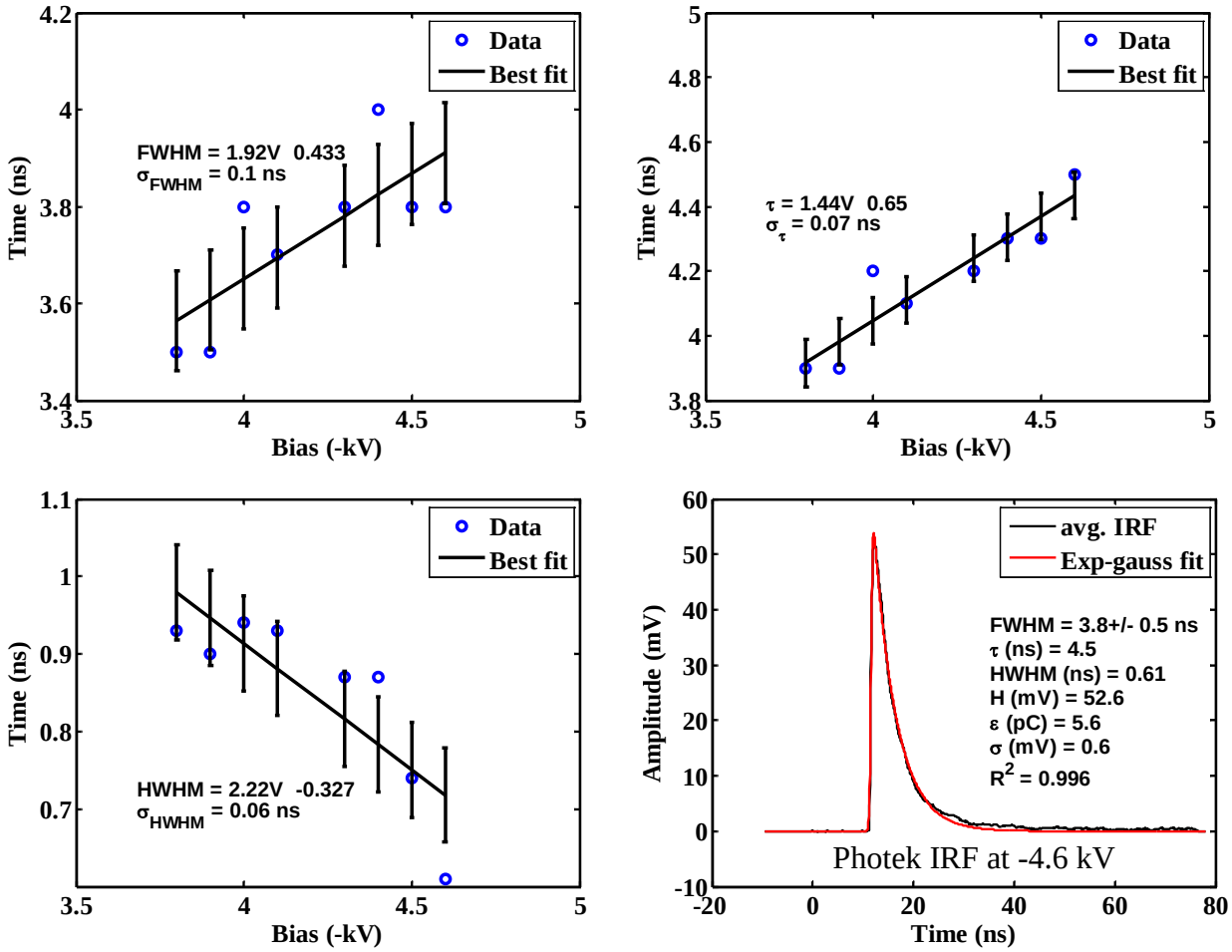

Figure 22 Extracted IRF timing parameters from averaged waveforms for the Photek PMT240 PMT as a function of detector bias. Also shown is a typical IRF taken at -4.6 kV.

In addition to measuring the average IRF from neutrons, the IRFs induced by gamma rays were also measured at IBL by measuring the decay gammas emitted by materials that were activated by neutrons during the neutron irradiation experiments. The goal of these measurements was to

observe if there were any changes in the IRFs due to the type of interacting particle: neutrons (protons) versus photons (electrons) in this case. These data are shown in Figure 23. The width parameter of the resulting IRF from photons, when compared with the neutron IRF, is noticeably reduced. The measured values for the Hamamatsu photon IRF are a FWHM of 4.2 ns, a Gaussian width of 2.1 ns and a decay component of 3.4 ns. Each of these values are ~ 500 ps less than the values observed for the neutron signal at the same applied voltage. The Photek, on the other hand, produced significantly different results. The Photek gamma IRF produced a signal that had a FWHM of only 1.1 ns, a Gaussian portion of 320 ps and a decay constant of only 1 ns. These values are approximately a factor of 3 less than the observed neutron values. While this was just a qualitative experiment and it has not been ruled out that at least some of the photons may have been interacting directly with the PMTs, the data do suggest that there are quantitative differences between the measured IRFs induced by photons and neutrons and, as a result, IRFs measured using photon sources should be corrected for this effect to give the best interpretation of neutron measurements.

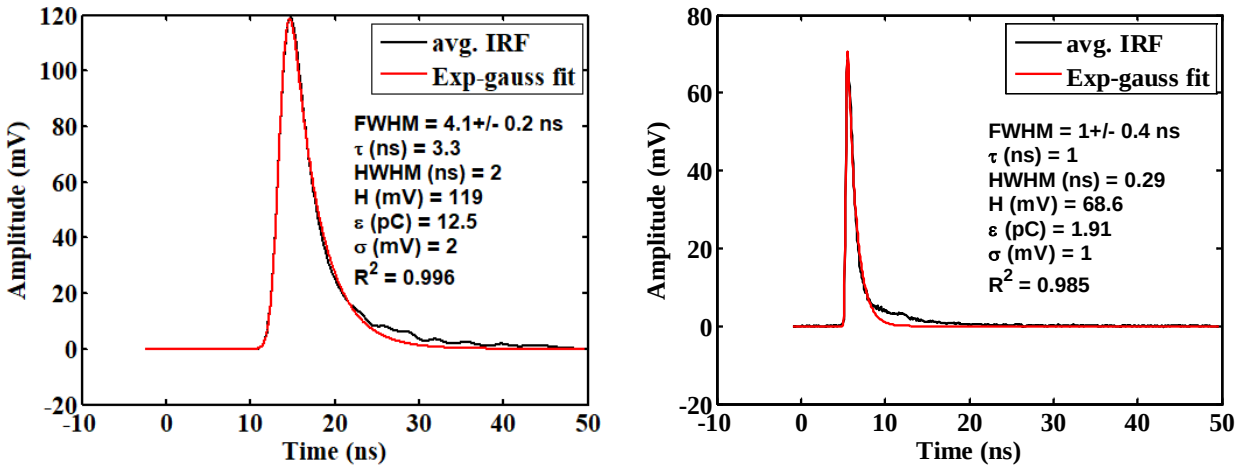

Figure 23 IRF measurement from background photons. Data shown for the Hamamatsu at -2.0 kV (left) and for the Photek at -4.6 kV on the right

4.3.2 IRF Analysis – Individual Peak Structure

The results of the independent analysis were obtained by assuming a sum of Gaussian functions, as shown functionally in equation 4-2.

$$\sum_{i}^{N} G(t,\mu,\sigma,C) = \frac{C_i}{\sqrt{2\pi\sigma_i^2}} \exp\left(-\frac{(t-\mu_i)^2}{2\sigma_i^2}\right),\ \sigma_i = \frac{FWHM_i}{2\sqrt{2\ln(2)}} \approx 0.4247 FWHM_i \qquad (4-2)$$

For each Gaussian peak there are three unknown variables: the peak amplitude, A; the centroid, μ; and the width parameter, σ. Thus, for a particular waveform there are a total of 3 x N unknowns, where N is the number of peak structures in the waveform. Since there are multiple unknown parameters, a non-linear least squares method was used to fit the data to the assumed model using the <fminsearch> function in MATLAB®. The convergence parameter for the fminsearch function utilizes the Nelder-Mead Simplex Method [82], where the convergence parameter is some value that is minimized at the zero value of the function. For these data the Chi-squared statistic of the fit, ε, was minimized as shown in equation 4-3.

$$\epsilon = \sum_{i}^{N} (yfit_i - G_i)^2 \qquad (4-3)$$

The non-linear routine requires an initial parameter for each unknown in the equation. The centroid location was found by using the fact that local maxima can be found by setting the first derivative equal to zero. Since the analytical description of the waveform is unknown, derivatives had to be taken numerically. Unfortunately, the acquired data have an inherent noise from the digitization of the waveform and taking numerical derivatives of the data just enhances the noise. Thus, a smoothing technique based on the derivative of the signal was applied to the waveform data to find the centroid locations. The smoothing of the data was accomplished by simply changing the time-bin resolution until a smoothing convergence was reached. Thus, to preserve the data the signal was first integrated and then differentiated twice – once to return the shape of the original waveform at a different resolution and the second derivative to find the zero crossings.

To avoid arbitrarily smoothing the data a convergence parameter was instituted. The convergence parameter chosen was the standard deviation of the background region that is visible prior to the neutron signal. The smoothing was considered converged once the standard error of the smooth waveform was equivalent to that of the background region. A bi-section method was implemented to control the convergence of the smoothing parameter. For example,

if the initial guess at the smoothing interval produced a standard deviation of the fit greater than the standard deviation of the background, the width of the time bin would be reduced and similarly, the bin width would be increased if the standard deviation of the fit produced a standard deviation less than the standard deviation of the noise. Once the appropriate bin width was chosen the zero crossing was determined to find the possible centroid locations and local maxima within the data. These values were used in conjunction with the pre-determined width parameter (2.5 ns for the Hamamatsu and 1.0 ns for the Photek) as the initial parameters for the non-linear least squares method. It is important to note that the smoothed waveform was used only to determine the initial parameters and the non-linear least squares method was applied to the actual data. A full description of this methodology and an example is given in Appendix G.

Typical fits to the data for both the Hamamatsu mod 5 and Photek PMT240 for the same coincident event are shown in Figure 24. There is a remarkable difference in the signal shape for the same neutron interaction. Noticeably the Hamamatsu PMT, for this particular event, only captured one prominent event, while the Photek PMT was able to resolve eight separate events from the same interaction. There are probably two more "events" on the Hamamatsu PMT signal trace that occurred after the main peak (10 -20 ns timescale) but are not resolved due to the tube resolution, ~ 3 ns. It is worth noting that this particular trend is not the case for every neutron event. The signals do correlate between the Hamamatsu and Photek PMTs on some events, but lack any obvious correlations in others. These observations suggest that averaging several events is the best way to capture the statistical nature of the measured neutron events. Validation of this premise will be discussed further in the following section. Additional waveforms with fits to the data are shown in Appendix C.

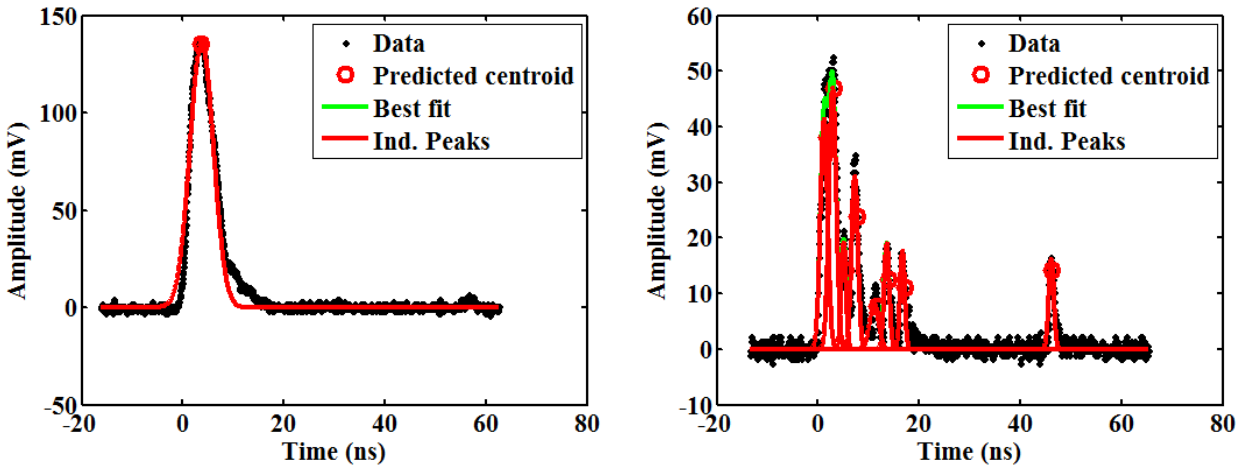

Figure 24 Best fit obtained using a sum of Gaussian functions. Signals shown for same coincident event. Hamamatsu at -2.0 kV shown on the left, Photek at -4.2 kV shown on the right

For each individual peak that was found, in each coincident waveform, the amplitude, FWHM, area under the peak and the location of the centroid were tabulated. These values were then binned and the probability was calculated. Shown in Figure 25 are the distributions for the measured FWHM obtained for the Hamamatsu, shown on the left, and for the Photek, shown on the right.

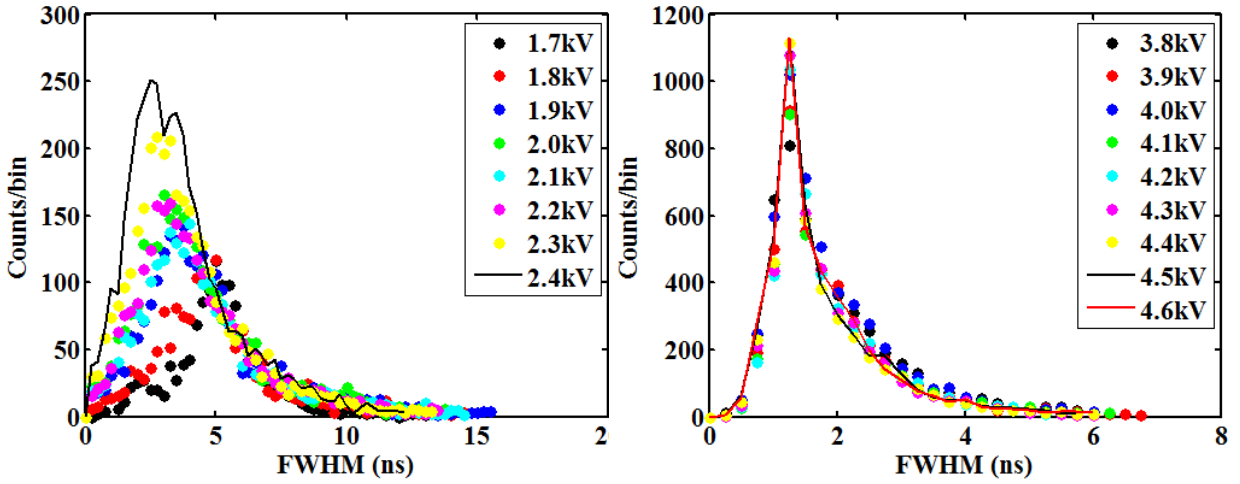

Figure 25 Probability distribution of the individual peak FWHM. Left – Hamamatsu, Right - Photek

The results for the Hamamatsu PMT FWHM distribution exhibit the same trend as the FWHM obtained from the average waveform analysis, where the FWHM increases as the applied voltage is decreased. However, these data suggest the FWHM observed in each individual "peak" within

a waveform is a much stronger function of the applied voltage at a rate of ~ -3.0 ns/kV versus the -0.5 ns/kV observed with the averaged IRF. The Photek FWHM agrees with the observed trend from the averaged IRF, where the FWHM is relatively independent of the applied voltage. In addition, the measured width of these data, ~ 1.5 ns, is comparable with the width of the Gaussian portion of the averaged IRF, ~0.9 ns, if the uncertainty (+/- 500 ps) introduced by "smoothing" the waveform is considered.

It should be noted that these data required extensive smoothing to be tractable. The nominal resolution of the smoothed data was ~ 1 ns for the Hamamatsu and ~ 500 ps for the Photek, which is partly why the FWHM using this method is slightly larger than the Gaussian portion obtained from averaging. The smoothing process and typical results are explained more thoroughly in Appendix G. This resolution when added in quadrature with the uncertainty derived from the width of the FWHM distribution, assuming Gaussian statistics, makes these data statistically poor, since the total uncertainty is a large fraction of the mean value. For example, the observed FWHM of each individual "peak" structure using this analysis for the Hamamatsu at -2.4 kV was 3 +/- 2 ns. When the resolution is included in this uncertainty, the FWHM becomes 3 +/- 2.5 ns. Thus, these data are only given as a qualitative assessment of what was observed within the averaged waveforms. These qualitative assessments lead to the conclusion that the shape of the average waveform is consistent with a characteristic PMT pulse convolved with a scintillator decay component.

The parameter that is relatable to the scintillator decay component is the distribution of secondary emissions with respect to the initial peak. A compilation of these data as a function of detector bias is shown in Figure 26. The decay component present in the Hamamatsu data (left) appears to change as a function of detector bias. This trend can be explained if the gain of the tube is considered. At lower bias settings the secondary emissions can no longer be resolved and, thus, cannot be differentiated from the baseline noise in the waveform. If this fact is considered, then it is not unreasonable to say that both tubes exhibit the same decay characteristics and they are independent of the applied voltage. In addition, when compared with the Photek tube there appears to be more structure in the Hamamatsu distribution. This can be explained by considering the nominal PMT response. The Hamamatsu tube can resolve three times fewer events for a given time interval as can the Photek. Thus, the Photek data are

smoother because of better statistics. As expected there is no visible change in the centroid distribution for the Photek tube as a function of bias. This result, as discussed previously, can be attributed to the micro-channel plate dynode structure within the PMT.

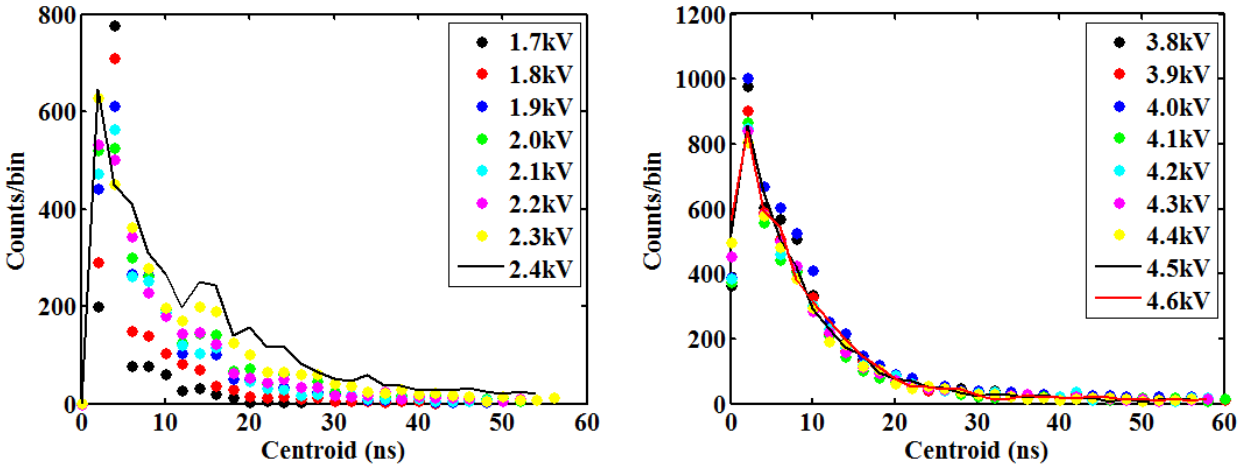

Figure 26 Distribution of Peak Amplitudes as a function of detector bias, Hamamatsu – left, Photek – right

The analysis of the centroid distribution was taken one step further. Since the Photek data are significantly smoother and relatively constant as a function of bias, the data were fit using a Gaussian distribution convolved with two separate decays. The result of this fit is shown in Figure 27. There are two noticeable decay components that are visible in these data. The first decay starts at 2 ns and then there is a slight inflection at ~ 10 ns. The results of the fit are consistent with a prompt scintillation state and a longer-lived triplet state. These are shown in the fit parameters listed, where the short lived state has a very narrow width and a 1.2 ns decay and the long lived state broadens the distribution to 4.4 ns because of the 7.7-ns decay component. The 1.2-ns decay constant is in exact agreement with the prompt decay constant quoted by the manufacturer (Eljen Technologies) [83]. The 7.7-ns longer-lived state is not unreasonable for a delayed-phosphorescence decay constant. Thus, from this analysis it can be inferred that the scintillator decay is indeed being measured in conjunction with the PMT response and that these components are being captured together in the average IRF analysis.

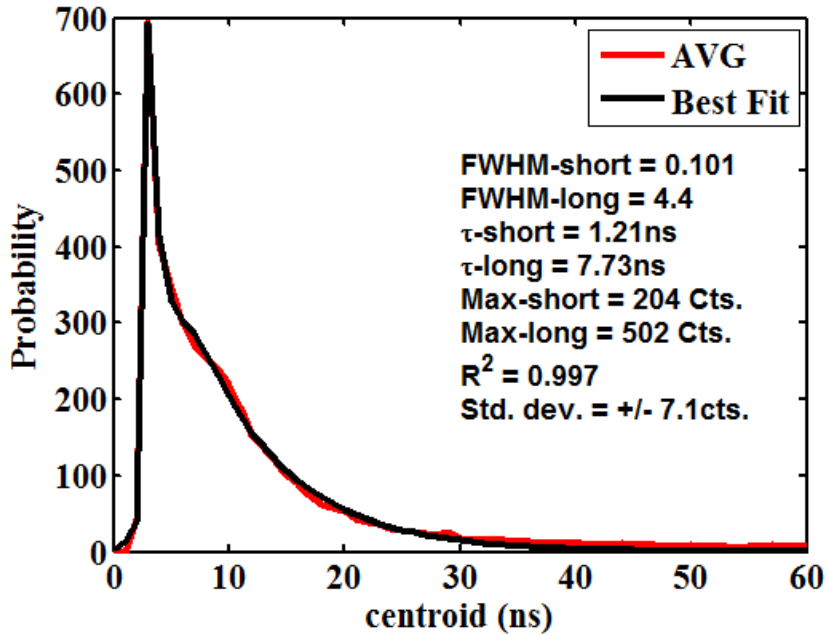

Figure 27 Photek PMT centroid distribution, shown is the average of the Photek data and a Gaussian fit convolved with two separate decay components given by tau

4.3.3 IRF Analysis –Light Output and Counting Efficiency

The other parameters extracted from the IRF analysis, the average peak amplitude and the average sensitivity (total area), are a measure of the energy deposited within the scintillator. The probability distributions for these two quantities extracted from the individual structure analysis are shown in Figure 28. The results for the Hamamatsu tube (left) and the Photek (right) are shown for the peak amplitudes (top) and sensitivity distributions (bottom), respectively.

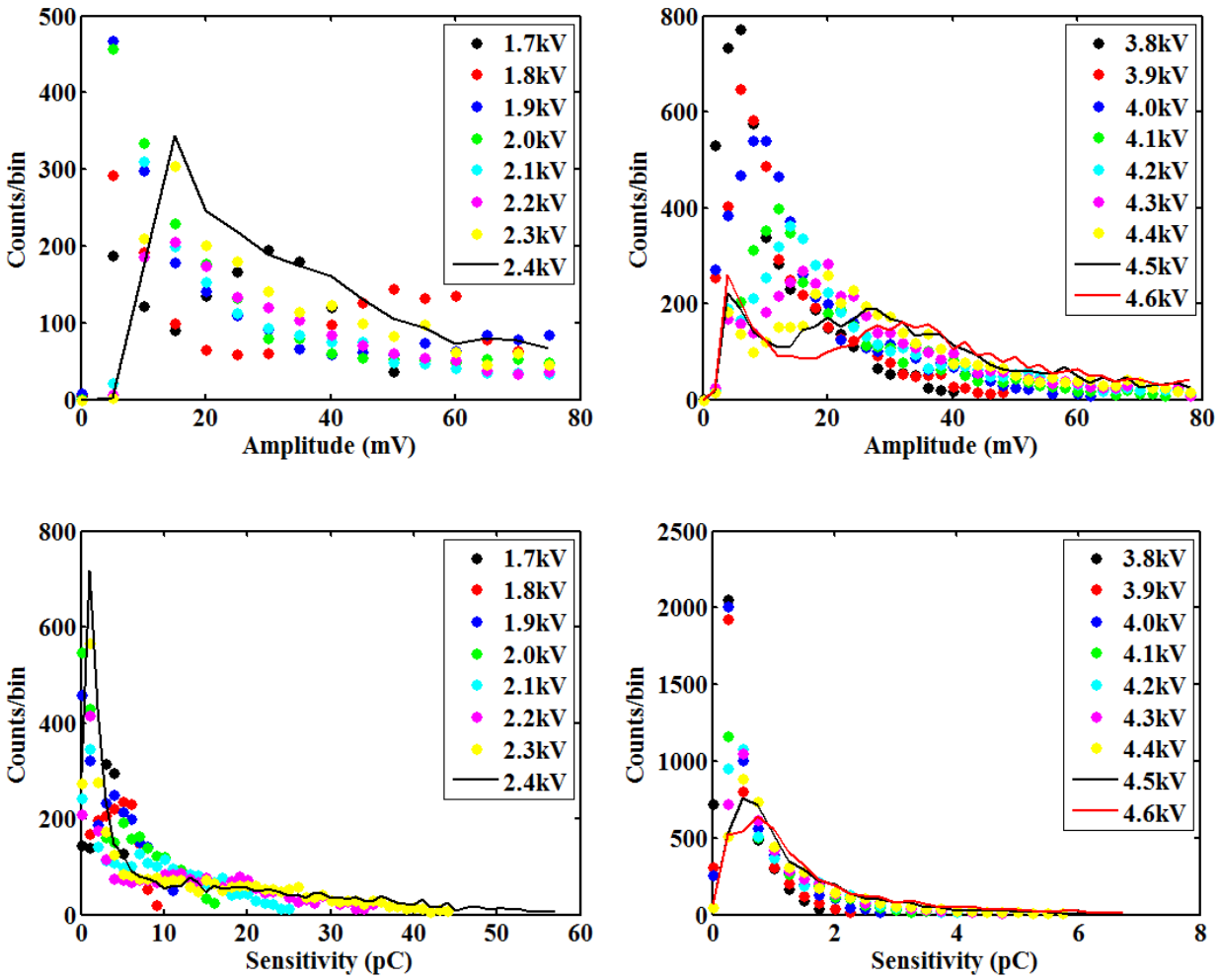

Figure 28 Maximum amplitude (top) and detector sensitivity (bottom) distributions for the Hamamatsu (left) and the Photek (right)

These data exhibit a shape that is consistent with the expected recoil proton distribution within the scintillator from the nominally 14.3-MeV neutron source at IBL. The expected proton spectrum was modeled with the MCNP6 code and is shown in Figure 29. The scalar neutron flux was binned as a function of energy and the proton distribution was calculated using the methodology presented previously in this work (see theory section). The section of these data that is proportional to the expected proton distribution lies in the long flat continuum region. The overabundance of low amplitude peaks that are observed are most likely from delayed light emissions in the scintillator from de-excitation of the triplet states. If this is the case, then a better measure of the energy deposited is the maxima and total integral distributions from the average IRF analysis. These data are similar to the independent data analysis in that their proportionality

is in the long flat continuum. Shown in Figure 30 are the distributions of the maxima values observed in each waveform for the Hamamatsu (left) and the Photek (right).

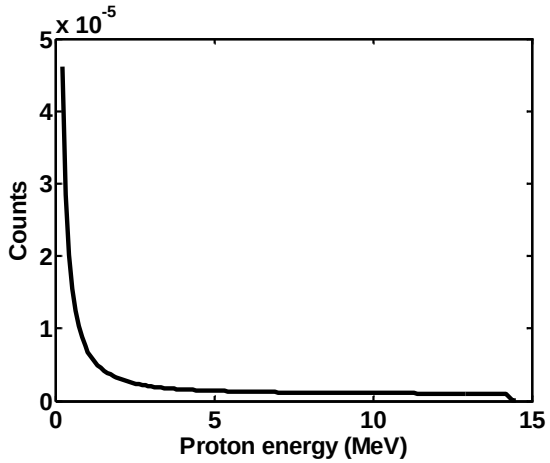

Figure 29 Differential proton spectrum, IBL DT neutron source

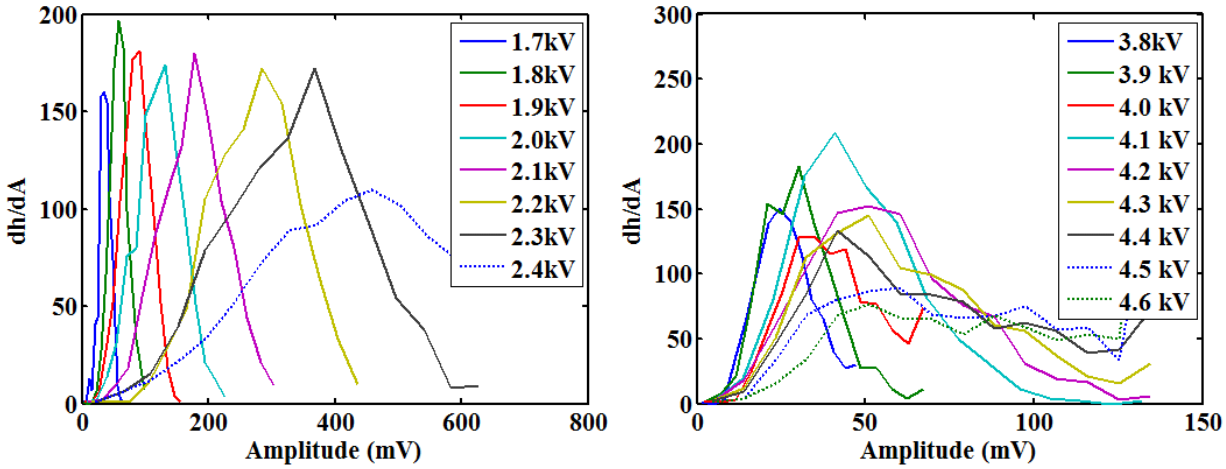

Figure 30 Maximum amplitude distribution as a function of applied voltage, Hamamatsu – left, Photek - right

To generate these distributions, the amplitudes were discretized into twenty-five, discreet bins. Therefore, the resolution increases as the applied voltage is increased. Thus, from these data it is not obvious as to why the experimental data is proportional to the theoretical values, but this can be explained by the differential representation of the data and the inclusion of the discriminator in the experiment. The discriminator is cutting out lower amplitude signals and, therefore, the data shown in Figure 30 are only a representative fraction of the expected theoretical value.

Since the experimentally obtained amplitude and sensitivity are consistent in shape with the expected proton energy distribution, the experimental quantities can be directly related to the theoretical values. In other words, the measured detector response is, and should be, proportional to the proton energy deposition, which in turn, is proportional to the scintillation light produced (MeV_{ee}). The expected energy spectrum for recoil protons is shown in the left in Figure 31, and the expected spectrum weighted by the light output function is shown on the right. These spectra were generated using the formalism presented earlier in section 3. The energy spectrum is the product of the differential proton spectrum (Figure 29) and proton energy, while the expected light output is the product of the differential proton spectrum and the corresponding light output in MeV equivalent. For this work the light output function (equation 3-24) utilized in the Stanton code was the assumed response [65].

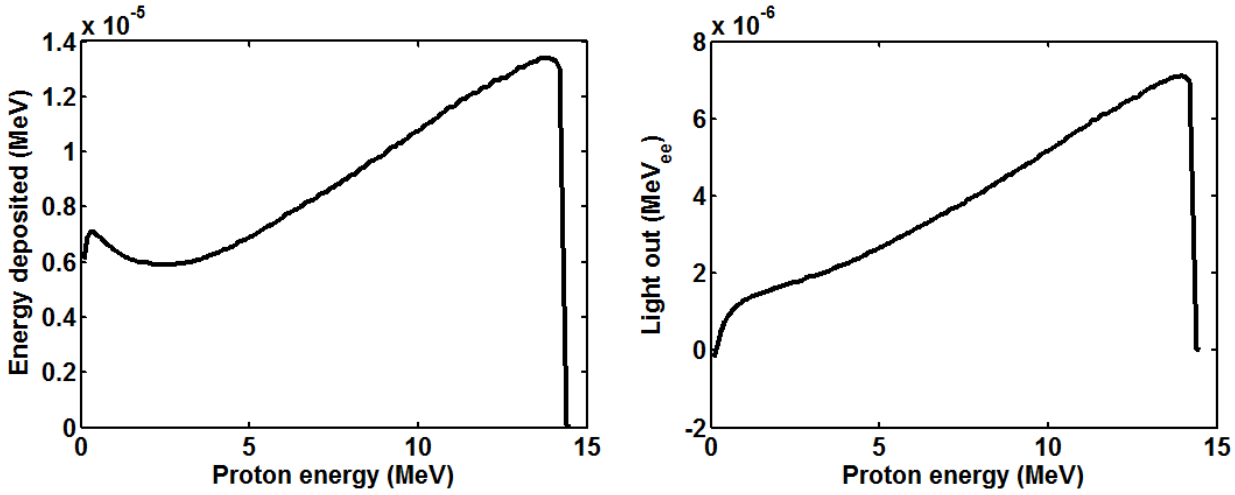

Figure 31 Expected recoil hydrogen spectrum with (right) and without (left) a detector response generated from a DT neutron source

To extract the light output equivalent (MeV_{ee}) from these experiments a proportionality constant needs to be established between the two quantities. This proportionality can be established by normalizing the expected and measured distributions to a quantity of one. Thus, the assumption for this normalization is that the maximum observable amplitude is equivalent to the maximum energy proton expected from the experiment and everything less than the maximum value is simply proportional. The normalization chosen for these data requires the data be integrated twice to generate a cumulative integral curve. For the analytical data this quantity is the amount of light produced as a function of energy and for the experimental data this corresponds with the

integral amplitude as a function of the amplitude. As an example, the normalized integral quantities are shown in Figure 32. When normalized the experimental and analytical data are similar in shape, but the normalized amplitude curve is slightly higher than the normalized energy deposition curve near zero. If this were a true proportionality the normalized count rate would vary from zero to one with an amplitude range from zero to some maximum value and this would be proportional to the energy range from zero to some maximum energy deposition. The downshift is caused by the minimum value being the discriminator value and not zero.

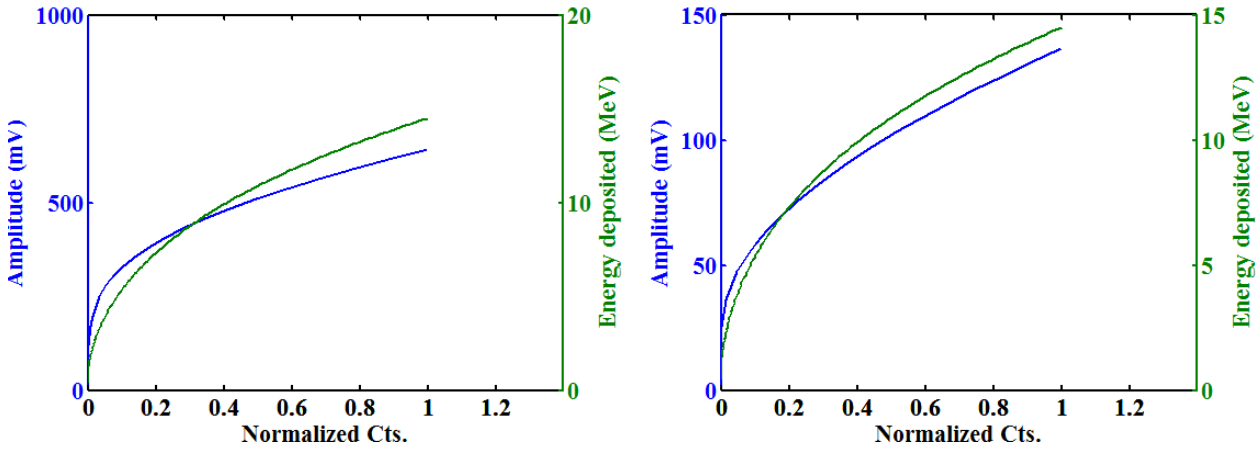

Figure 32 Normalized integral quantities in terms of amplitude and energy. Hamamatsu at -2.0 kV-left, Photek at -4.6 kV-right

This relationship, as shown in Figure 33, is clearly seen when the amplitude is represented as a function of the expected light output value from the light equivalency correlation used in the Stanton code, which is proportional to the energy deposited. These relationships were found from the normalization process, which is simply equating the two quantities with the common variable being the normalized count rate. A clear linear region is seen in the proportionality relationship and this is where the amplitude is directly proportional to the expected light output. The departure from the linear regime is the effect of the discriminator. The value of the intercept corresponds to the magnitude of the discriminator level for a particular bias setting. Physically, this is the proton energy deposition that produces a signal that has a peak height in volts that is equivalent to the discriminator value. The slope of this line is the proportionality constant and it has units of mV/MeV_{ee}. The discriminator values obtained for each bias setting are shown in Figure 34. The discriminator value inferred from the normalization follows a linear trend, much like the efficiency curve shown in Figure 16.

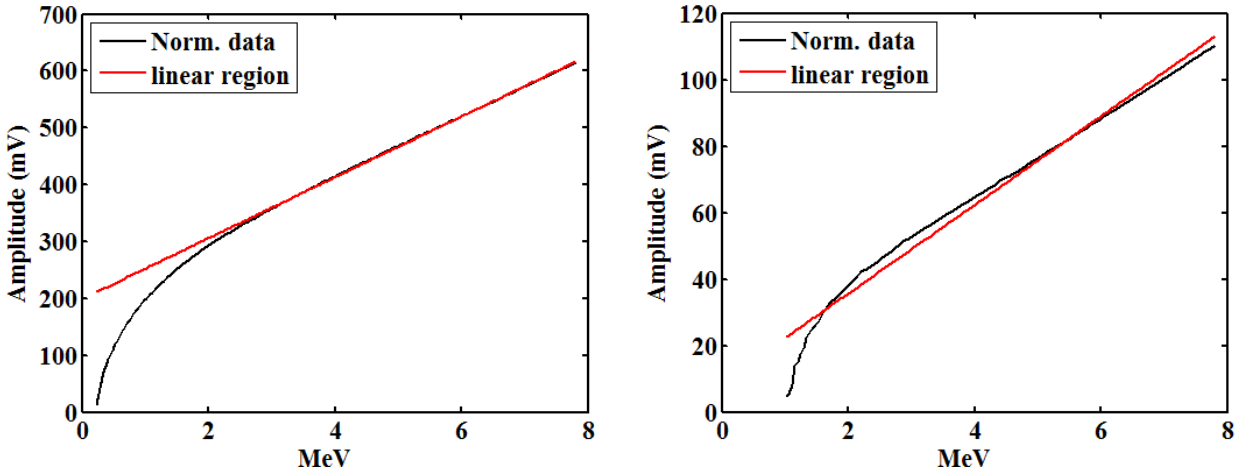

Figure 33 Proportionality curve between the observed amplitude and the expected light output. Correlations shown for the Hamamatsu at -2.4 kV (left) and the Photek at -4.6 kV (right)

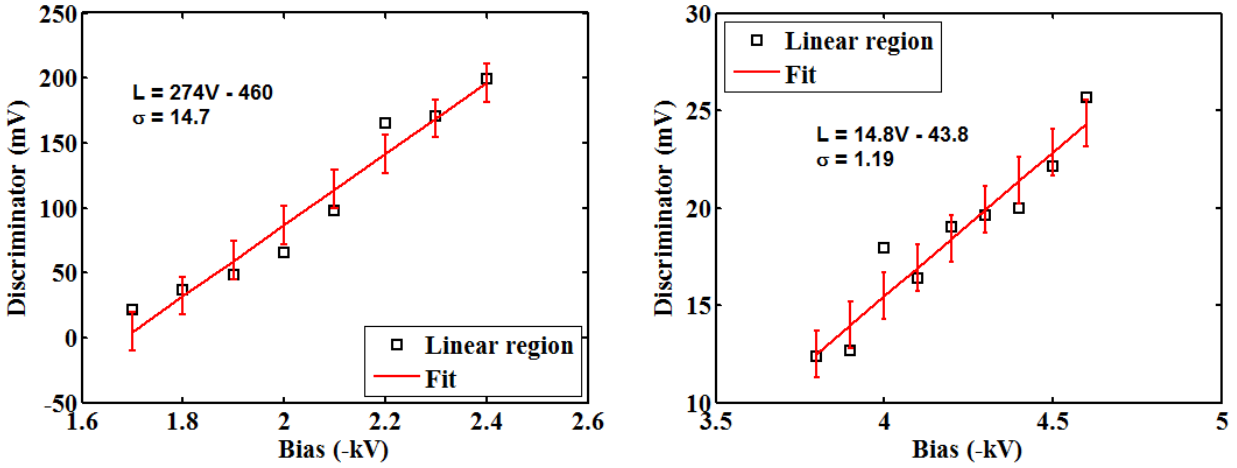

Figure 34 Inferred discriminator value, or 0 MeVee equivalence as a function of applied voltage. Data shown for the Hamamatsu (left) and the Photek (right)

When the proportionality constant (the slope of the line in Figure 33) is factored out of the relationship (shown in Figure 33) that equates the amplitude to the MeV_{ee}, the result reproduces the Stanton correlation, which is shown in Figure 35. The relationships measured in these data depart drastically from the Stanton curve at around 3 MeV, which for these experiments is nominally the minimum energy deposited to produce a signal equivalent to the discriminator setting. If all measured signals were well above the discriminator level, then these results would produce much better agreement with the Stanton correlation at the lower energies. Additional

data could be taken at more discriminator values to further validate this technique. This, however, at present, will be left for future work.

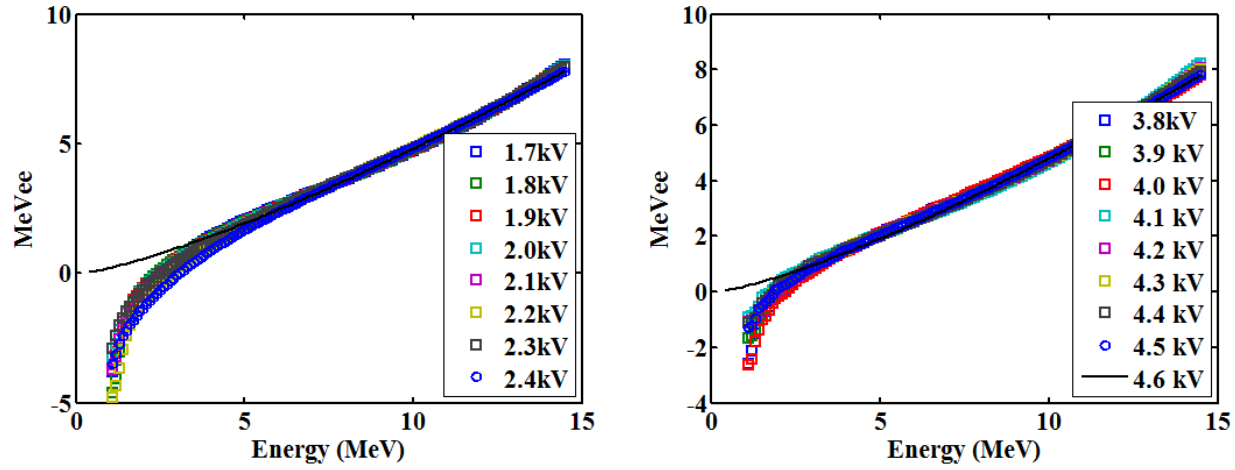

Figure 35 Experimental data normalized to the Stanton correlation. Data shown for the Hamamatsu (left) and the Photek (right)

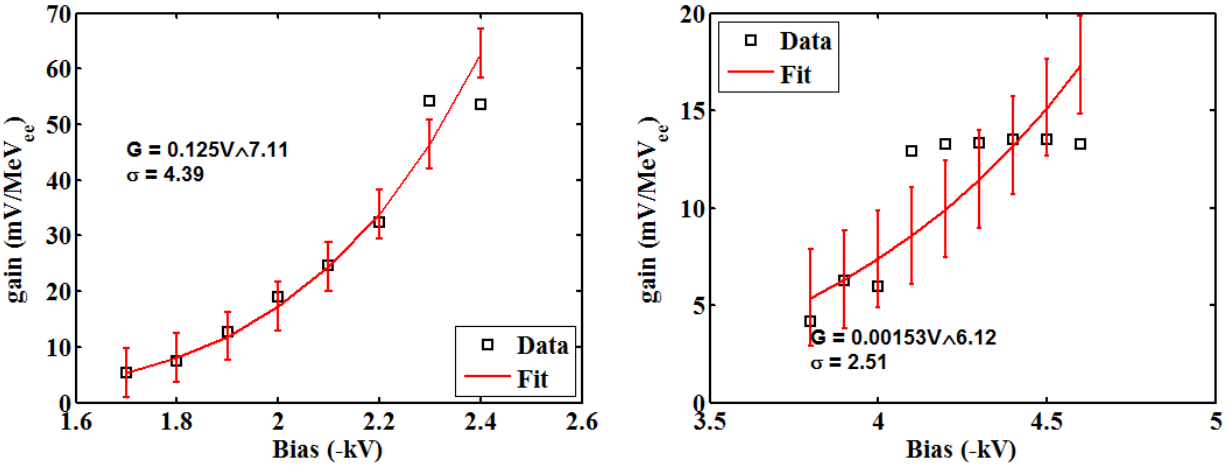

Figure 36 Proportionality constant, mV/MeVee, as a function of applied voltage. Data shown for the Hamamatsu (left) and the Photek (right)

The proportionality constant in terms of mV/MeV_{ee} when considered as a function of bias, as shown in Figure 36, can be used to measure the PMT gain. However, a better measure of the tube gain is the total charge deposited as a function of bias. This measure of tube gain will be discussed further in a later section. The true utility of correlating a measured peak-height amplitude to the energy deposited is to provide an understanding of the measured values from these experiments and use this understanding to provide a predictive capability for future

experiments. This however, requires this relationship to be known in an absolute sense, which can be extracted by multiplying the Stanton correlation by the proportionality constants obtained as a function of bias from these data. These relationships are shown in Figure 37 for the Hamamatsu (left) and the Photek (right). Notice the discriminator value that was measured previously has been removed from these correlations.

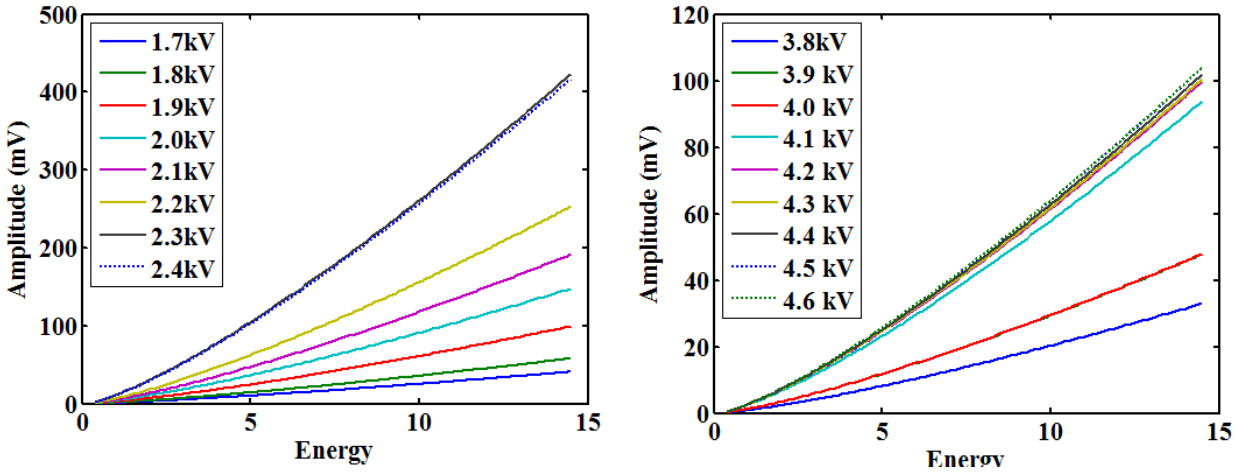

Figure 37 Absolute mV/MeVee correlation as a function of applied voltage. Data shown for the Hamamatsu (left) and the Photek (right)

To demonstrate the validity of this technique, these relationships were used to transfer the calculated counting efficiency as a function of discriminator from the IRF measurement to a counting efficiency as a function of proton energy deposition. The value for the proton energy was found through interpolation using the inverse of the relationship that was shown in Figure 37. The discriminator value that was used was found from the normalization intercept, as shown in Figure 34. The results of this analysis are shown in Figure 38. Notice that both the Hamamatsu and the Photek data are compared with the theoretical efficiency calculated from the expected proton distribution. These values are no longer dependent on either the PMT type that was used to acquire the data or the voltage that was applied.

These data were calculated for the non-coincident tube, but the count rates were taken with the coincident PMT. This was done for a couple of reasons. Firstly, complete correlations for this analysis were only done for the non-coincident PMT for reasons described previously and there was a loss of coincident PMT data due a glitch in the digitizer. Secondly, by doing this analysis it shows the equivalency between the experimental discriminator of one PMT to the theoretical

discriminator of the opposing PMT. Thus, by default this analysis provides a pulse amplitude equivalency between the two PMTs at the specified voltages. These results are tabulated and listed in Appendix H.

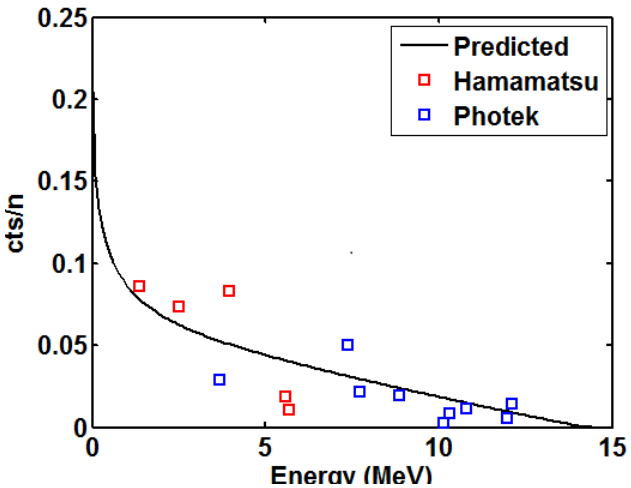

Figure 38 Efficiency curve calculated using the method described previously.

4.3.4 IRF Analysis – PMT Gain and absolute efficiency

A better measure of the tube gain and sensitivity is the amount of charge measured, or the area under the peak, for a given bias setting. The same technique, as discussed in the previous section, was applied to the sensitivity distribution from the average IRF analysis. The normalization coefficient was compared as a function of applied voltage, as shown in Figure 39.

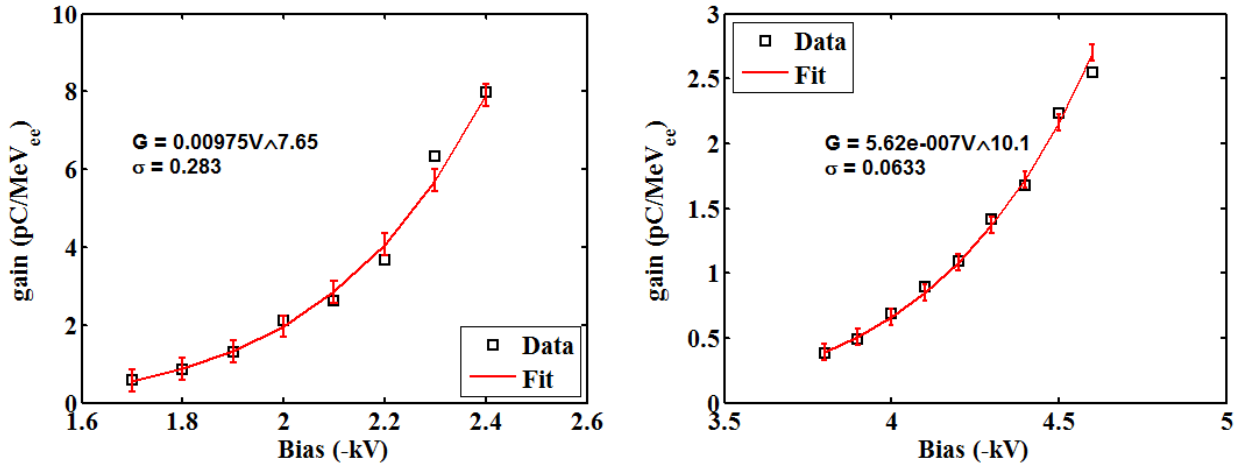

Figure 39 Proportionality constant, pC/MeVee, as a function of applied voltage. Measure of the tube gain. Data shown for the Hamamatsu (left) and the Photek (right)

Notice the gain coefficient curve follows the expected power law trend for both the Hamamatsu and Photek. These data were compared with previous data taken with these tubes at the Primary Standards Lab (PSL) at Sandia National Laboratories. The same NTOF detector used in these experiments was previously irradiated with a Controlatron, D-T neutron source that nominally emits D-T neutrons isotropically at a rate of ~ 2E7 neutrons per shot. The sensitivity, pico-coulombs per incident neutron, was inferred by measuring the 4pi neutron yield with an absolutely calibrated Pb Probe (yield +/- 7%) and the number of incident neutrons was inferred by calculating the solid angle subtended by the source and the detector. The measured sensitivities as a function of applied bias is a measure of the absolute gain for the PMT. For convenience the experimental arrangement at the PSL is shown in Figure 40.

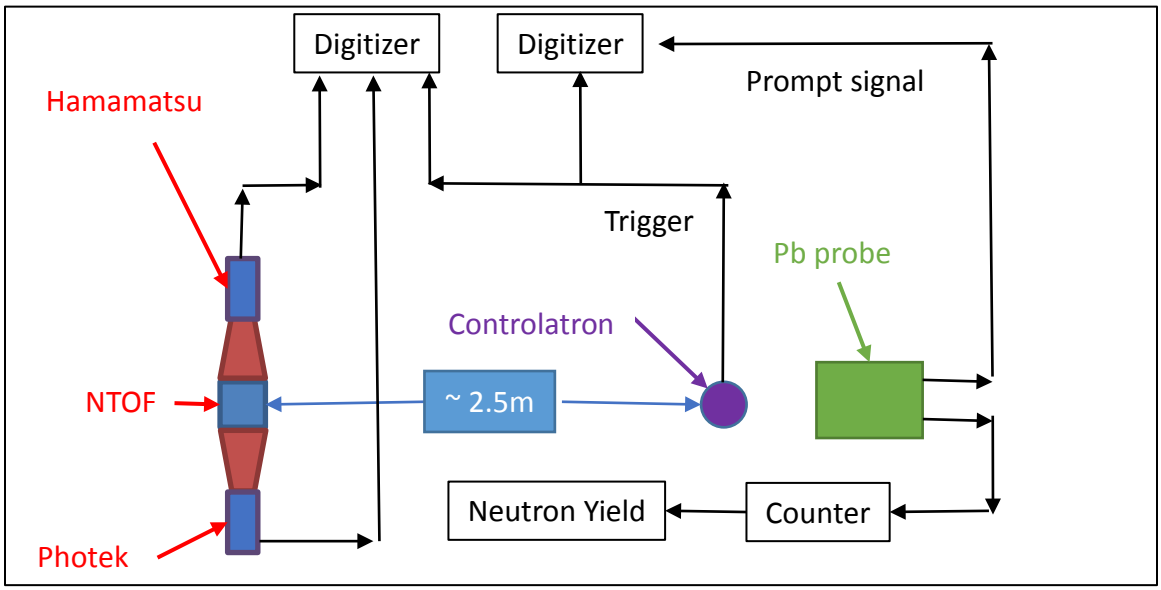

Figure 40 Experimental arrangement for measuring absolute sensitivity and gain using a 2E7 D-T controlatron D-T neutron source with an absolutely calibrated Pb probe (Yield +/- 7 %)

Multiple waveforms were averaged and then integrated to provide the sensitivity and, thus, the gain for both the Hamamatsu and Photek tubes. The data for the experiments at PSL are shown for the Hamamatsu (left) and the Photek (right) in Figure 41. The measured value of the exponent for the same Hamamatsu tube from the PSL experiments was 7.63. The gain coefficient for the Hamamatsu agrees within less than a percent of the PSL data and the Photek gain coefficient is within 5% of the observed value from the PSL data. It is important to note, that the gain can only be calculated once the energy dependence (discriminator value) is removed from the data. Thus, the process of obtaining the absolute proportionality constant is absolutely

necessary if the PMT gain is desired from these data. This necessity becomes obvious when these correlations are compared to the average charge collected for the average IRF. These data are omitted here, but are shown in Appendix I.

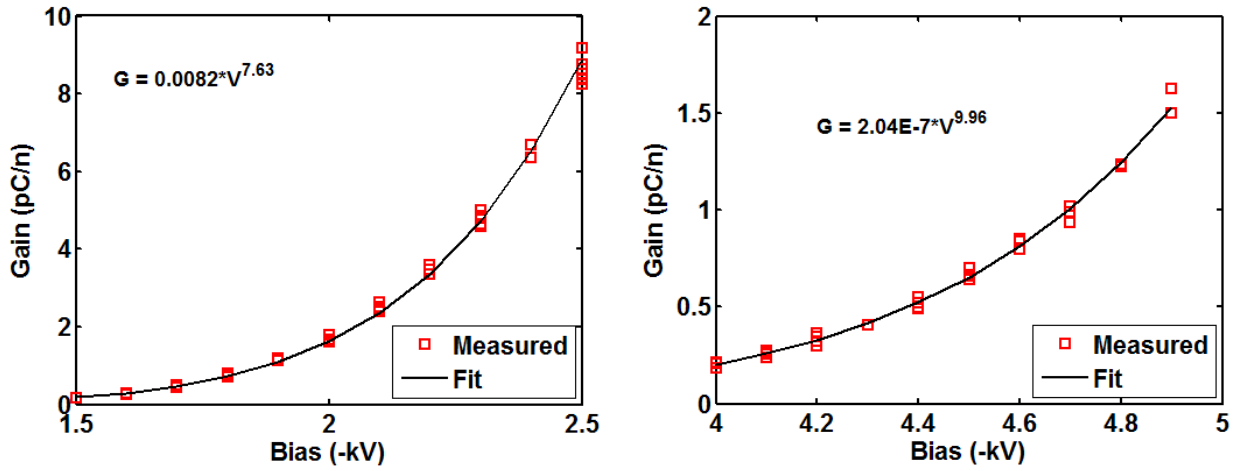

Figure 41 Gain curves from previous data taken at the Primary Standards Lab. Hamamatsu shown on the left, Photek shown on the right

By using the gain curves from both the IBL and PSL experiments and calculating the absolute efficiencies, this technique can be validated. Charge collection efficiency was calculated by taking the ratio of the gain measured at the Ion Beam Laboratory at the average MeV_{ee} (3.22 at 7.25 MeV) and the gain measured at the Primary Standards Lab. By comparing these data, the average efficiency can be calculated since the units for these experiments are average pC/interacting neutron and the unit from the PSL data was pC/incident neutron. Thus, taking the ratio gives the interacting to incident neutron ratio or the average detector efficiency. Shown previously in Figure 38 is the expected proton distribution for the incident neutron fluence, which is consistent with the neutron source at the IBL. From this figure the maximum proton production efficiency is ~ 21% per incident neutron, or 1 proton is generated within the scintillator for every 5 incident neutrons. Taking the ratios of the two quantities for both the Hamamatsu and Photek tubes produces an absolute efficiency of 25% and 10%, respectively. These values are independent of bias and thus, when compared with the expected collection efficiencies of all the charge produced by protons is ~100% for the Hamamatsu and ~ 50% for the Photek, assuming no discrimination is used. The over-prediction of 25% versus 21% is considered minor given the crudeness of the analysis. However, there is confidence in this result

since this suggests the Hamamatsu is more sensitive by a factor of two when compared with the Photek. This difference in sensitivities is not a surprising result since the Hamamatsu has a mesh type dynode and the Photek has a micro-channel plate. The micro-channel plate can produce low amplitude signals that are indistinguishable from the baseline of the signal, which may explain the reduction in the apparent sensitivity.

The utility of measuring the absolute efficiency is the ability to integrate these quantities into a neutron transport model and provide a predictive capability for the neutron yield for future experiments. This requires knowing the conversion from energy deposited, which is calculated in the model, to absolute charge deposition. The absolute correlation, derived from this work, is shown in Figure 42 for both the Hamamatsu tube (left) and the Photek tube (right). These relationships were found by multiplying the proportionality constant (pC/MeV$_{ee}$), which was shown previously in Figure 39, and the Stanton correlation. The proportionality constant was derived using the same methodology as presented earlier in this section. These results are shown in Appendix I. The modeling efforts for this work are discussed further in the next section.

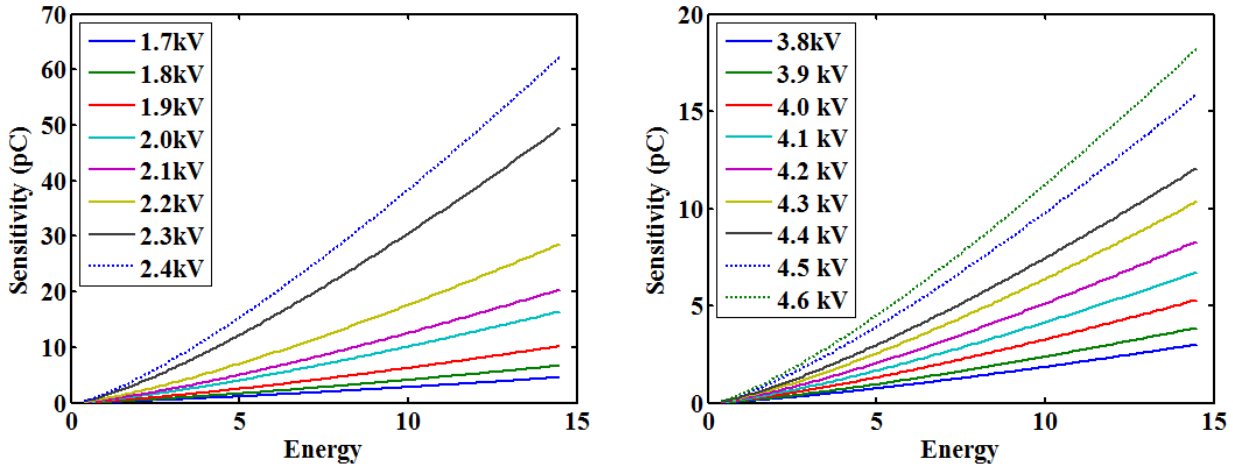

Figure 42 Absolute pC/MeVee correlation as a function of applied voltage. Data shown for the Hamamatsu (left) and the Photek (right)

5 Neutron transport model of the Z-Machine

The goal of this work was to couple the experimentally obtained IRF and sensitivity to modeled results and compare to MagLIF NTOF measurements, but unfortunately at the time of writing this dissertation, data had yet to be taken at the Z-Facility with detectors for which the

characteristics had been measured. However, results from a neutron transport model were coupled to representative IRF values and compared with three past MagLIF experiments to show the utility and methodology for transferring calibrations from one geometry to another. For this work, the neutron transport model, developed in MCNP6, was exclusive to line-of-sight 270 (LOS270) at the Z-experimental facility, where presently two individual NTOF detectors reside. As mentioned previously, the two detectors on LOS270 are located coaxially and are separated by a distance of 2 meters at 9.5 and 11.5 meters from the source, respectively. Both detectors have a cylindrical EJ-228 scintillator that is 2.54 cm thick with a diameter of 7.62 cm. The detector closest to the source is of a single PMT design, in which the scintillator edge is viewed by a single Hamamatsu mod 4 PMT that is coupled to the scintillator via a Lucite light guide. The detector at 11.5 meters is of a dual PMT design, in which the scintillator is viewed on edge, equidistant, by two, independent PMTs coupled through Lucite light guides. The two PMTs chosen for this design are a Photek PMT240 and a Hamamatsu mod 5.

The results of the transport model provided the time and energy dependent scalar neutron flux, as described previously, for both the 9.5 and 11.5-meter detector locations. The Stanton MeV_{ee} correlation was folded into the results and the IRF that was measured previously at the Idaho State University LINAC for the single-PMT, Hamamatsu-mod 4 detector was convolved with the MCNP6 results that had been modified by a light output correction. The derivation of the relationship between light output and neutron flux was discussed previously in section 3. The results of these forward-fit, convolved calculations, were compared with three NTOF signals that were acquired from MagLIF shots 2850, 2851, and 2852 for both detector locations. For each waveform the following parameters have been inferred – the ion temperature, the liner aerial density, and the relative neutron yield.

5.1 Line-of-sight 270 (LOS270)

The MCNP6 model of LOS270 was comprised of all major components that are fielded on a typical MagLIF experiment. The general layout and a cross-sectional view of the MCNP rendition are shown in Figure 43. For comparision the same geometry cross-section from the 2-D build drawings are shown in Figure 44. Figure 43 and Figure 44 depict several components that are fielded on nearly every experiment. These components will be described in more detail in

order of proximity to the source: the MagLIF target, neutron collimator, vacuum region, mid-point gamma shield, and the mezzanine NTOF shield housing.

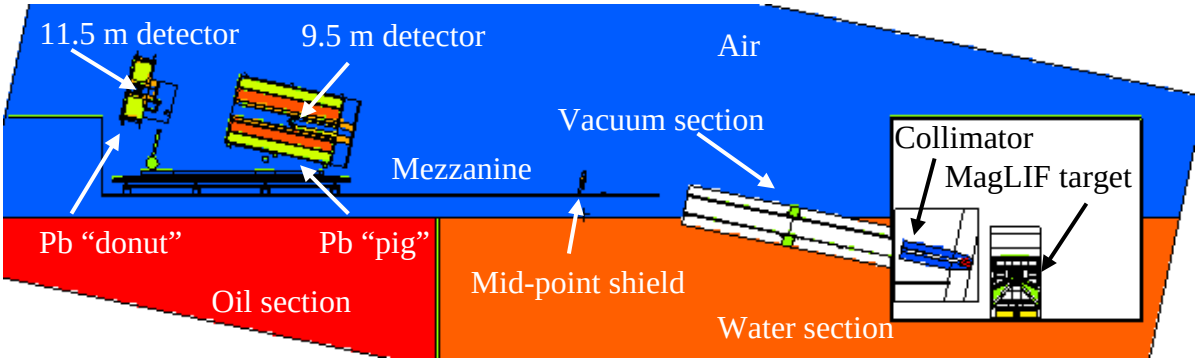

Figure 43 MCNP geometry of the typical configuration for line of sight 270

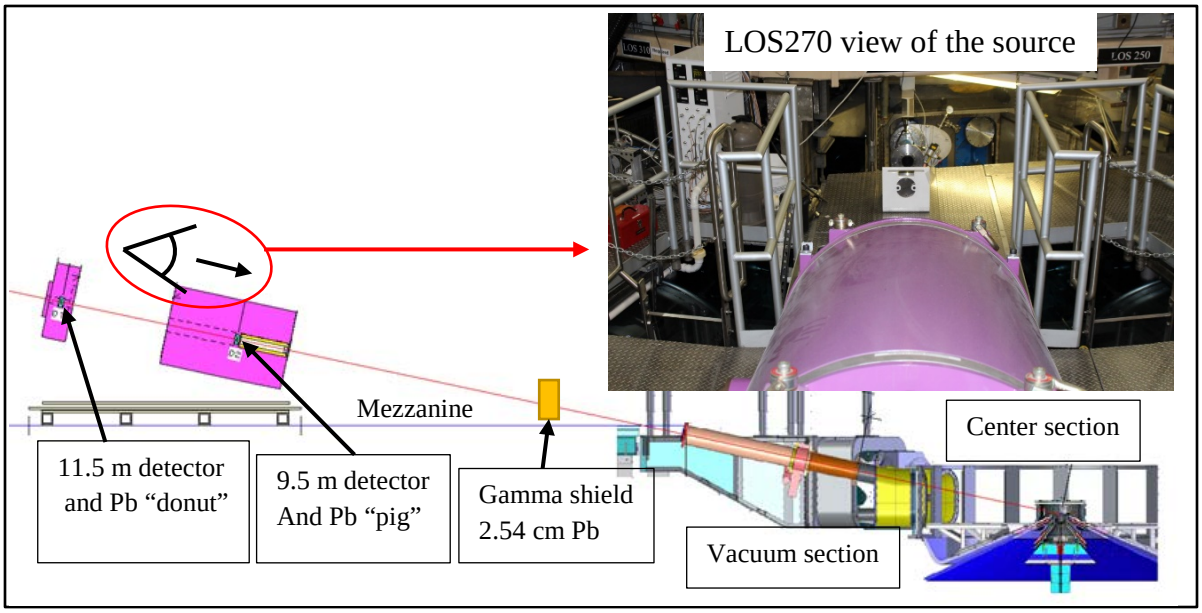

Figure 44 Cross-section view of LOS270 and typical shielding material required

Within the target chamber of the Z-machine there are two components relevant to the neutron transport, the MagLIF target and the neutron collimator. The nominal MagLIF target consists of a deuterium gas at 60 psi encased in a beryllium annulus that is nominally 1 cm tall, has an inner diameter of 0.01 cm and a wall thickness of ~ 0.015 cm. Surrounding the target area are the magnetic coils and the blast shield. Below the target are the power flow components and the magnetic insulated transmission lines (MITLs) that are required for coupling energy to the target.

Shown in Figure 45 are the MCNP version of the MagLIF target and power flow components along with a typical MagLIF target (center) and the physics associated with imploding the MagLIF target (right).

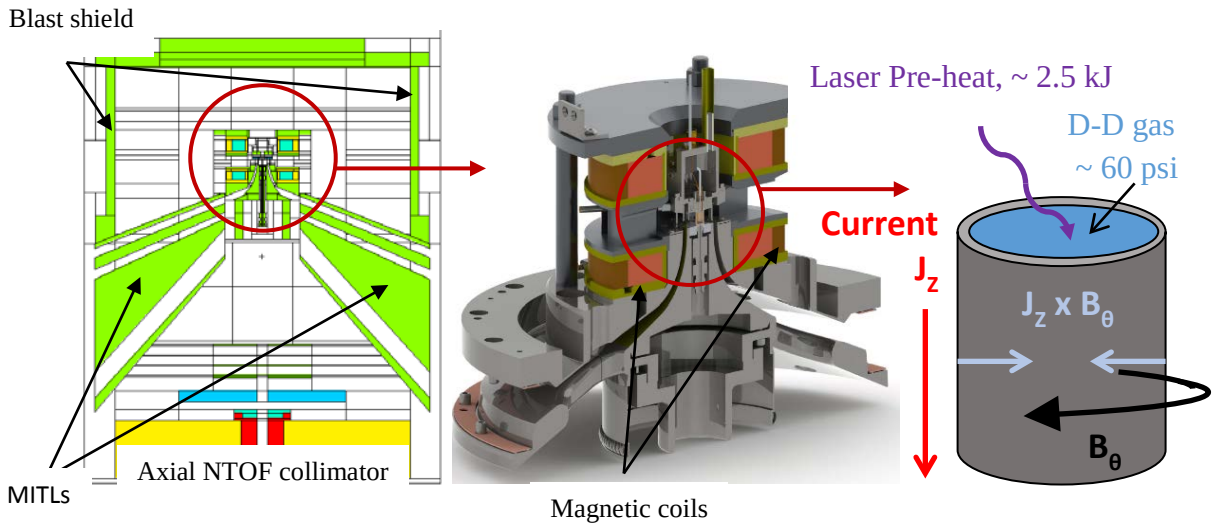

Figure 45 Typical MagLIF target (center). MCNP rendition shown on the left and the relevant MagLIF physics are shown on the right. MCNP model of the target region developed by K.D. Hahn

Inside the target chamber but outside the blast shield is a TIVAR (high molecular weight polyethylene) collimator, shown in Figure 46. This collimator is tilted at an angle of 12 degrees above the target, to match the pitch of the detector placement. The collimator has a 0.64-cm thick, 15-cm diameter, stainless steel plate in the front with a 0.95-cm diameter pin-hole. Directly behind the stainless steel plate is a 12.7-cm long, 7.62-cm diameter tungsten plug. The pin-hole opens up to a 1.27-cm aperture that runs the length of the tungsten plug. Behind the plug the aperture increases in diameter to 4.84-cm which runs through the entire 40-cm long collimator which is composed of high molecular weight polyethylene. 40-cm of high molecular weight polyethylene is approximately equal to ten D-D neutron mean-free-paths in length. This reduces the neutron fluence by ~ four orders-of-magnitude outside the collimated region.

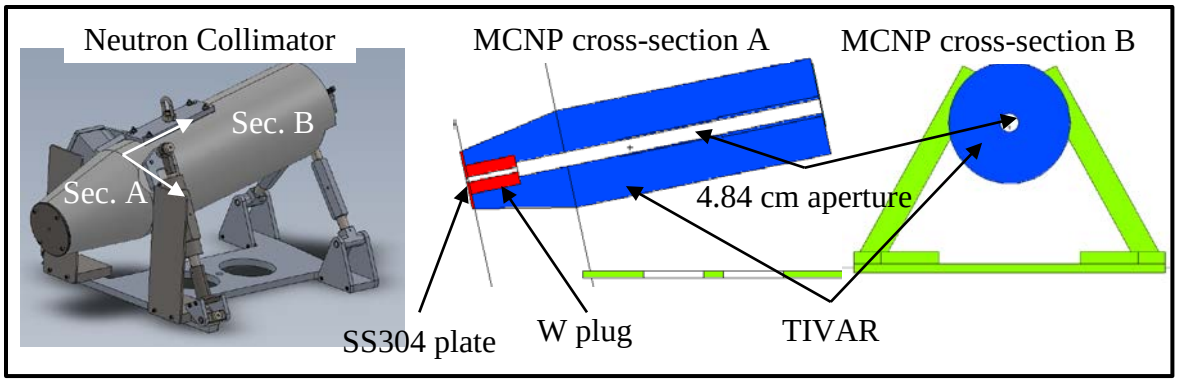

Figure 46 Hi-Density polyethylene neutron collimator. Shown are the as built (left), and the MCNP version (right)

Outside of the center stack is a 4.3-m long evacuated pipe with a 0.64-cm thick stainless steel gate valve window and a 0.64-cm thick glass vacuum-alignment window. These components are depicted in Figure 47 as the section was designed, built, and modeled.

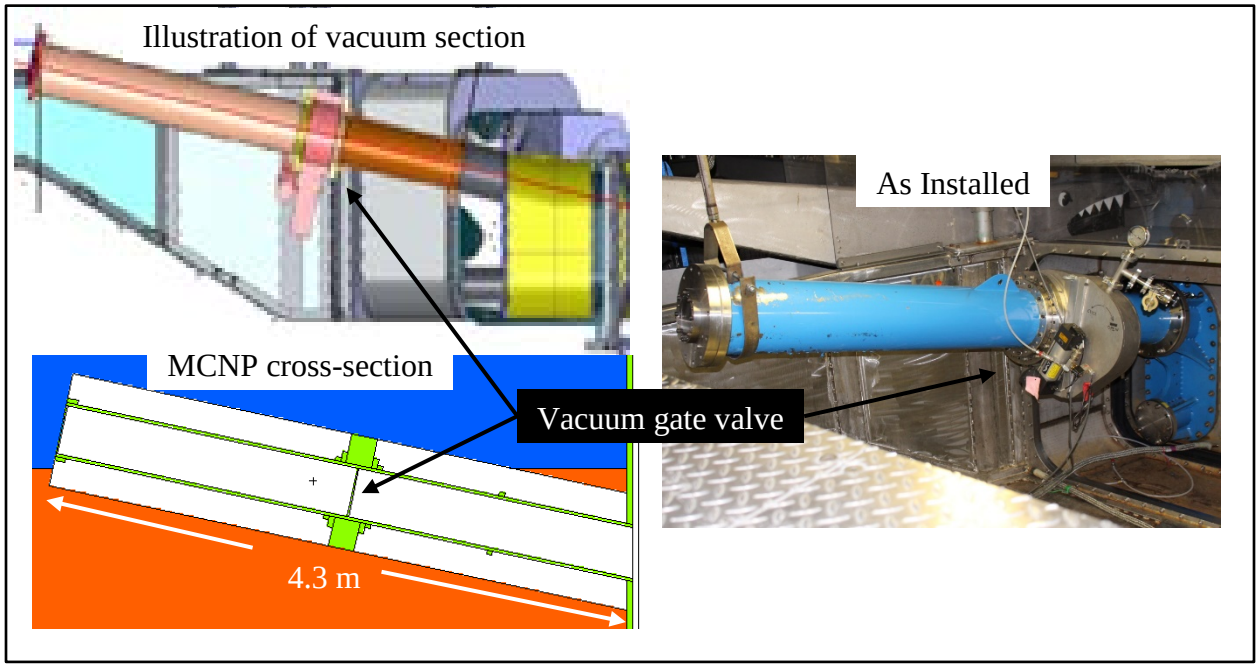

Figure 47 Vacuum section in LOS-270

Outside of the evacuated pipe is a 2.54-cm thick, Pb plate with a diameter of 13.3-cm as shown in Figure 48. This shielding is nominally placed at the mid-point location between the source and the 9.5-meter detector as shown previously in Figure 44.

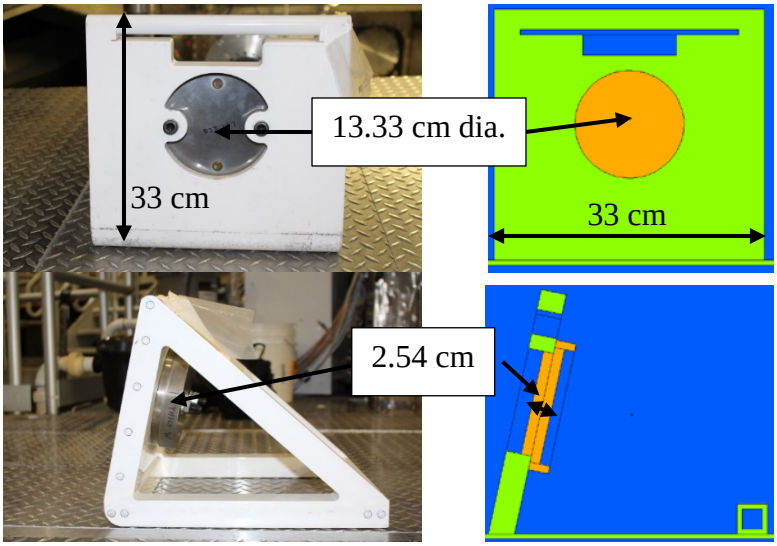

Figure 48 Adjustable mid-point shielding, 1" Pb disk is shown

Then 4.5 m of air separates this mid-point shield and the shield that houses the first of two NTOF detectors. A detailed view of the detector shield housing (affectionately referred to as the "pig") is shown in Figure 49. The first NTOF detector is a single-PMT, paddle detector and is located 9.5 meters from the source. Directly behind this pig is second shield, which is referred to as the "donut". This shield houses a dual-PMT, paddle detector and is located 11.5 meters from the source. Within the pig are concentric layers of paraffin, borated polyethylene (5 w/o) and lead from the outer to the most inner annulus. Placed directly in the line-of-sight is an additional 2.54-cm of lead on the front of the pig and 1.27-cm of lead on the front of the donut. The donut, or the 11.5-meter detector location, was designed after the fact and includes two layers of lead, while the main body of the shield is composed of paraffin. The alternating layers of lead with the paraffin is designed to reduce the photon background from surrounding material and to reduce the gamma background from de-excitation of the deuterium produced in the shield from neutron capture on hydrogen. This shield was designed to limit the number of large angle scattered neutrons from reaching the detector and from the large bremsstrahlung signal that always precedes the neutron signal. Also shown in Figure 48 is how the source views each detector.

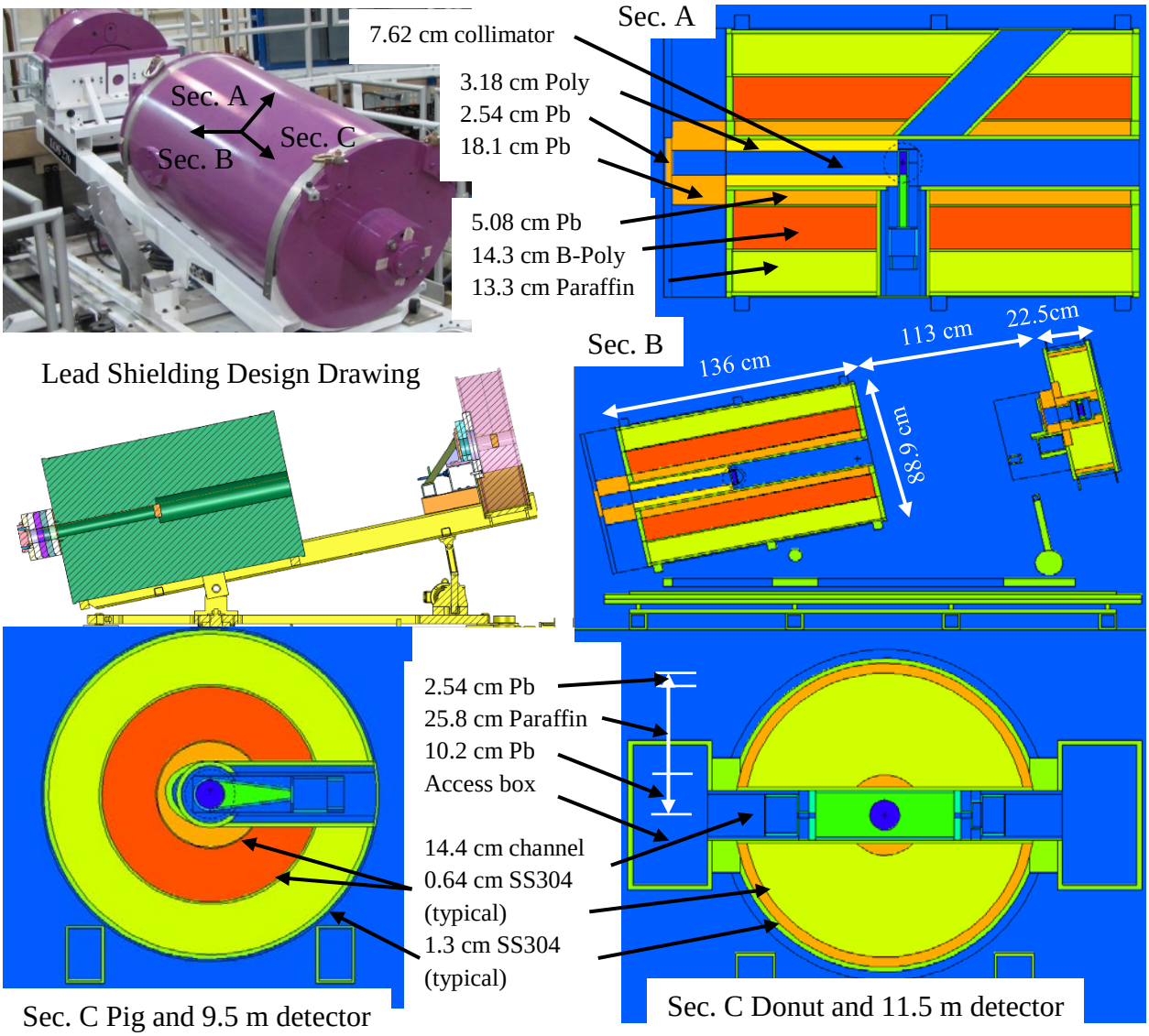

Figure 49 LOS270 Mezzanine NTOF Shielding

The difficulty with modeling this geometry is the source to detector distance. The range of time necessary to capture both the primary and down-scattered portion of the neutron signal for the 11.5-meter detector is 500-700 ns. To match the resolution of the experimental signal of 500 ps this requires 400 discrete time intervals in the signal. A sampling of 1000 particles, or 3% uncertainty in the sampling, means 400000 particles need to reach the detector. The detector subtends a solid angle of 5e-5 steradians, which means at a minimum 10^{13} source particles need to be used. For a single core calculation with a modest geometry, MCNP can process 10^{6} particles per second. This means the calculation will need to run for 10^{7} seconds or 2777 hours or

116 days. Thus, the problem requires the use of variance reduction and the utilization of high performance computing.

In a typical problem variance reduction is implemented through biasing the neutron source into a cone that subtends a solid angle with the detector of interest. However, this limits the control volume of the problem to the direct line-of-sight geometry and this is not feasible for a typical MagLIF experiment. At the time of the stagnation of the pinch, the beryllium liner can reach densities on the order of 60 – 80 g/cc, which increases the probability of neutron scattering through all angles of emission directly from the target area to the detector. In a typical MagLIF NTOF signal there is a low-level, but still significant continuum that is visible after the primary neutron signal that lasts for typically 150 nsec. This continuum corresponds to neutrons scattering off of the beryllium liner from 0 to 180 degrees. This is a very difficult parameter to capture with a Monte Carlo code.

MCNP has a variety of built in techniques that can be implemented to sample areas that are of interest that are naturally under-sampled. The most common techniques implemented are forced collisions, direction biasing, and weight windows, which can be defined spatially, temporally, or kinetically. Unfortunately, using these techniques are not straightforward and not always useable at the same time. Thus, developing a biasing scheme can require multiple iterations and can be just as time consuming as the calculation itself. For our specific problem, weight windows are not ideal because they are more effective in problems with a large amount of attenuating material, but it does make the other two methods used for this problem, source biasing and forced transport, more efficient. The most under-sampled region of the problem is the large angle scatter from the beryllium liner. Thus, the source was changed from isotropic to directional to sample a larger reaction rate from this contribution. This does require changing the weight of each individual history to keep the Monte Carlo sampling fair. The second technique that was implemented was the use of a dxtran sphere. The dxtran sphere encapsulates the scintillator region and particles are forced in the direction of the sphere. The weight of the particle is changed accordingly along the flight-path to correct for un-natural transport of the particle. Once the particle is within the dxtran sphere the particle transport returns to analog sampling.

6 MCNP Model results

At this point, it is worth reviewing the purpose of developing a detailed MCNP6 model and why it is necessary to understand the IRF measurement. A typical MagLIF NTOF signal from the 9.5-meter detector location is shown in Figure 50. The problem with this signal is the apparent structure in the signal. This is clearly seen in the residual, shown on the right of Figure 50, of the data and the idealized Brysk model. The motivation of this study was to determine if this structure and the low, long continuum was caused by the source, the attenuating environment or inherent noise from the PMT or the digitizer.

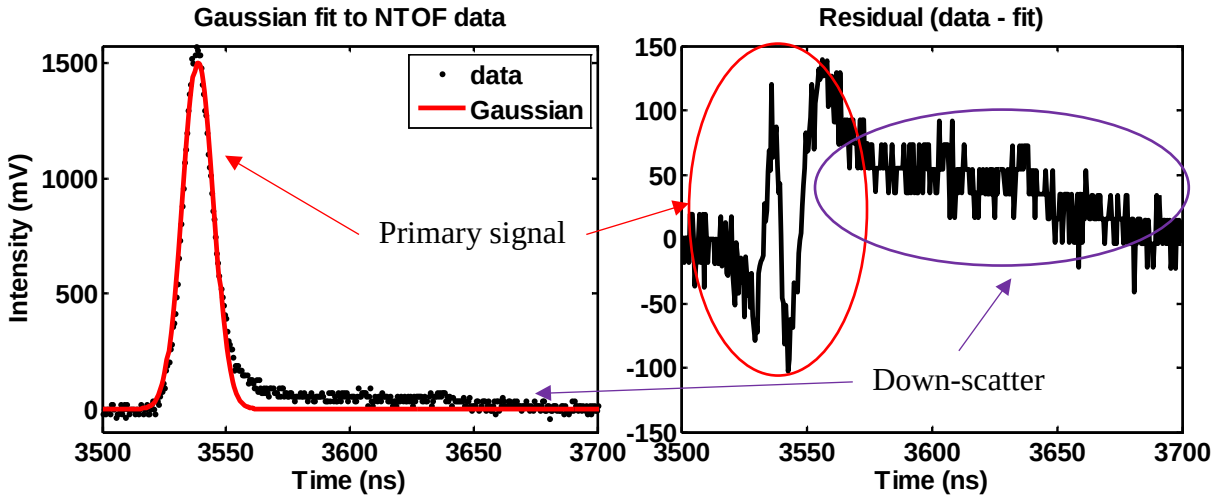

Figure 50 LOS 270 NTOF signal from the Hamamatsu mod 4 PMT 9.5-meter detector

The utility of using a Monte Carlo code such as MCNP6 is the flexibility of the input parameters, such as geometry, perturbations and neutron source description. For this work the parameters that were varied were the ion temperature, which changes the energy distribution of the neutron source, and the density of the beryllium liner, which changes the geometry description of the source. As the plasma reaches stagnation, the beryllium liner will be compressed and thus the density can vary throughout the pinch. For these calculations, a steady state assumption is made and therefore the source and liner properties are fixed at that moment in time. While physically this may not be true, this assumption makes the problem tractable and the results can be used to provide intuition into the relevant physics that are present in the experiment. For each parameter mentioned a singular model was developed to match these conditions. The ion temperature for the shots considered varied from 1 to 2.8 keV and for the data presented here, the areal density of

the liner was fixed at 1.2 g/cm^2 or a mass density of 80 g/cm^3 (43X the theoretical density). As a starting point, it was determined through modeling, that this value for the beryllium was most representative of the target conditions at stagnation. The neutron yield for each shot was can be determined by applying the appropriate constant for the detector sensitivity and MeVee for the detector bias setting. Ideally, a library should be developed for each parameter, where the ideal model is found by determining the best fit to the experimental data using a chi-squared analysis. This, however, will be left for future work.

Below in Figure 51, is an MCNP generated time-of-flight spectrum, in terms of MeV$_{ee}$ per source neutron, at an ion temperature of 2.8 keV and a beryllium liner areal density of 1.2 g/cm^2 for the 9.5-meter location (left) and the 11.5-meter location (right). The structure present in the spectrum is from the temporal broadening of neutron scattering from the resonance region from the lead and iron directly in the source-to-detector line-of-sight. Slight changes in the neutron energy from attenuation at different locations with respect to the detector vary the peak width in time. Also present in the spectrum, ~ 100 ns after the main peak for both locations, is a long flat continuum with a slight peak formation at 550 ns (left) and 675 ns (right).

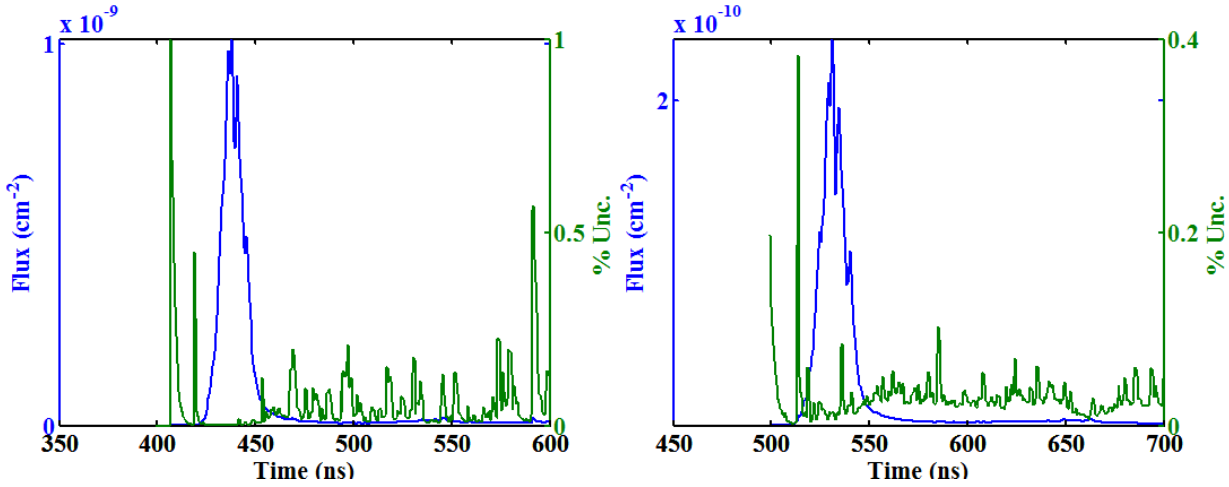

Figure 51 MCNP results for 9.5 m detector at 2.8 keV

This continuum corresponds to the down-scattered neutrons off of the compressed beryllium liner at stagnation. The shape of the continuum is consistent with the forward and backward preferential scattering angles present in the differential cross-section. This directionality causes a downshift of the measured neutron energy to ~ 2.4 and ~ 1.8 MeV at those locations. These trends are consistent regardless of detector location. There is one additional feature, however,

that is seen in the back detector signal and not the front. The peak region is much narrower and more structure appears on the leading edge, just before the maxima. This extra feature is caused by the additional neutron removal from the scintillator material in the front detector.

These MCNP results were convolved with the IRF values for the Hamamatsu mod 4 PMT from the Idaho State LINAC using a fast Fourier transform technique. The convolved result from the model was then compared with the measured data by normalizing the integral value. The measured data are then normalized to the modeled data at some location on the leading edge specified by a fraction of the maximum value. For these data the point on the leading edge that corresponds to 50% of the maximum value was chosen. However, there is structure on the leading edge that is not quite captured in the model and thus does make this normalization point somewhat arbitrary. The result of the convolution and normalization process are shown in Figure 52 for the 9.5-meter location at an ion temperature of 2.8 keV and a beryllium areal density of 1.2 g/cm^2. The modeled results were compared with MagLIF shot #2850 from this location. The comparison of the 11.5-meter location for the same parameters and shot number are shown in Figure 53.

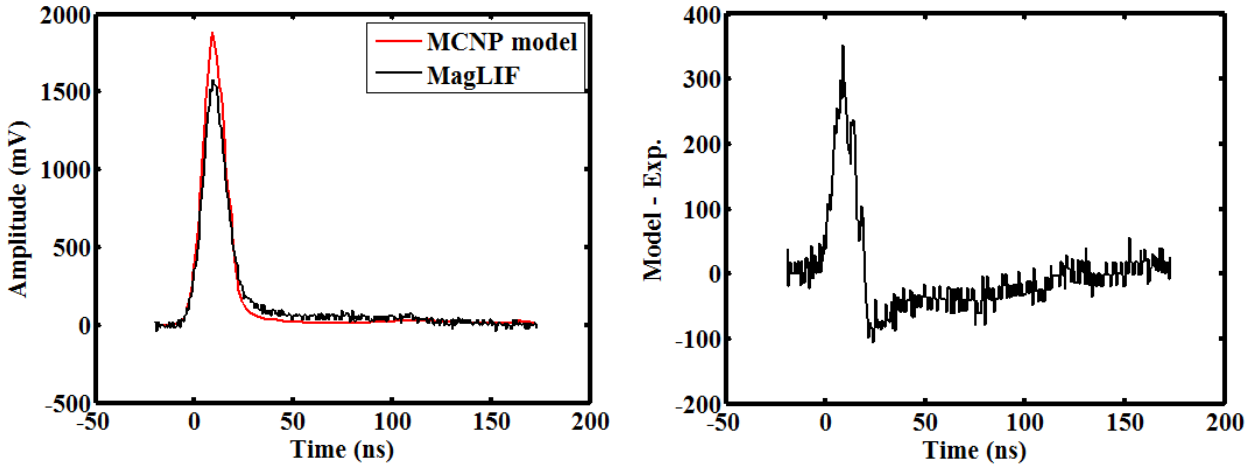

Figure 52 Comparison of modeled to experimental data for Shot#2850 at an ion temperature of 2.8 keV (left) and the residual (model – experiment) of the fit (right)

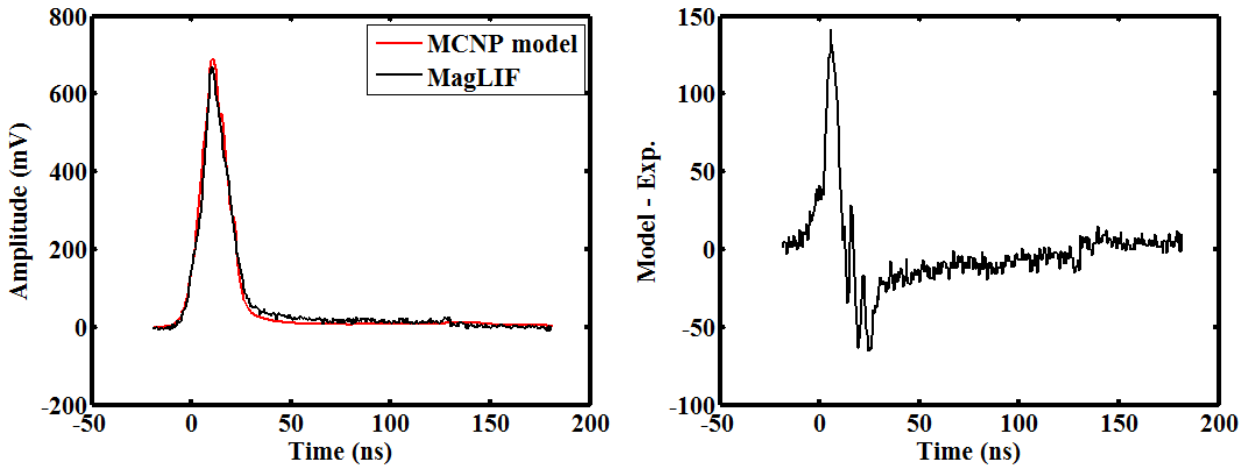

Figure 53 Comparison of modeled to experimental data for Shot#2850, 11.5 m detector at an ion temperature of 2.8 keV (left) and the residual (model – experiment) of the fit (right)

A couple of things can be pointed out by comparing the results in Figure 52 and Figure 53. First, the convolution of the modeled result tends to smooth out most of the structure that is seen in the MCNP solution. Secondly, the modeled result tends to over predict the main peak region and under predict the down-scattered region. By normalizing the area under each curve the result will always show where the deficiencies are in the model by exaggerating the dominant region of the data. In this case this result is caused by statistically under-sampling the down-scattered region. Statistically poor areas of the model will almost always produce a result that is less than expected. The third noticeable feature is the width parameter of the spectrum. It appears in both results, but this model at 2.8 keV convolved with an instrument response function is a slight over prediction in the ion temperature. Since this model result overestimated the temperature a new model was run with a temperature of 2.6 keV. The MCNP results are shown in Figure 54 for both the 9.5 and 11.5-meter detector locations. Similarly, the convolved and normalized result to MagLIF shot #2850 are shown in Figure 55 and Figure 56 for the front and back detector locations, respectively.

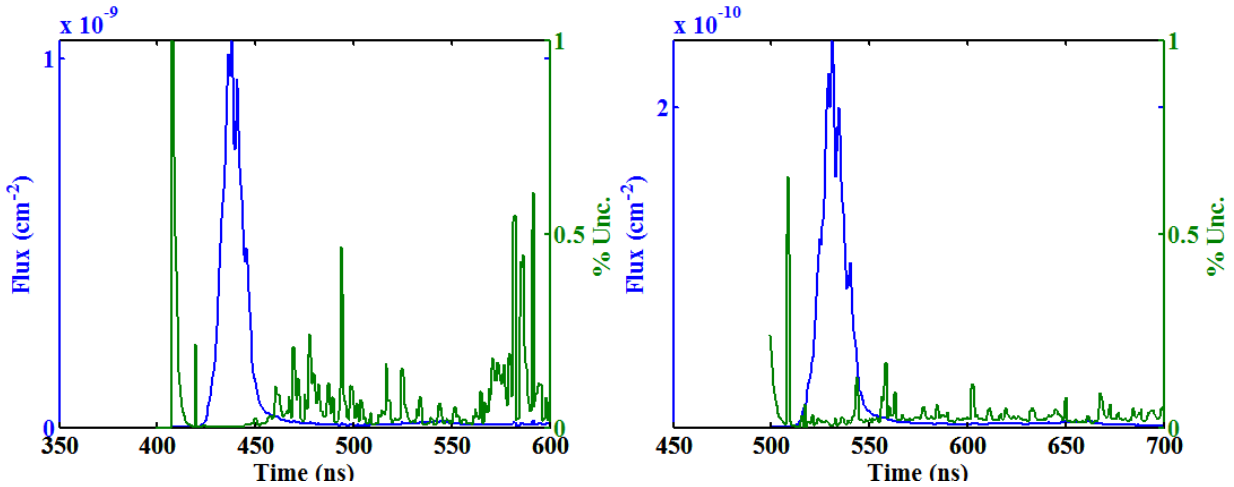

Figure 54 MCNP results for both the 9.5 m detector (left) and the 11.5 meter detector (right) at 2.6 keV

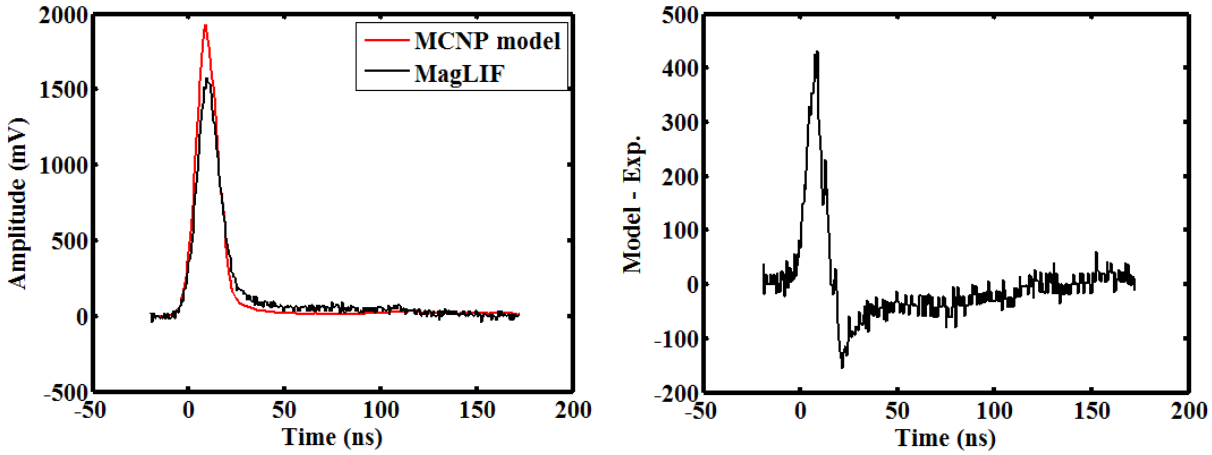

Figure 55 Comparison of Shot#2850 to the 9.5 meter detector modeled at an ion temperature of 2.6 keV (left) and the residual (model – experiment) of the fit (right)

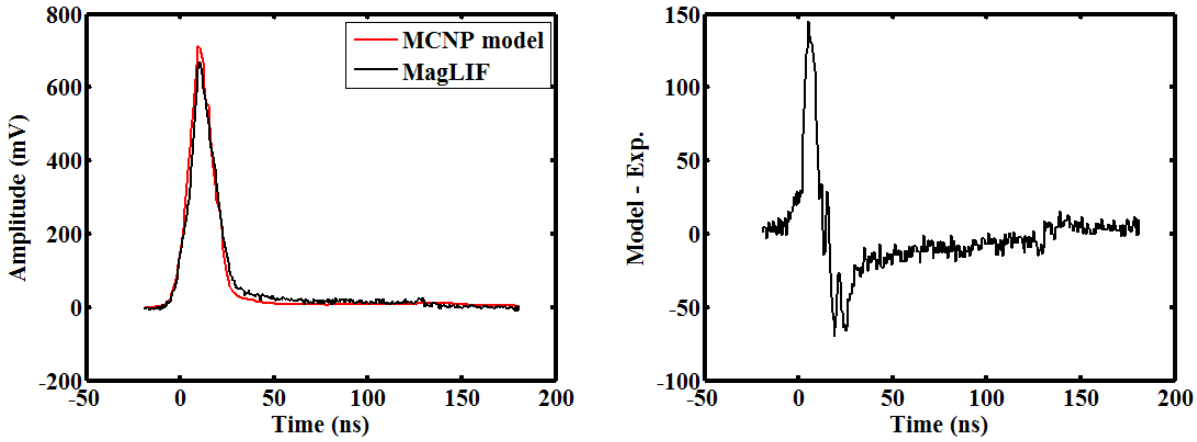

Figure 56 Comparison of Shot#2850 to the 11.5 m detector modeled at an ion temperature of 2.6 keV (left) and the residual (model – experiment) of the fit (right)

Notice that in both cases these models even at a lower temperature exhibit similar structure as the results for the 2.8-keV source, but the width parameter is more representative of the measured result. The result of the better fit decreases the observed residual between the modeled and experimental data, mainly in the peak region. Normalizing the data by the integral value shows where the modeled result departs the most from the measured data. If the ion temperature is under-predicted in the model, the maximum value of the model will under-predict the maximum value of the measured data and similarly an over-prediction in the temperature results in over-predicting the measured maximum value. This feature is the most obvious when comparing the results since it is the most dominate feature in the data. This effect can be seen when comparing the results for the 11.5-meter detector at 2.8 and 2.6 keV.

The second feature that is dominant in these data is the nodule that exists at lower amplitude on the leading edge of the measured signal. Since the modeled result was normalized to 50% of the maximum value, it is obvious from the residual that the model results do not produce the nodule with the same resolution. Thus, the normalization value causes the appearance of an over-prediction in the ion temperature, which may not be the case. Thus, the uncertainty of the procedure for predicting the ion temperature of a particular experiment needs to be discussed. The relationship between the measured width of a spectrum and the ion temperature in the time domain is given by the following relationship as shown previously in equation 1-9a [31].

$$\Delta t = 0.778\left[\frac{ns}{m\sqrt{keV}}\right] d\sqrt{kT_i}\ for\ DD\ neutrons \qquad [1-9a]$$

This equation can be rearranged and solved for the ion temperature, kT_i. Using this relationship, the uncertainty in the ion temperature can be determined for a given uncertainty in the width parameter using standard error propagation.

$$kT_i = \left(\frac{\Delta t}{0.778d}\right)^2, \delta_{kT_i} = \frac{2\Delta t\delta t}{(0.778d)^2}\ or\ \frac{\delta_{kT_i}}{kT_i} = \frac{2\delta t}{\Delta t} \qquad [6-1]$$

Thus, for data taken at the front detector at an ion temperature of 2.6 keV with an uncertainty of +/- 1 ns, the corresponding uncertainty in the ion temperature is 0.436 keV. However, the best uncertainty that can be obtained is limited by the resolution of the data acquisition. If a 500-ps digitizer resolution is assumed, the best possible uncertainty for these conditions is 0.218 keV. This result is consistent with the modeled results assuming the IRF is constant when comparing

the results at 2.8 and 2.6 keV for the front detector. Combining the uncertainty of the current IRF measurements with the uncertainty associated with the digitizer resolution yields an ion temperature and uncertainty of 2.6 +/- 0.5 keV from shot #2850. While presently this uncertainty is a large fraction of the ion temperature, efforts can be made in future work to reduce this uncertainty to the minimum value possible. Likewise, for the back detector an additional uncertainty of 1 nanosecond is added in quadrature to the previous uncertainty for the width parameter to account for the normalization. This approach still produces an inferred ion temperature of 2.6 +/- 0.5 keV, since the additional uncertainty is balanced by the improved accuracy resulting from the additional distance to the detector.

The other parameter of interest is the beryllium liner aerial density, which affects the shape of the low energy tail of the NTOF spectrum. The ratio of scattered to un-scattered neutrons from the beryllium liner can be approximated using the following equation, where r is the radius of the beryllium cylinder and σ_s is the microscopic elastic scattering cross-section. The value of the mean-free-path is written in both standard notation and in terms of rho-r, which is the true quantity of interest.

$$R = \frac{\phi_{scatter}}{\phi_{primary}} = 1 - \exp\left(-\frac{r}{\lambda}\right), \lambda = (N_{Be}\sigma_s)^{-1} = \left(\frac{N_A \rho_{Be} r \sigma_s}{r}\right)^{-1} \qquad [6-2]$$

Re-arranging this equation for the number density of beryllium and applying the standard rules of error propagation, the uncertainty in the areal density can be found from the measured uncertainty.

$$\rho r = \frac{\ln(1-R)}{N_A \sigma_s}, \delta_{\rho r} = \frac{\delta_R}{N_A \sigma_s (1-R)} \qquad [6-3]$$

Thus, for an uncertainty of 10% in the measured ratio, the corresponding uncertainty for a rho-r of 1 g/cm^2, assuming an elastic scattering cross-section of 2.4 barns at 2.5 MeV, will be 0.2 g/cm^2. If 10% uncertainty is assumed for the model results, then the measured value for the rho-r will be 1.2 +/- 0.2 g/cm^2. This result is in agreement with the expected value of ~ 1 g/cm^2.

Another parameter of interest is the total neutron yield. While this number cannot be predicted absolutely since the sensitivity has not been measured for these detectors, the MCNP model

results when compared with the measured responses do predict the appropriate trend for the total neutron yield. The accepted values for the neutron yields, as determined from indium activation, on these three shots were 3 x 10^{12}, 1 x 10^{12}, and 2 x 10^{12}, respectively. The values from the modeled results are shown for comparison in Table III.

Table III Comparison of relative neutron yields inferred from normalization to measured data

Shot #	Temperature (keV)	9.5 m detector Yield Ratio (Meas./MCNP)	11.5 m detector Yield Ratio (Meas./MCNP)
2850	2.6	2.06E+12	3.44E+12
2851	1.3	7.71E+11	1.24E+12
2852	2.1	1.45E+12	2.27E+12

Similar results to those shown for shot #2850 are presented for MagLIF shots #2851 and #2852. Shot #2851 was modeled assuming an ion temperature of 1.3 keV and shot #2852 was modeled assuming an ion temperature of 2.1 keV. The modeled results for the front and back detector are shown on the left and right, respectively, in Figure 57 for shot#2851 and Figure 58 for shot#2852. The convolved, normalized results were compared with the NTOF data acquired on those two shots. The results for shot#2851 are shown in Figure 59 and Figure 60 while the results for shot #2852 are shown in Figure 61 and Figure 62.

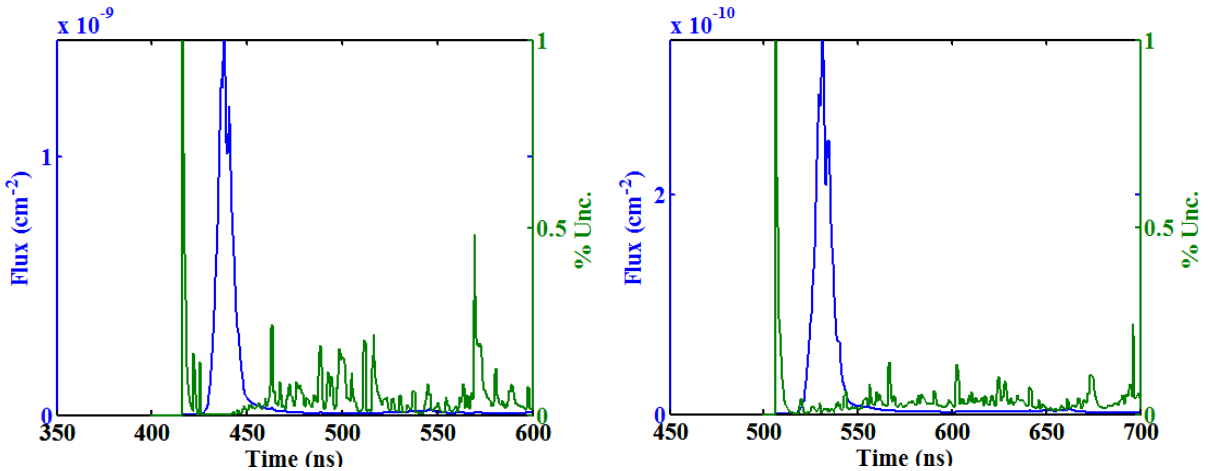

Figure 57 MCNP results for the 9.5 m detector (left) and the 11.5 m detector (right) at 1.3 keV (Shot#2851)

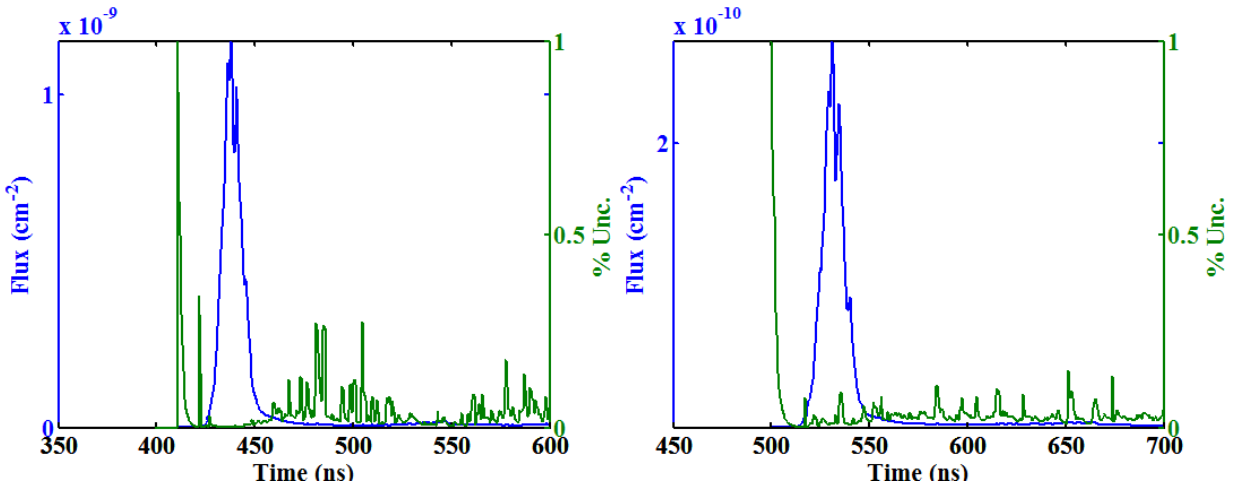

Figure 58 MCNP results for the 9.5 m detector (left) and the 11.5 m detector (right) at 2.1 keV (Shot#2852)

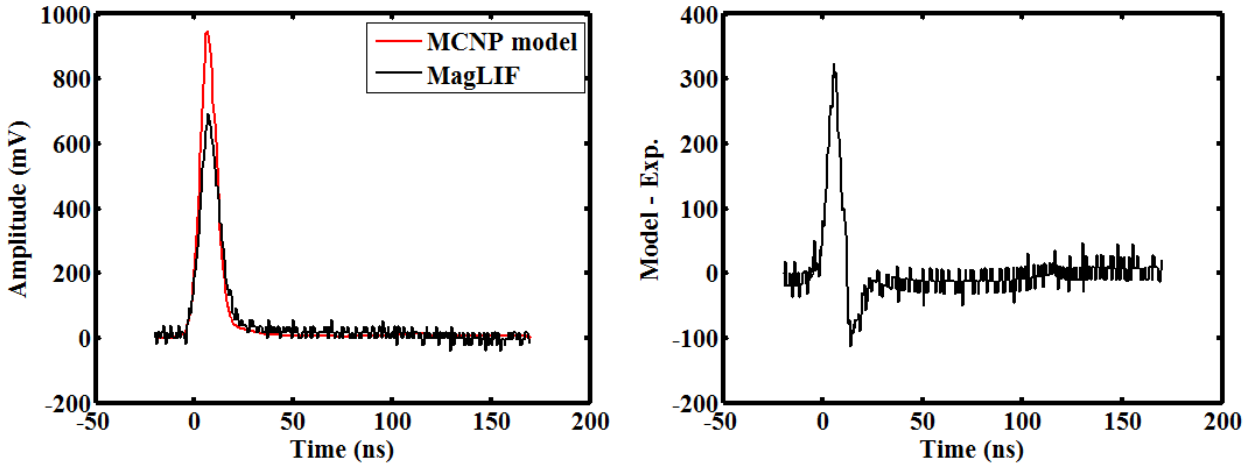

Figure 59 Shot#2851 compared with the model results for the 9.5 meter detector at 1.3 keV

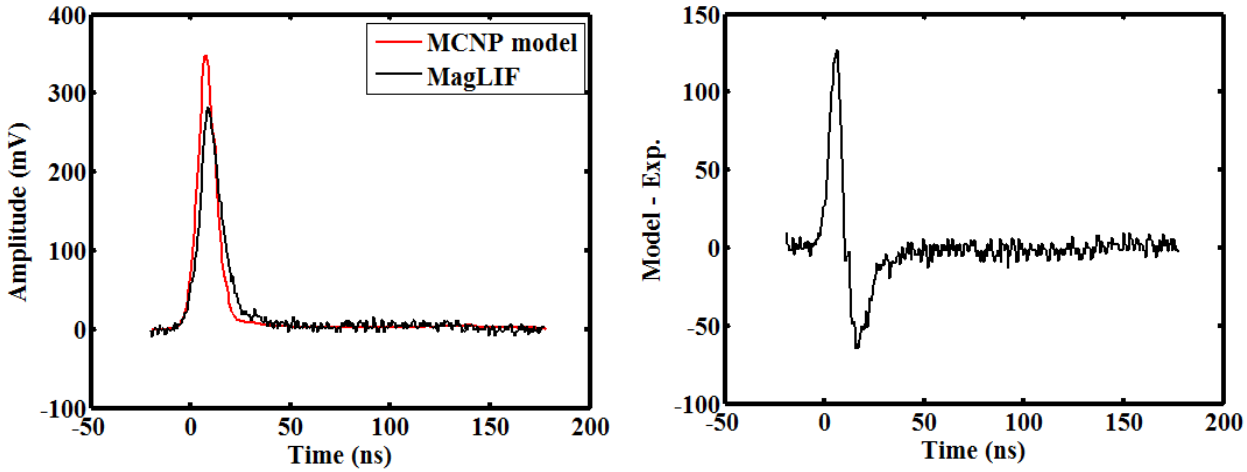

Figure 60 Shot#2851 compared with the model results for the 11.5 meter detector at 1.3 keV

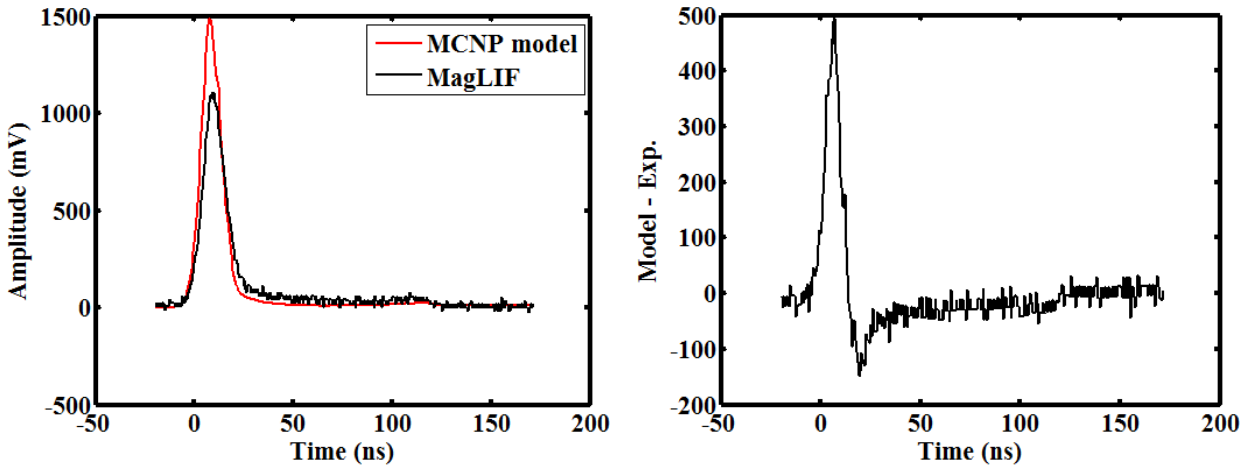

Figure 61 Shot#2852 compared with the model results for the 9.5 meter detector at 2.1 keV

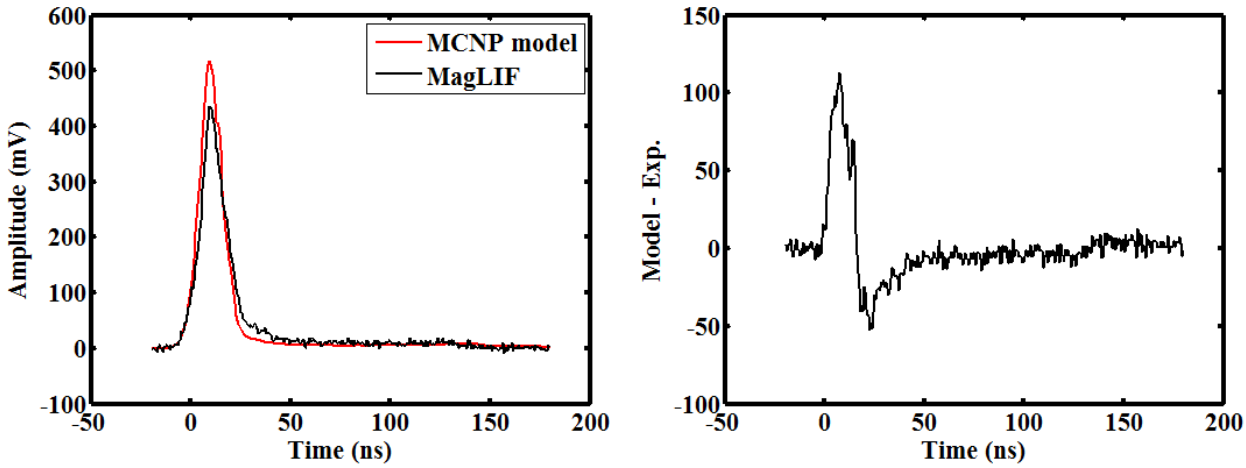

Figure 62 Shot#2852 compared with the model results for the 11.5 meter detector at 2.1 keV

The comparison of the convolved model result to NTOF data acquired on shots #2851 and #2852 provide similar results to those discussed for shot #2850. In either case, independent of detector, there is an over-prediction of the peak amplitude and an under-prediction of the beryllium down-scatter region. This again can largely be attributed to the statistical under-sampling of the down-scattered region and other possible deficiencies within the model. It is important to remember that all models deviate from reality regardless of the detail included. However, by comparing the model results with actual NTOF data show that, while improvements can be made, the results of this work provide promising and exciting results by constraining the ion temperature, areal density, and neutron yield.

7 Future work

The results for this work show the novelty of obtaining the instrument response function and detector sensitivity by measuring single neutron events in coincidence with the associated alpha particle from the D-T reaction. While the experimental and analytical techniques are shown to work, significant improvements can be made to reduce the large relative uncertainties in the measurement. In addition, a proof-of-principle showing the utility of coupling modeled and experimental results to constrain the ion temperature, beryllium liner density, and neutron yield were presented. The uncertainty within this model can be reduced, which in turn will reduce the uncertainty of the inferred values. In addition, this model can be used in the future to re-design LOS270 and other lines-of-sight, such that more favorable neutron measurements can be made.

8 Conclusion

Detector characterization is important and essential to understanding neutron measurements made in support of inertial confinement fusion (ICF) experiments. For this work the focus was on neutron time-of-flight diagnostics fielded at the Z-experimental facility with emphasis on the Magnetized Liner Fusion (MagLIF) concept. Results were presented here on the characterization in time and energy space of an NTOF detector consisting of EJ-228 scintillator and two independent PMTs, a Hamamatsu-mod 5 and Photek-PMT240. This characterization was done by measuring single-neutron, induced events in the scintillator. Observation of single-neutron event measurements were insured by measuring the associated alpha particle and neutron produced from the D-T reaction in kinematic coincidence. The results of these experiments provided the time dependent instrument response function and the detector sensitivity as a function of applied voltage to cover the entire dynamic range of the detector.

While this detector has not yet been fielded on any MagLIF experiments, the development of a predictive capability was desired. As a proof-of-principle, a detailed model of line-of-sight 270 at the Z-machine was developed in MCNP6 to correct for geometry issues when transferring the calibration results from a light lab setting to the Z-environment. Representative values for the instrument response function for the current detectors fielded on MagLIF experiments were convolved with the modeled results. These results were compared with data collected on three

previous MagLIF experiments. The comparison shows the model results can be used to constrain three parameters that are relevant for diagnosing the plasma performance and confinement – the plasma ion temperature, the beryllium liner areal density, and the neutron yield.

9 References

[1] H.P. Furth, "Magnetic Confinement Fusion," *Science,* vol. 249, no. 4976, pp. 1522-1527, 1990.

[2] James J. Duderstadt and Gregory A. Moses, Inertial Confinement Fusion, 1982.

[3] "About ITER," [Online]. Available: https://www.iter.org/proj/inafewlines.

[4] D.V. Rose, "Three-dimensional electromagnetic model of the pulsed power Z-pinch accelerator," *Physical Review Special Topics - Accelerators and Beams,* vol. 13, 2010.

[5] E.I. Moses, "Ignition on the National Ignition Facility," *Journal of Physics: Conference Series,* vol. 112, 2008.

[6] T.R. Boehly et al, "Initial Performance results of the OMEGA laser system," *Optics Communications,* vol. 133, no. 1/6, pp. 495-506, 1997.

[7] R.B. Spielman et al, "Wire-array z pinches as intense x-ray sources for inertial confinement fusion," *Plasma Phys. Control. Fusion,* vol. 42, 200.

[8] S.A. Slutz et al, "Pulsed-power-driven cylindrical liner implosions of laser preheated fuel magnetized with an axial field," *Physics of Plasmas,* vol. 17, p. 056303, 2010.

[9] Stephen A. Slutz adn Roger A. Vesey, "High-Gain Magnetized Inertial Fusion," *Physical Review Letters,* vol. 108, p. 025003, 2012.

[10] Patrick K. Rambo et al, "Z-Beamlet: a multikilojoule, terawatt-class laser system," *Applied Optics,* vol. 44, no. 12, 2005.

[11] Brent Jones et al, "A Renewed Capability for Gas Puff Science on Sandia's Z Machine," *IEEE Transactions on Plasma Science,* vol. 42, no. 5, 2014.

[12] C.A. Coverdale et al, "Deuterium gas-puff Z-pinch implosions on the Z accelerator," *Physics of Plasma,* vol. 14, 2007.

[13] A.L. Velikovich et al, "Z-pinch plasma neutron sources," *Physics of Plasma,* vol. 14, 2007.

[14] G. A. Rochau et al, "High performance capsule implosions driven by the Z-pinch dynamic hohlraum," *Plasma Physics and Controlled Fusion,* vol. 49, 2007.

[15] C.W. Barnes et al, "Experimental configuration fo direct drive cylindrical implosions on the OMEGA Laser," *Review of Scientific Instruments,* vol. 70, 1999.

[16] R.L. McCrory et al, "OMEGA ICF experiments and preparation for direct drive ignition on NIF," *Nuclear Fusion,* vol. 41, no. 10, 2001.

[17] T.R. Dittrich et al, "Review of indirect-drive ignition design options for the National Ignition Facility," *Physics of Plasma,* vol. 6, 1999.

[18] E.L. Dewald et al, "First hohlraum drive studies on the National Ignition Facility," *Physics of Plasma,* vol. 13, 2006.

[19] E.L. Dewald et al, "X-ray conversion efficiency of high-Z hohlraum wall materials for indirect drive igniton," *Physics of Plasma,* vol. 15, 2008.

[20] F.H. Seguin et al, "Spectrometry of charged particle fusion from inertial-confinement-fusion plasmas," *Review of Scientific Instruments,* vol. 74, 2003.

[21] H. Azechi et al., "Review of ICF plasma diagnostics," *Fusion Engineering and Design,* vol. 34/35, pp. 37-44, 1997.

[22] M. J. Moran and J. Hall, "Nuclear diagnostics in support of inertial confinement fusion experiments," *Review of Scientific Instruments,* vol. 68, 1997.

[23] K.D. Hahn et al, "Fusion-neutron measurements for magnetized liner inertial fusion experiments on the Z accelerator," *Journal of Physics: Conference Series,* vol. 717, 2016.

[24] T. J. Murphy et al, "Neutron time-of-flight and emission time diagnostics for the National Ignition Facility," *Review of Scientific Instruments,* vol. 72, 2001.

[25] V. Yu. Glebov et al, "Prototypes of National Ignition Facility neutron time-of-flight detectors tested on OMEGA," *Review of Scientific Instruments,* vol. 75, 2004.

[26] L. Cranberg and J. S. Levin, "Inelastic scattering of neutrons from iron by time-of-flight," *Physical Review Letters,* vol. 100, no. 1, 1955.

[27] G. F. Bogdanov et al., "The measurement of fast-neutron spectra by time-of-flight methods," *Journal of Nuclear Energy,* vol. 3, pp. 148-157, 1956.

[28] A.J. Nelson et al., "A novel method for modeling the neutron time of flight detector response in current mode to inertial confinement fusion experiments," *Review of Scientific Instruments,* vol. 83, 2012.

[29] H. Brysk, "Fusion neutron energies and spectra," *Plasma Physics,* vol. 15, pp. 611-617, 1973.

[30] R.A. Lerche et al., "Laserfusion ion temperatures determined by neutron time-of-flight techniques," *Applied Physics Letters,* vol. 31, no. 15, 1977.

[31] R. A. Lerche and B.A. Remington, *Review of Scientific Instruments,* vol. 61, 1990.

[32] P. F. Knapp, D. B. Sinars, and K. D. Hahn, "Diagnosing suprathermal ion populations in Z-pinch plasmas using fusion neutron spectra," *Physics of Plasma,* vol. 20, 2013.

[33] D. Klir et al, "Fusion neutron detector for time-of-flight measurements in z-pinch and plasma experiments," *Review of Scientific Instruments,* vol. 82, 2011.

[34] C. J. Forrest et al, "High resolution spectroscopy used to measure inertial confinement fusion neutron spectra on OMEGA," *Review of Scientific Instruments,* vol. 83, 2012.

[35] M. R. Gomez et al., *PRL,* vol. 113, 2014.

[36] P.F. Schmit et al, *PRL,* vol. 113, 2014.

[37] V. Yu Glebov et al, "Neutron bang time detector based on a light pipe," *Review of Scientific Instruments,* vol. 79, 2008.

[38] R. A. Lerche et al, "Neutron emission time measurements for ICF targets," *Review of Scientific Instruments,* vol. 59, 1988.

[39] R. A. Lerche, D.W. Phillion, and G. L. Tietbohl, "25 ps neutron detector for measuring ICF target burn history," *Review of Scientific Instruments,* vol. 66, 1995.

[40] D. C. Wilson et al, "Diagnosing ignition with DT reaction history," *Review of Scientific Instruments,* vol. 79, 2008.

[41] M.A. Russotto and R.L. Kremens, "Measurement of fuel ion temperatures in ICF implosions using current-mode neutron time-of-flight detectors," *Review of Scientific Instruments,* vol. 61, 1990.

[42] R. Hatarik et al, "Analysis of the neutron time-of-flight spectra from inertial confinement fusion experiments," *Journal of Applied Physics,* vol. 118, 2015.

[43] T. Dreyer et al, "Calibration and validation of a time of flight detector," *Nuclear Instruments and Methods in Physics Research,* vol. A309, pp. 184-189, 1991.

[44] M. A. Bonura et al, "A technique for verifying the input response function fo neutron time-of-flight scintillation detectors using cosmic rays," *Review of Scientific Instruments,* vol. 85, 2014.

[45] J. A. Brown et al., "Relative light yield and temporal response of a stilbe-doped bibenzyl organic scintillator for neutron detection," *Journal of Applied Physics,* vol. 115, 2014.

[46] R. Hatarik et al., "Characterizing time decay of bibenzyl scintillator using time correlated single photon counting," *Review of Scientific Instruments,* vol. 83, 2012.

[47] B. A. Remington, R. A. Lerche, and M. D. Cable, "Ion temperature analysis of implosions of DT filled capsules," *Review of Scientific Instruments,* vol. 61, 1990.

[48] T.J. Murphy, R.E. Chrien, K.A. Klare, "Interpretation of neutron time-of-flight signals from current-mode detectors," *Review of Scientific Instruments,* vol. 68, 1997.

[49] K.D. Hahn et al, "Fusion-neutron-yield, activation measurements at the Z accelerator: Design, analysis, and sensitivity," *Review of Scientific Instruments,* vol. 85, 2014.

[50] M. J. Moran et al, "Deterium-tritium neutron yield measurements with the 4.5 m neutron-time-of-flight detectors at NIF," *Review of Scientific Instruments,* vol. 83, 2012.

[51] C.L. Ruiz et al, "Absolute calibration of a total yield indium activation detector for DD and DT neutrons," *Review of Scientific Instruments,* vol. 63, 1992.

[52] C.J. Waugh, M.J. Rosenberg,A.B. Zylstra, J.A. Frenje, F.H. Sequin,R.D. Petrasso,V. Yu. Glebov, T.C. Sangster, and C. Stoeckl, "A method for in situ absolute DD yield calibration of neutron time-of-flight detectors on OMEGA using CR-39-based proton detectors," *Review of Scientific Instruments,* vol. 86, 2015.

[53] S.R. Mirfayzi et al., "Calibration of time of flight detectors using laser-driven neutron source," *Review of Scientific Instruments,* vol. 86, 2015.

[54] K.D. Hahn et al., "Calibration of neutron-yield diagnostics in attenuating and scattering environments," *Review of Scientific Insturments,* vol. 83, 2012.

[55] J.B. Birks, The Theory and Practice of Scintillation Counting, Oxford: Pergamon Press, 1964.

[56] G. F. Knoll, Radiation Detection and Measurement 4th edition, New York: Wiley, 2010.

[57] H. Stemlicht, G.C. Niman, and G. W. Robinson, "Triplet-Triplet Annihilation and Delayed Fluorsecence in Molecular Aggregates," *The Journal of Chemical Physics,* vol. 38, 1963.

[58] R. Batchelor et al, "The response of organic scintillators to fast neutrons," *Nuclear Instruments and Methods,* vol. 13, pp. 70-82, 1961.

[59] National Nuclear Data Center, Brookhaven National Laboratory, "ENDF/B-VII.1 Library Retrieval & Plotting," 2011. [Online]. Available: http://www.nndc.bnl.gov/sigma/.

[60] J. B. Czirr, D. R. Nygren, and C. D. Zafiratos, "Calibration and performance of a neutron time of flight detector," *Nuclear Instruments and Methods,* vol. 31, pp. 226-232, 1964.

[61] G. V. O'Rielly, N. R. Kolb, and R. E. Pywell, "The response of plastic scintillator to protons and deuterons," *Nuclear Instruments and Methods in Physics Research A,* vol. 368, pp. 745-749, 1996.

[62] S. A. Pozzi et al, "Monte CArlo and analytical models of neutron detection with scintillation detectors," *Nuclear Instruments and Methods,* vol. A582, pp. 629-637, 2007.

[63] Andreas Enqvist et al, "Neutron light output response and resolution function in EJ-309 liquid scintillation detectors," *Nuclear Instruments and Methods in Physics Research A,* vol. 715, pp. 79-86, 2013.

[64] R. A. Cecil, B. D. Anderson, and R. Madey, "Improved predictions fo neutron detection efficiency for hydrocarbon scintillators from 1 MeV to about 300 MeV," *Nuclear Instruments and Methods,* vol. 161, pp. 439-447, 1979.

[65] Noel R. Stanton, "A Monte Carlo program for calculating neutron detection efficiencies in plastic scintillator," 1971.

[66] V.V. Verbinski et al, "Calibration of an organic scintillator for neutron spectrometry," *Nuclear Instruments and Methods* , vol. 65, pp. 8-25, 1968.

[67] Lisa G. Chiang et al, "Method to correlate CFD discriminator level and energy deposition by neutrons and photons in a fast plastic scintillating detector," 2000.

[68] J.D. Styron et al, "Predicting the sensitivity of the beryllium/scintillator layer neutron detector using Monte Carlo and experimental response functions," *Review of Scientific Instruments,* vol. 85, 2014.

[69] M. Anghinolfi et al, "The response function of organic scintillators to fast neutrons," *Nuclear Instruments and Methods,* vol. 165, pp. 217-224, 1965.

[70] C. Carasco, "Organic scintillators response function modeling for Monte Carlo simulation of time-of-flight measurements," *Applied Radiation and Isotopes*, vol. 70, pp. 1367-1369, 2012.

[71] J. K. Dickens, "SCINFUL: A Monte Carlo based computer program to determine a scintillator full energy response to neutron detection for En between 0.1 and 80 MeV: User's Manual and FORTRAN program listing," 1988.

[72] Sara A. Pozzi, Enrico Padovani, Marzio Marseguerra, "MCNP-PoliMi: a Monte-Carlo code for correlation measurements," *Nuclear Instruments and Methods in Physics Research A*, vol. 513, pp. 550-558, 2003.

[73] C. Bahr et al, "Calculation of neutron response functions in complex geometries with the MCNP code," *Nuclear Instruments and Methods in Physics Research A*, vol. 411, pp. 430-436, 1998.

[74] R. J. Kurz, "A 709/7090 FORTRAN II program to compute the neutron-detection efficiency of plastic scintillator for neutron energies from 1 to 300 MeV," Berkeley, CA, 1964.

[75] D. C. Irving et al, "05R, A general-purpose monte carlo neutron transport code," 1965.

[76] R. E. Textor and V.V. Verbinski, "O5S: a Monte Carlo code for calculating pulse height distributions due to monoenergetic neutrons incident on organic scintillators," 1968.

[77] S.A. Pozzi et al, "MCNPX-PoliMi for nuclear nonproliferation applications," *Nuclear Instruments and Methods in Physics Research A*, vol. 694, pp. 119-125, 2012.

[78] B. Antolkovic and Z. Dolenec, "The neutron induced 12C(n,n')3-alpha reaction at 14.4 MeV in a kinematically complete experiment," *Nuclear Physics*, vol. A237, pp. 235-252, 1975.

[79] C. L. Ruiz et al., "Progress in obtaining an absolute calibration of a total deuterium-tritium neutron yield diagnostic based on copper activation," *Review of Scientific Instruments*, vol. 83, 2012.

[80] Hamamatsu Photonics, "Photomultiplier Tubes," 2014. [Online]. Available: http://www.hamamatsu.com/us/en/index.html.

[81] Photek, "Photomultipliers," [Online]. Available: http://www.photek.com/products/photomultipliers.html.

[82] Lagarias, J. C., J. A. Reeds, M. H. Wright, and P. E. Wright, ""Convergence Properties of the Nelder-Mead Simplex Method in Low Dimensions."," *SIAM Journal of Optimization.*, vol. 8, no. 1, 1998.

[83] Eljen Technologies, "Plastic Scintilators," 2016. [Online]. Available: http://www.eljentechnology.com/products/plastic-scintillators.

10 Appendix A – Cable compensation analysis and average IRFs for data acquired with the RG-223 cable

A cable compensation algorithm was developed to correct the data acquired with the RG-223 cabling for signal attenuation and dispersion. The attenuation function was inferred by measuring 1000, 2.5-V, 10-ns wide, logic pulses, with firstly a 3 foot RG-223 cable and secondly with the 170-feet of RG-223 used in the data acquisition. These measurements are representative of the "ideal" waveform and the attenuated waveform. The results for these measurements along with the same signal measured with 120-feet of LMR-600 cable are shown in Figure 63. The results of this measurement show extreme signal distortion and a ~ 40% reduction in the signal amplitude in the data acquired with the RG-223 cabling and a 10% reduction in signal amplitude with negligible signal distortion for the LMR-600 cabling. Thus, all the data acquired for the RG223 was later compensated using a fast Fourier analysis, while the losses associated with the LMR600 cabling were deemed negligible since fast Fourier de-convolution adds unnecessary noise to the measured signal.

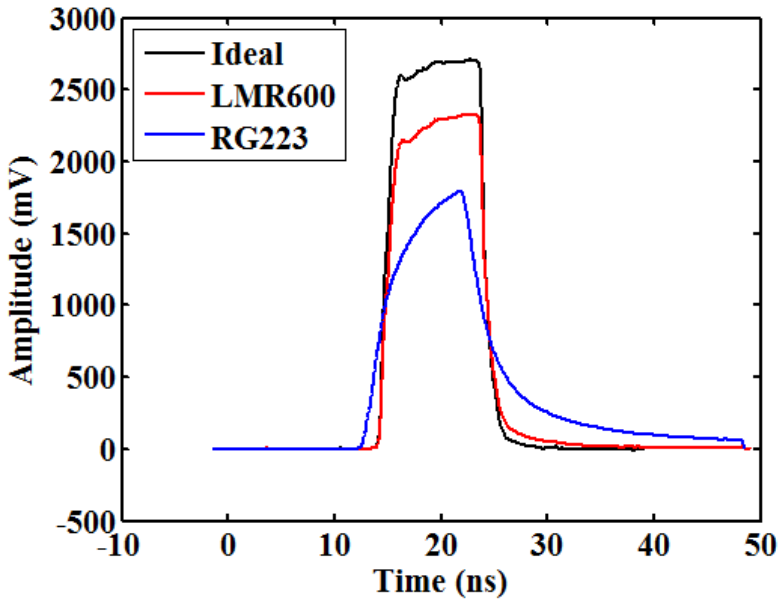

Figure 63 Cabling attenuation measured with a 10-ns wide, 2.5-V logic pulse using 170 feet of RG223 and 120 feet of LMR600

For this work, reducing the FWHM of the observed data was investigated. For example, two different sets of cabling with the same impedance, but with different propagation velocities were used for these experiments. The RG223 cabling is a standard 50-ohm cable with a propagation

velocity of 0.66c whereas the LMR600 cabling has a propagation velocity of 0.87c. This change in velocities can be observed in the FWHM of the coincidence signal, where the ratio of the FWHM values were equivalent to the ratio of the propagation velocities. This should be the case assuming the particles of interest, the alpha and neutron, arrive at the prospective detectors at the same time.

10.1 Hamamatsu mod-5 data acquired with the Photek PMT240 in coincidence with the 110 degree SBD

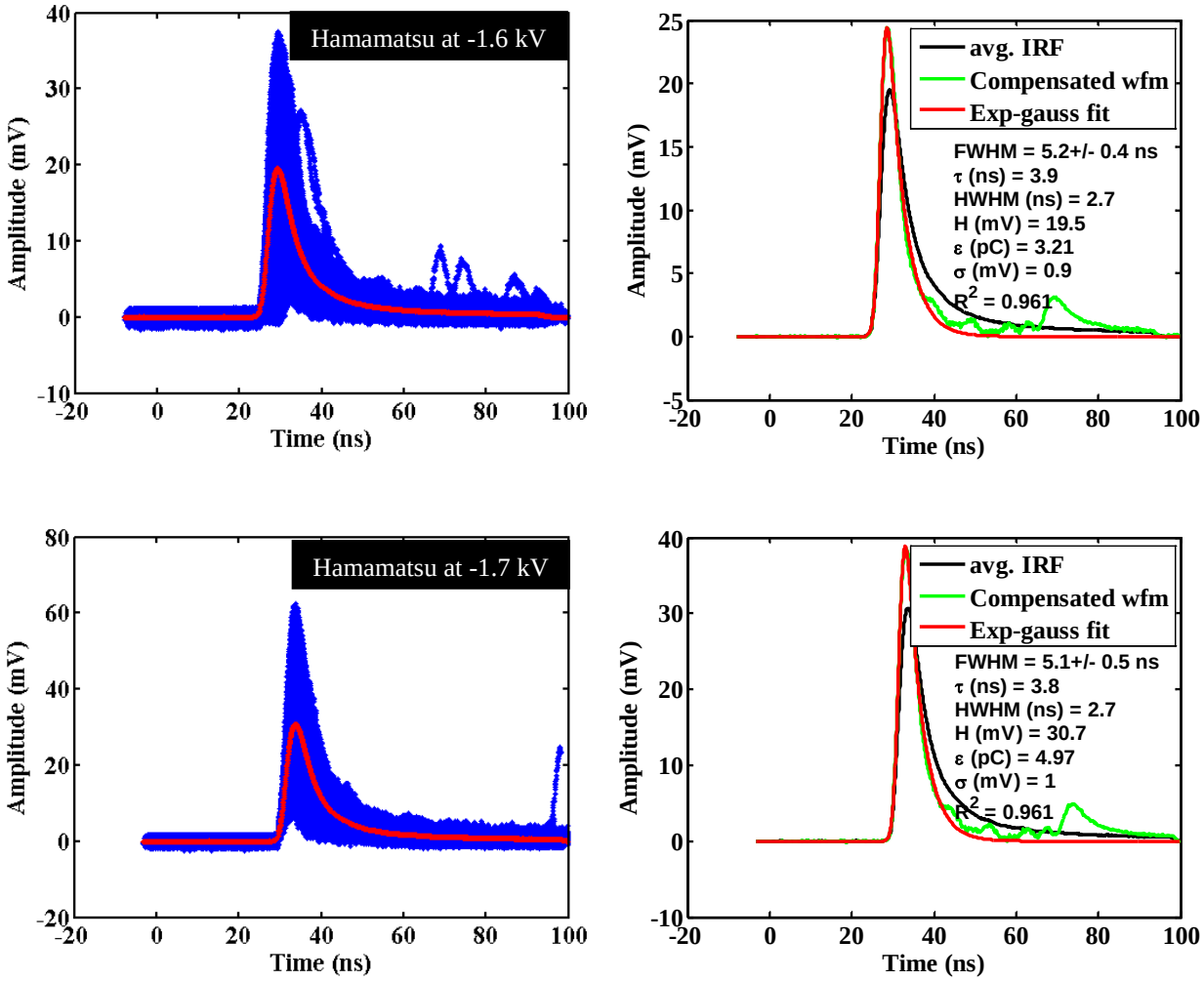

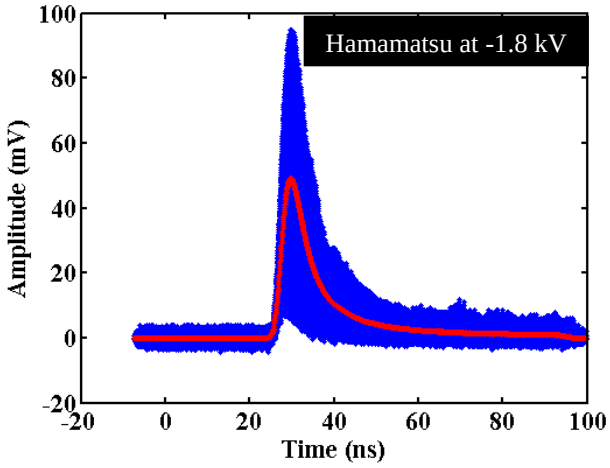

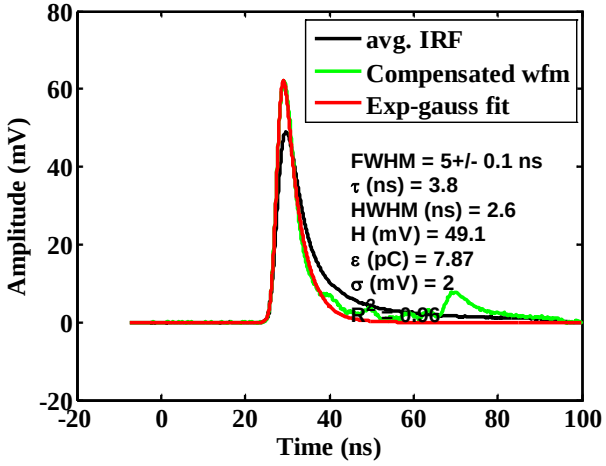

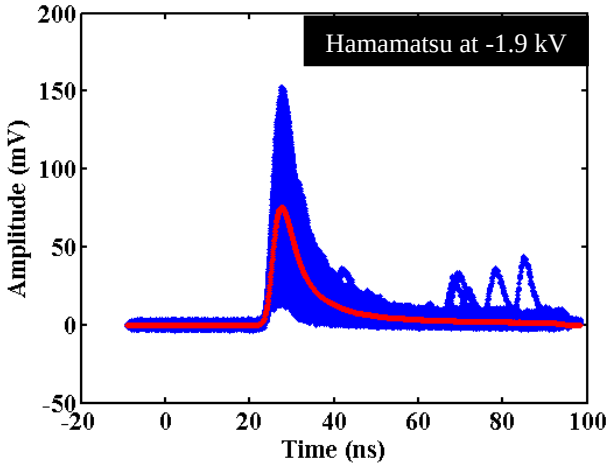

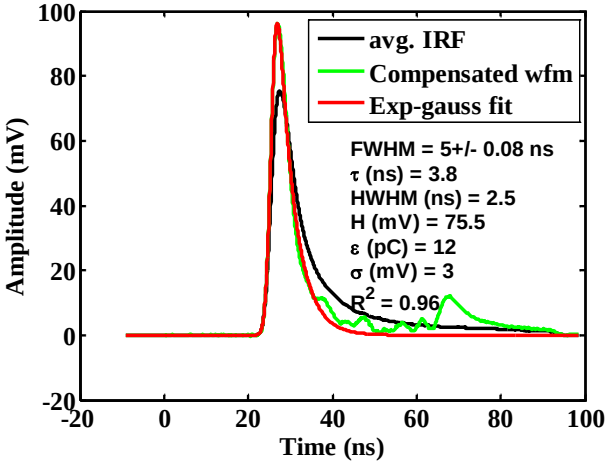

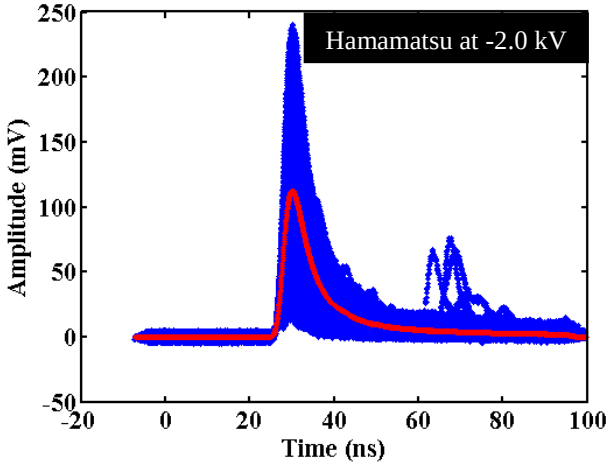

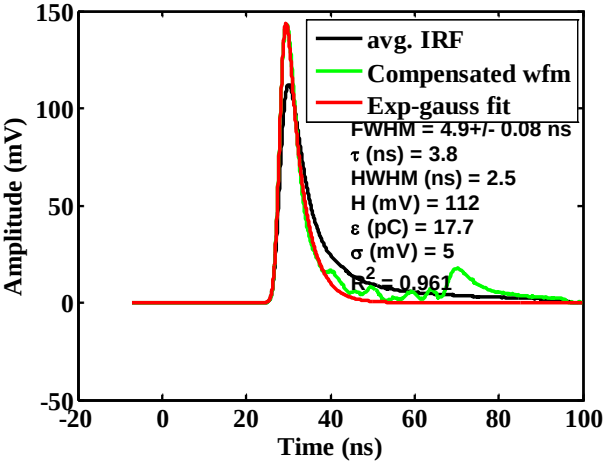

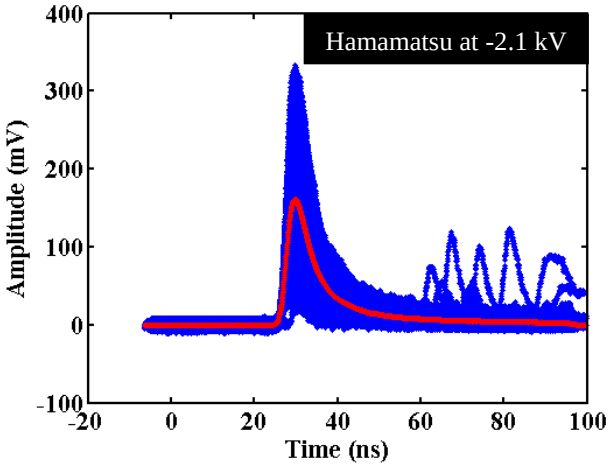

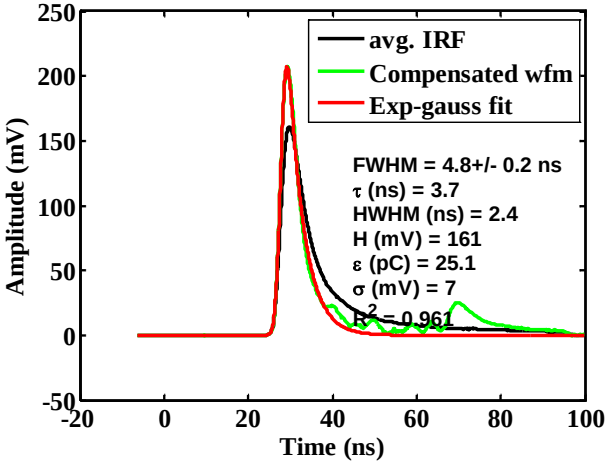

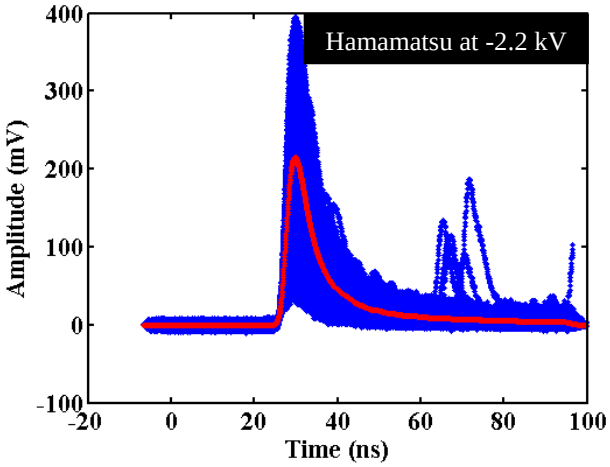

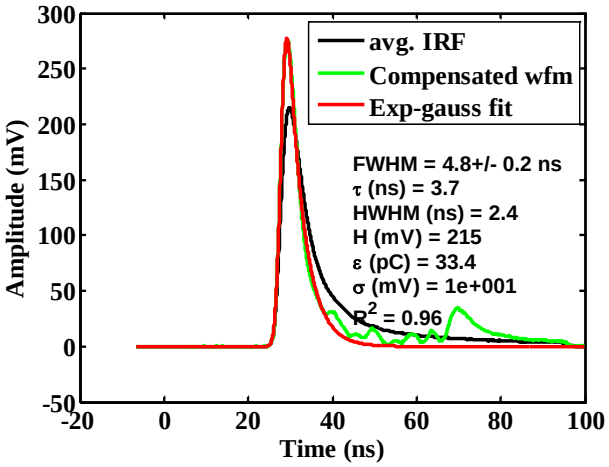

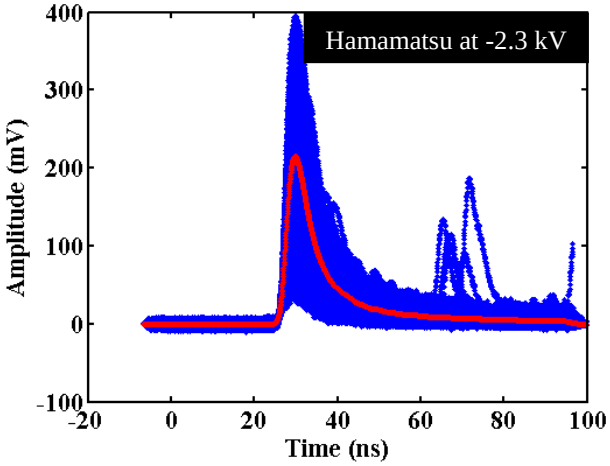

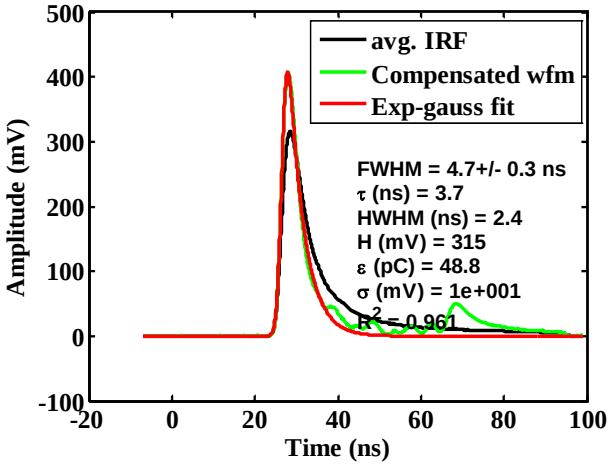

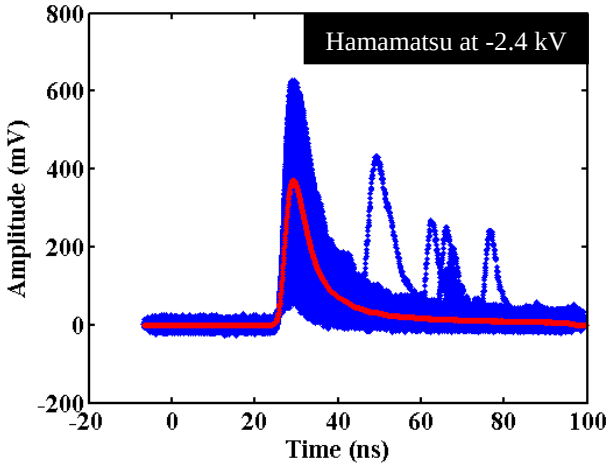

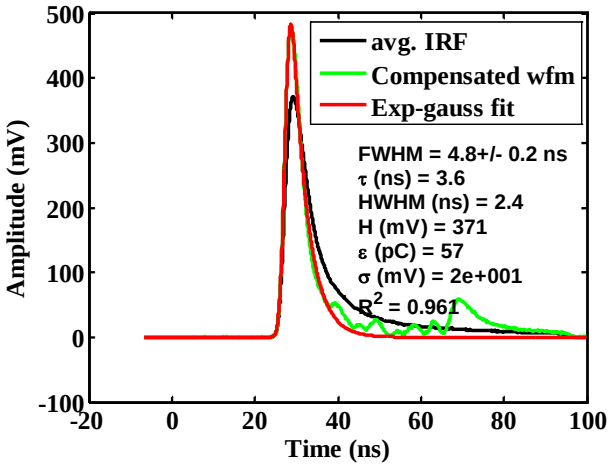

10.2 Data acquired for the Hamamatsu mod-5 with the Hamamatsu in coincidence with the 110-degree SBD

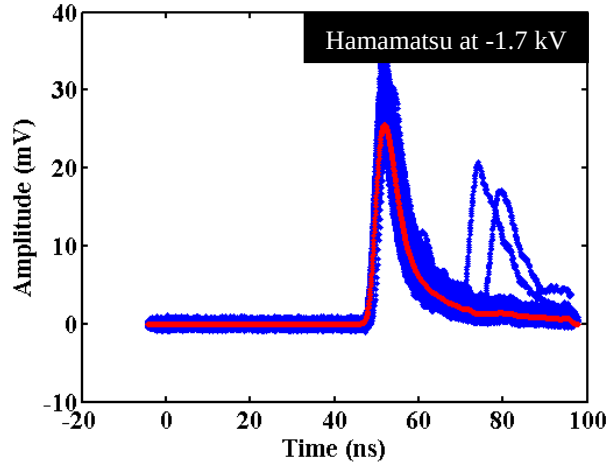

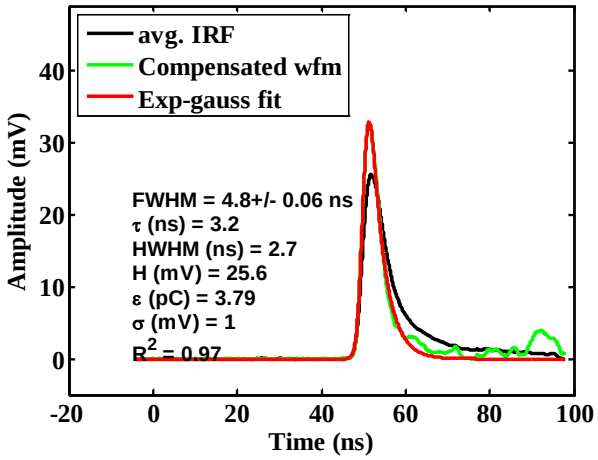

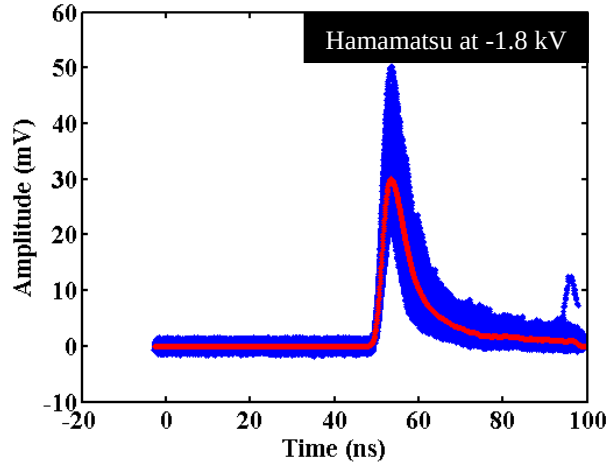

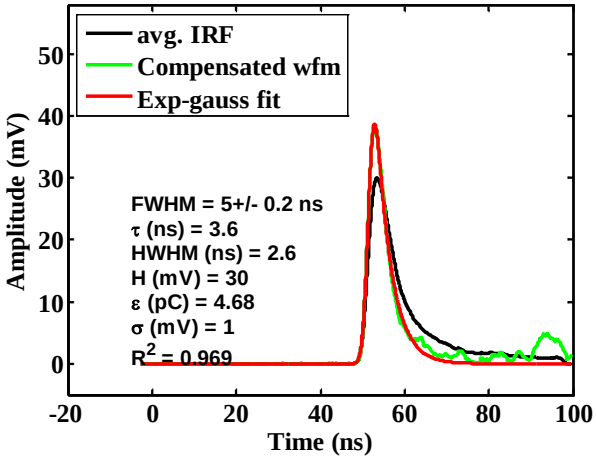

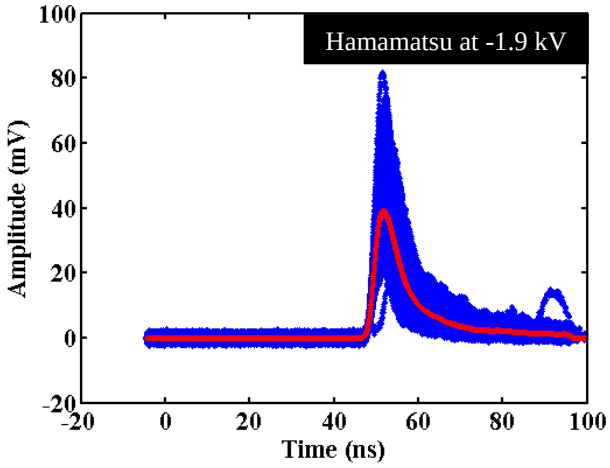

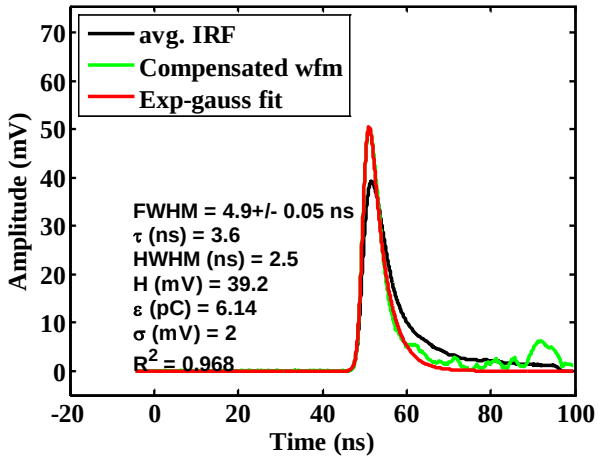

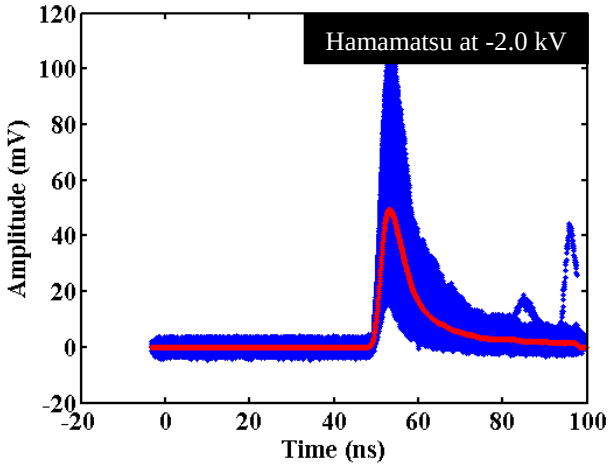

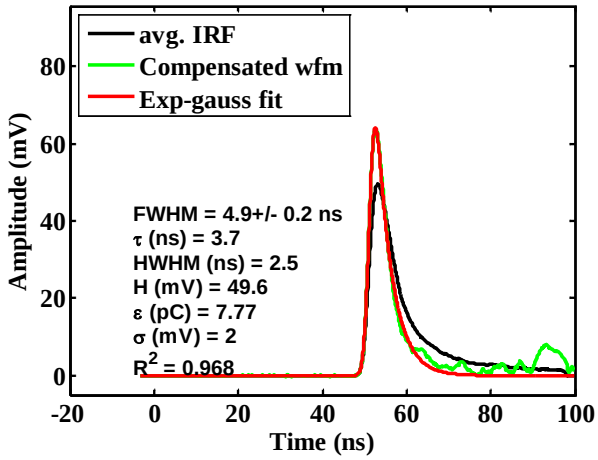

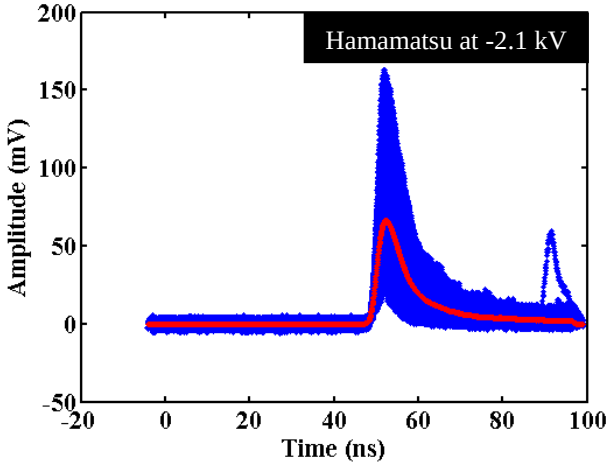

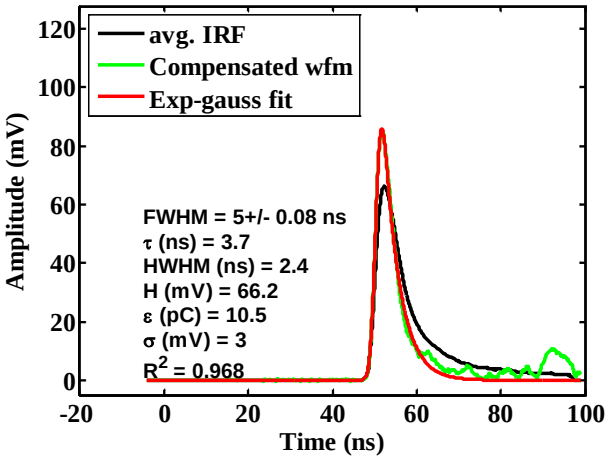

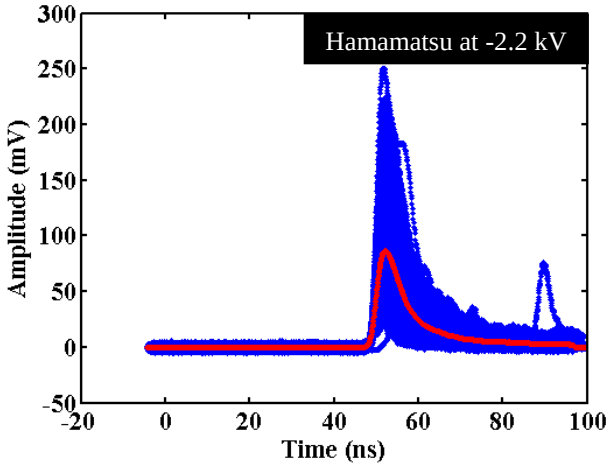

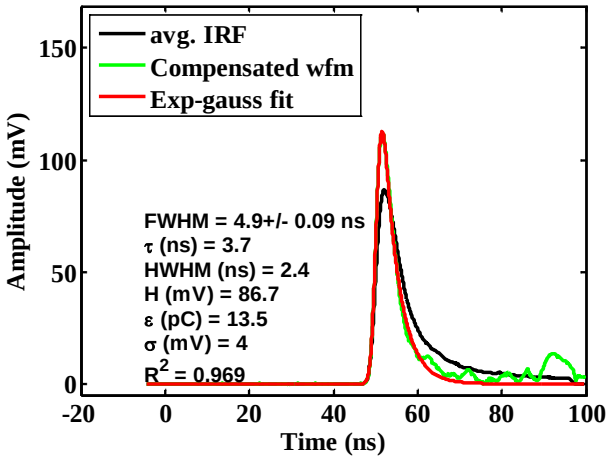

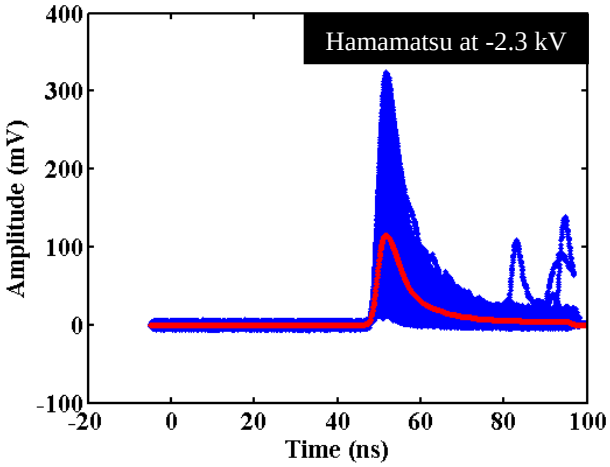

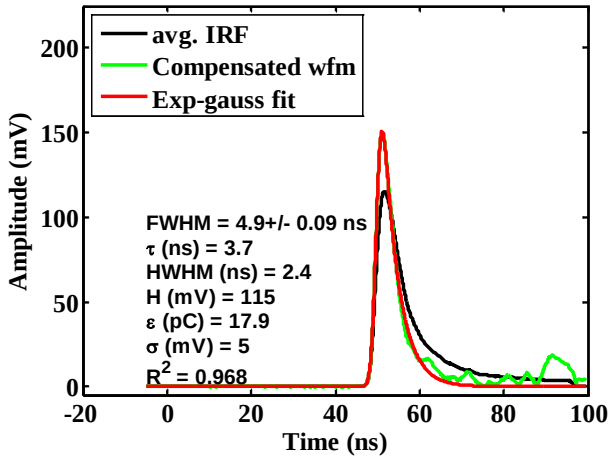

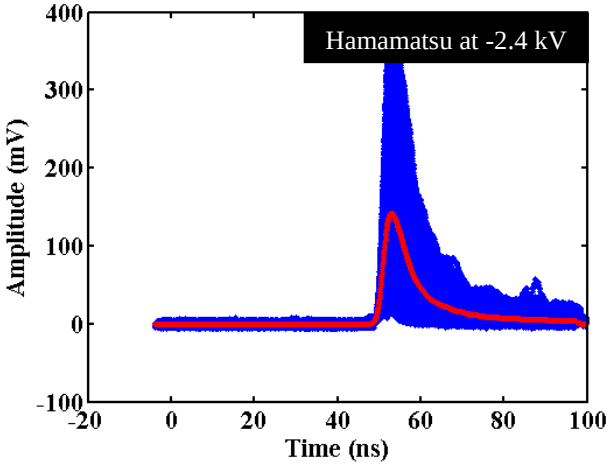

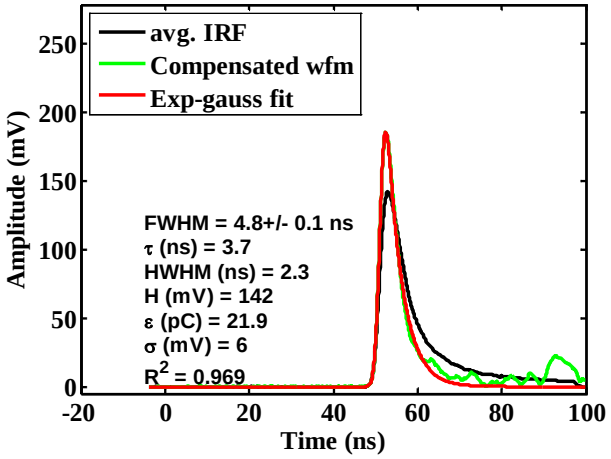

10.3 Data acquired for the Photek PMT240 with the Hamamatsu mod-5 in coincidence with the 110-degree SBD

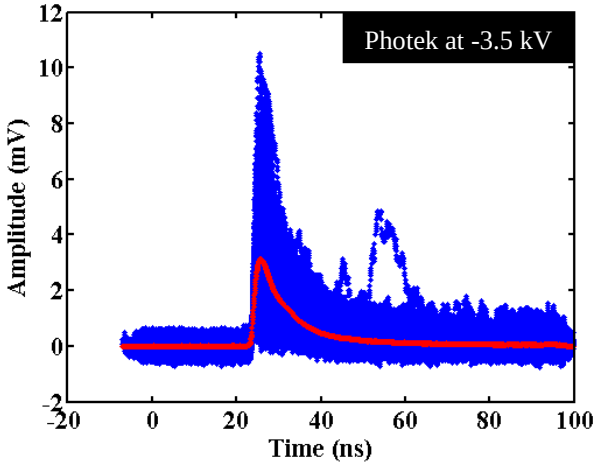

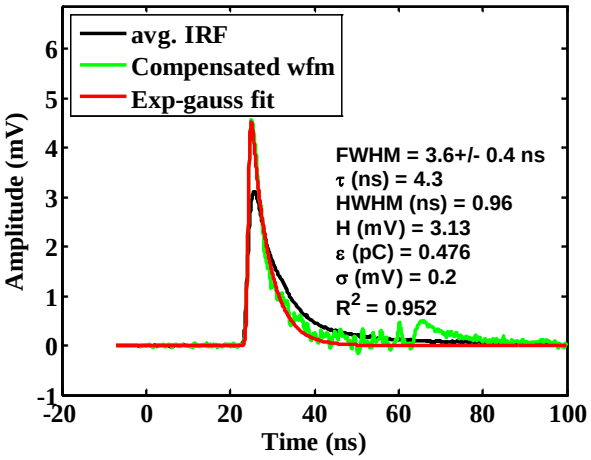

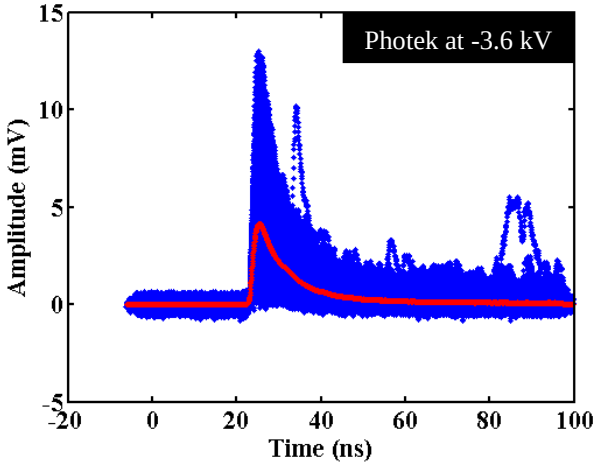

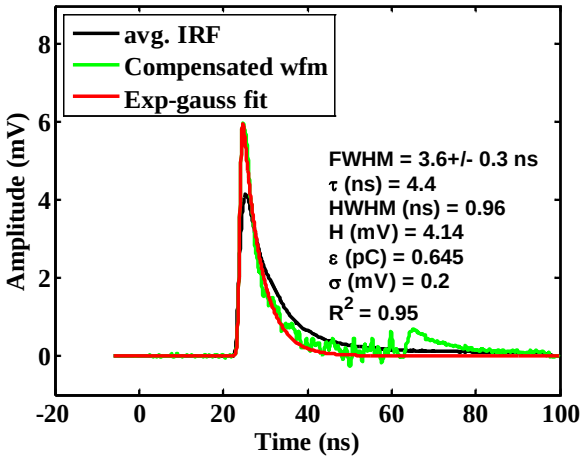

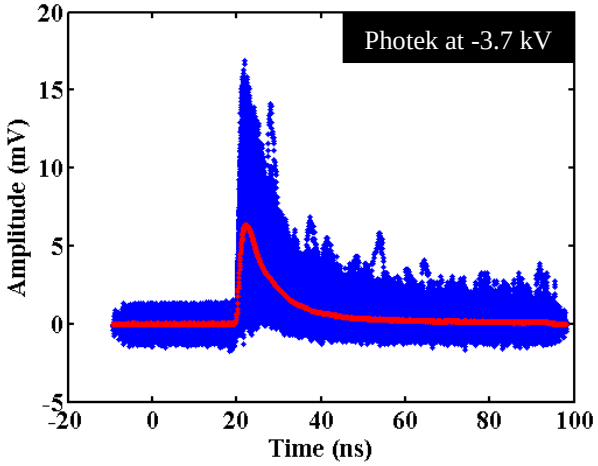

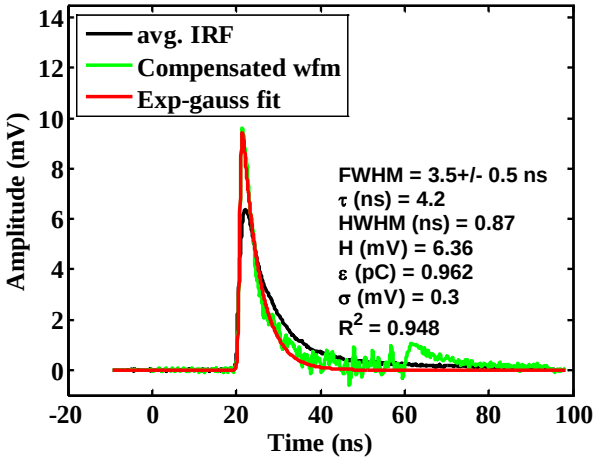

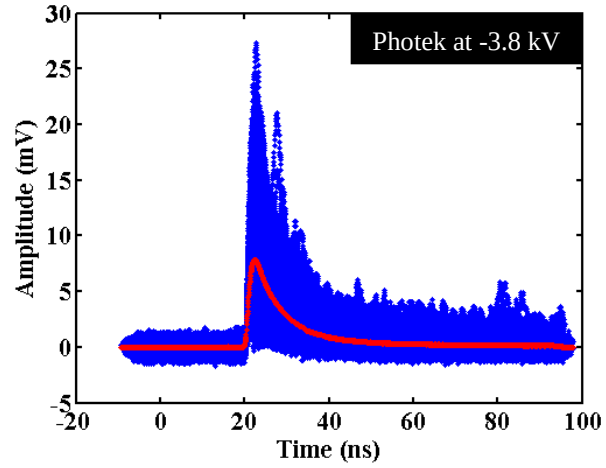

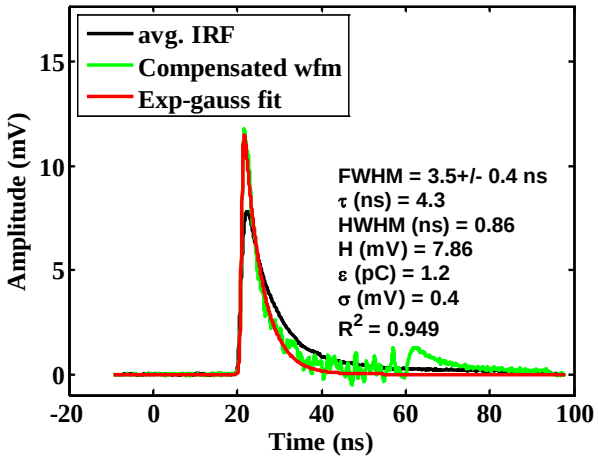

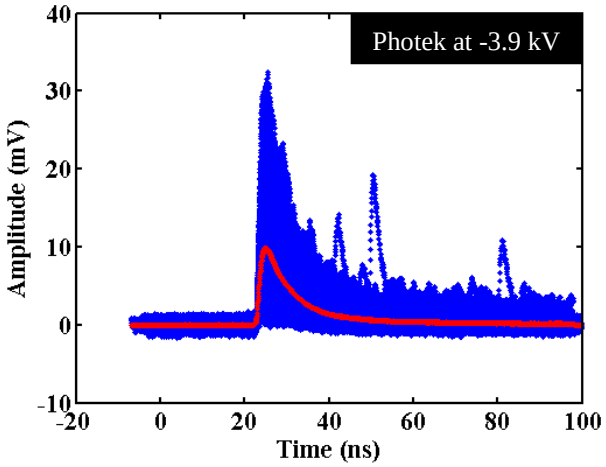

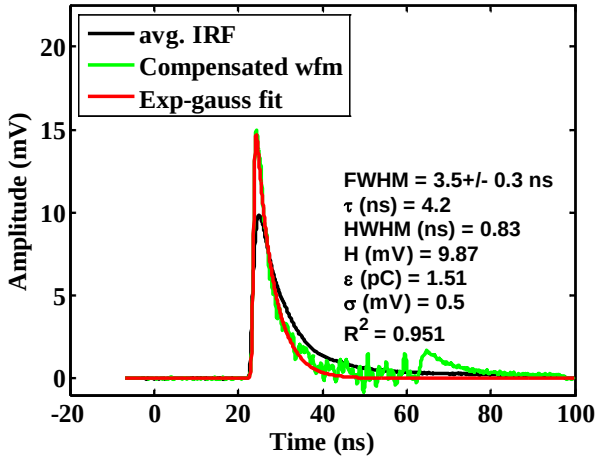

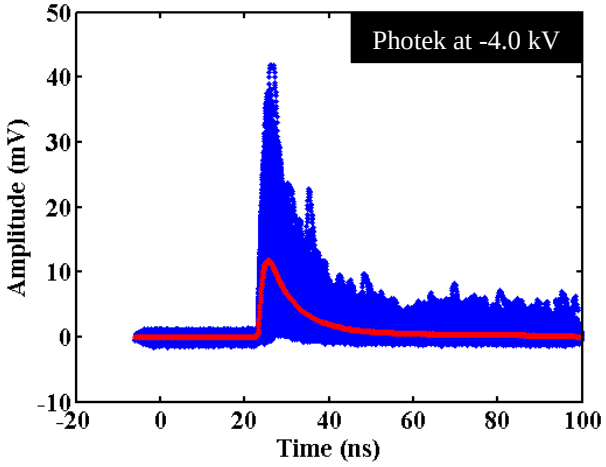

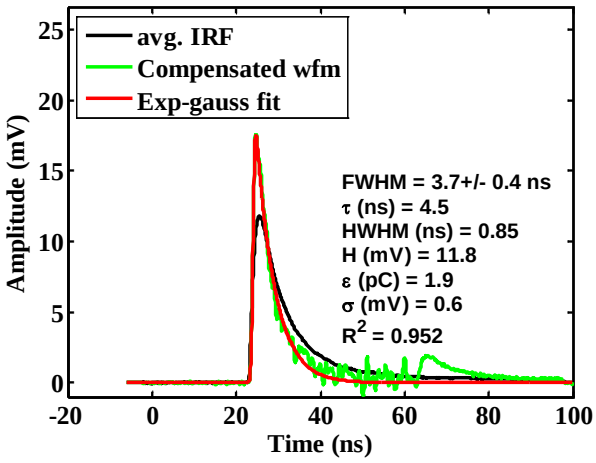

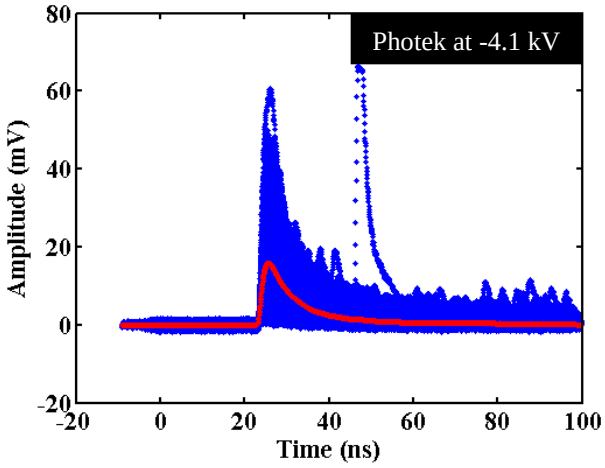

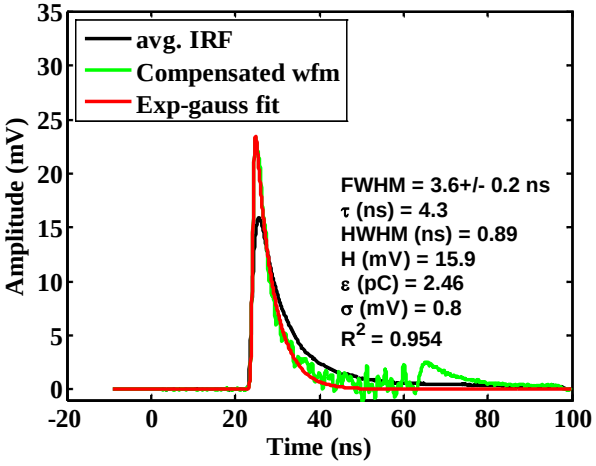

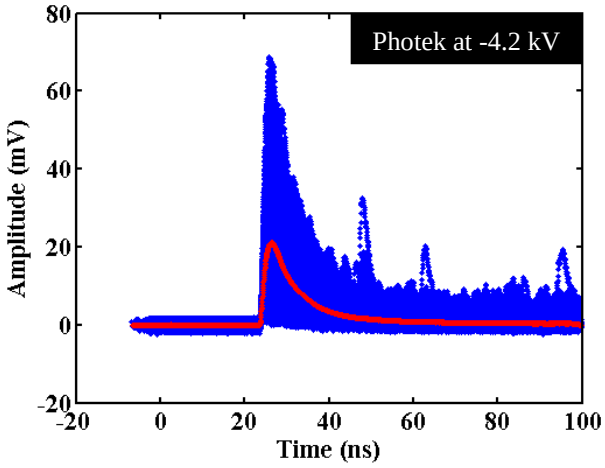

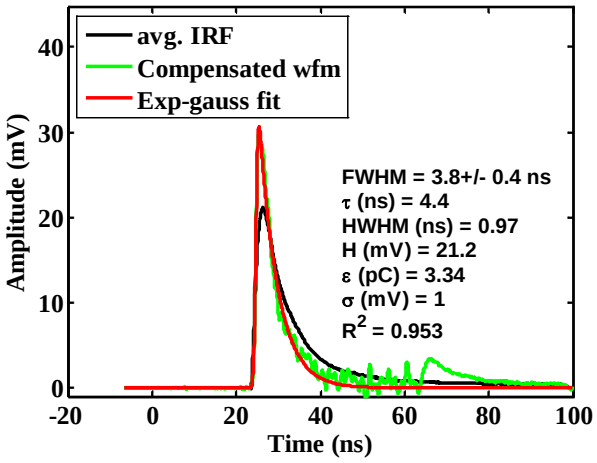

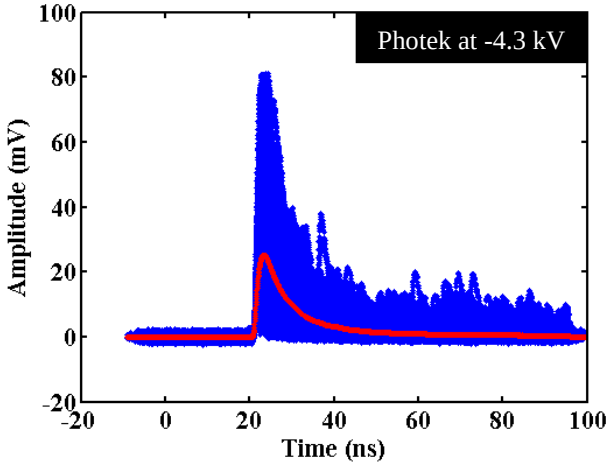

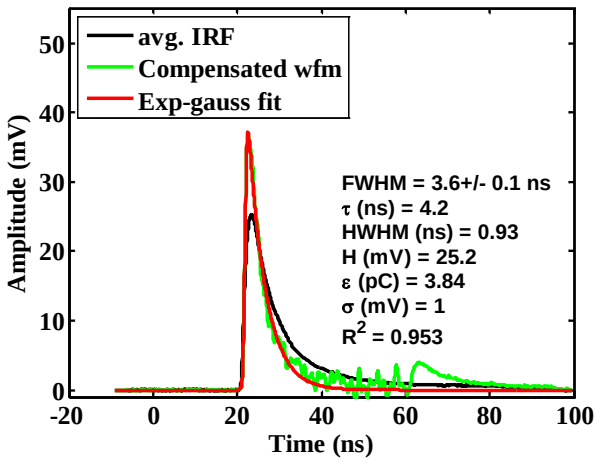

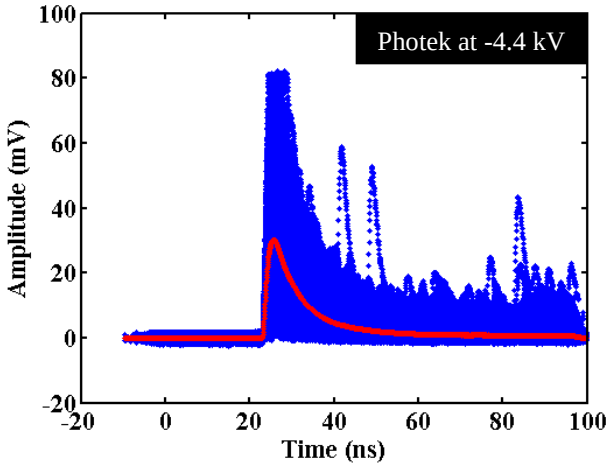

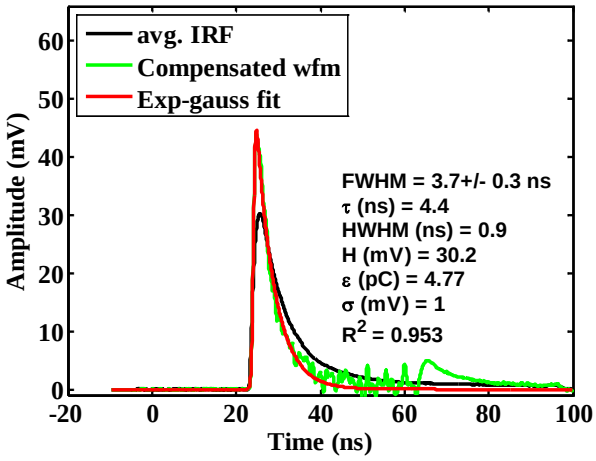

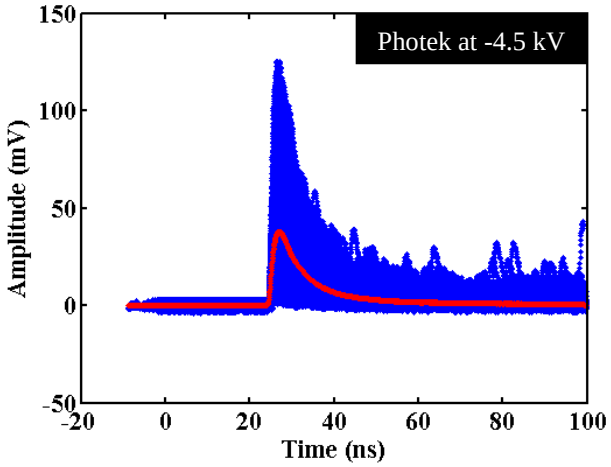

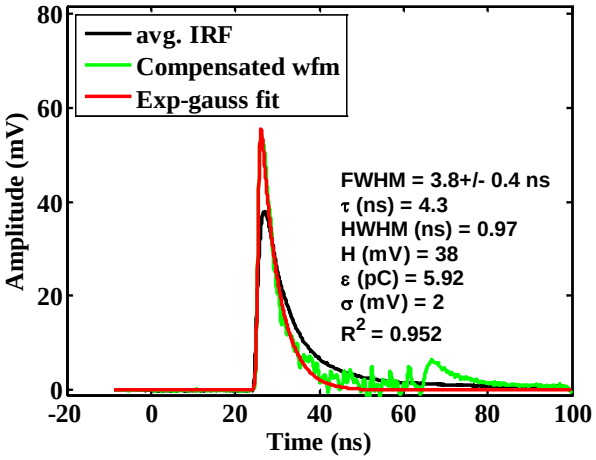

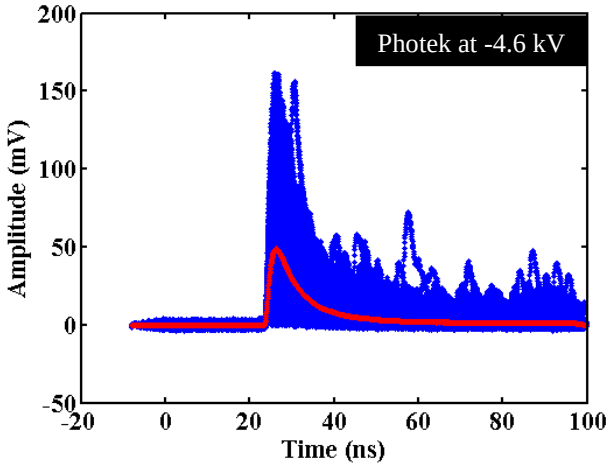

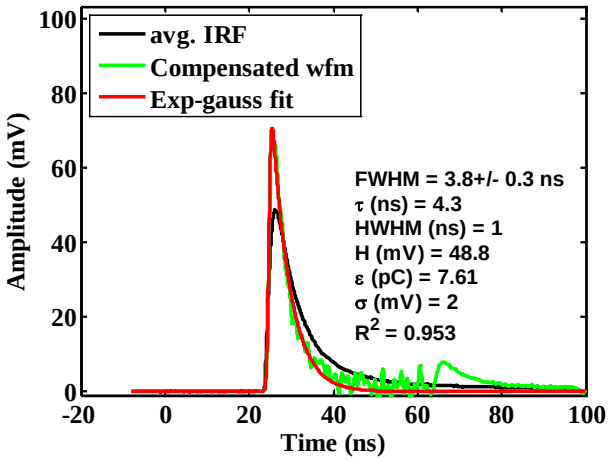

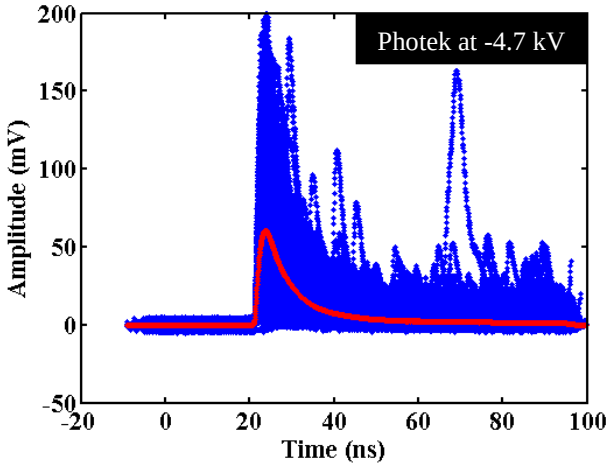

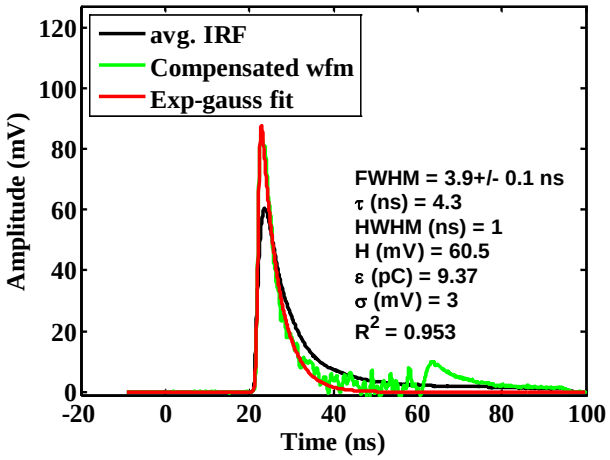

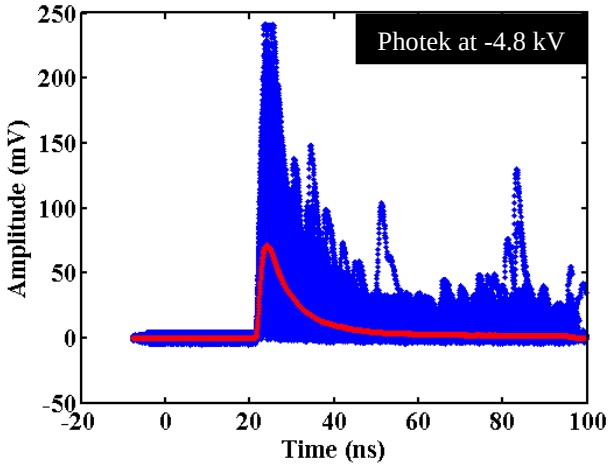

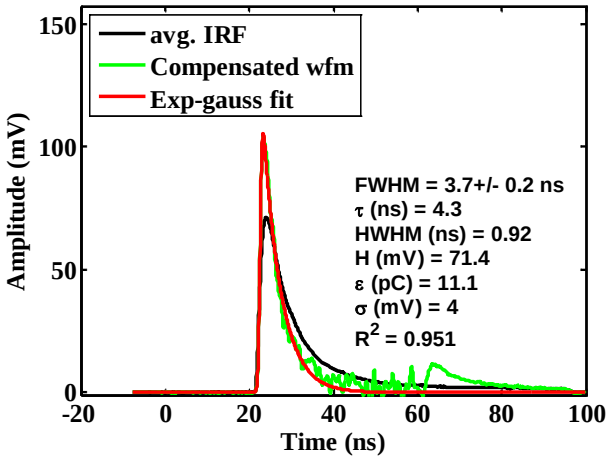

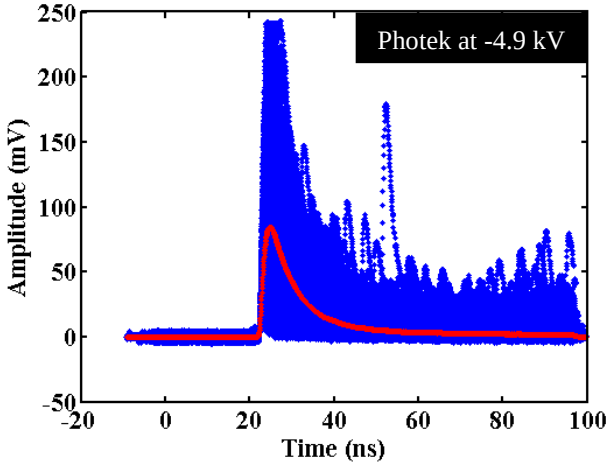

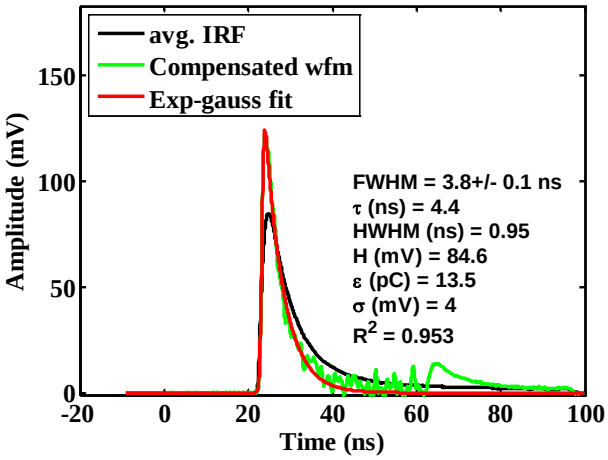

10.4 Data acquired for the Photek PMT240 with the Photek PMT240 in coincidence with the 110-degree SBD

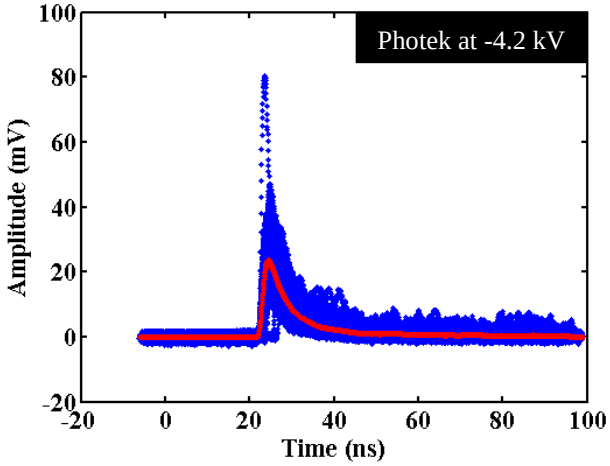

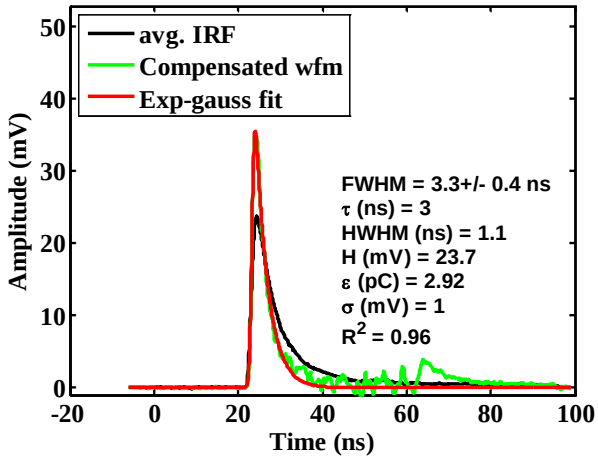

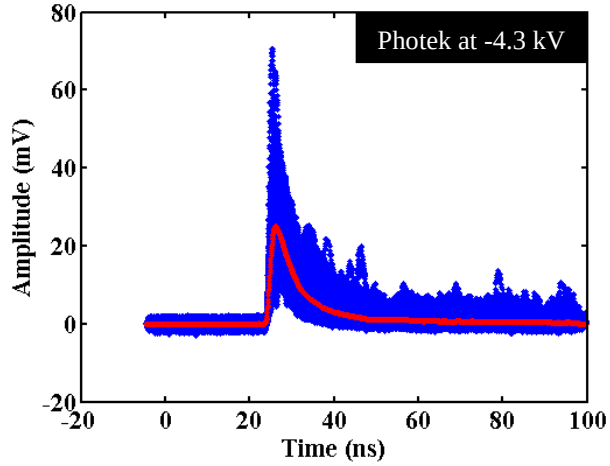

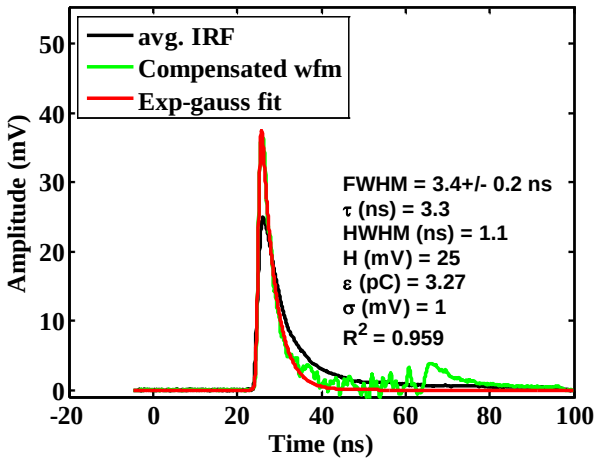

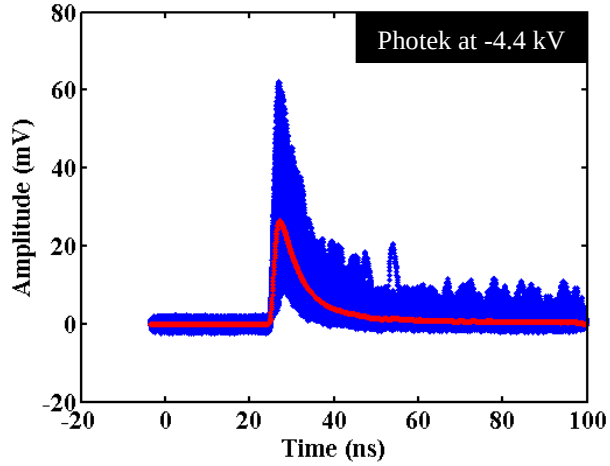

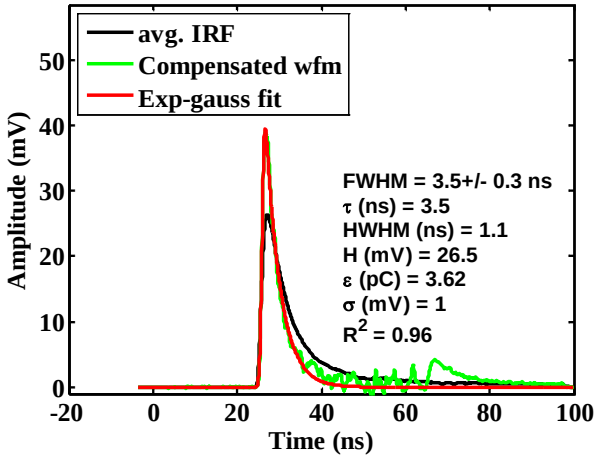

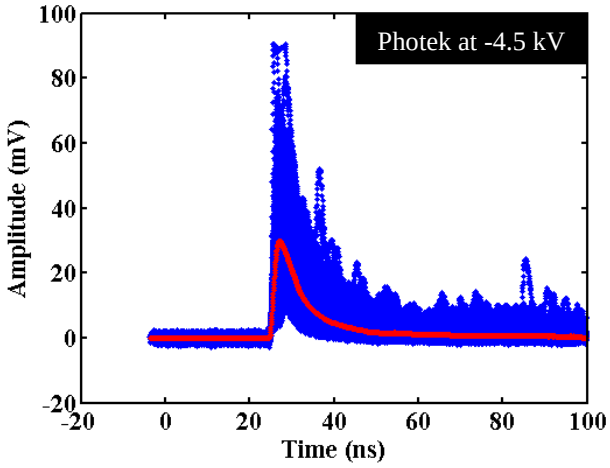

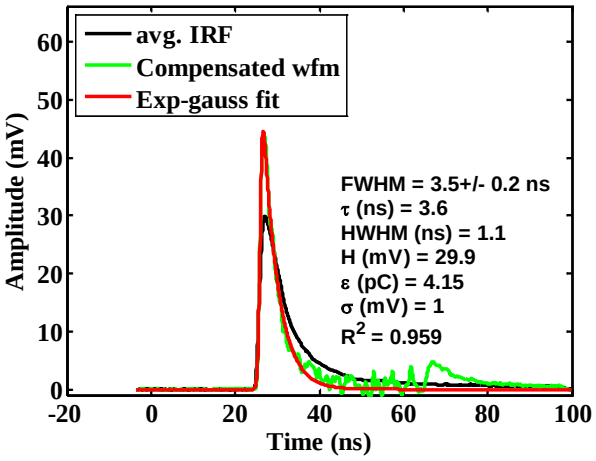

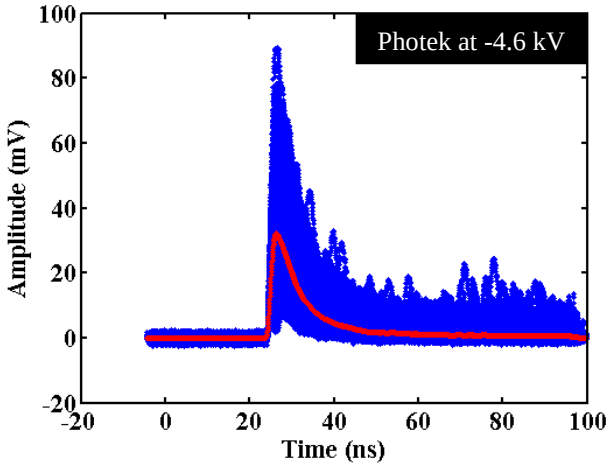

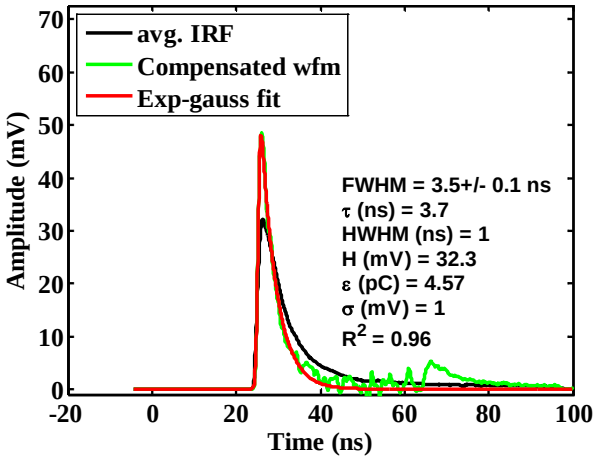

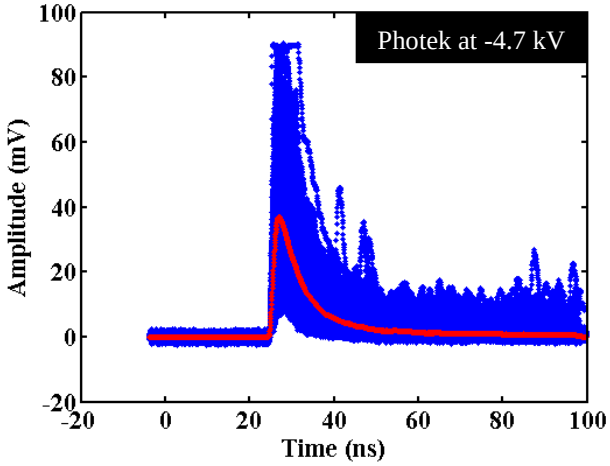

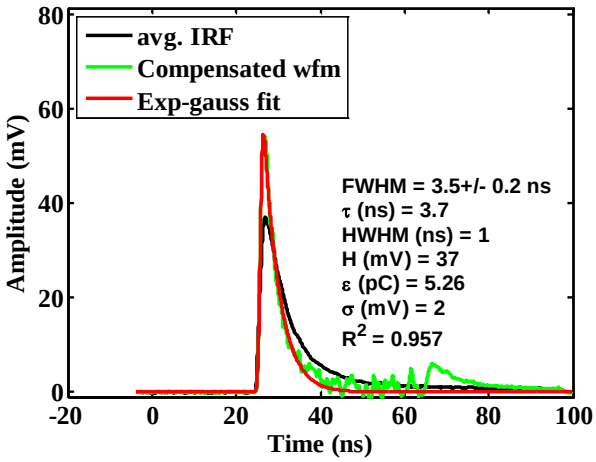

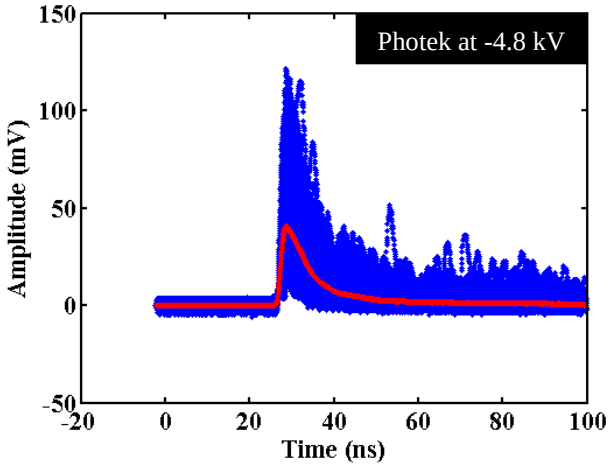

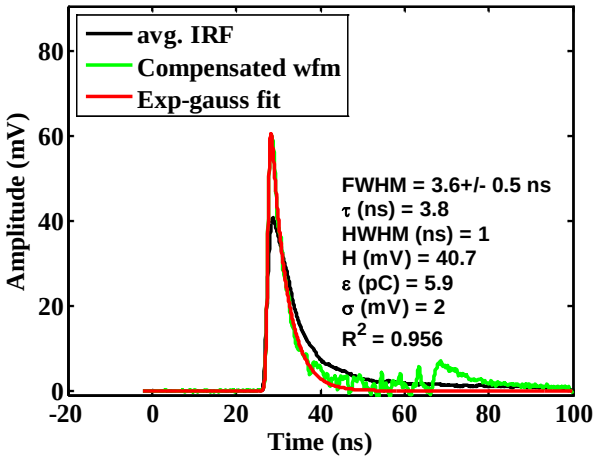

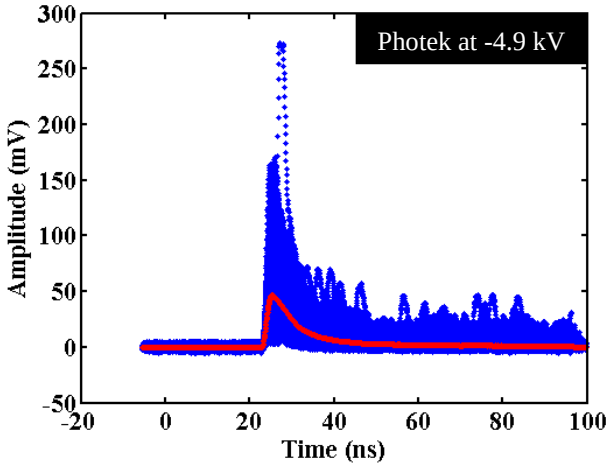

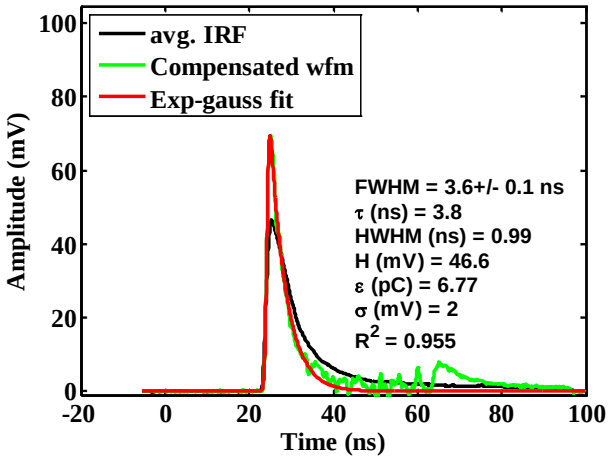

11 Appendix B - Waveforms and fits to the data using a sum of Gaussian functions for a D^+ ion acceleration potential of 50 keV

11.1 Data acquired for the Hamamatsu mod-5 at -1.8 kV with the Photek PMT240 in coincidence with the 110-degree SBD

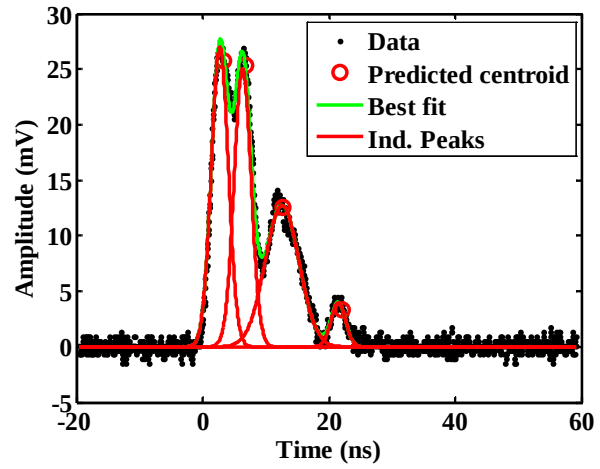

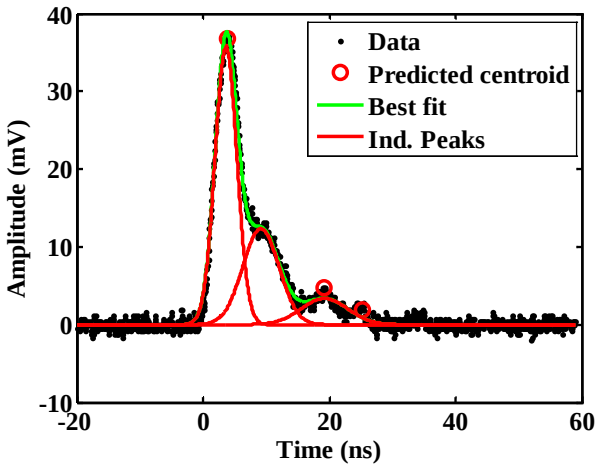

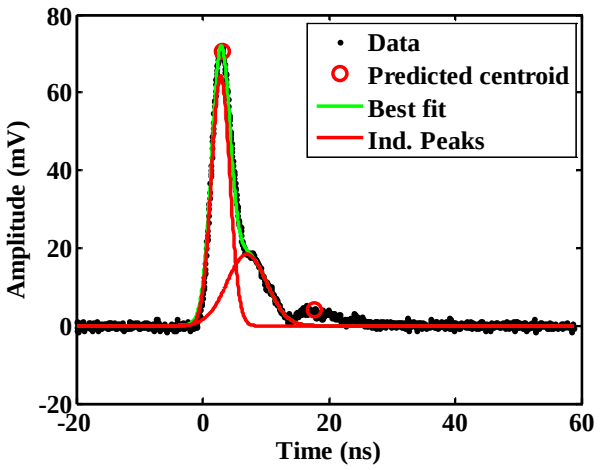

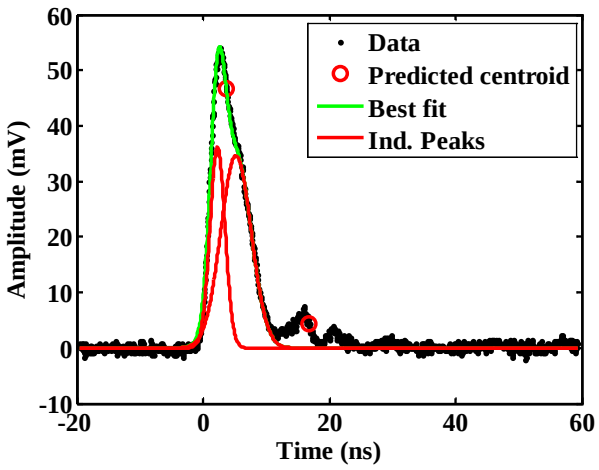

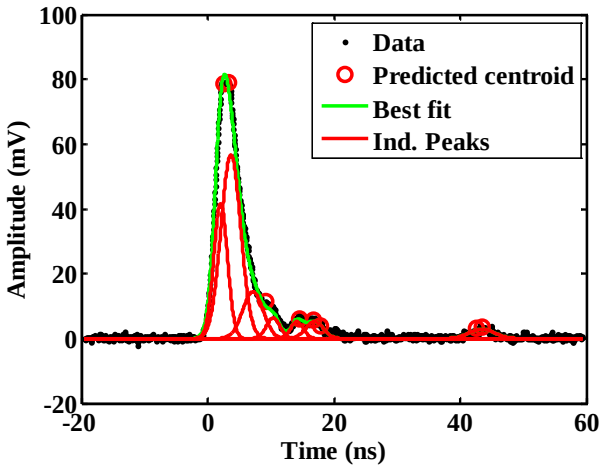

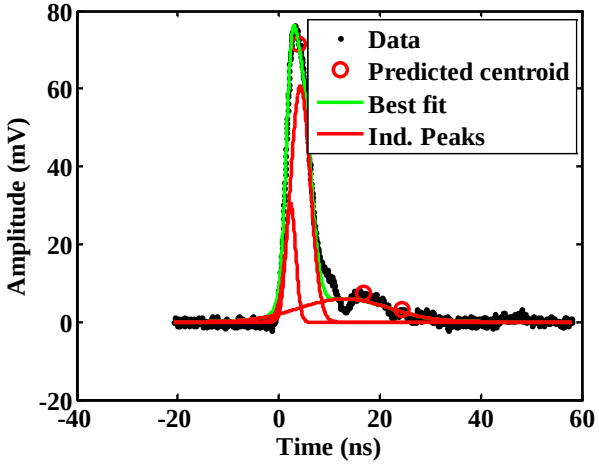

11.2 Data acquired for the Hamamatsu mod-5 at -1.9 kV with the Photek PMT240 in coincidence with the 110- degree SBD

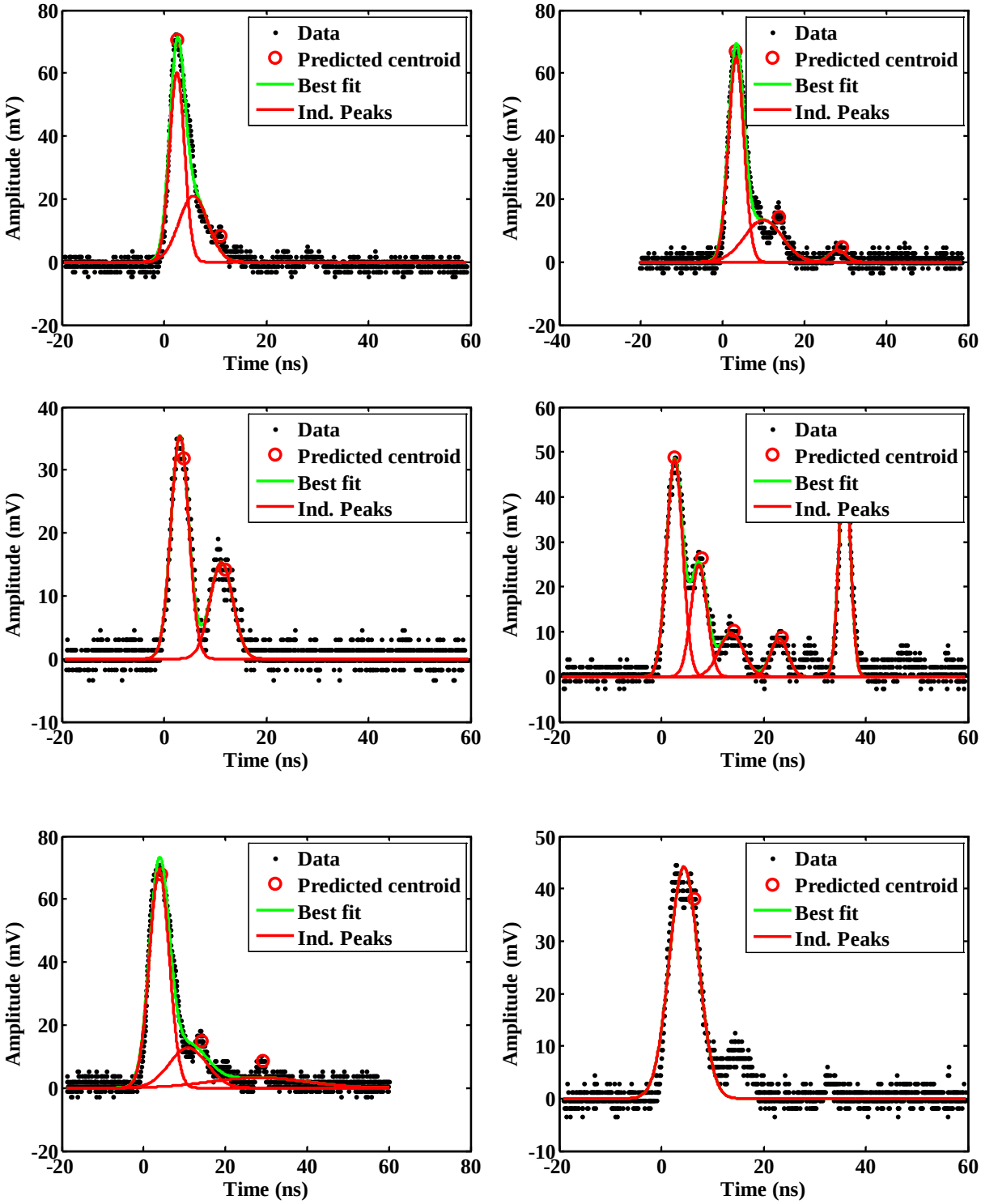

11.3 Data acquired for the Hamamatsu mod-5 at -2.0 kV with the Photek PMT240 in coincidence with the 110-degree SBD

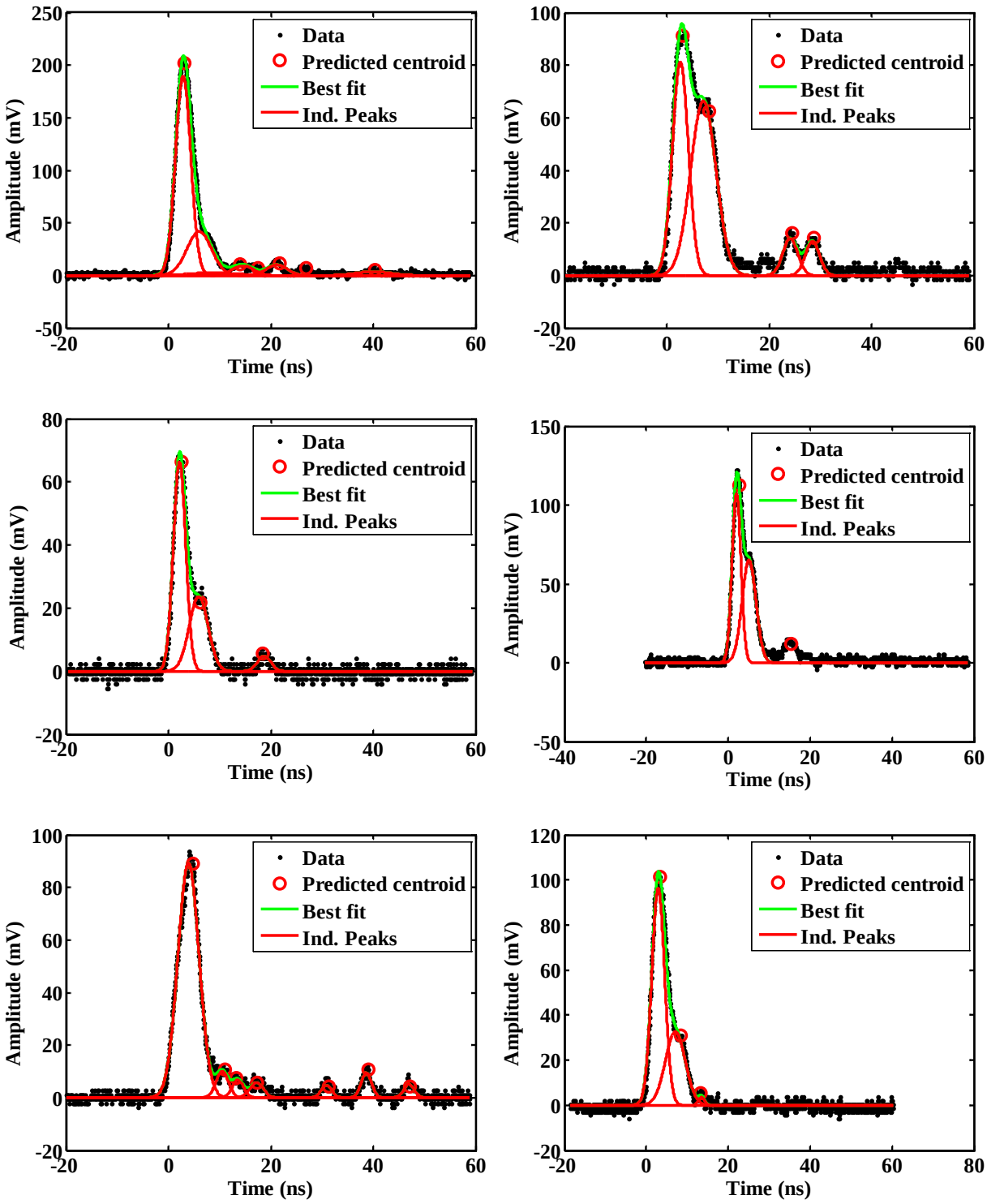

11.4 Data acquired for the Hamamatsu mod-5 at -2.1 kV with the Photek PMT240 in coincidence with the 110-degree SBD

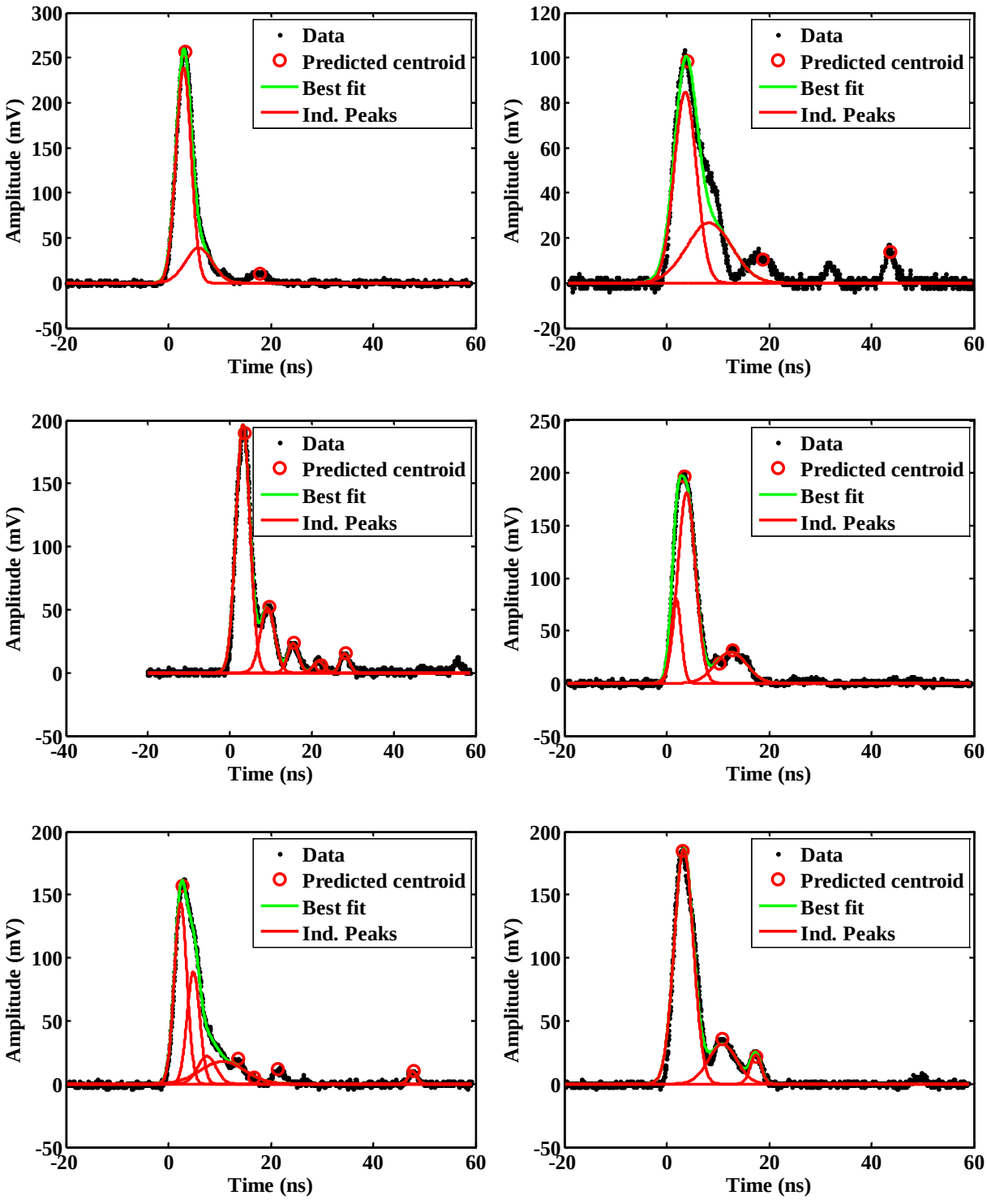

11.5 Data acquired for the Hamamatsu mod-5 at -2.2 kV with the Photek PMT240 in coincidence with the 110-degree SBD

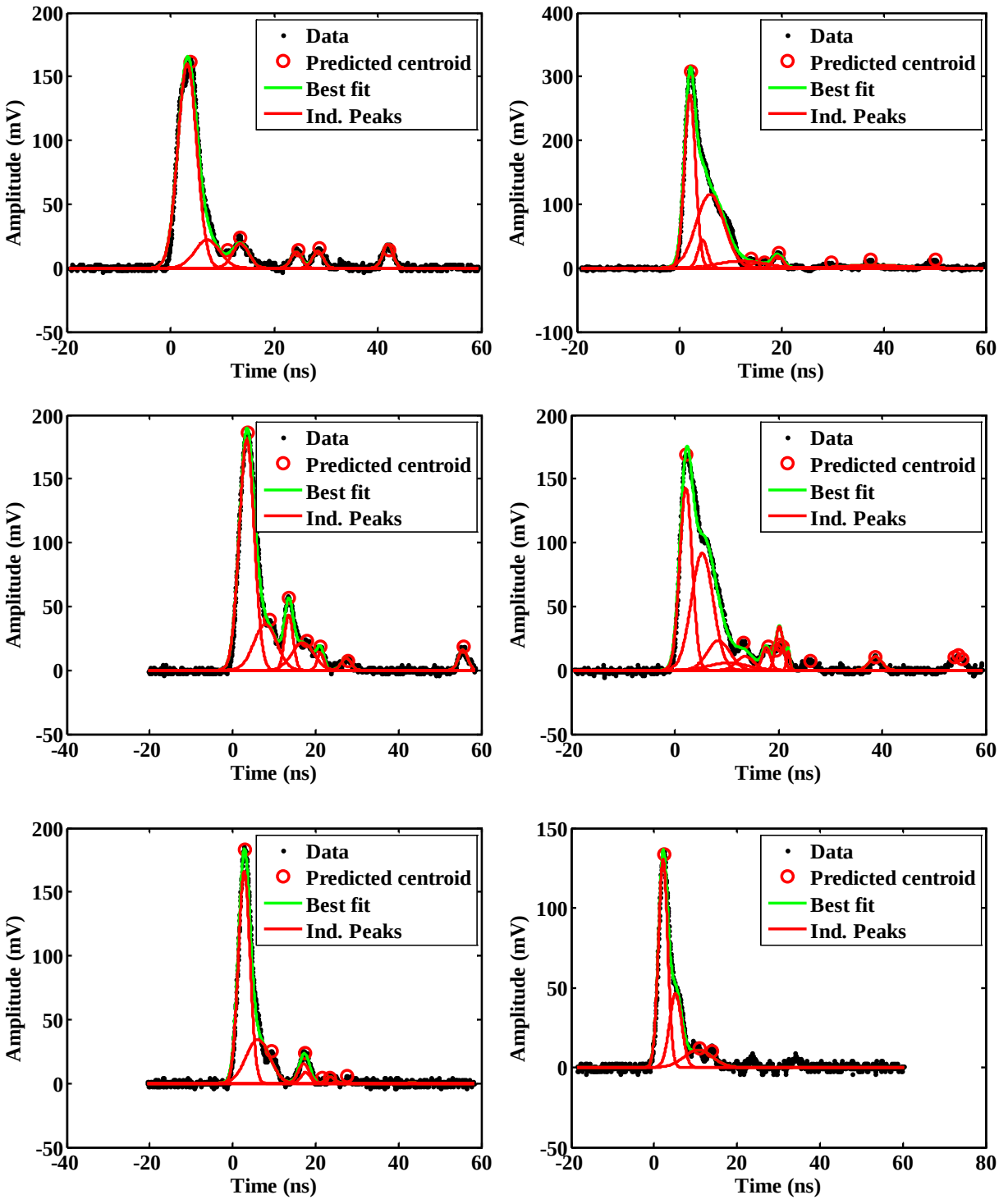

11.6 Data acquired for the Hamamatsu mod-5 at -2.3 kV with the Photek PMT240 in coincidence with the 110-degree SBD

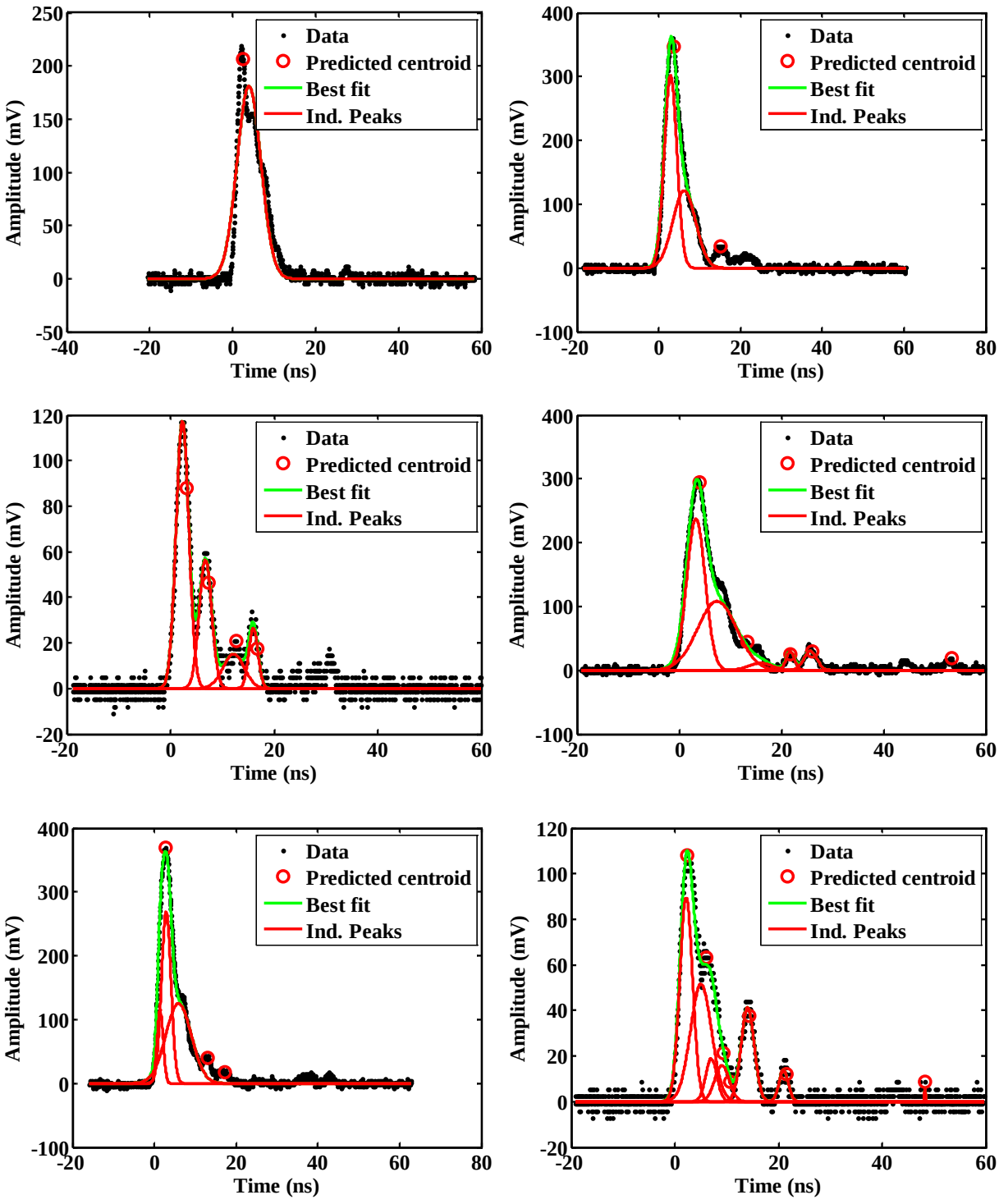

11.7 Data acquired for the Hamamatsu mod-5 at -2.4 kV with the Photek PMT240 in coincidence with the 110-degree SBD

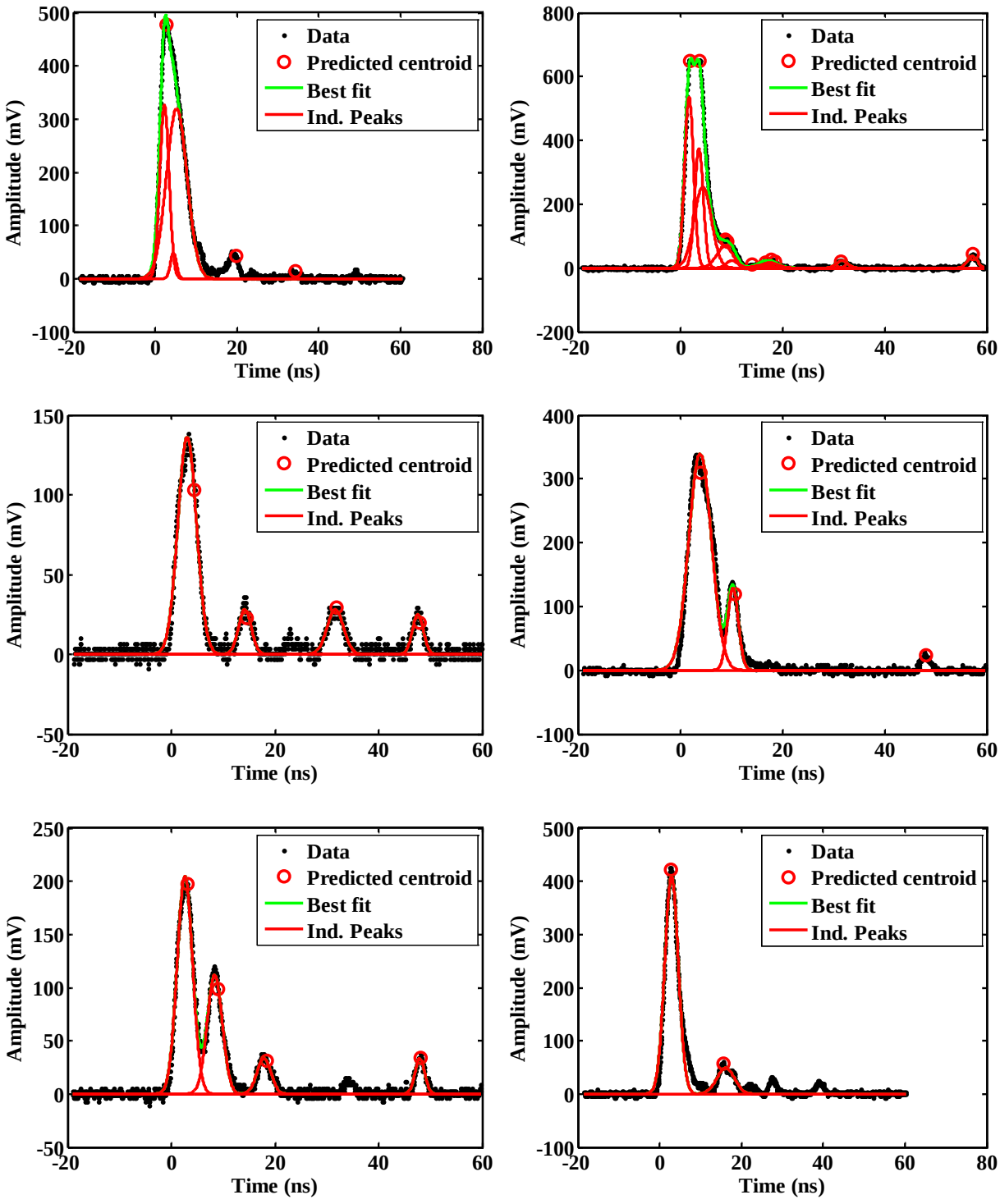

11.8 Data acquired for the Hamamatsu mod-5 at -2.0 kV with the Hamamatsu mod-5 in coincidence with the 110-degree SBD

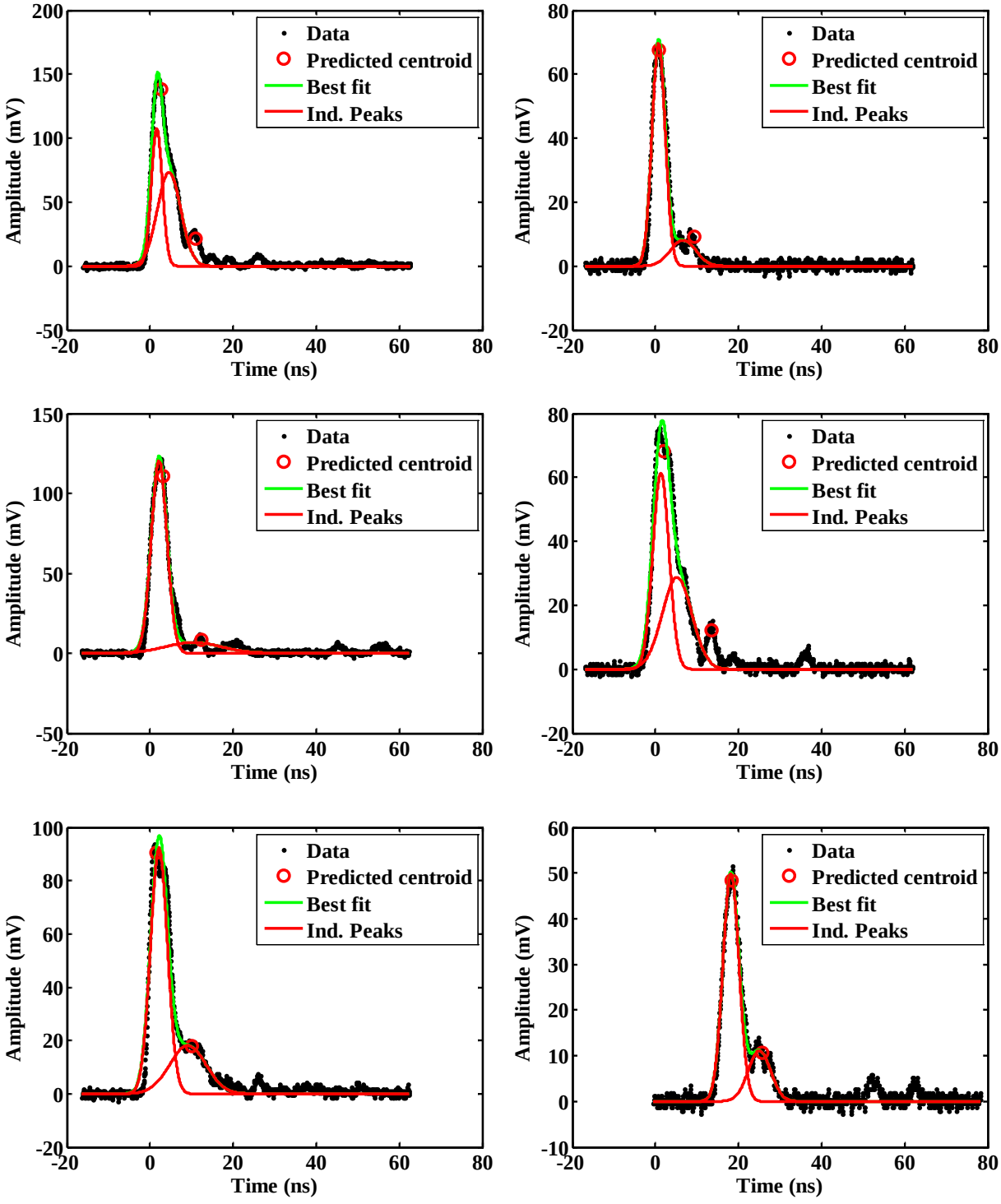

11.9 Data acquired for the Photek PMT240 at -3.9 kV with the Hamamatsu mod-5 in coincidence with the 110-degree SBD

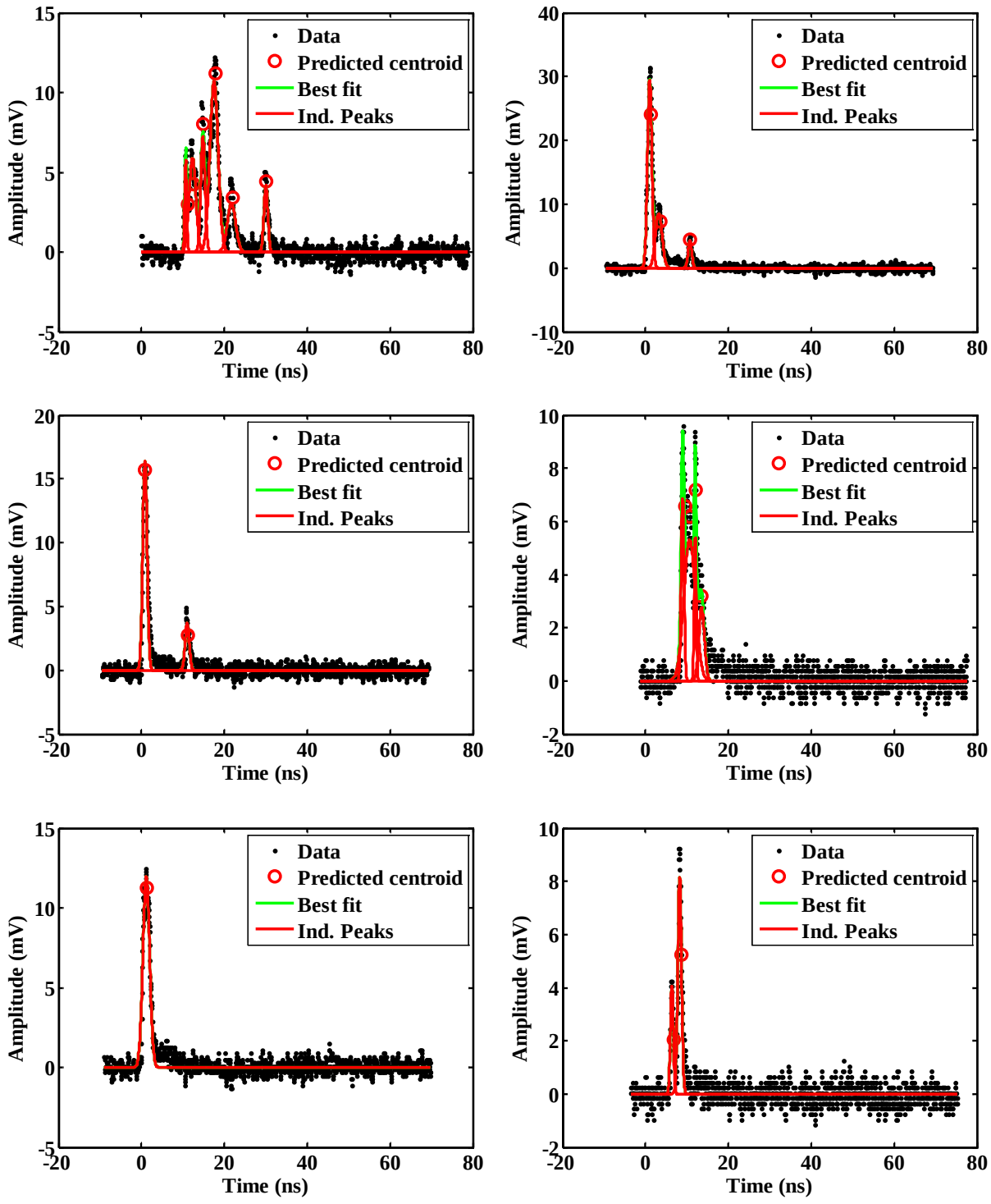

11.10 Data acquired for the Photek PMT240 at -4.0 kV with the Hamamatsu mod-5 in coincidence with the 110-degree SBD

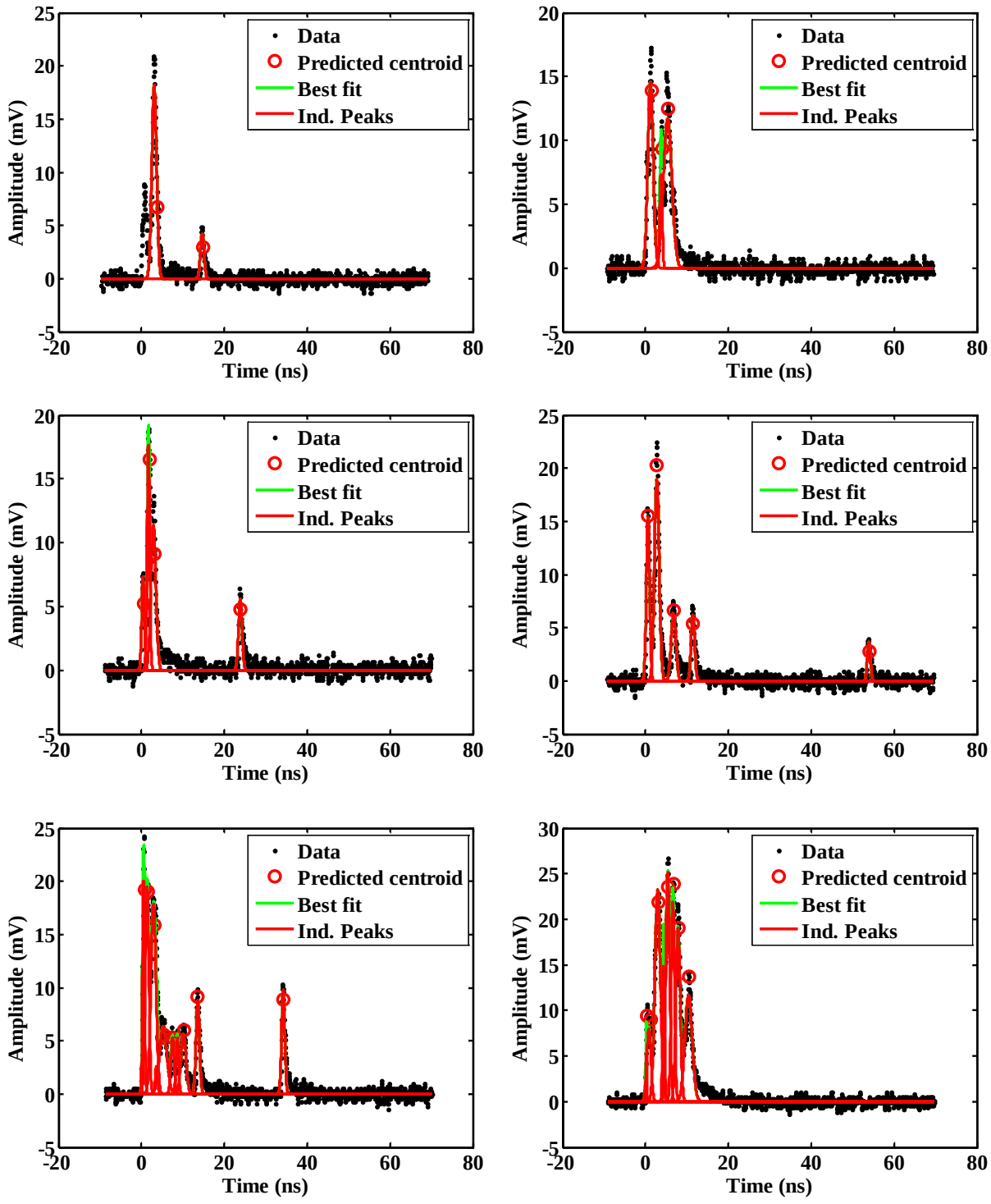

11.11 Data acquired for the Photek PMT240 at -4.1 kV with the Hamamatsu mod-5 in coincidence with the 110-degree SBD

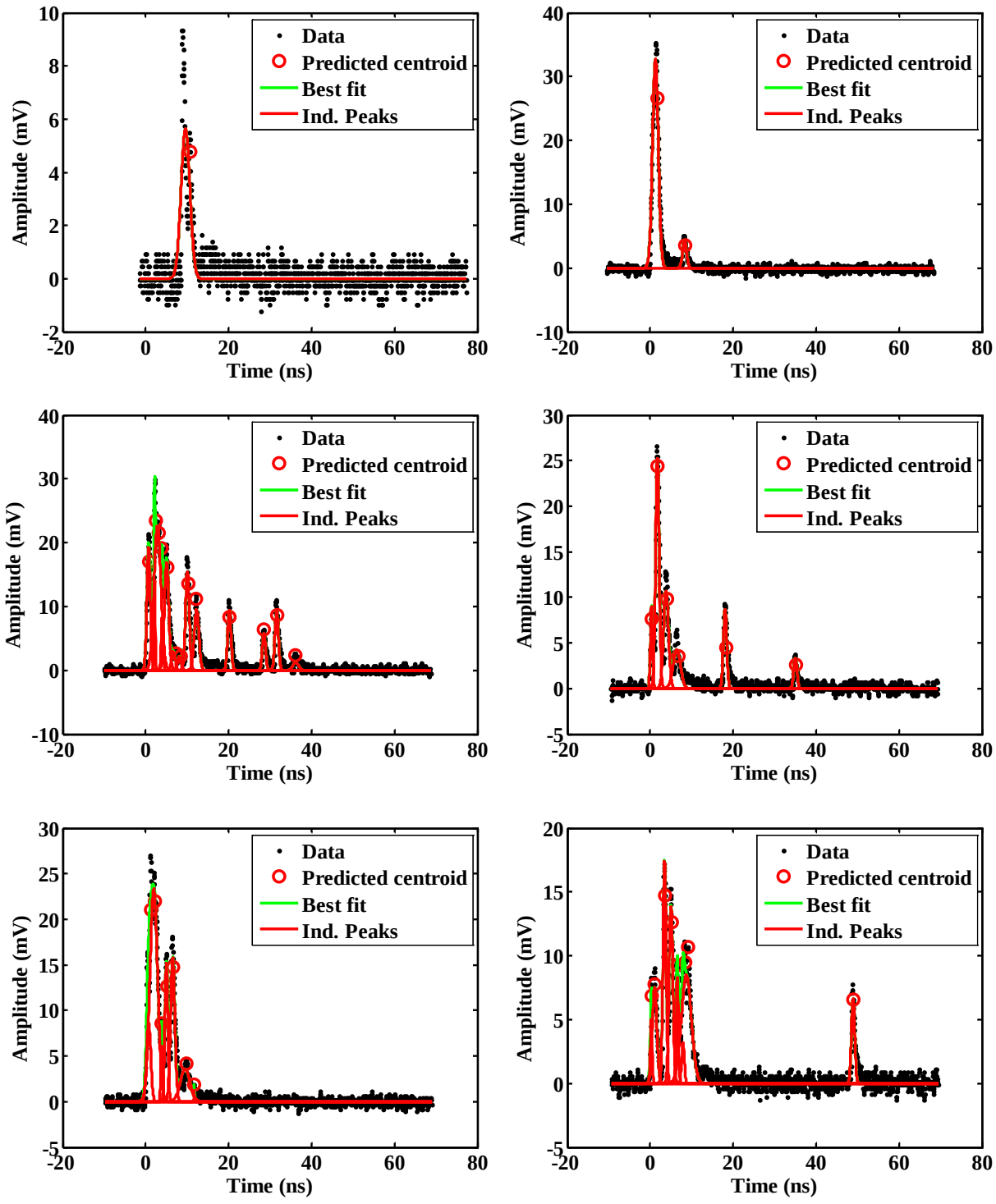

11.12 Data acquired for the Photek PMT240 at -4.2 kV with the Hamamatsu mod-5 in coincidence with the 110-degree SBD

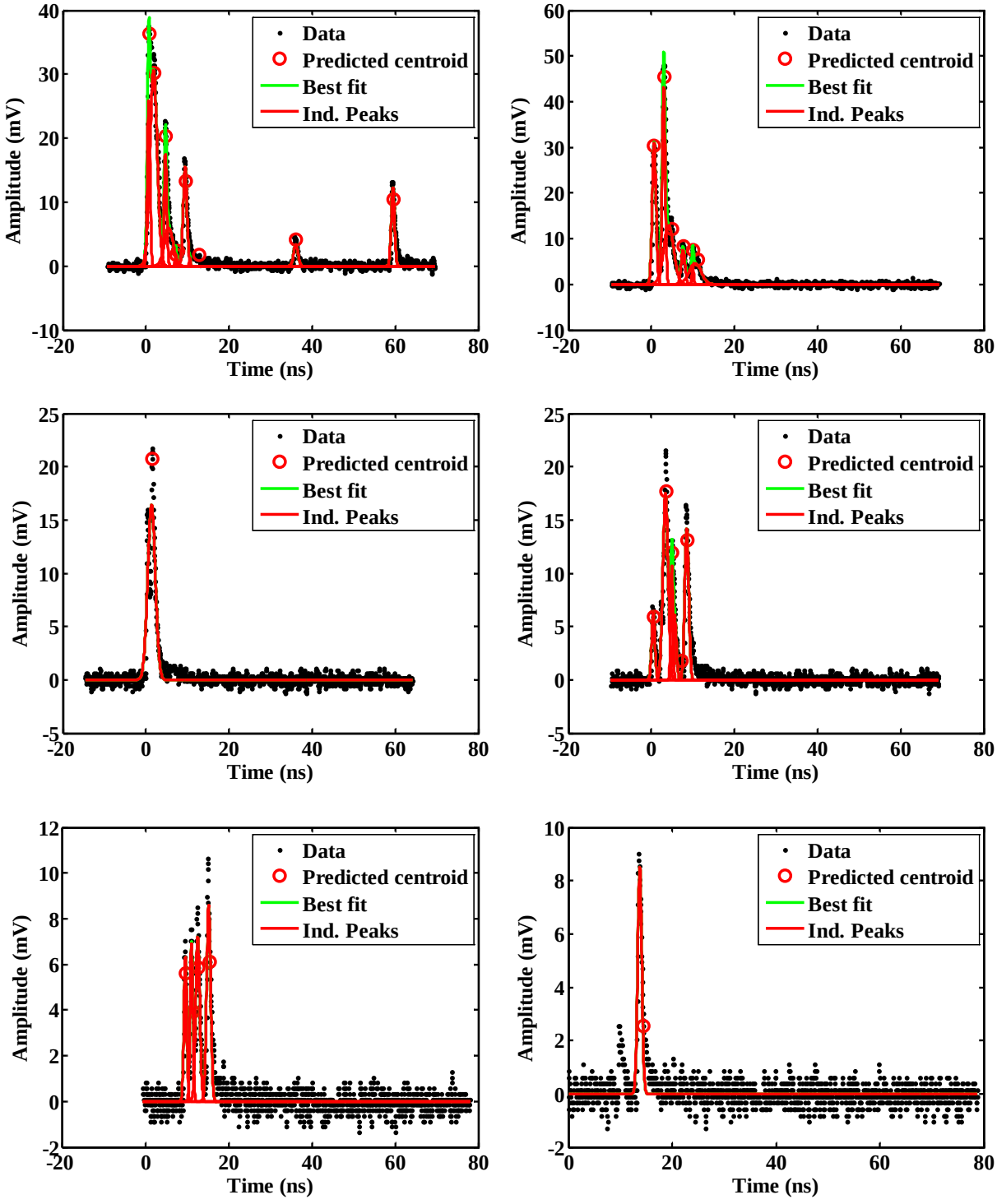

11.13 Data acquired for the Photek PMT240 at -4.3 kV with the Hamamatsu mod-5 in coincidence with the 110-degree SBD

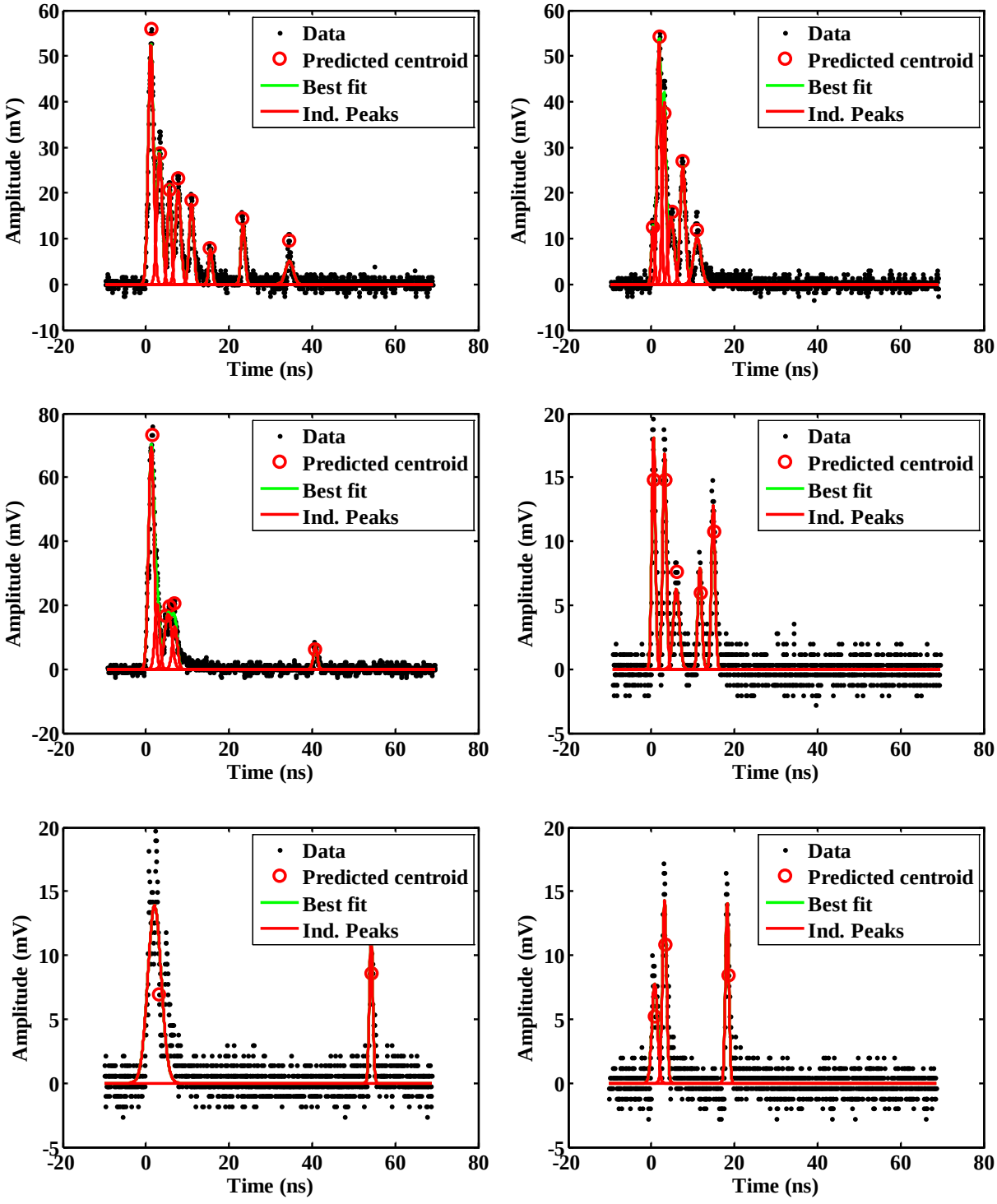

11.14 Data acquired for the Photek PMT240 at -4.4 kV with the Hamamatsu mod-5 in coincidence with the 110-degree SBD

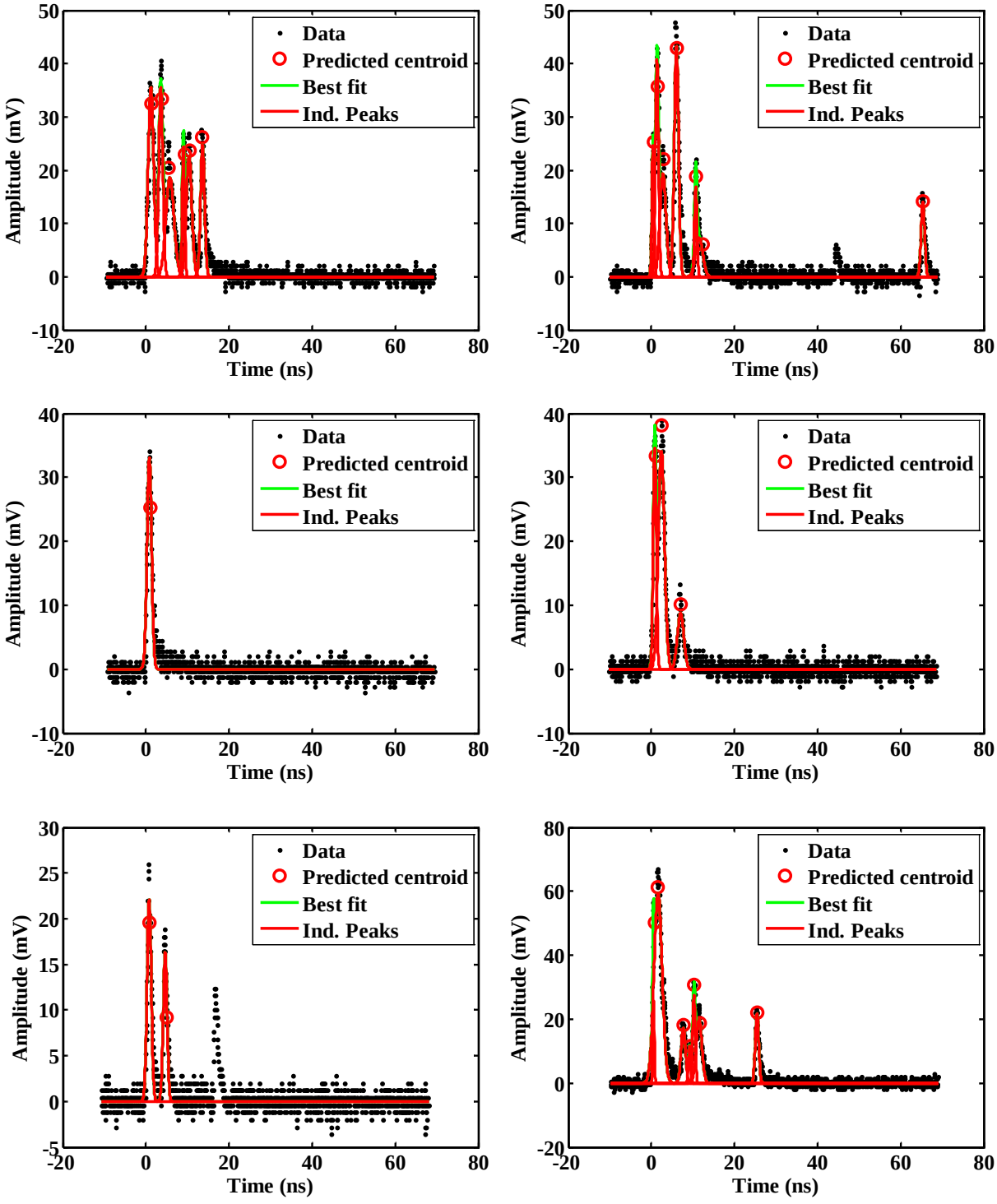

11.15 Data acquired for the Photek PMT240 at -4.5 kV with the Hamamatsu mod-5 in coincidence with the 110-degree SBD

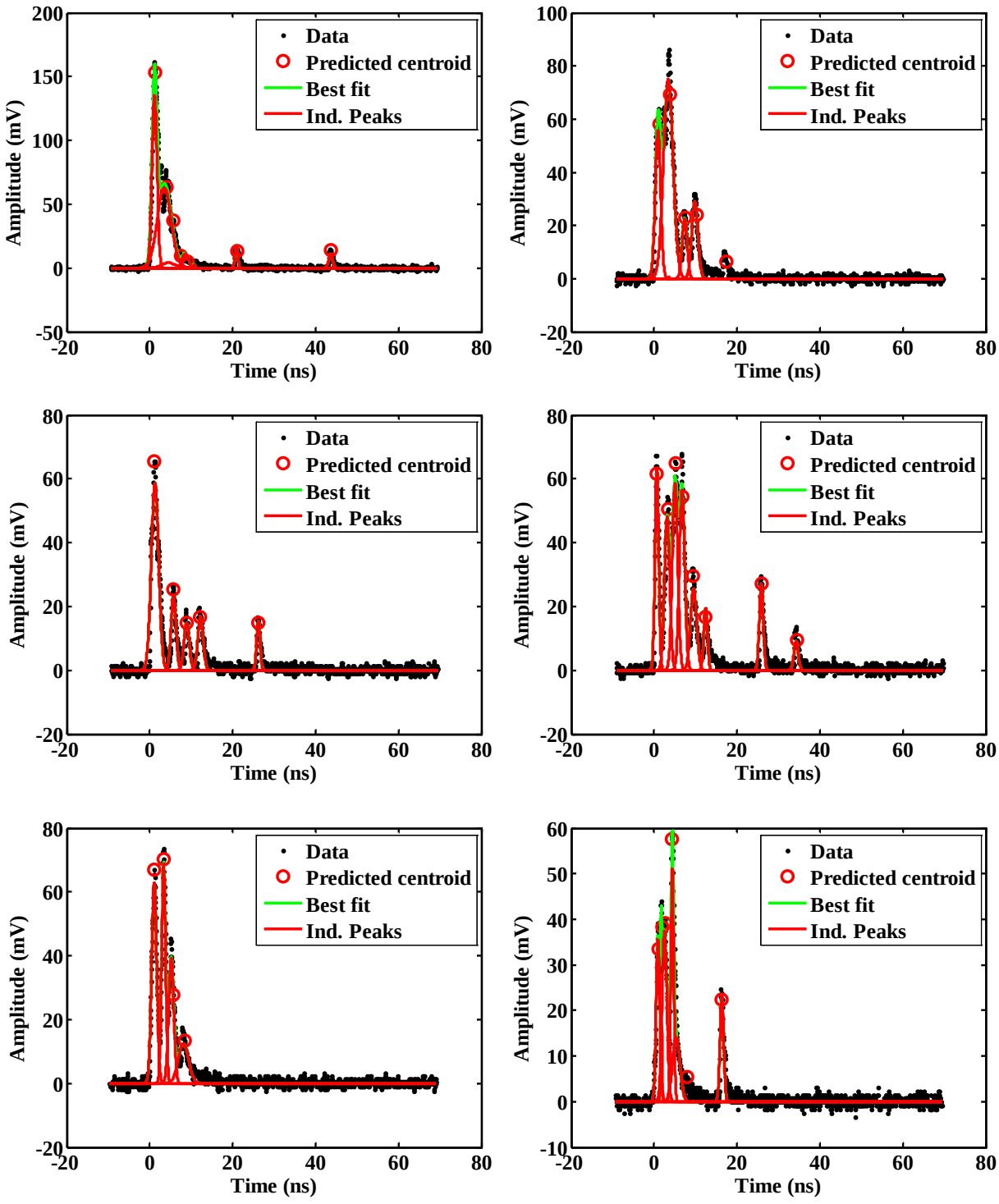

11.16 Data acquired for the Photek PMT240 at -4.6 kV with the Hamamatsu mod-5 in coincidence with the 110-degree SBD

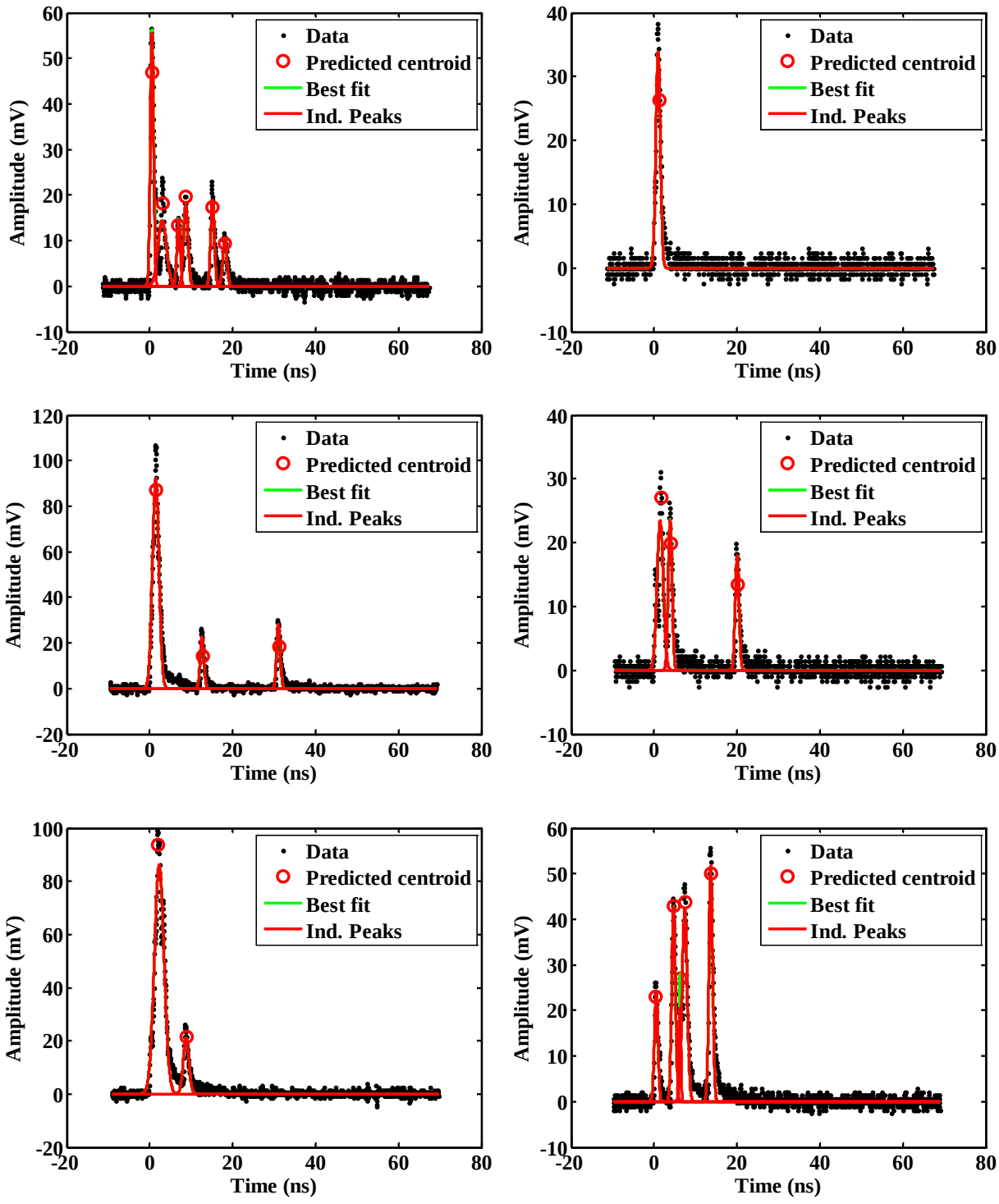

11.17 Data acquired for the Photek PMT240 at -4.6 kV with the Photek PMT240 in coincidence with the 110-degree SBD

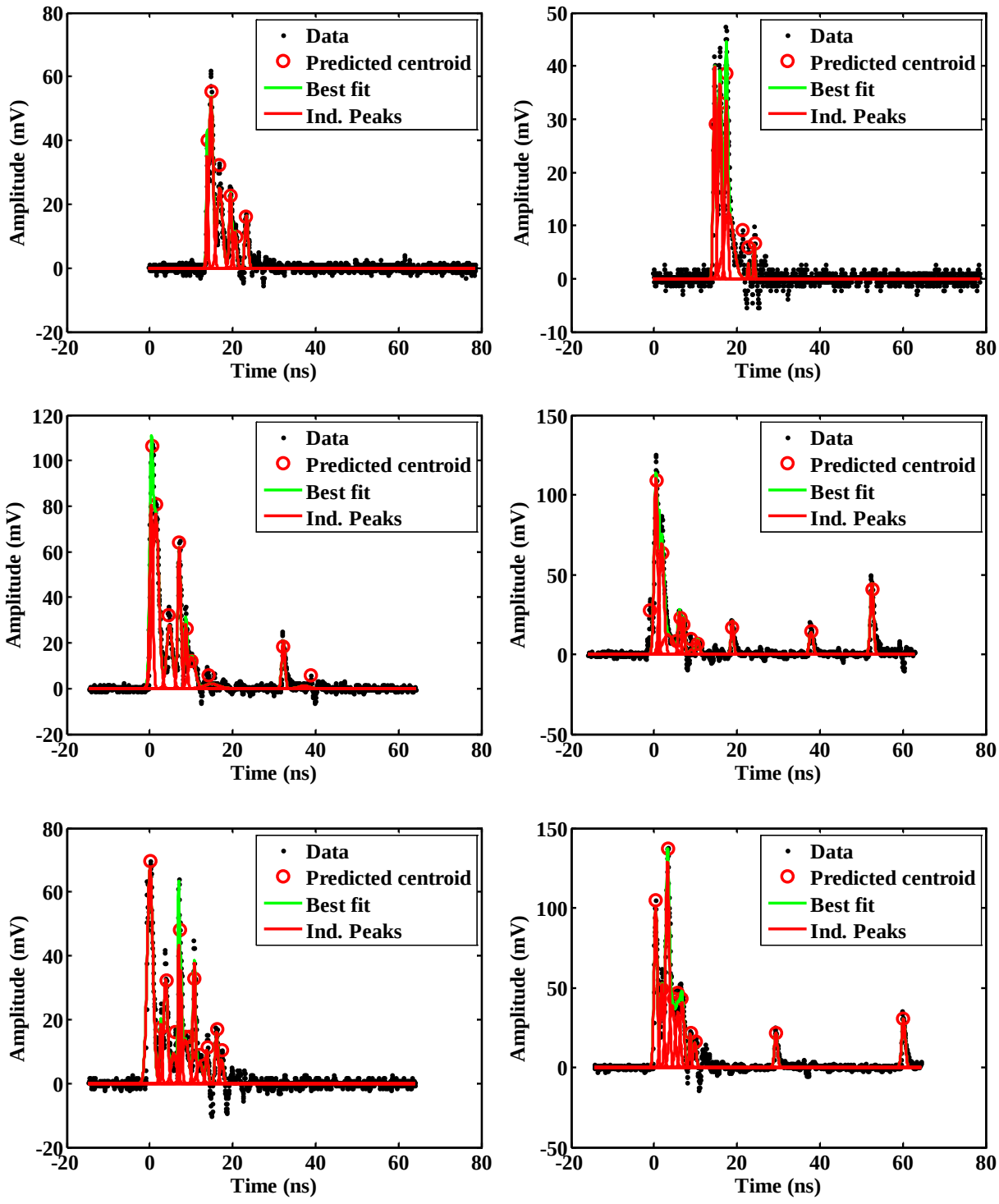

12 Appendix C - Waveforms and fits to the data using a sum of Gaussian functions for a D^+ ion acceleration potential of 175 keV

12.1 Data acquired for the Hamamatsu mod-5 at -1.7 kV with the Photek PMT240 in coincidence with the 110-degree SBD

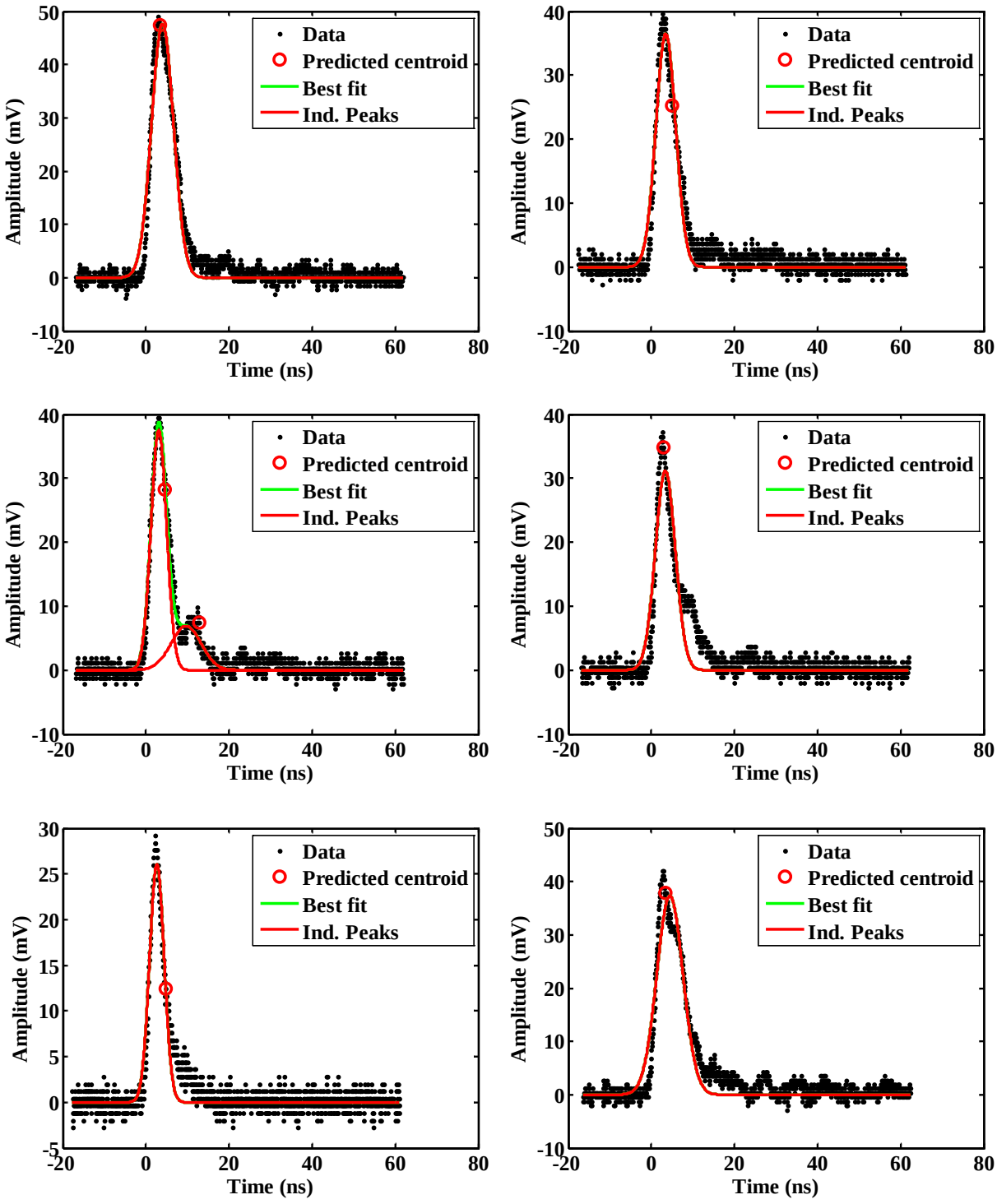

12.2 Data acquired for the Hamamatsu mod-5 at -1.8 kV with the Photek PMT240 in coincidence with the 110-degree SBD

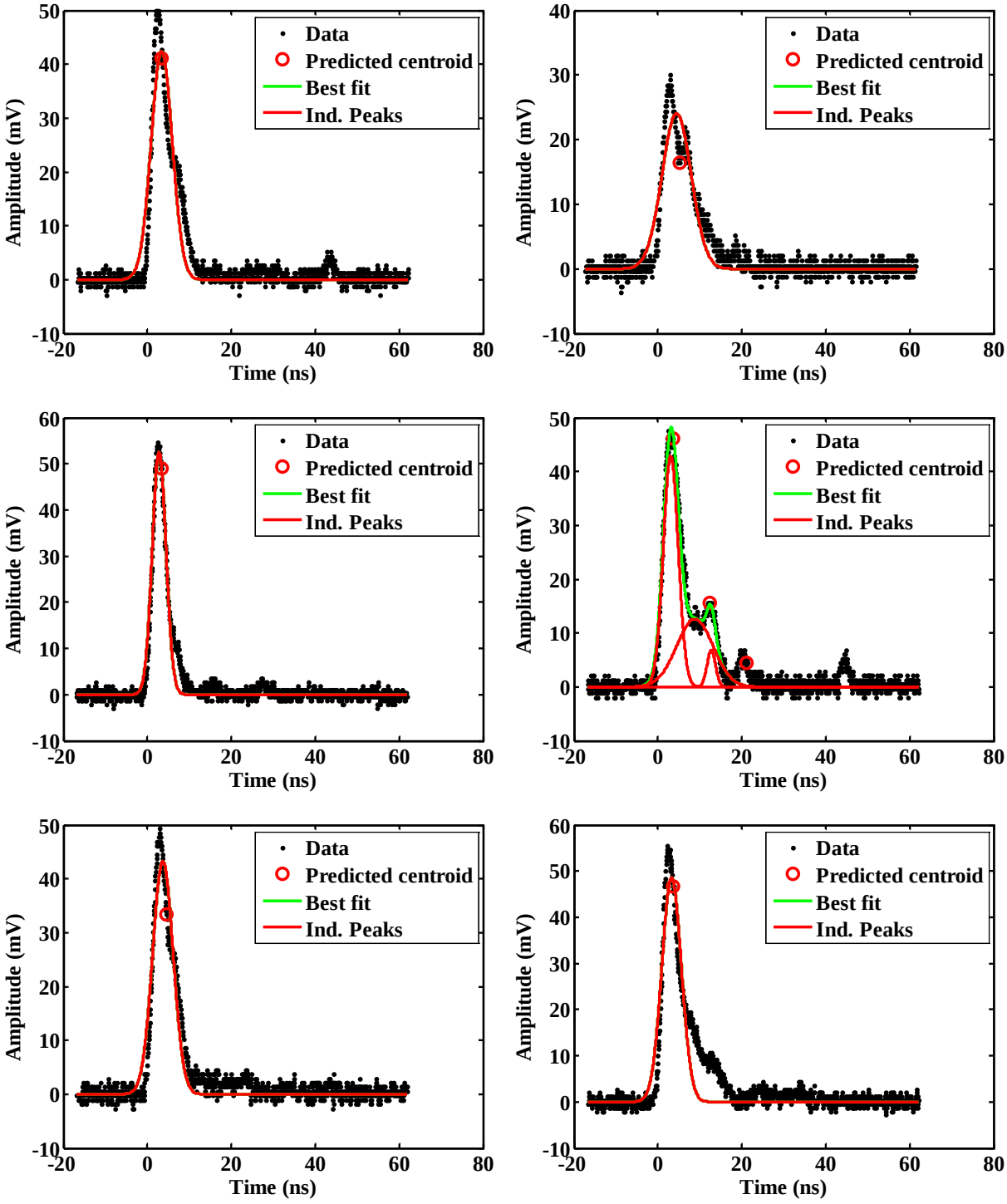

12.3 Data acquired for the Hamamatsu mod-5 at -1.9 kV with the Photek PMT240 in coincidence with the 110-degree SBD

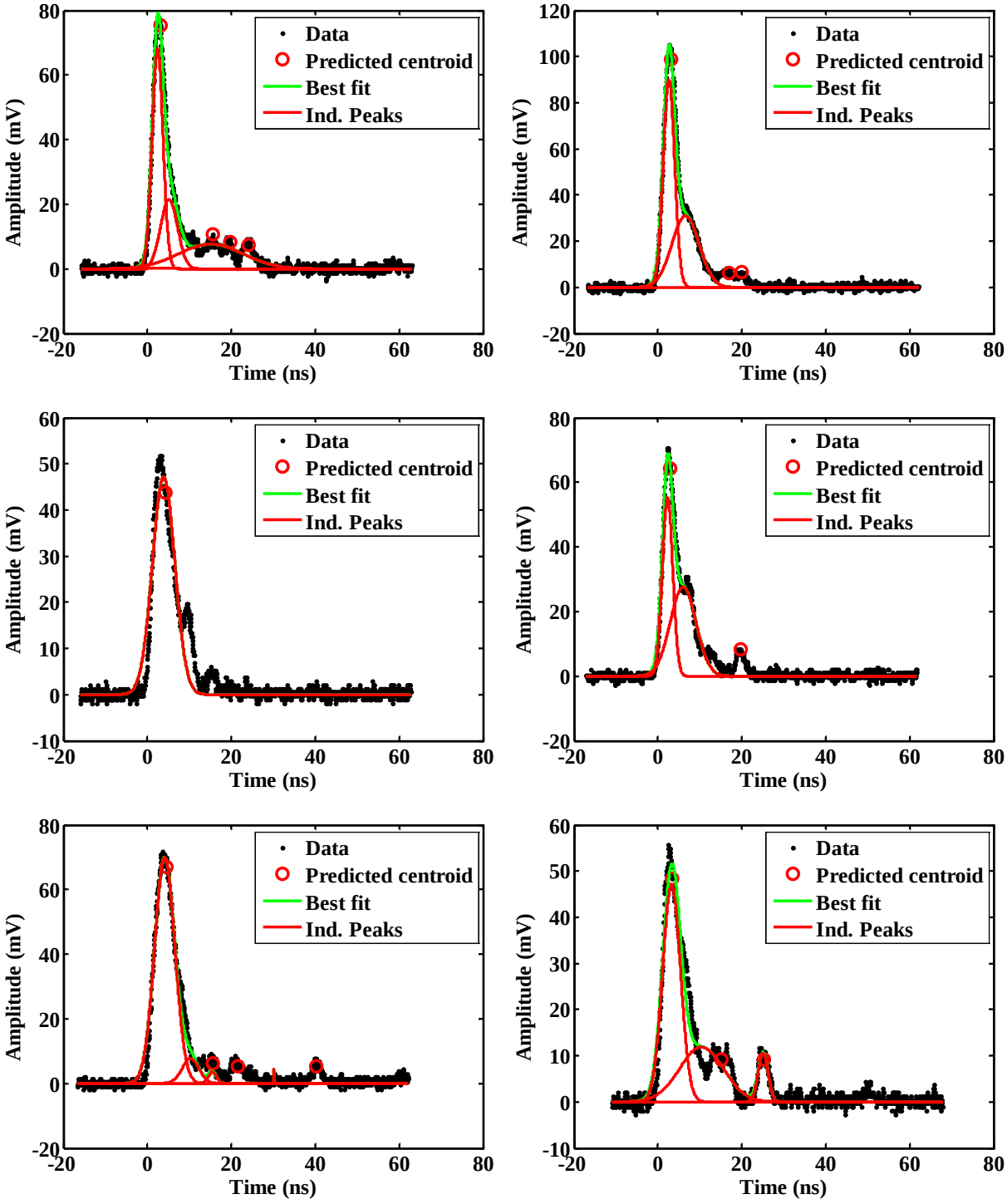

12.4 Data acquired for the Hamamatsu mod-5 at -2.0 kV with the Photek PMT240 in coincidence with the 110-degree SBD

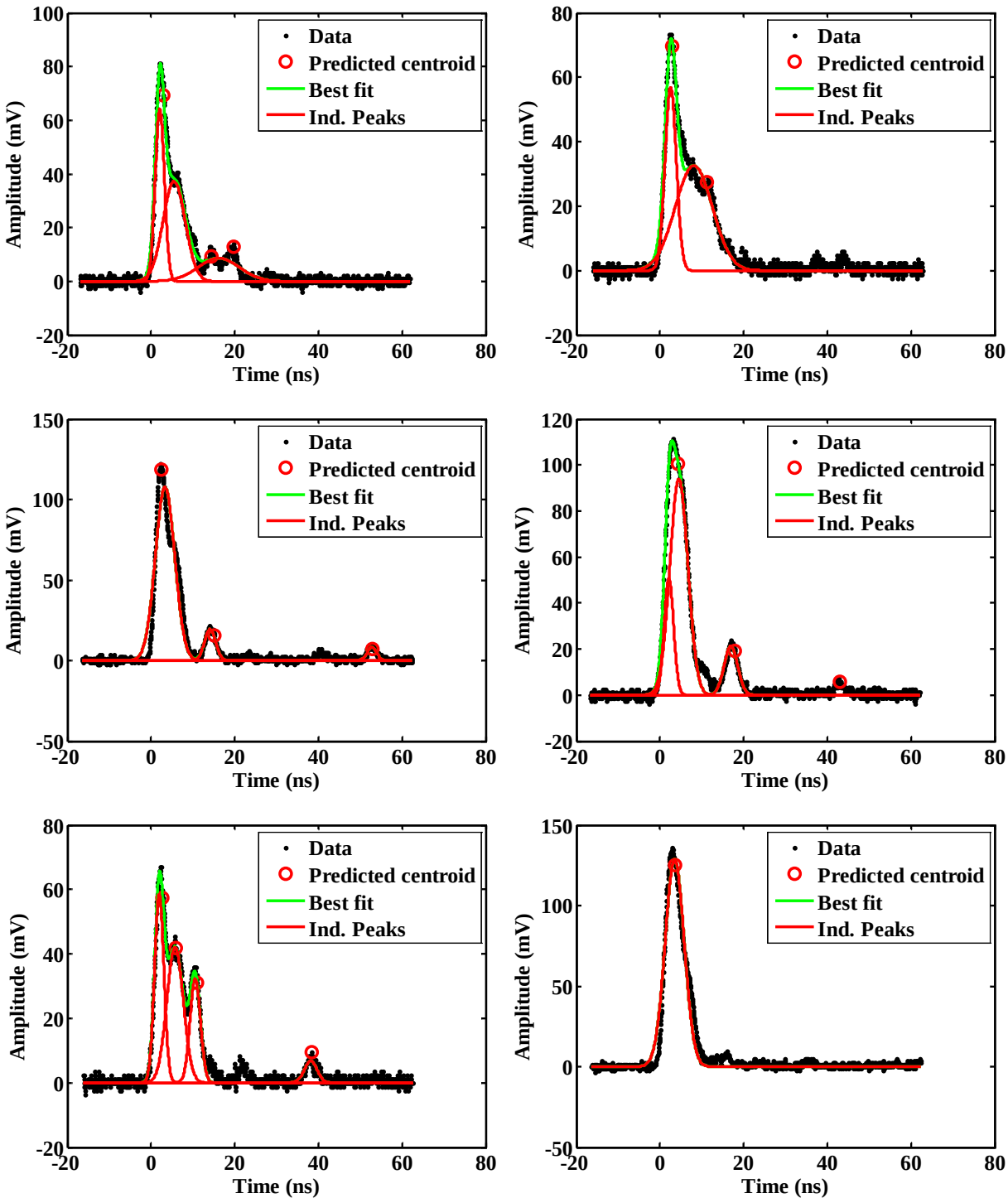

12.5 Data acquired for the Hamamatsu mod-5 at -2.1 kV with the Photek PMT240 in coincidence with the 110-degree SBD

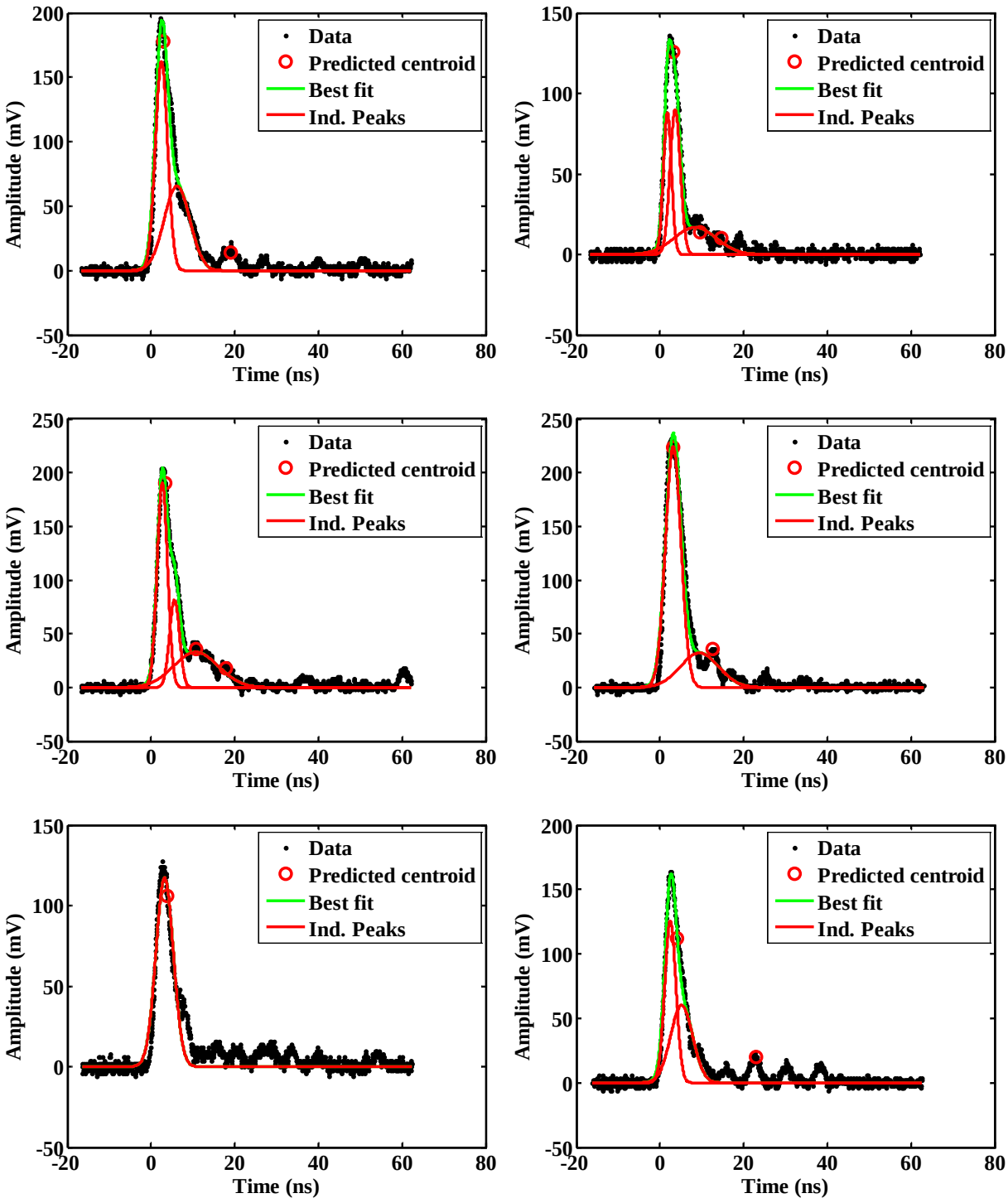

12.6 Data acquired for the Hamamatsu mod-5 at -2.2 kV with the Photek PMT240 in coincidence with the 110-degree SBD

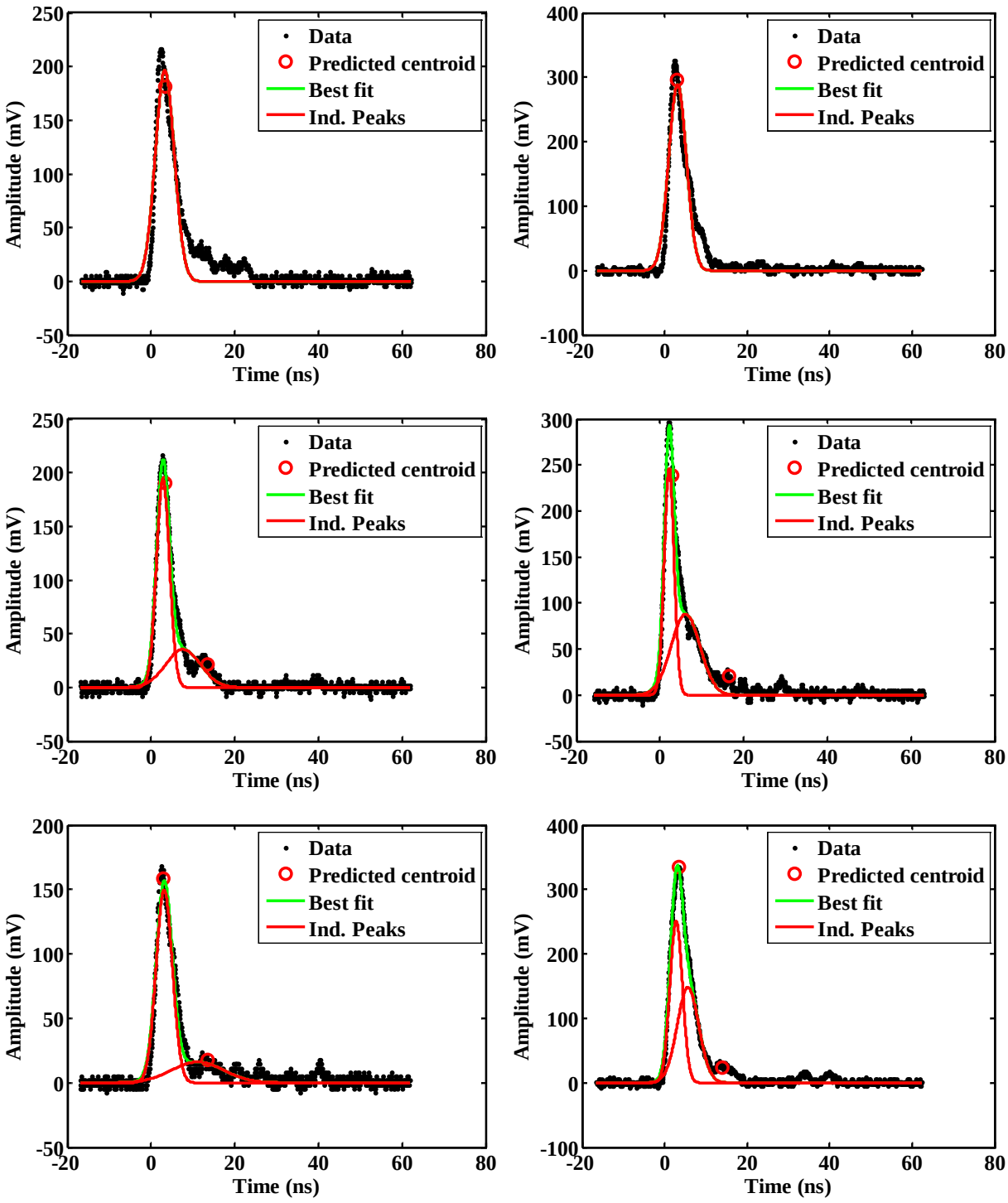

12.7 Data acquired for the Hamamatsu mod-5 at -2.3 kV with the Photek PMT240 in coincidence with the 110-degree SBD

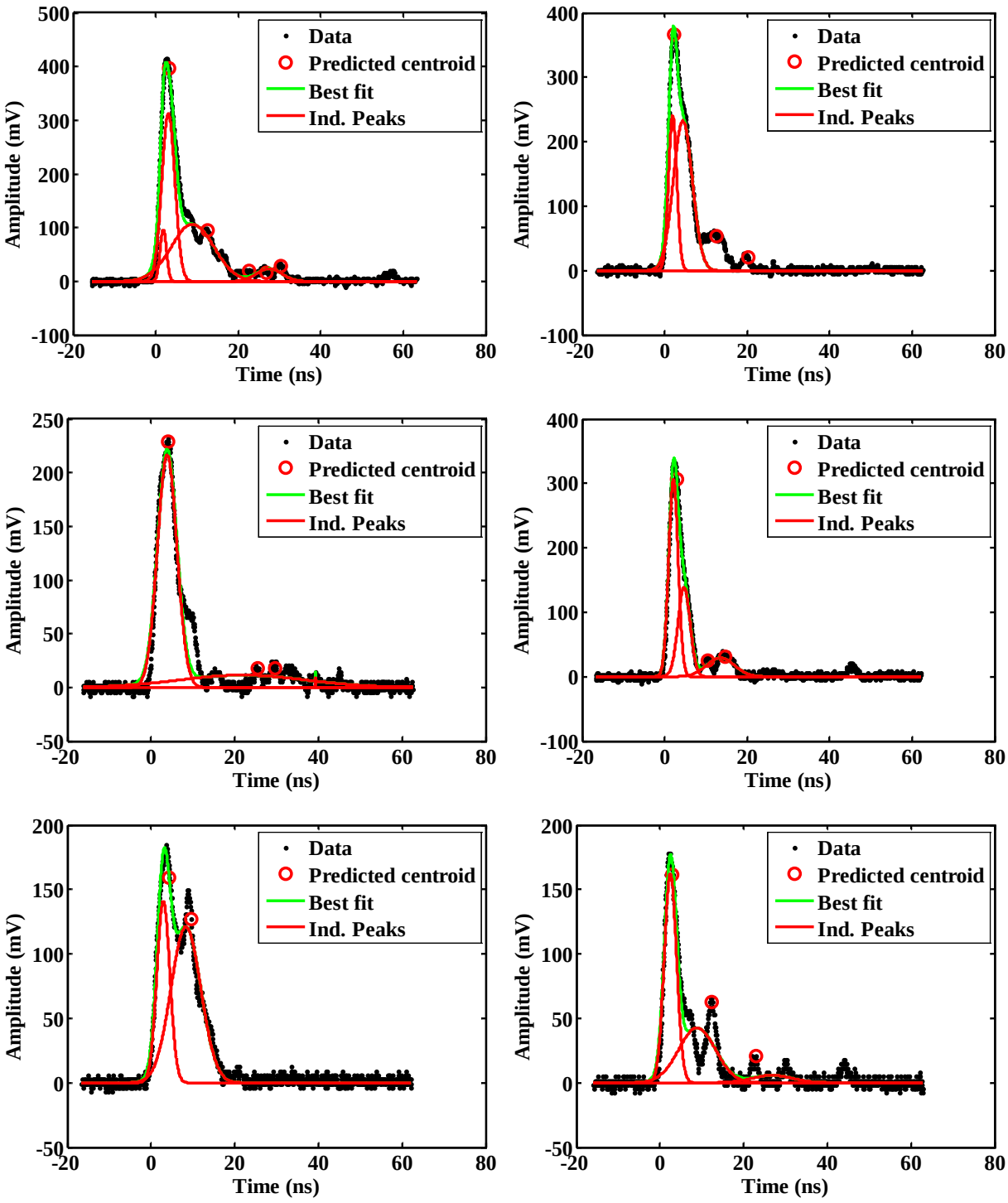

12.8 Data acquired for the Hamamatsu mod-5 at -2.4 kV with the Photek PMT240 in coincidence with the 110-degree SBD

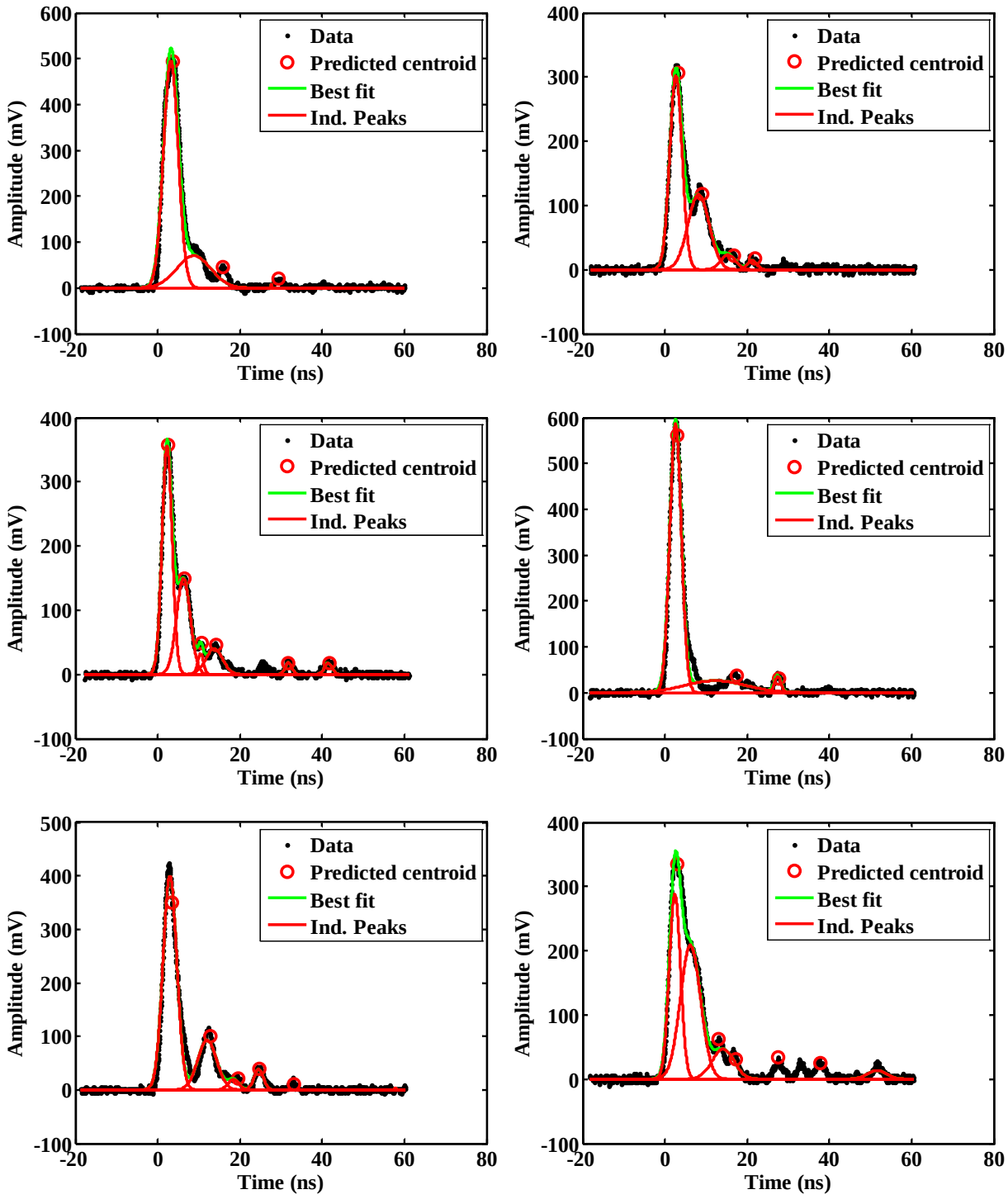

12.9 Data acquired for the Hamamatsu mod-5 at -2.0 kV with the Hamamatsu mod-5 in coincidence with the 110-degree SBD

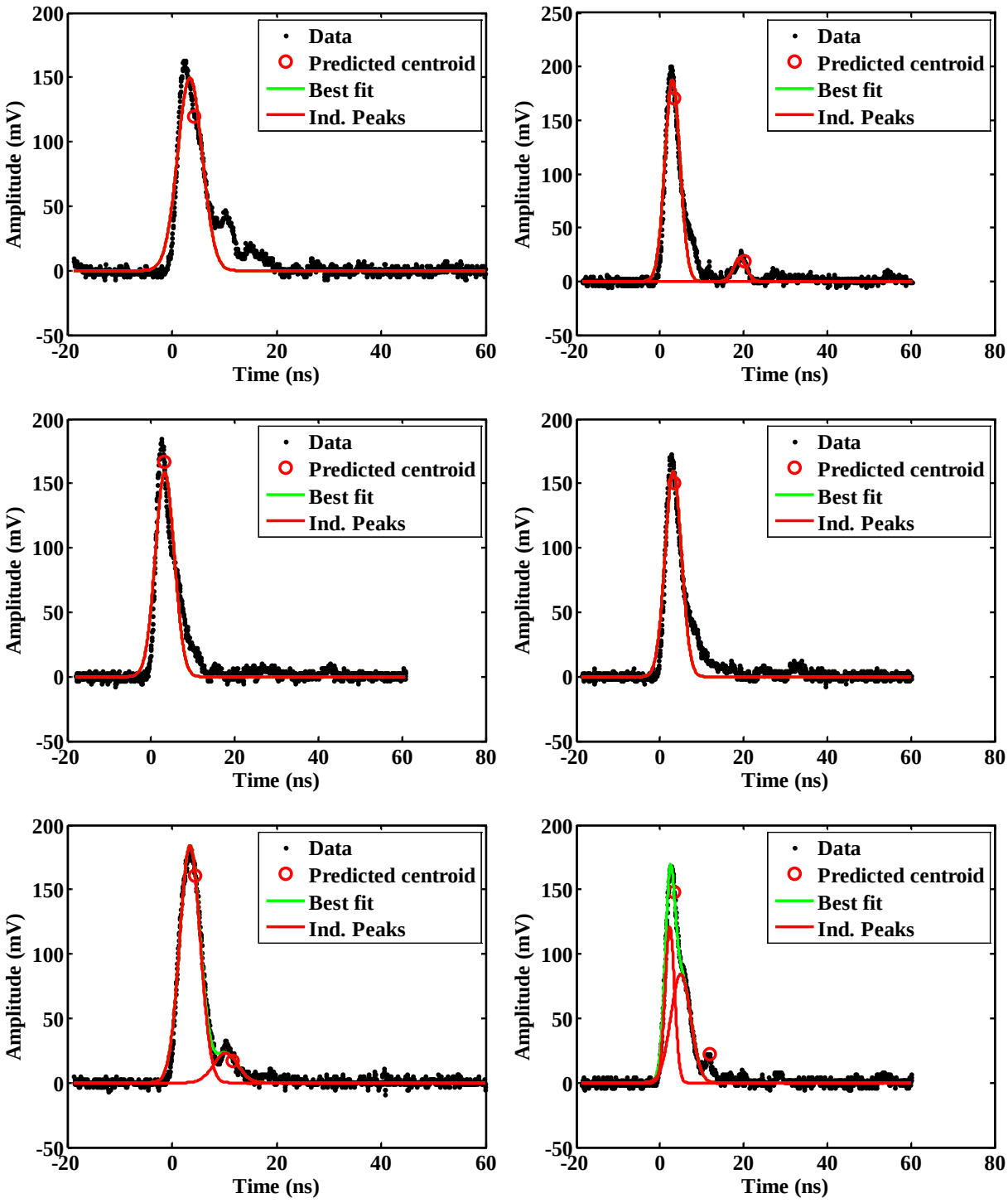

12.10 Data acquired for the Hamamatsu mod-5 at -2.3 kV with the Hamamatsu mod-5 in coincidence with the 110-degree SBD

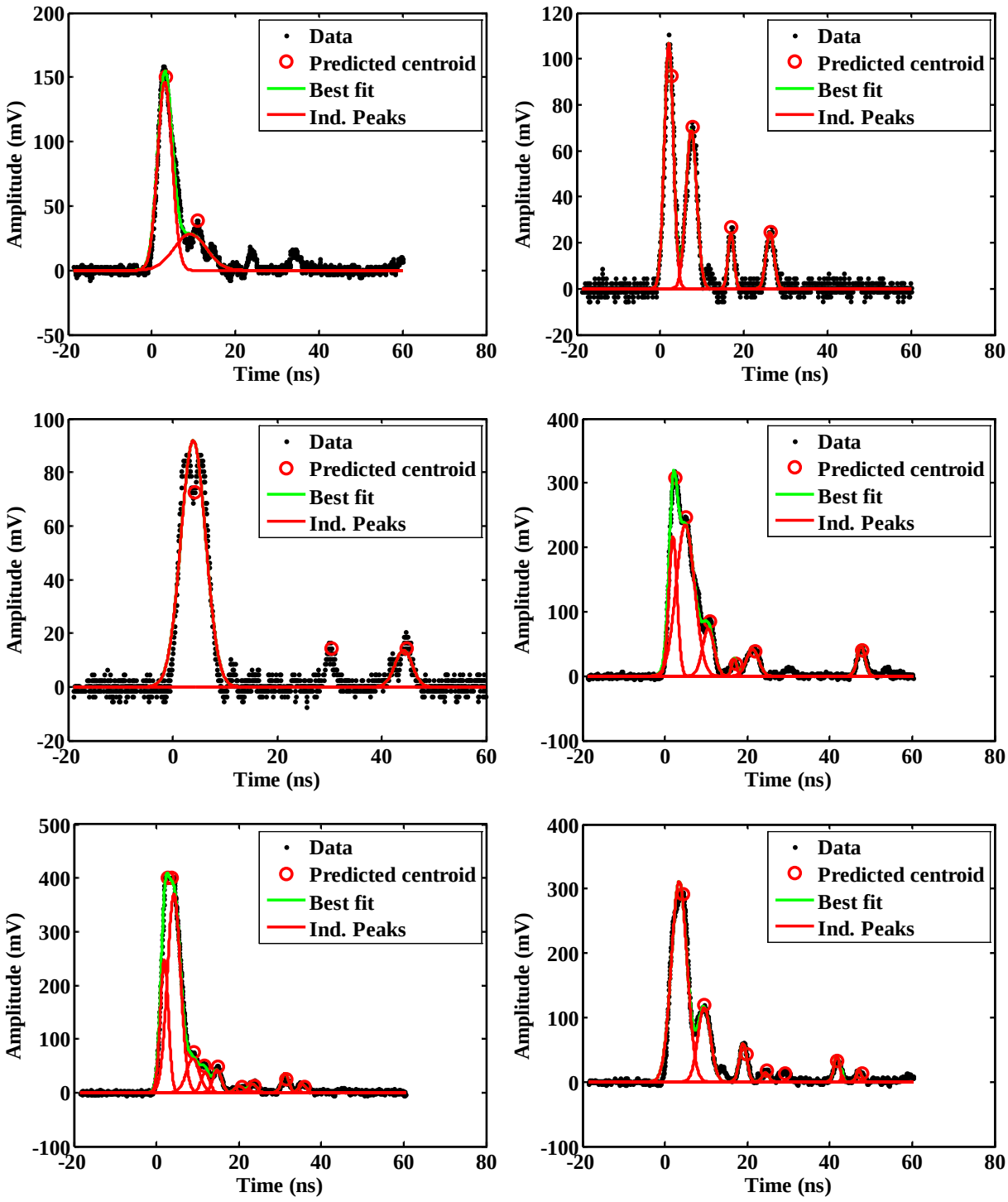

12.11 Data acquired for the Hamamatsu mod-5 at -2.4 kV with the Hamamatsu mod-5 in coincidence with the 110-degree SBD

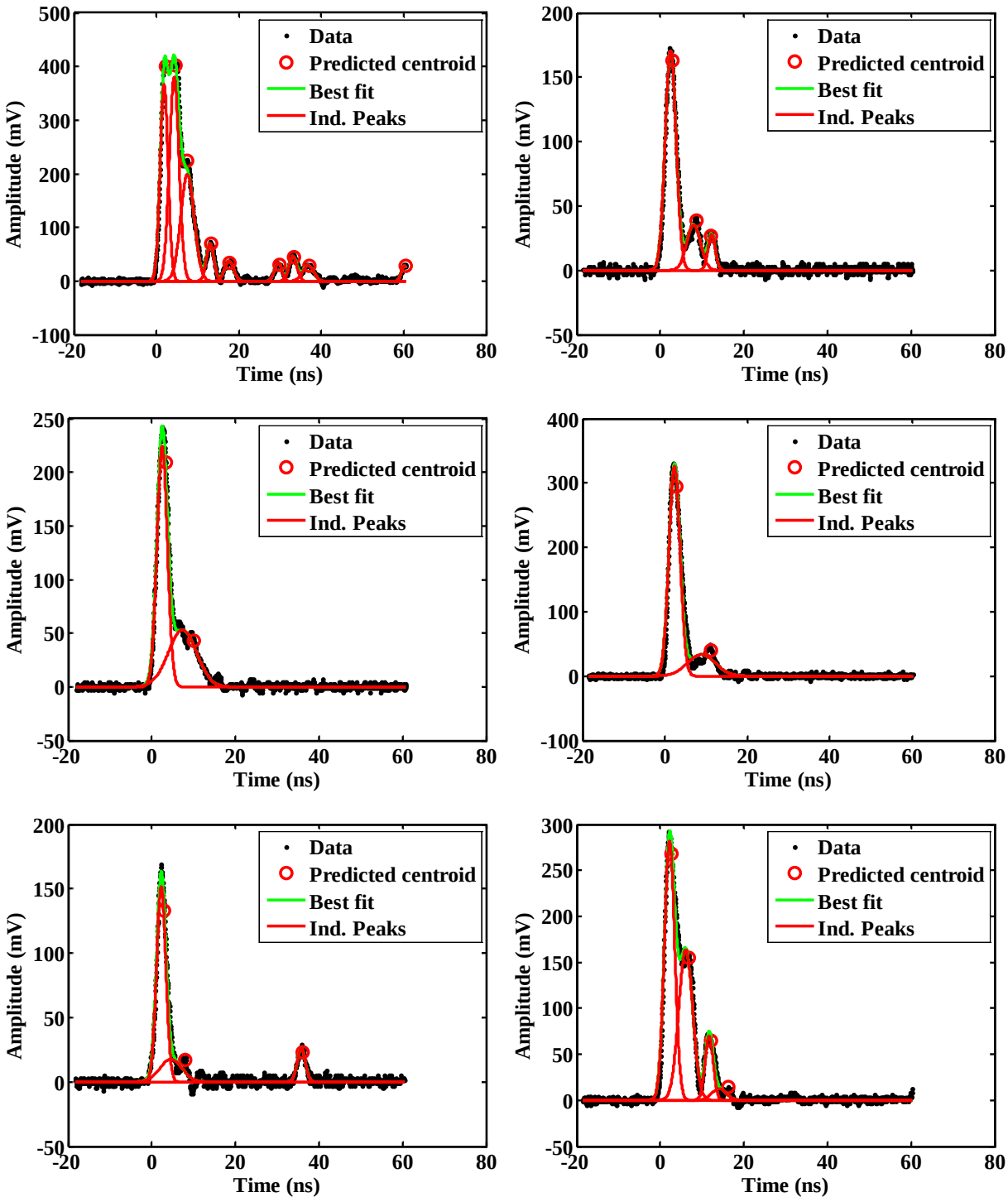

12.12 Data acquired for the Photek PMT240 at -3.8 kV with the Hamamatsu mod-5 in coincidence with the 110-degree SBD

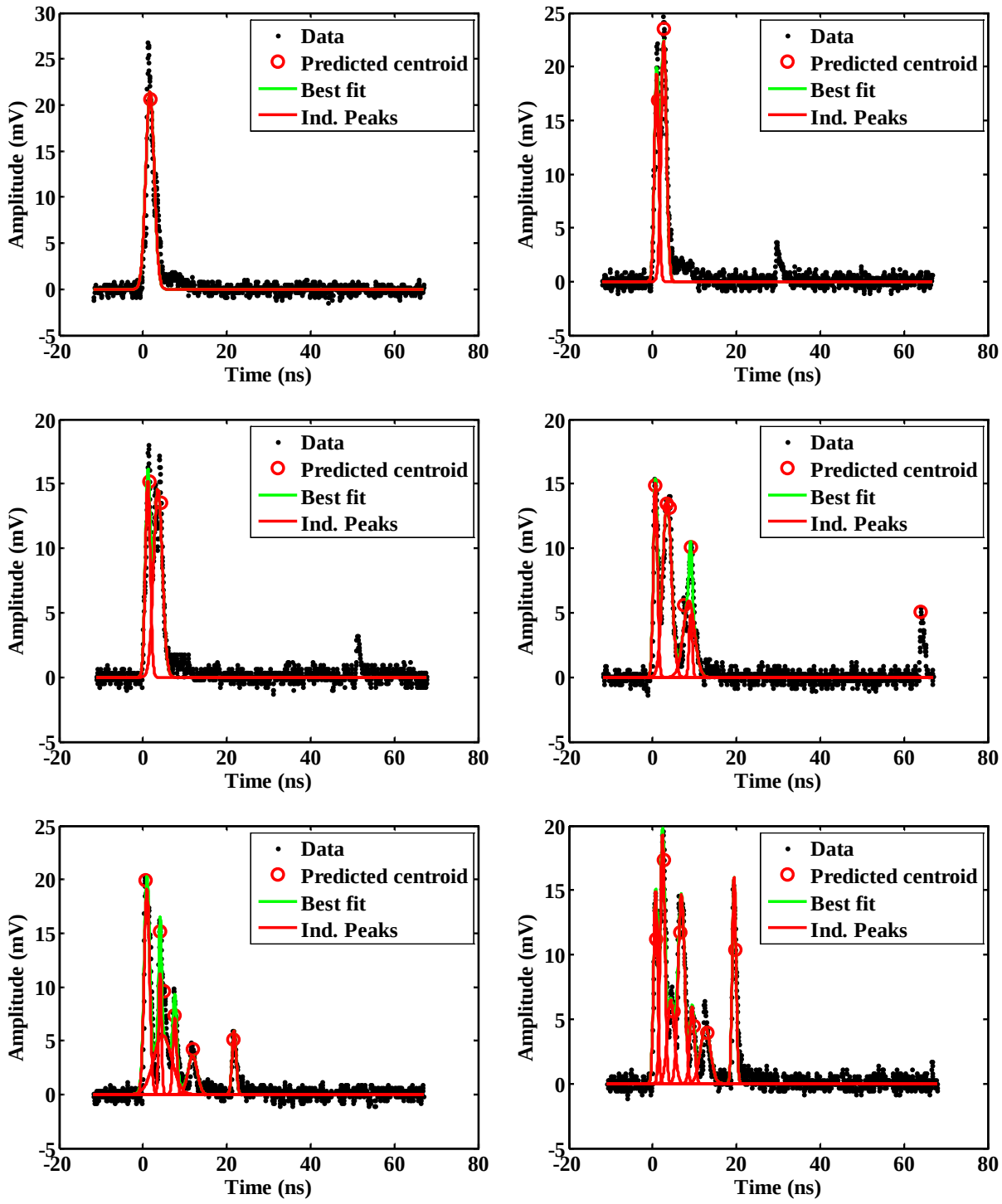

12.13 Data acquired for the Photek PMT240 at -3.9 kV with the Hamamatsu mod-5 in coincidence with the 110-degree SBD

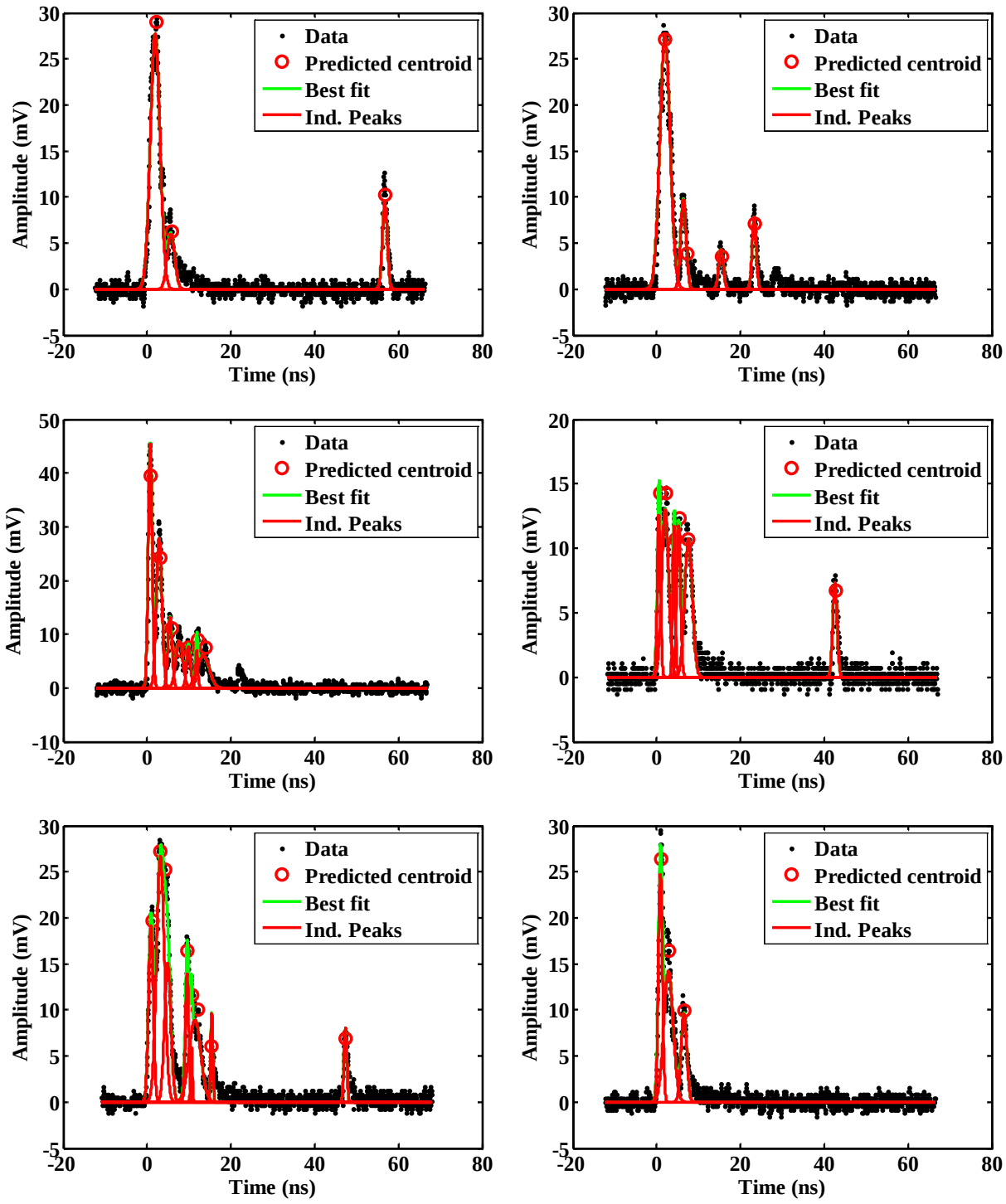

12.14 Data acquired for the Photek PMT240 at -4.0 kV with the Hamamatsu mod-5 in coincidence with the 110-degree SBD

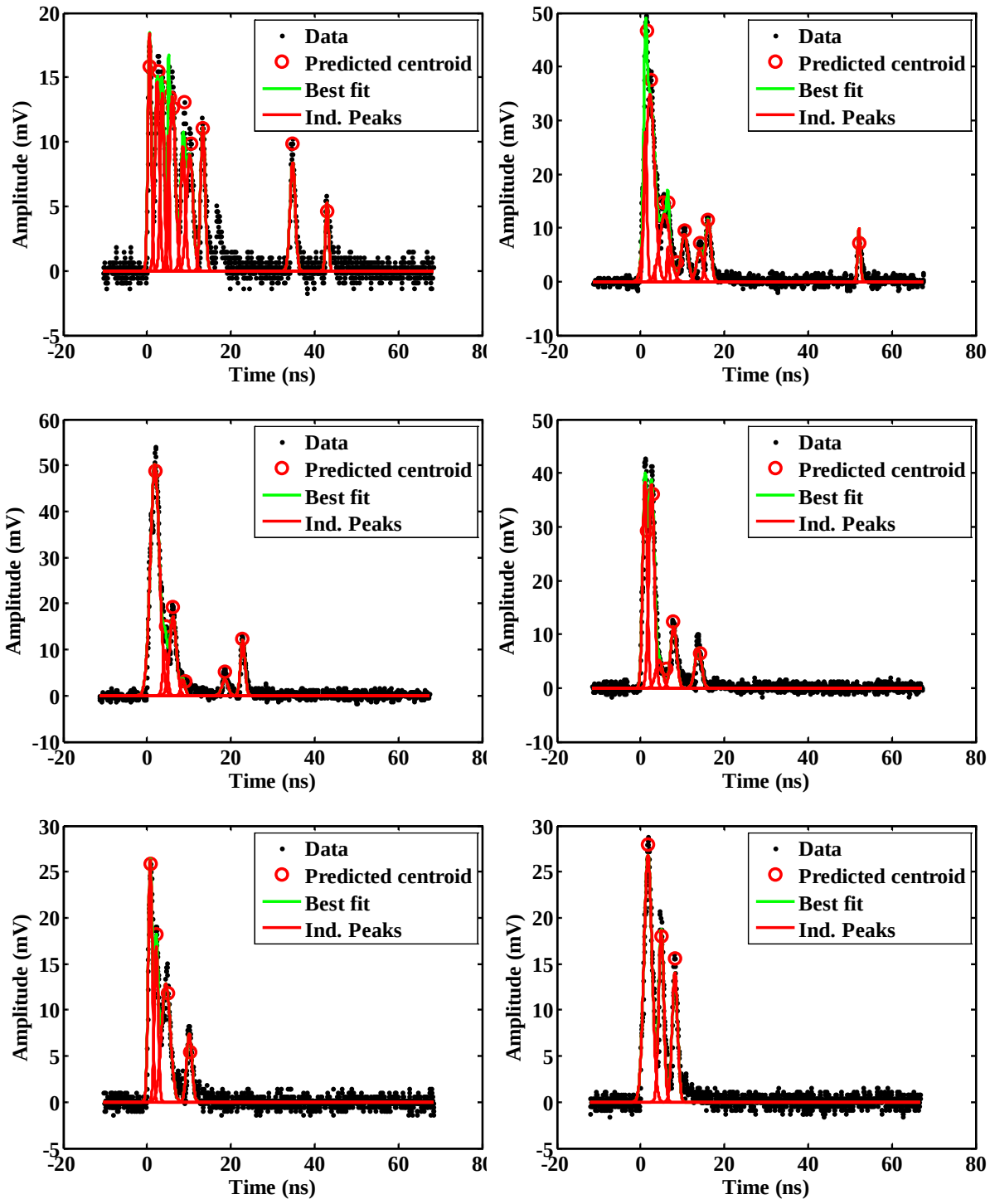

12.15 Data acquired for the Photek PMT240 at -4.1 kV with the Hamamatsu mod-5 in coincidence with the 110-degree SBD

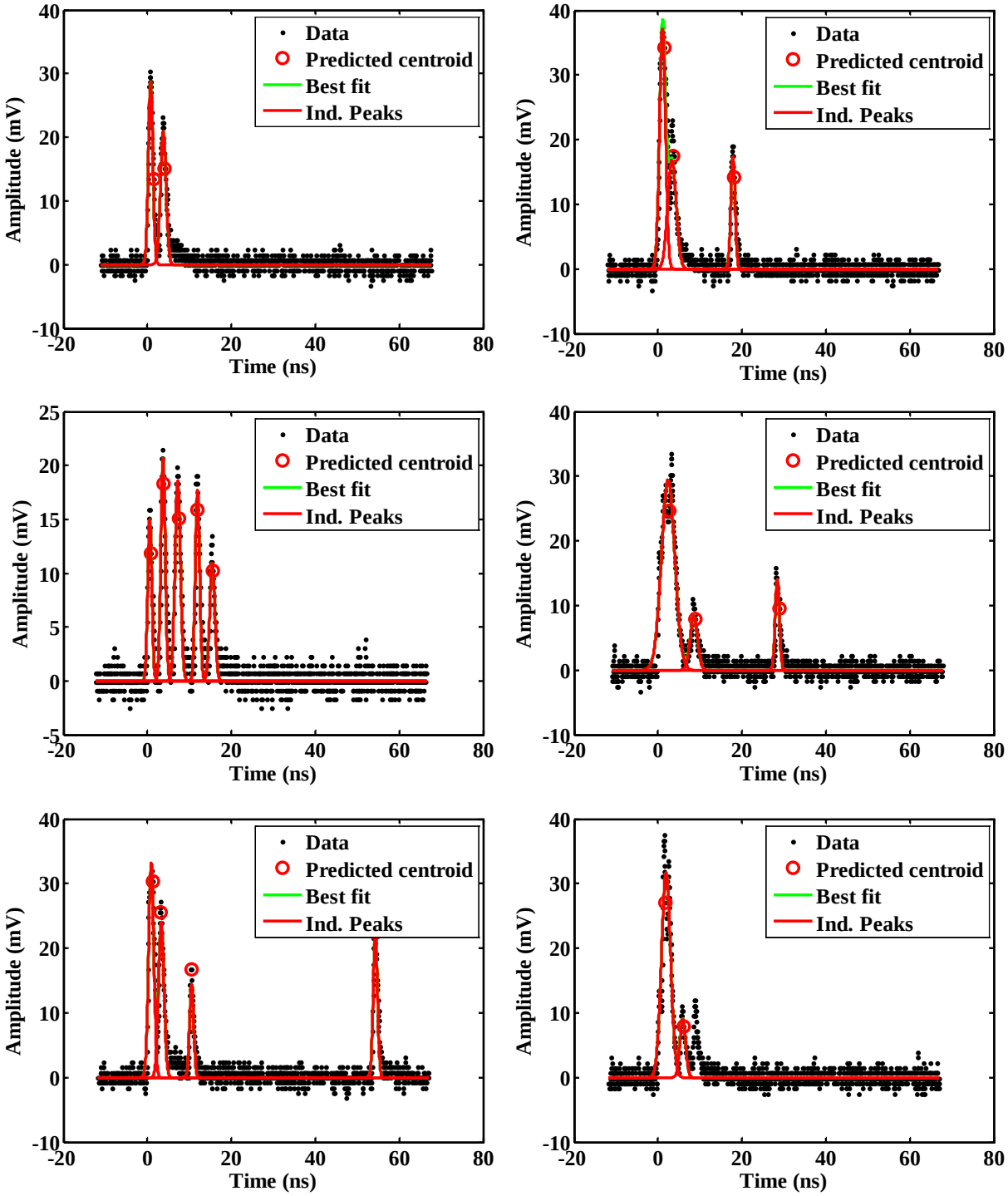

12.16 Data acquired for the Photek PMT240 at -4.3 kV with the Hamamatsu mod-5 in coincidence with the 110-degree SBD

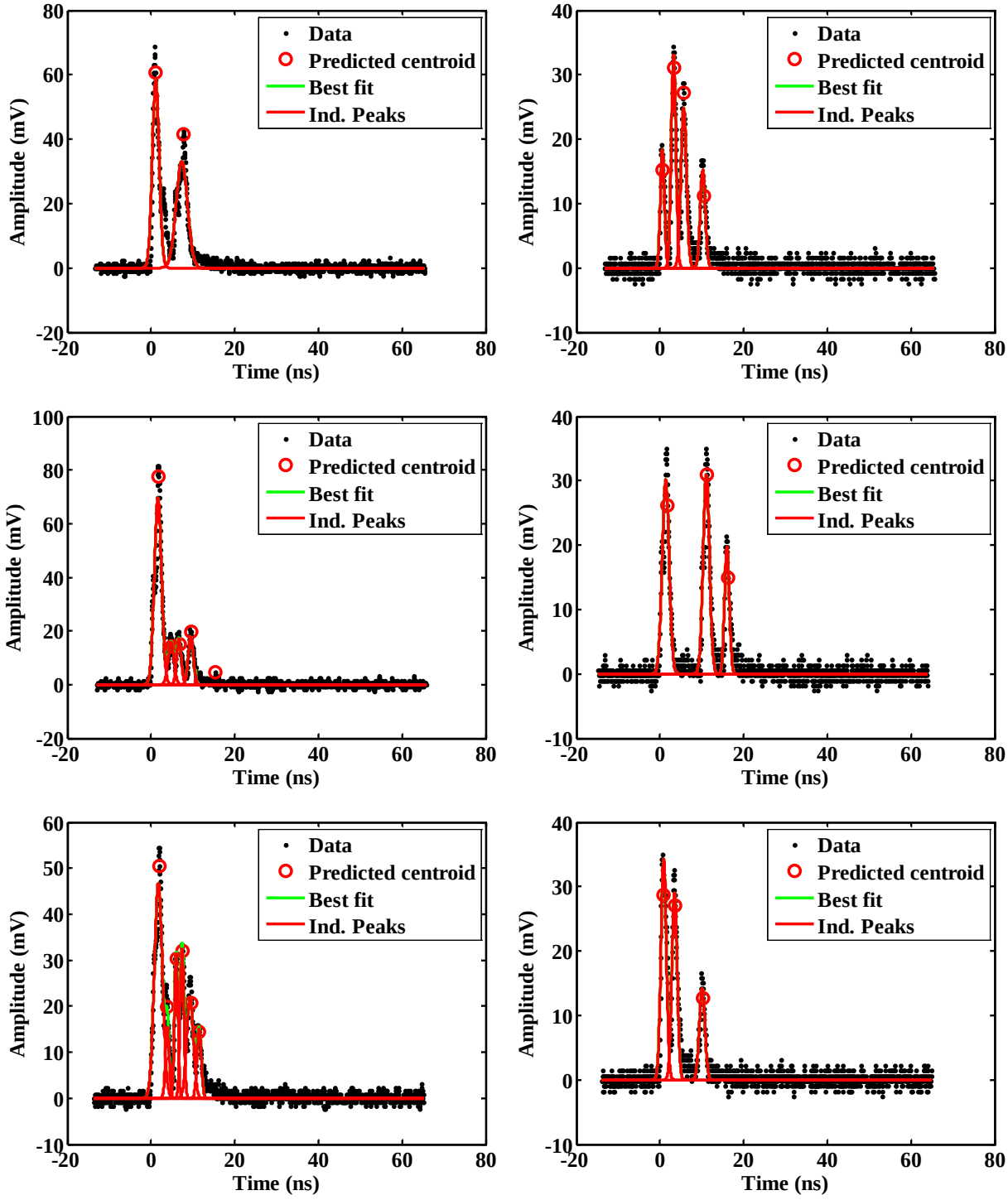

12.17 Data acquired for the Photek PMT240 at -4.4 kV with the Hamamatsu mod-5 in coincidence with the 110-degree SBD

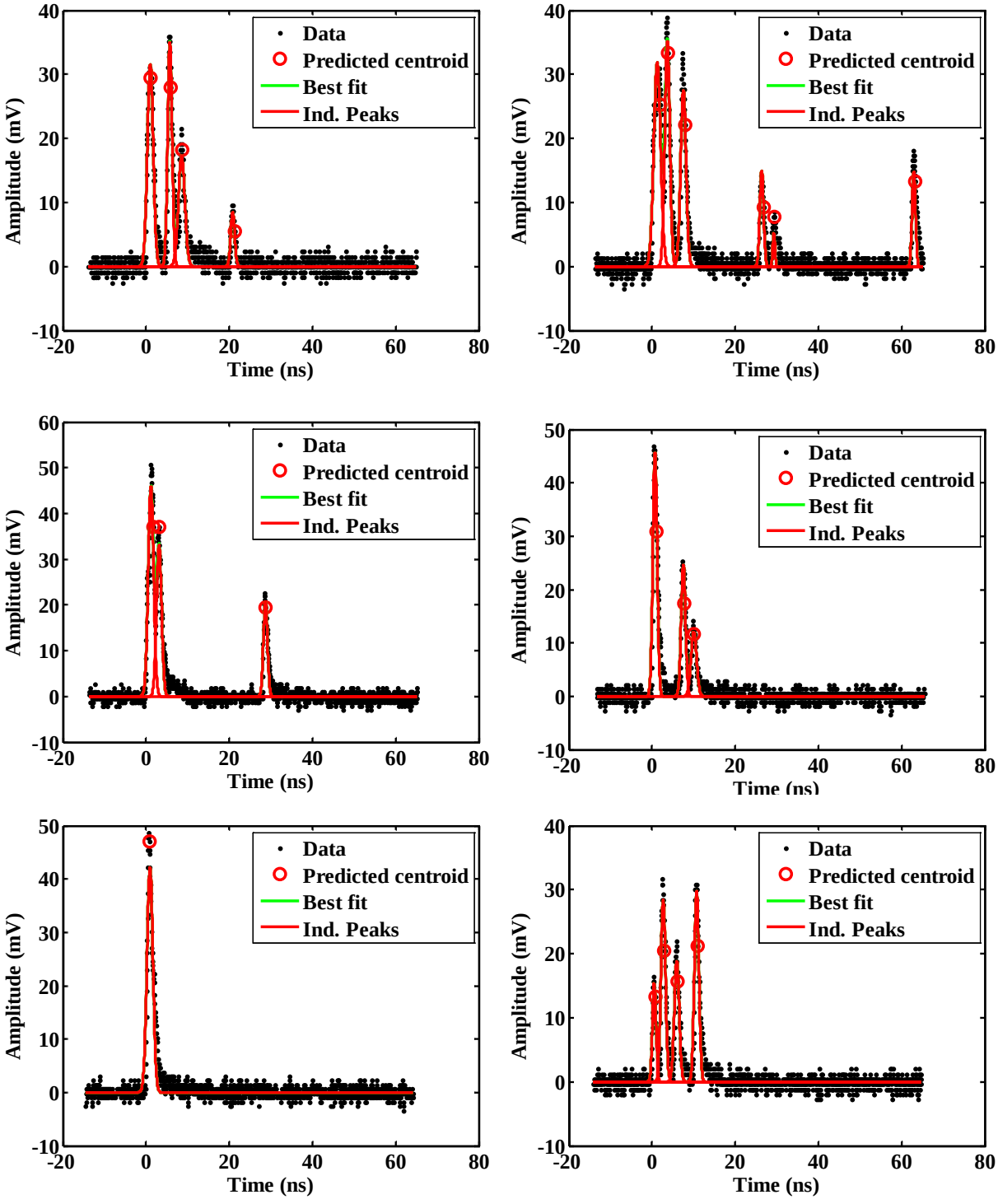

12.18 Data acquired for the Photek PMT240 at -4.5 kV with the Hamamatsu mod-5 in coincidence with the 110-degree SBD

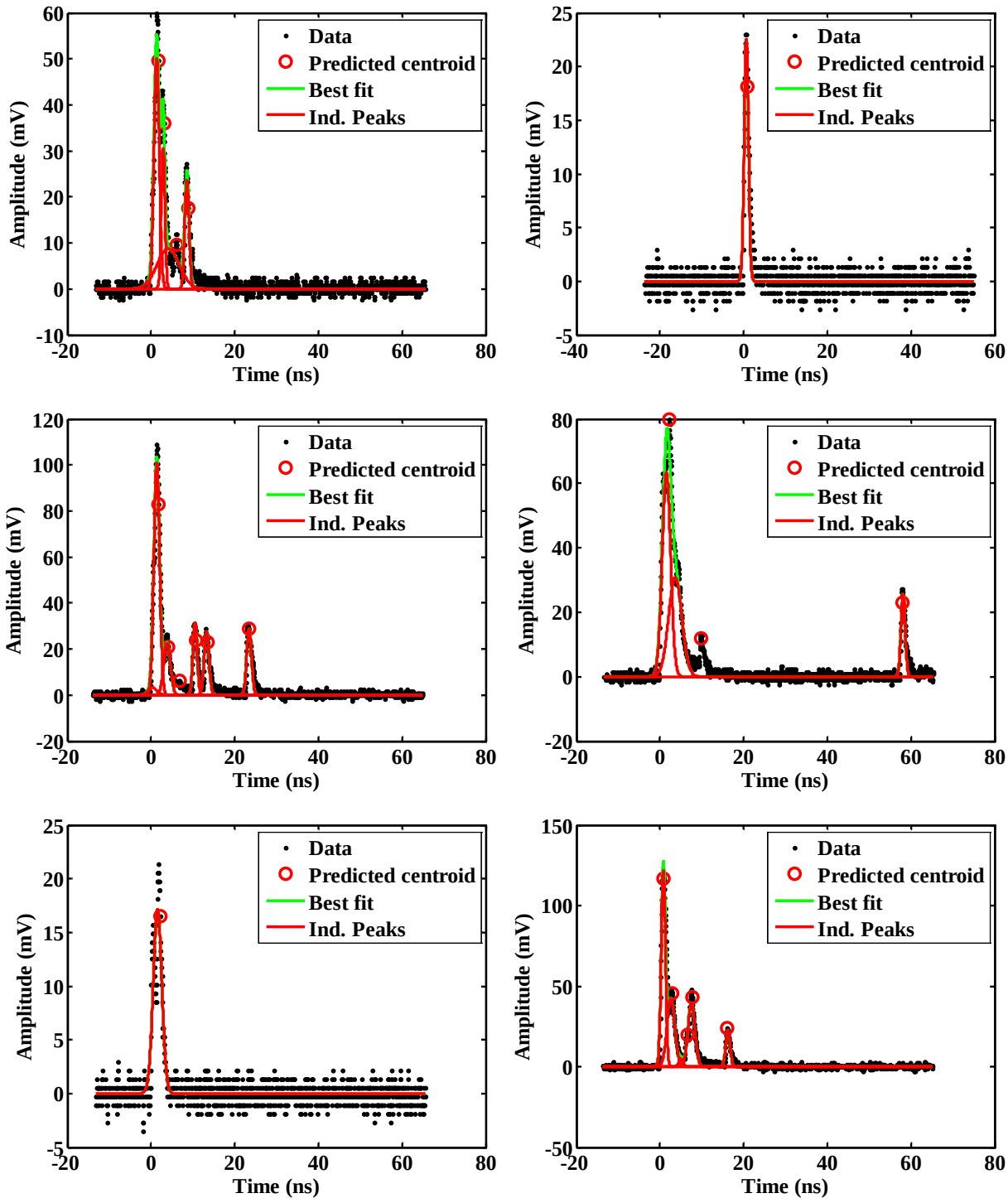

12.19 Data acquired for the Photek PMT240 at -4.6 kV with the Hamamatsu mod-5 in coincidence with the 110-degree SBD

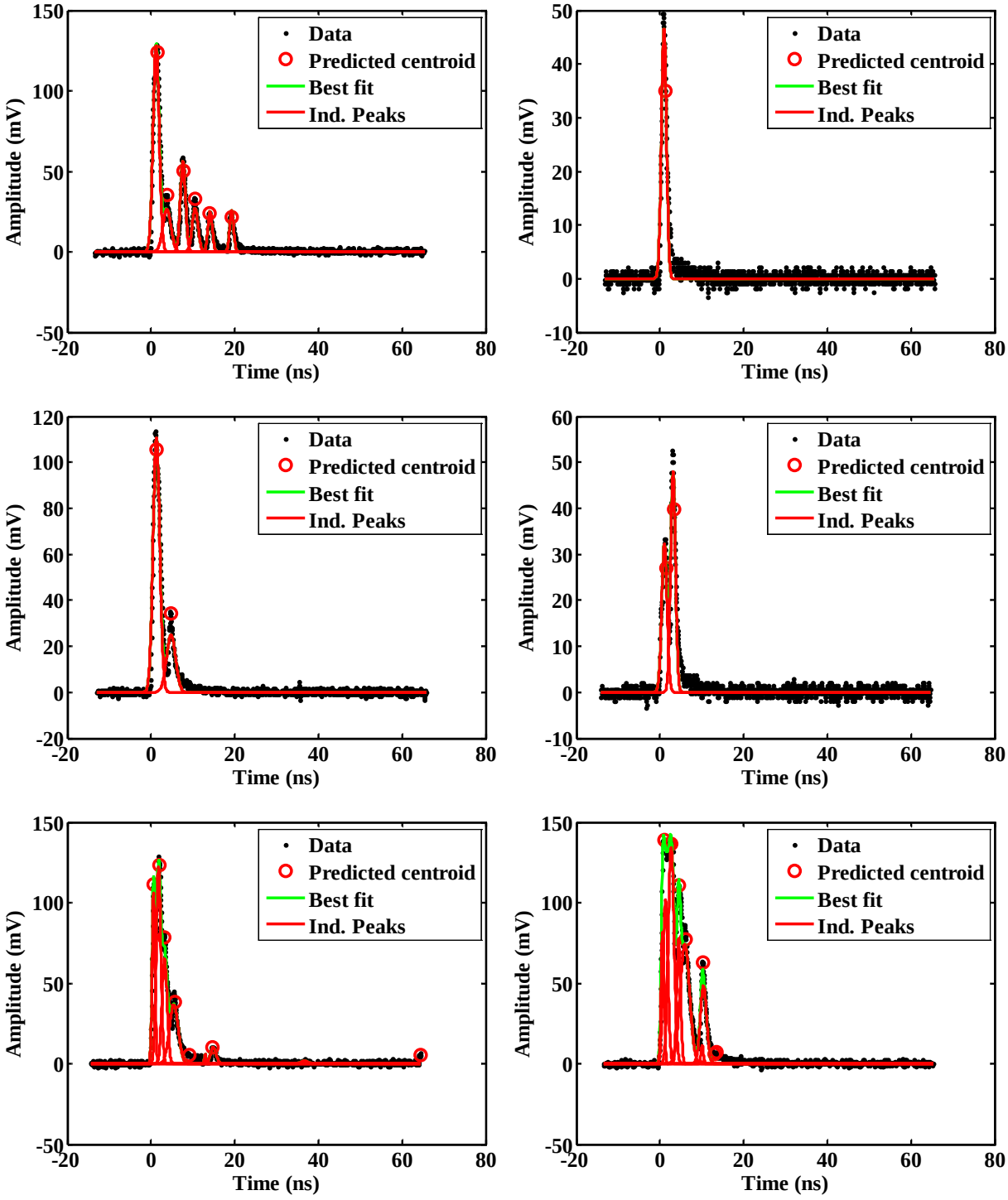

12.20 Data acquired for the Photek PMT240 at -4.2 kV with the Photek PMT240 in coincidence with the 110-degree SBD

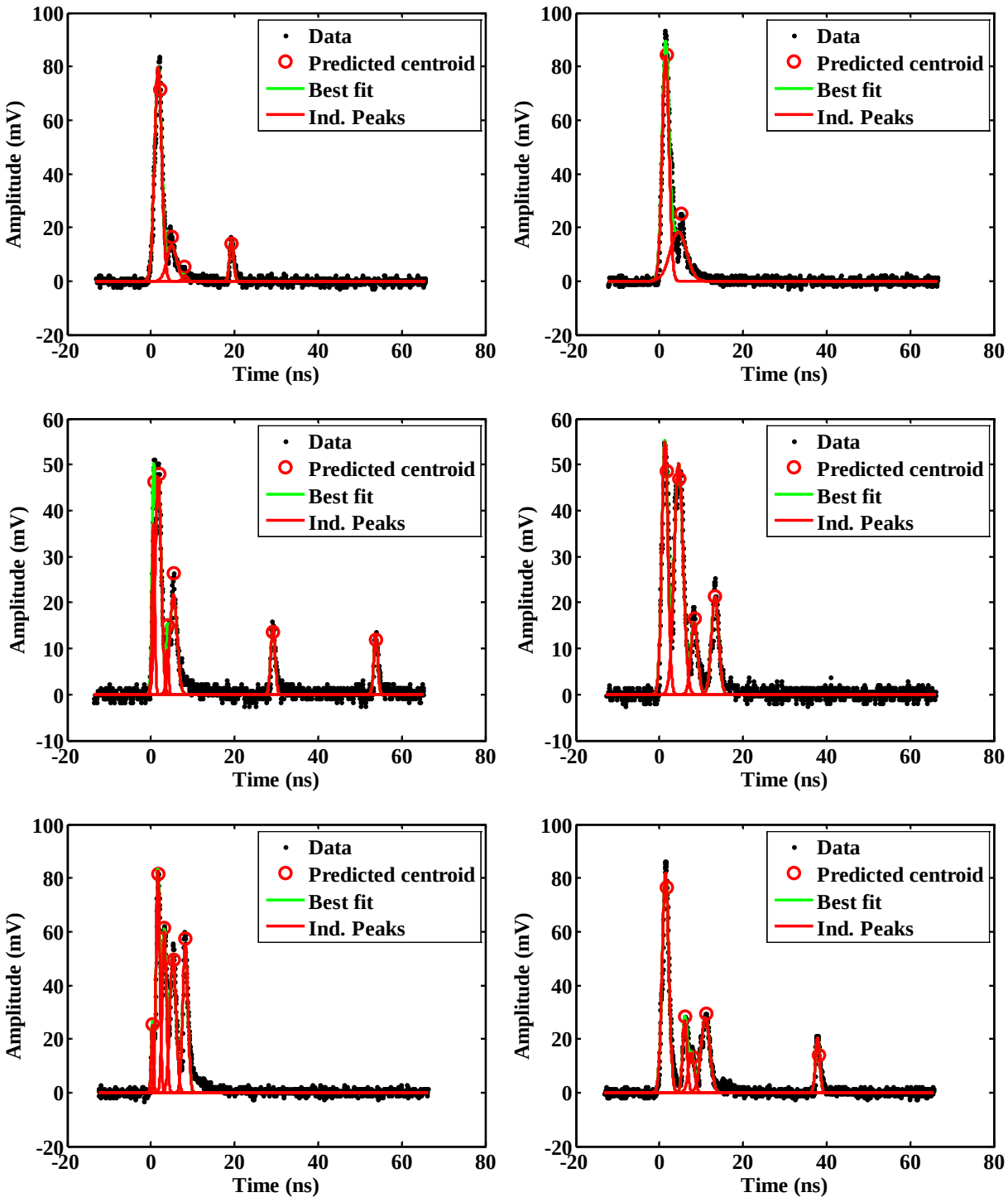

13 Appendix D - Average waveform analysis for a D^+ ion acceleration potential of 50 keV

13.1 Hamamatsu data taken with the Photek PMT240 in coincidence with the 110 degree SBD

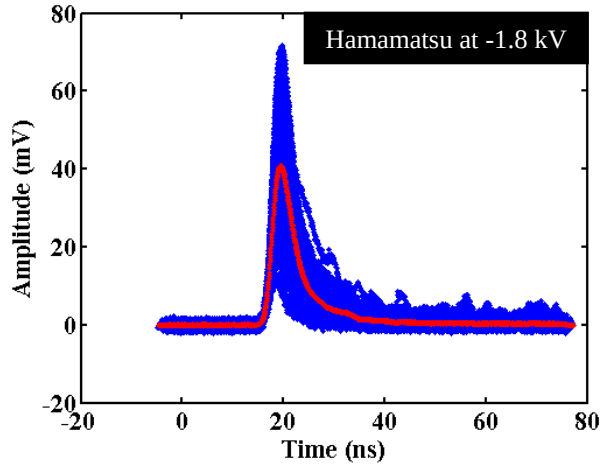

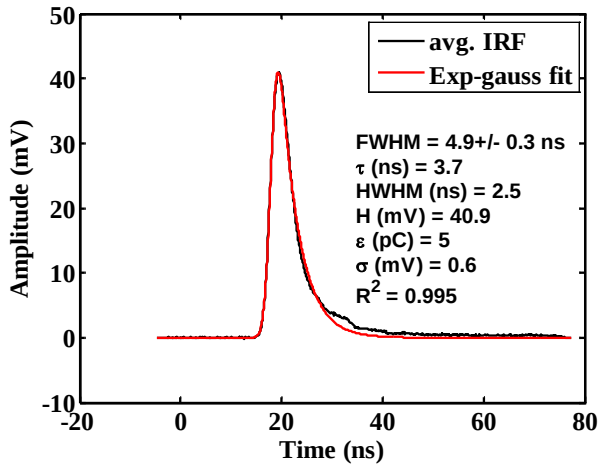

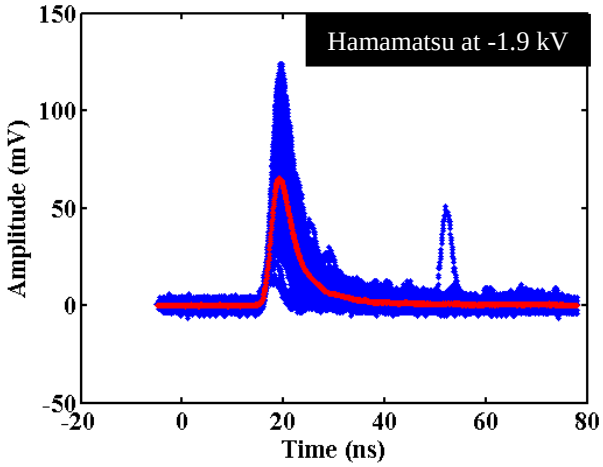

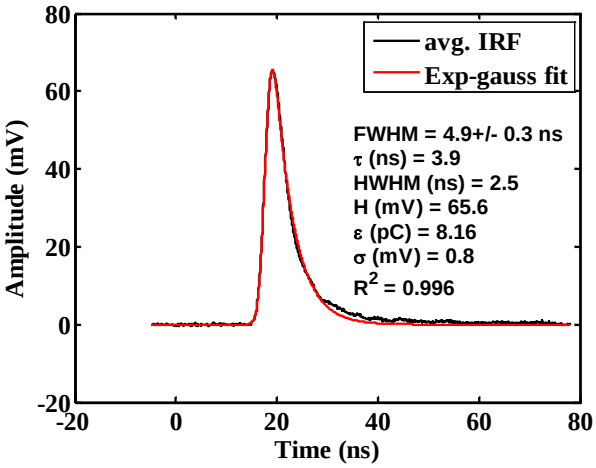

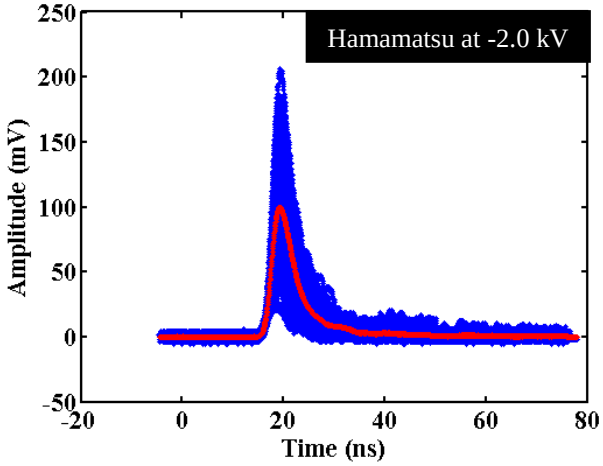

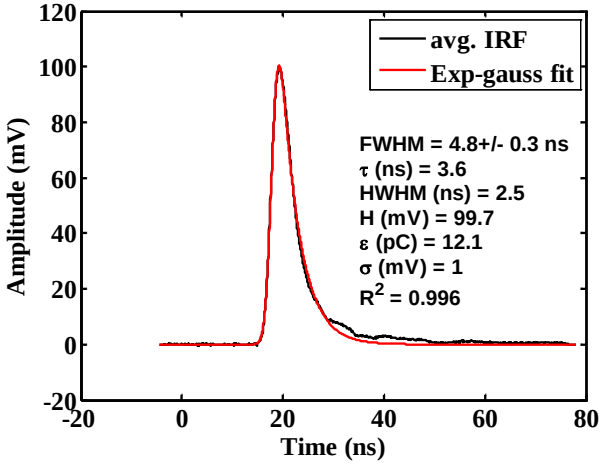

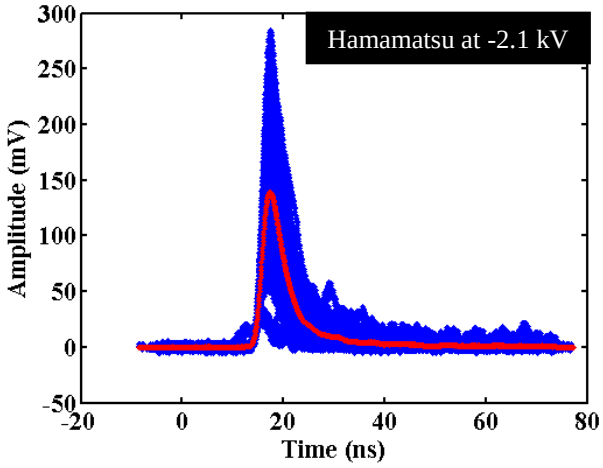

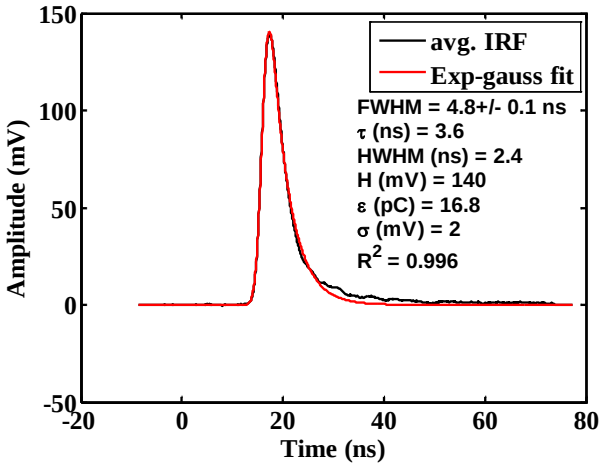

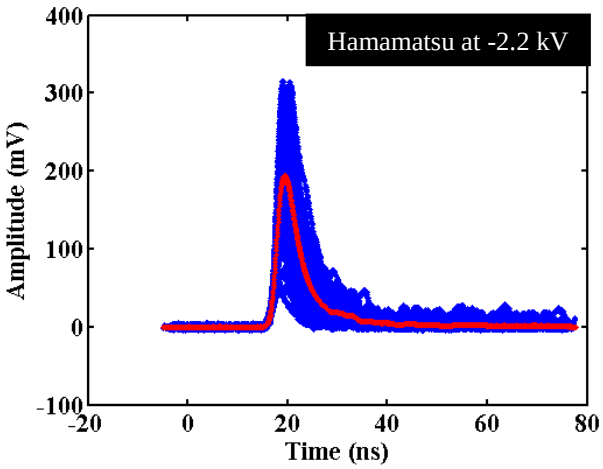

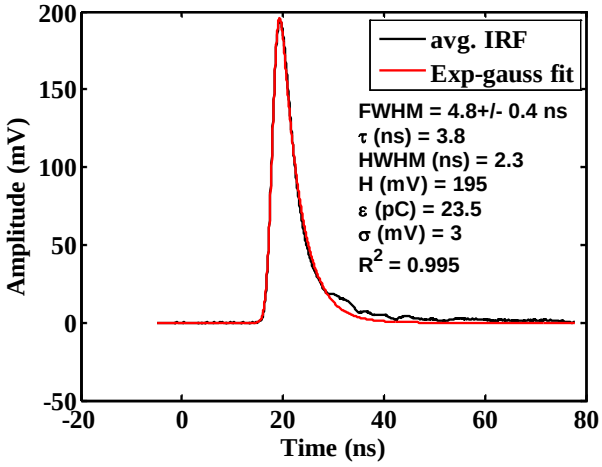

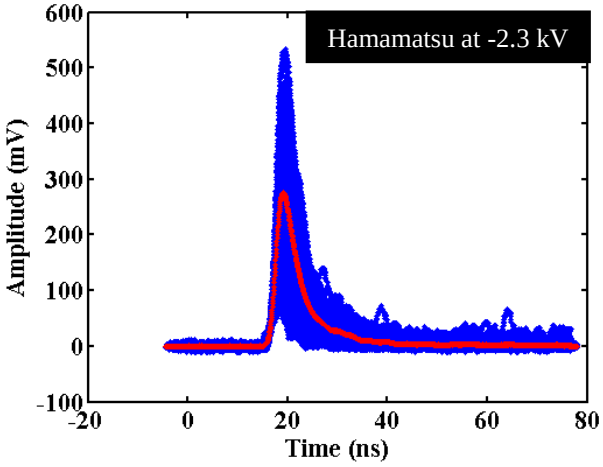

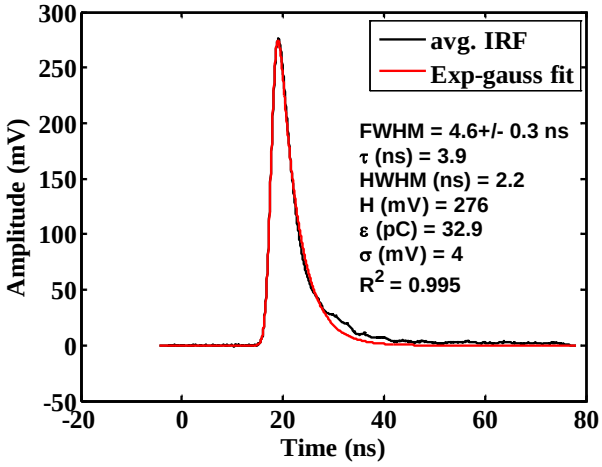

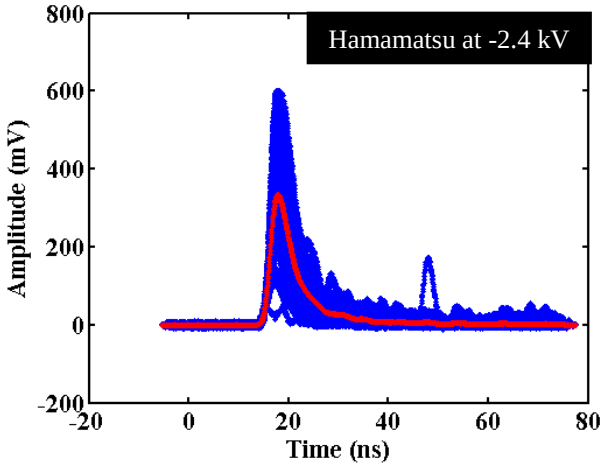

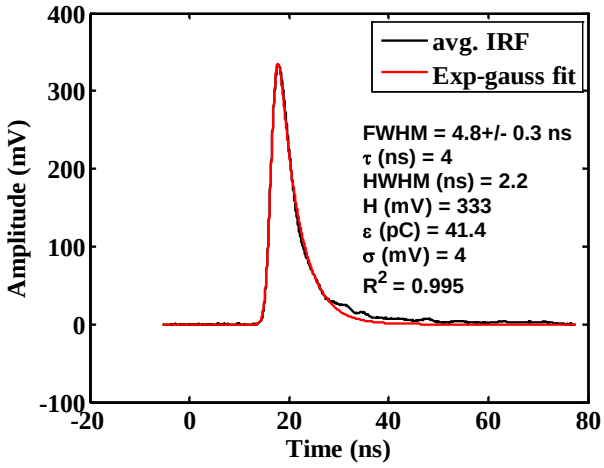

13.2 Data taken with the Hamamatsu mod-5 with the mod-5 in coincidence with the 110 degree SBD

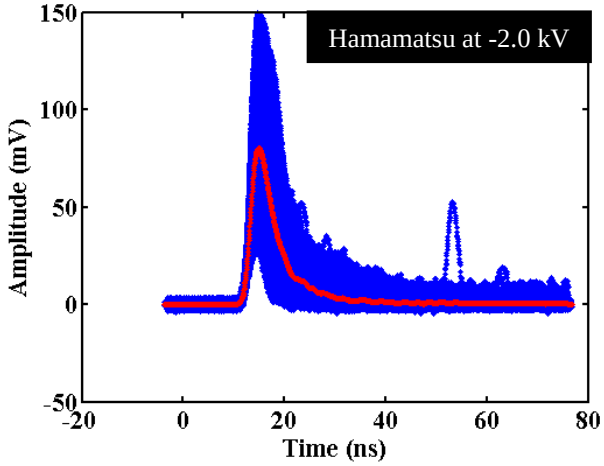

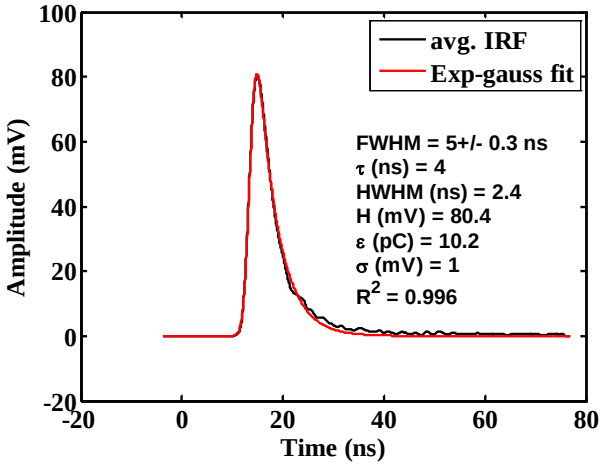

13.3 Data taken with the Photek PMT240 with the Hamamatsu in coincidence with the 100 degree SBD

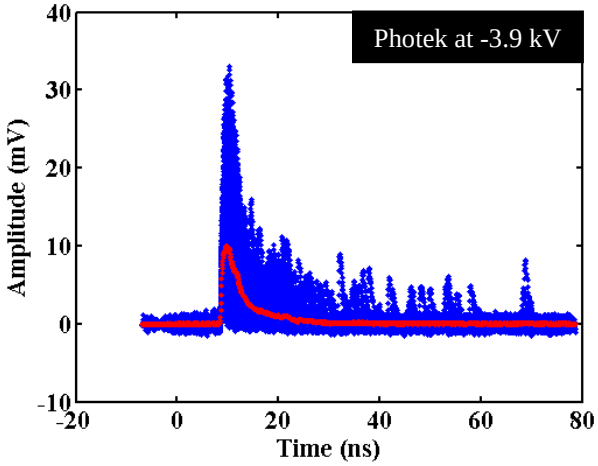

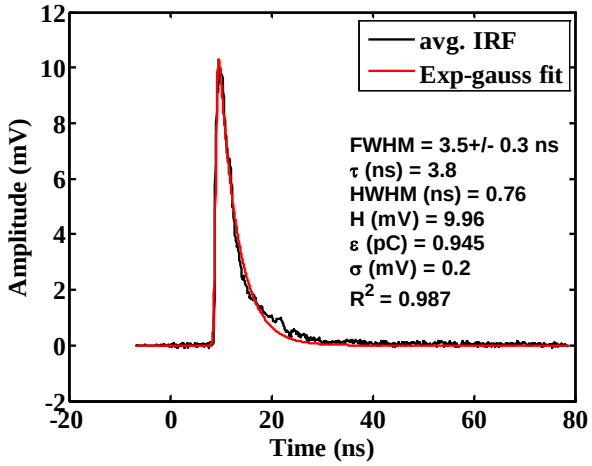

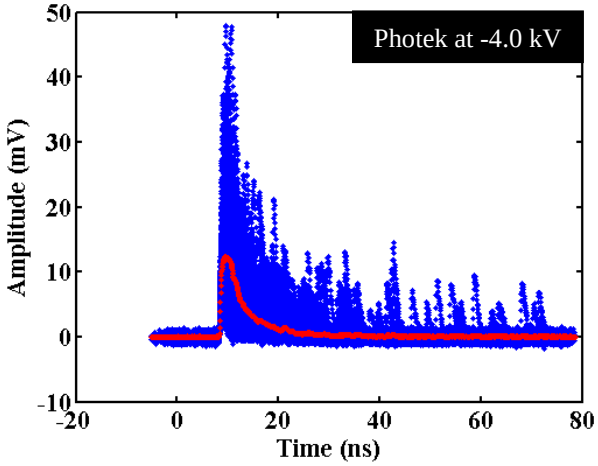

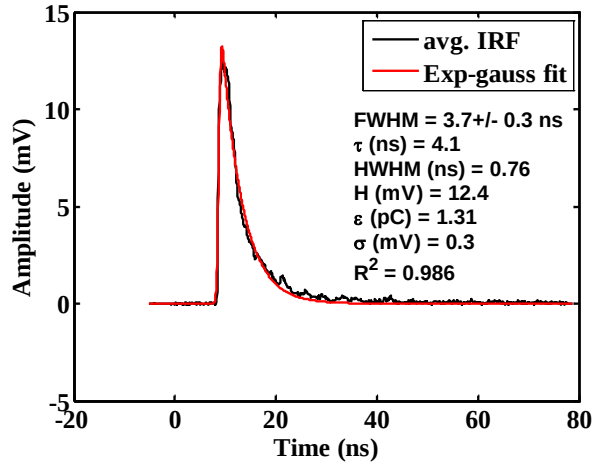

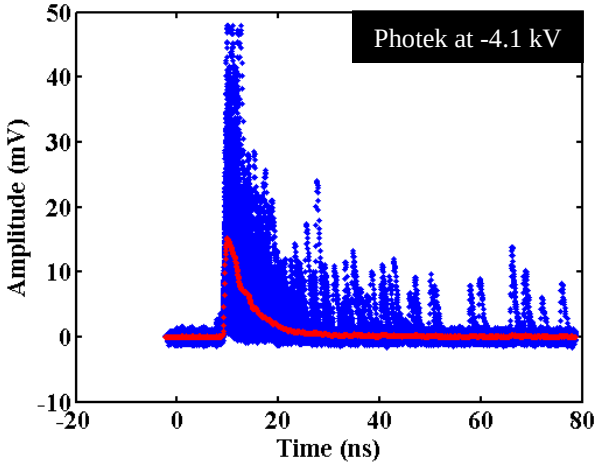

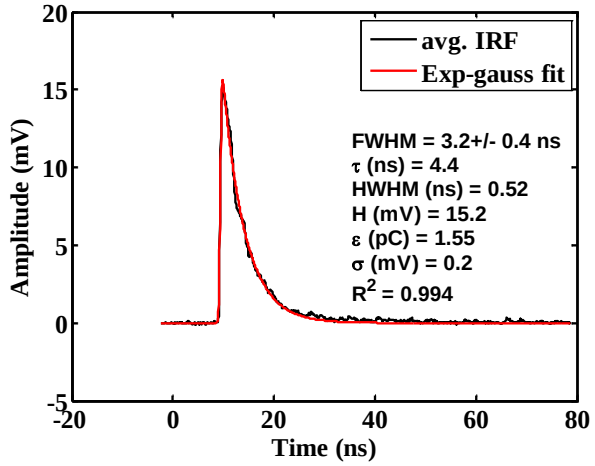

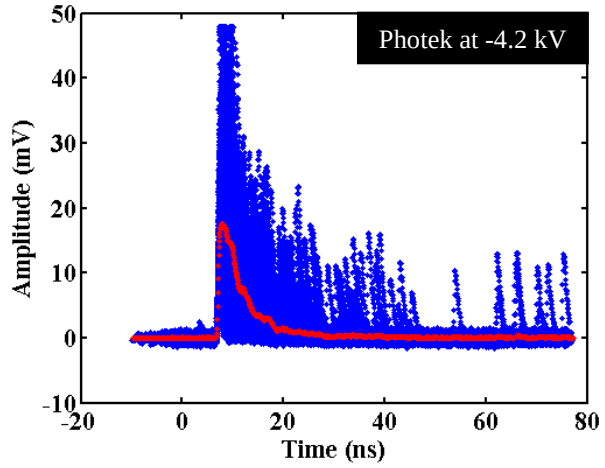

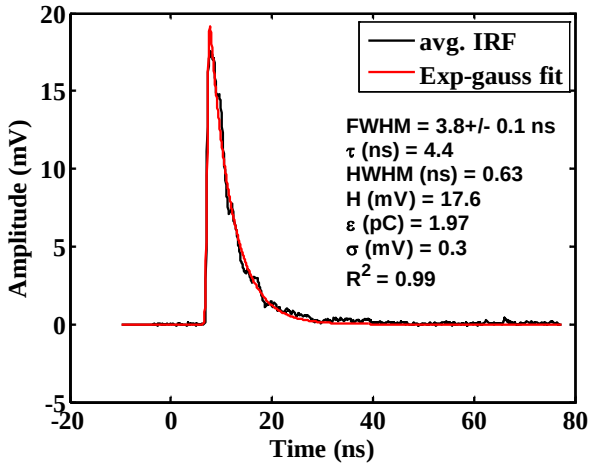

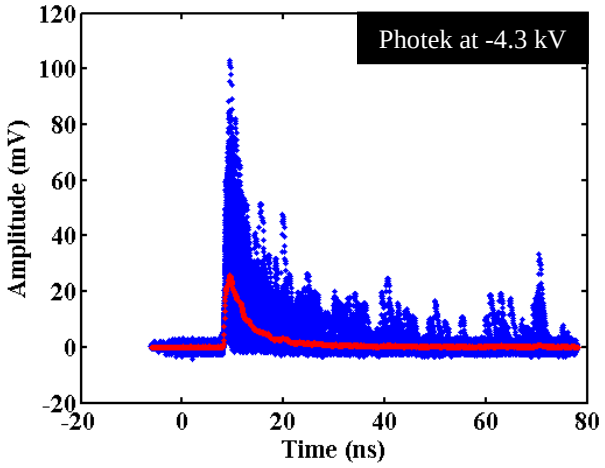

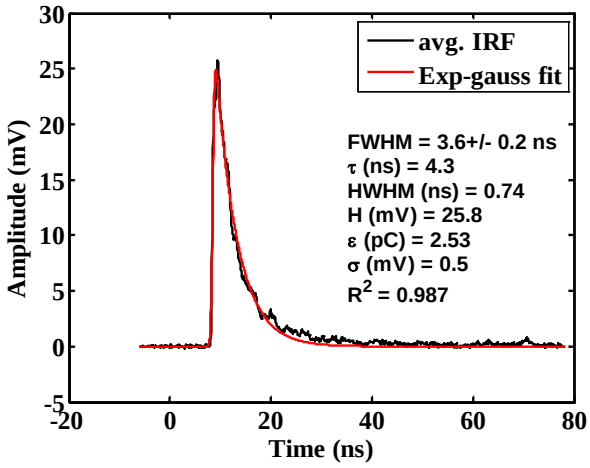

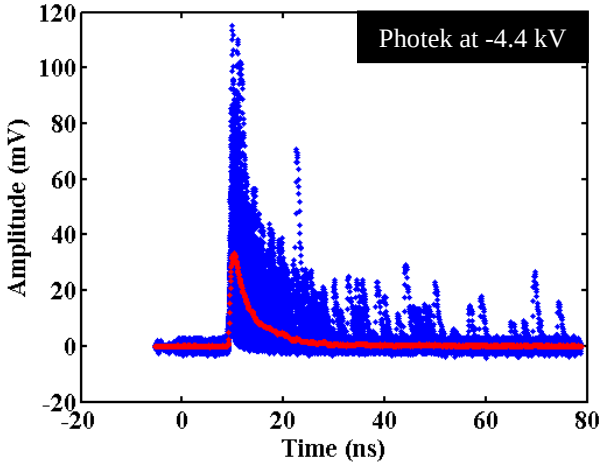

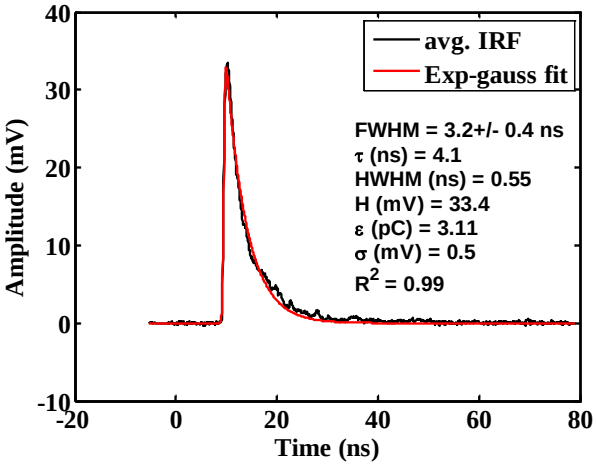

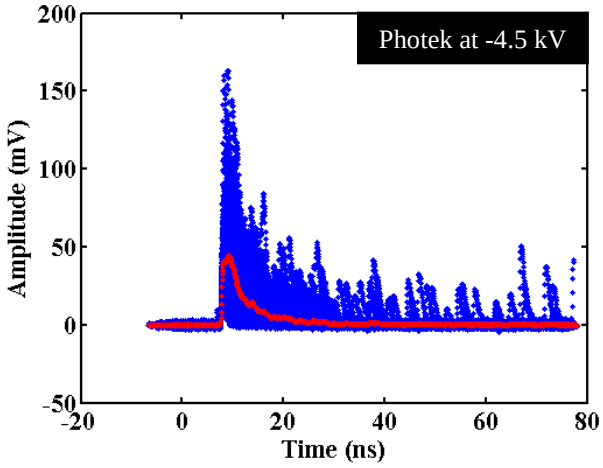

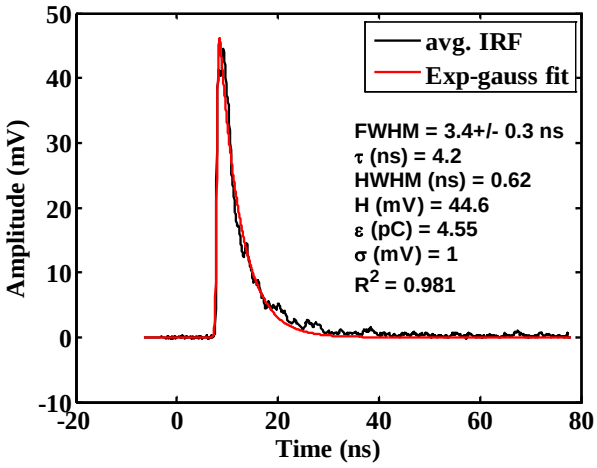

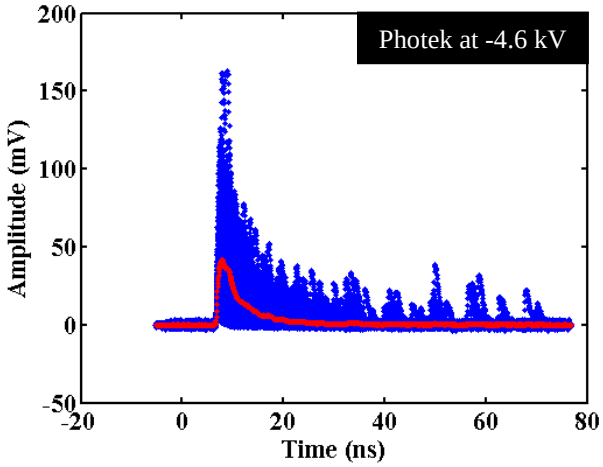

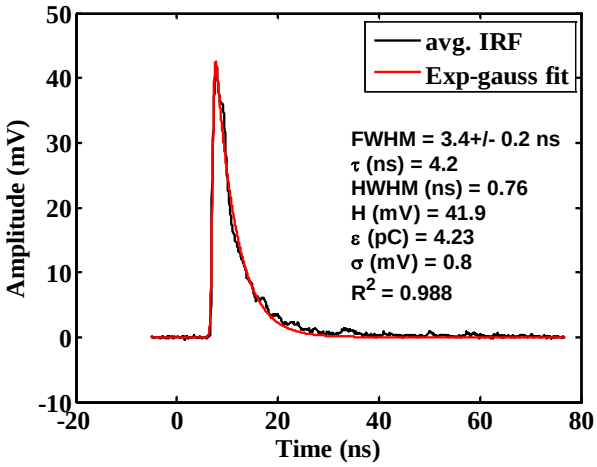

13.4 Data taken with the Photek PMT240 with the PMT240 in coincidence with the 110 degree SBD

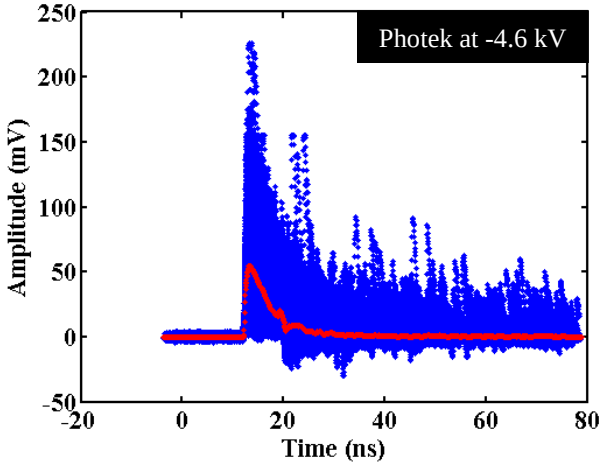

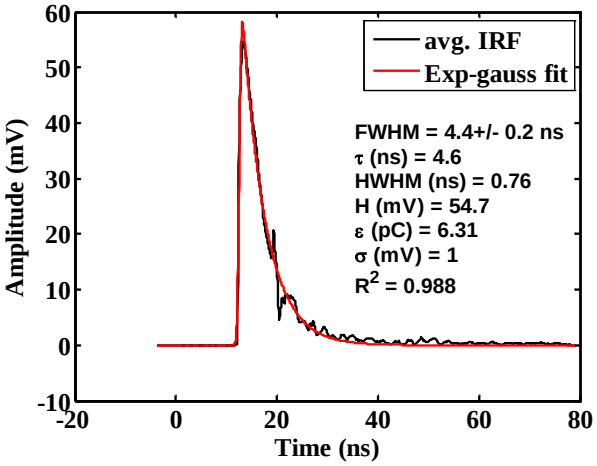

14 Appendix E - Average waveform analysis for a D^+ ion acceleration potential of 175 keV

14.1 Data taken with the Hamamatsu mod-5 with the Photek PMT240 in coincidence with the 110 degree SBD

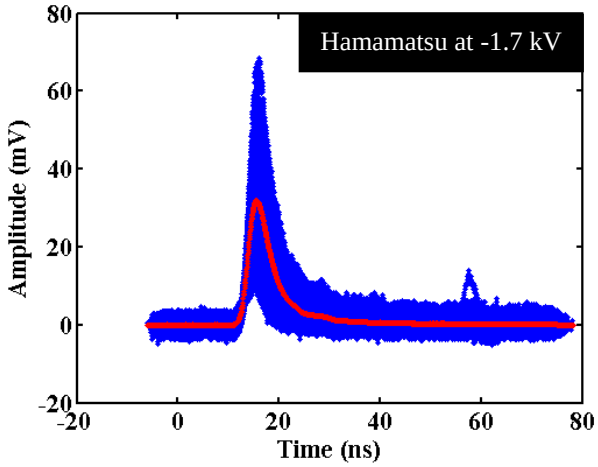

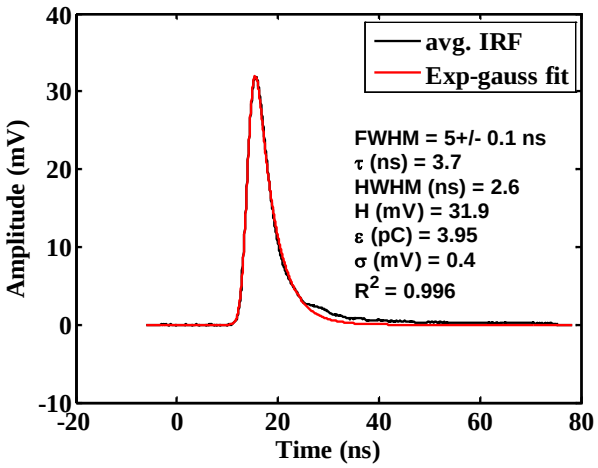

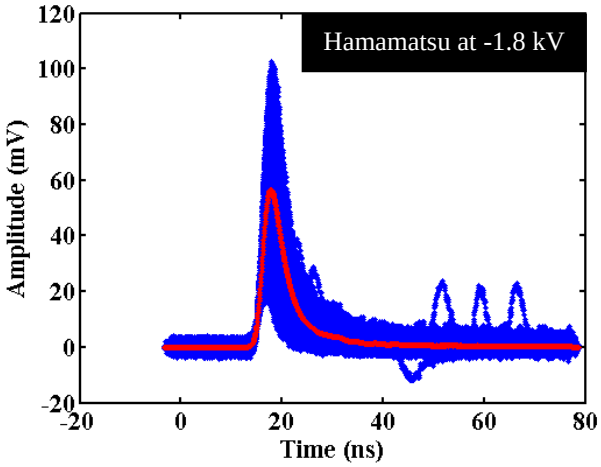

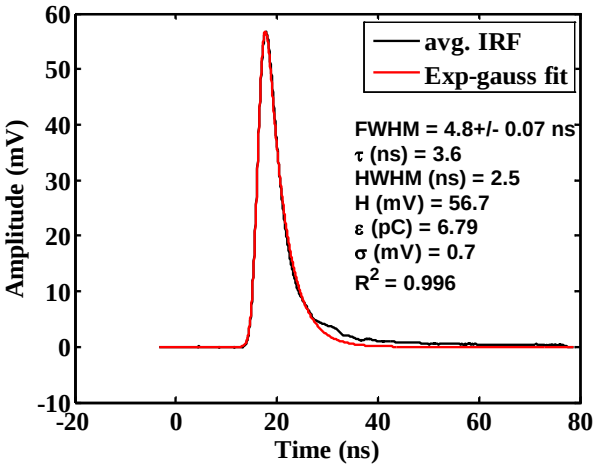

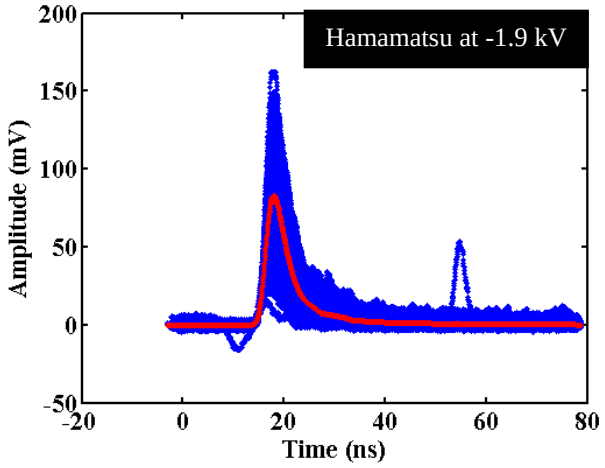

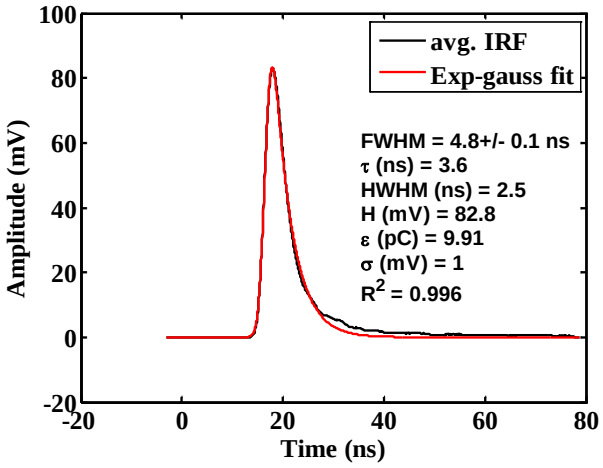

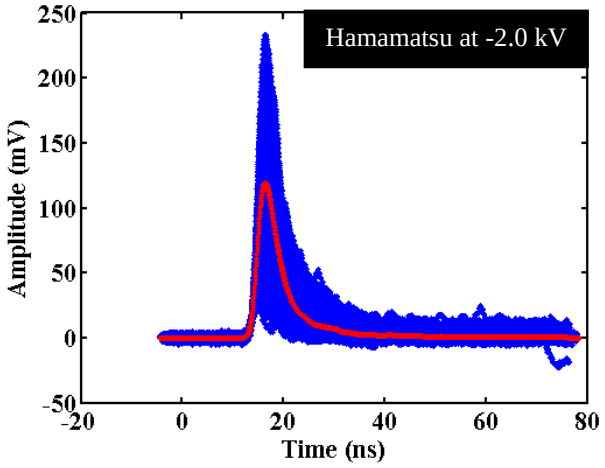

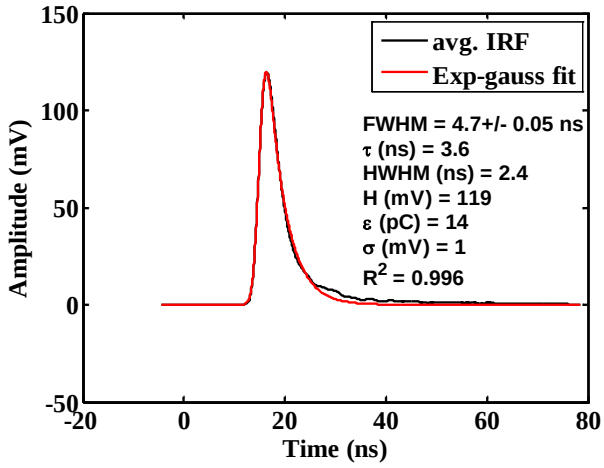

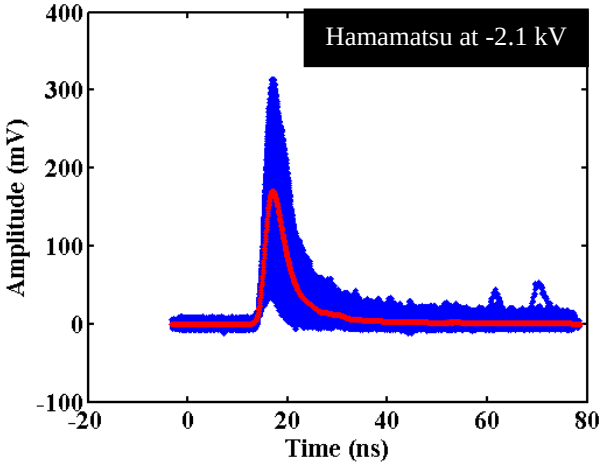

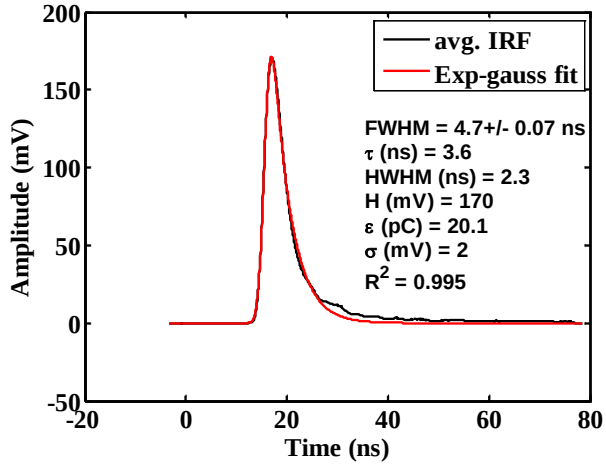

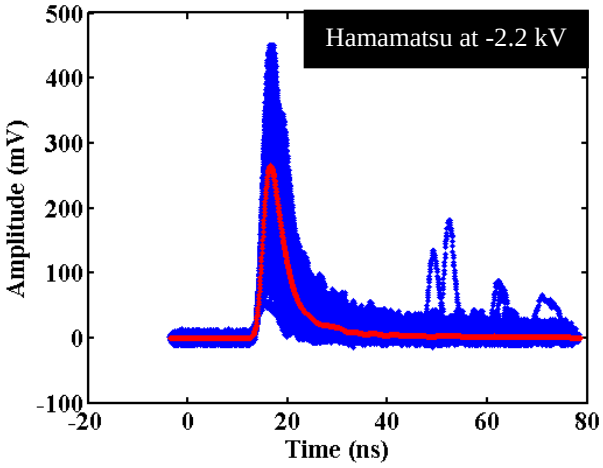

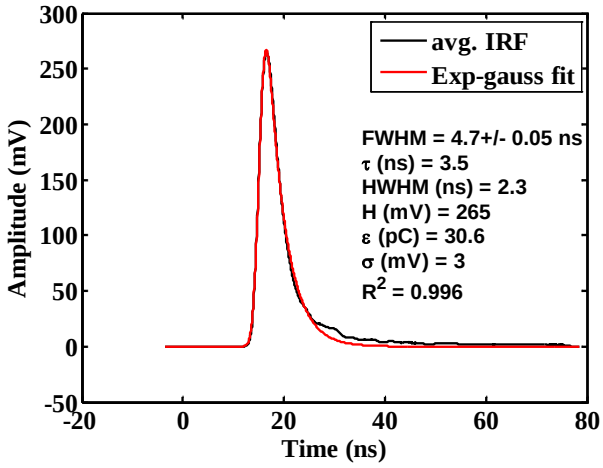

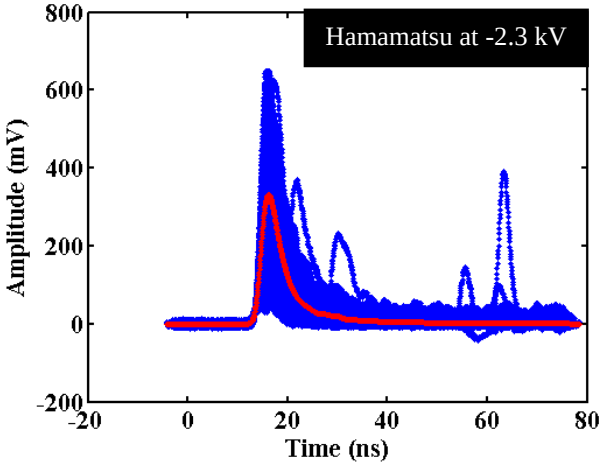

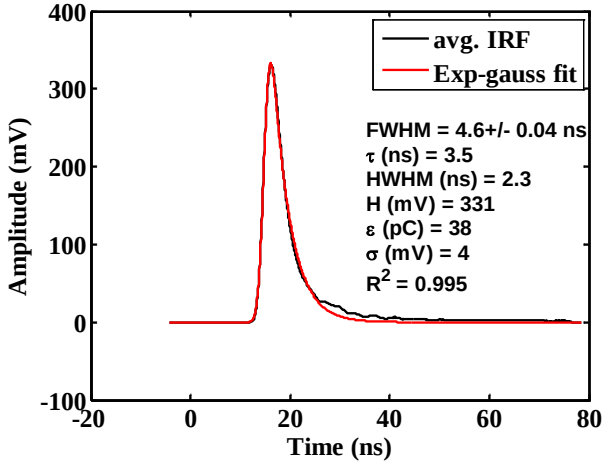

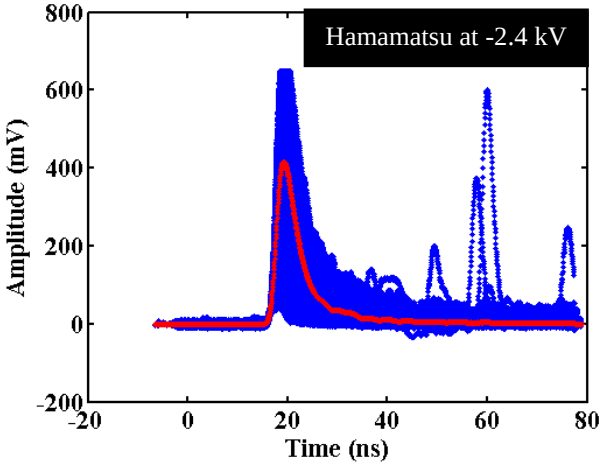

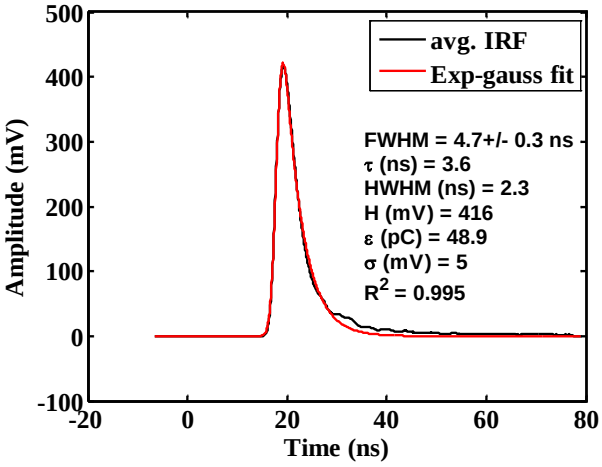

14.2 Data taken with the Hamamatsu mod-5 with the Hamamatsu mod-5 in coincidence with the 110 degree SBD

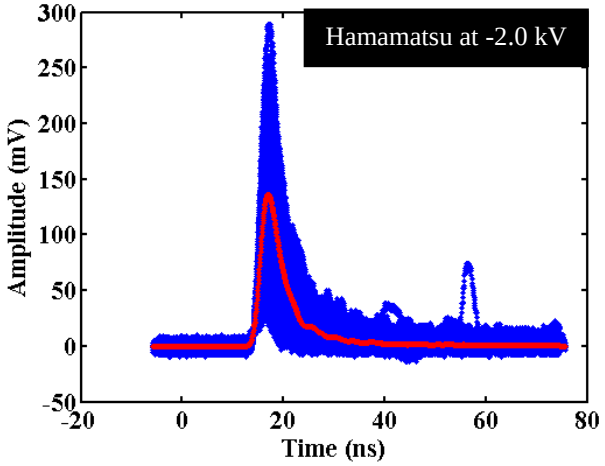

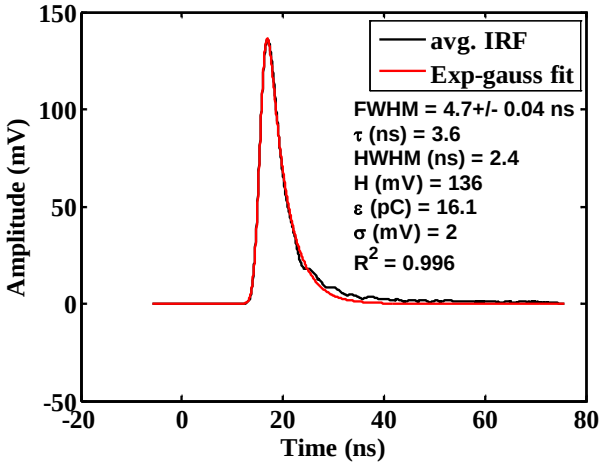

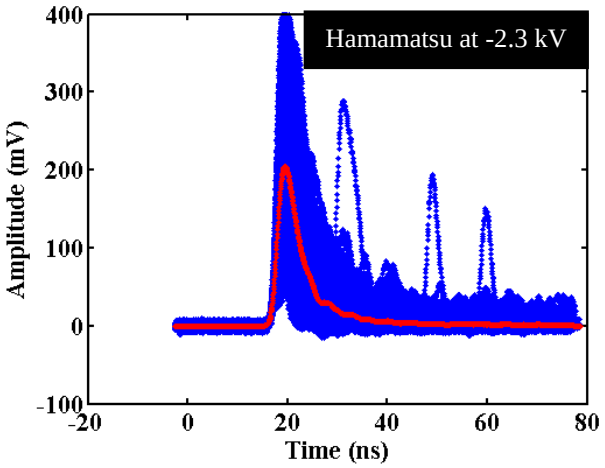

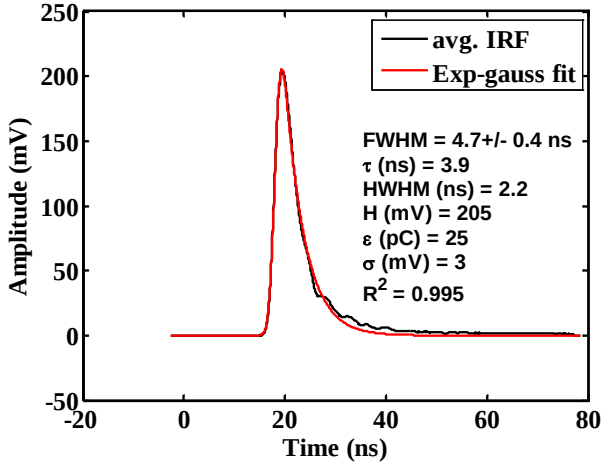

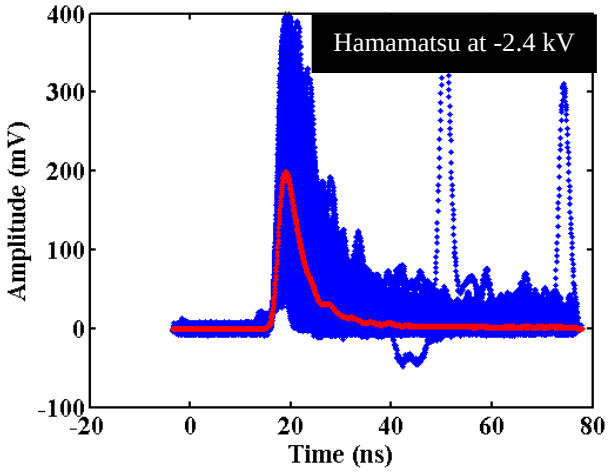

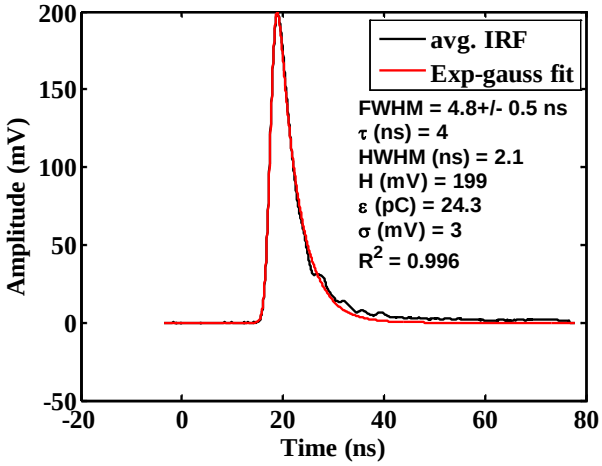

14.3 Data taken with the Photek PMT240 with the Hamamatsu mod-5 in coincidence with the 110-degree SBD

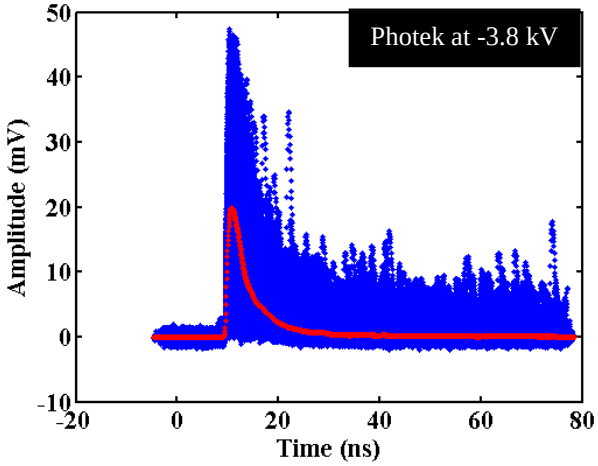

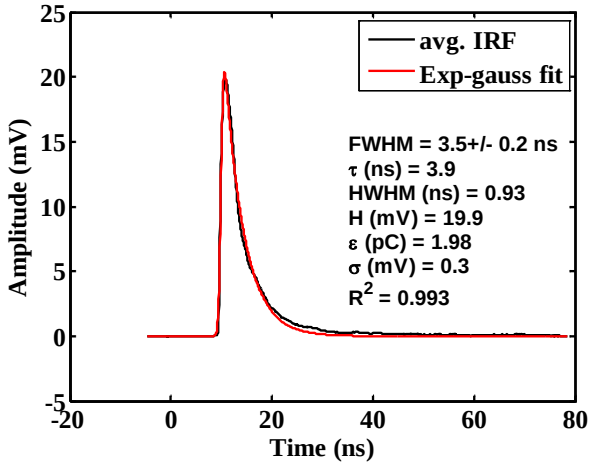

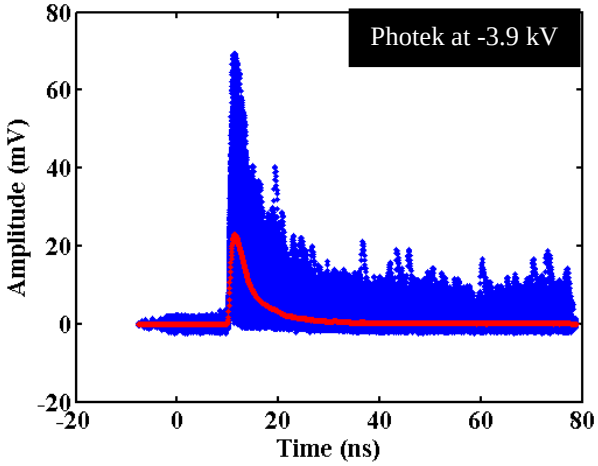

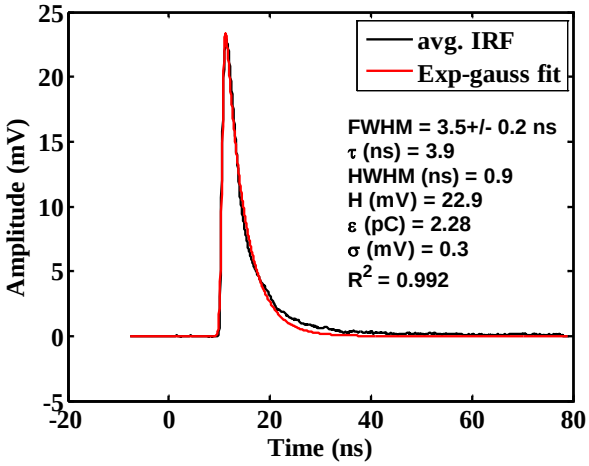

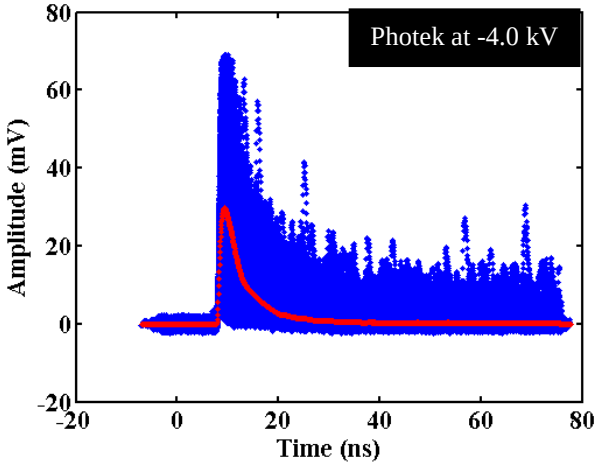

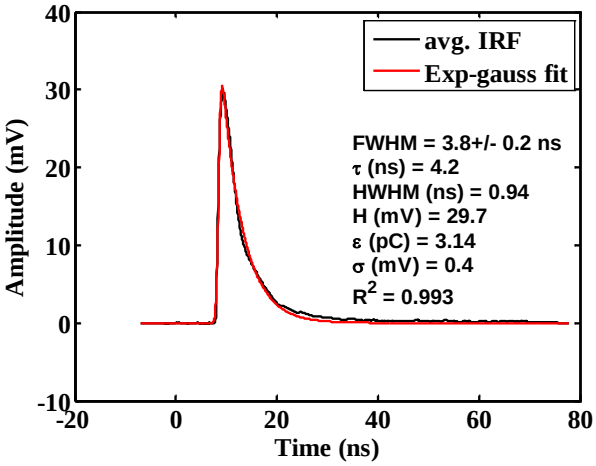

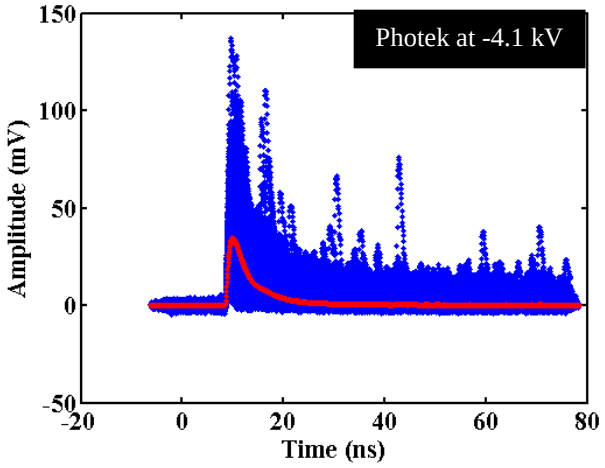

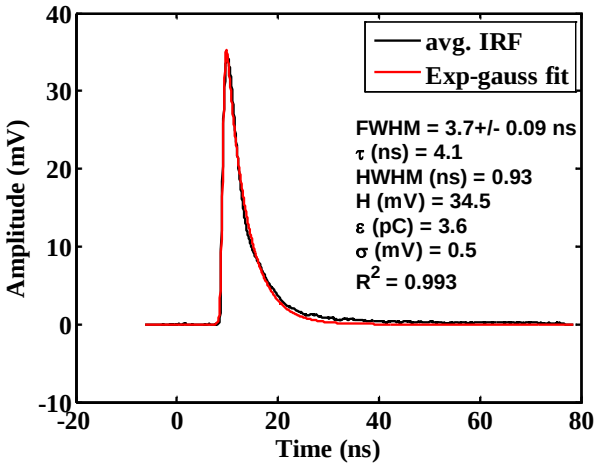

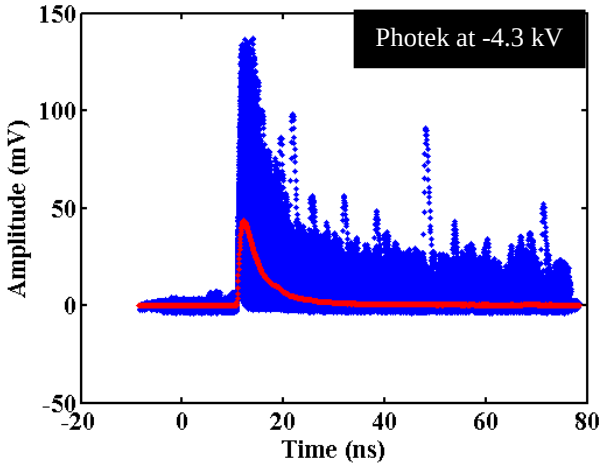

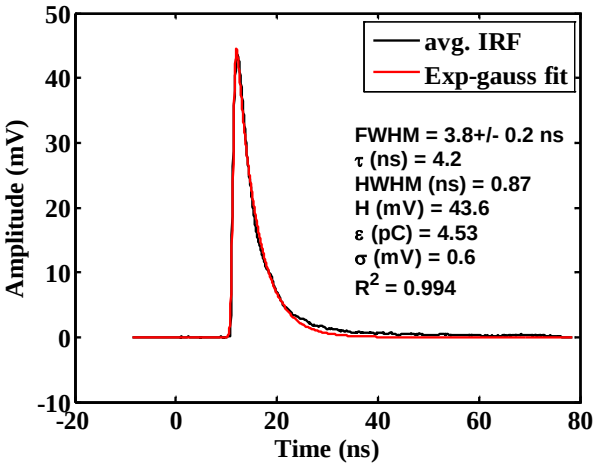

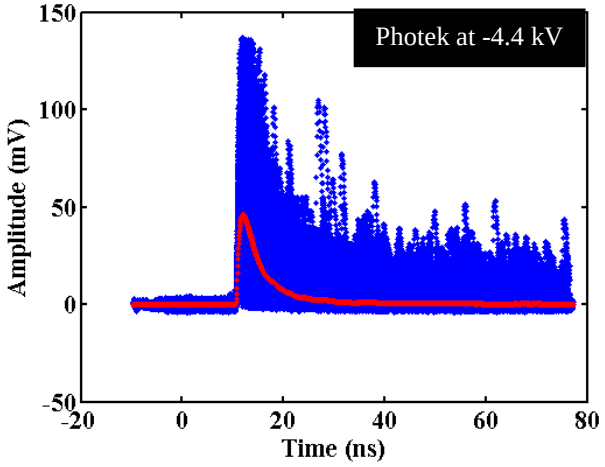

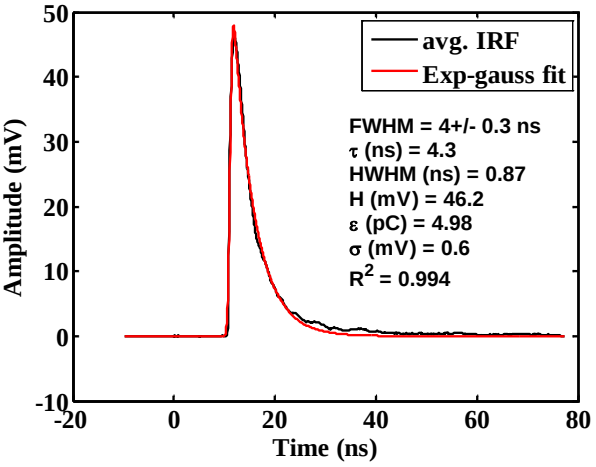

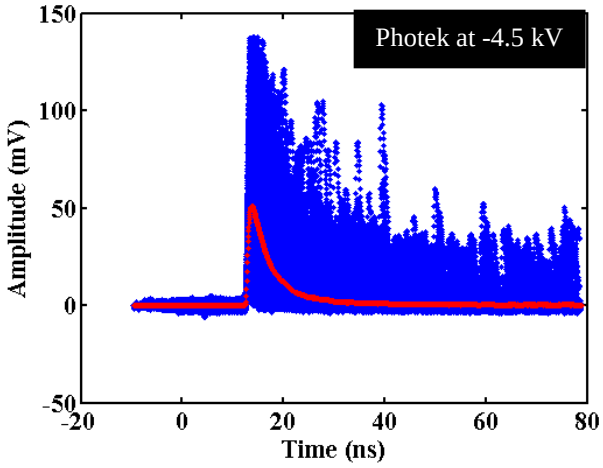

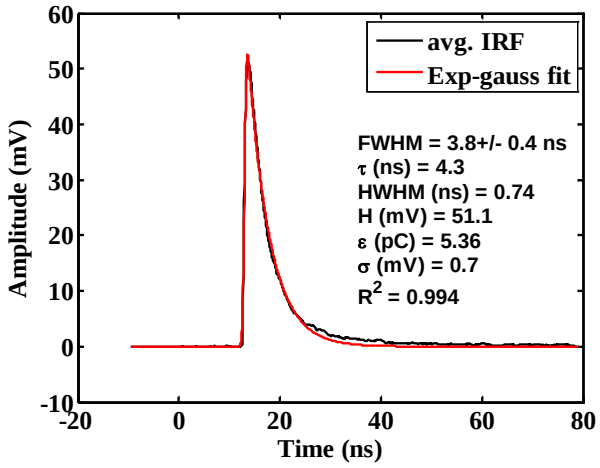

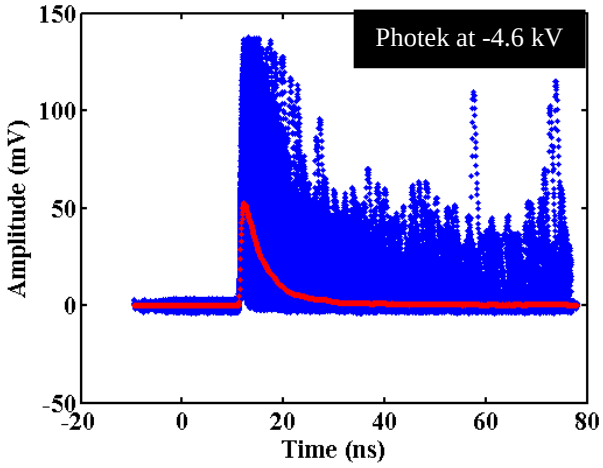

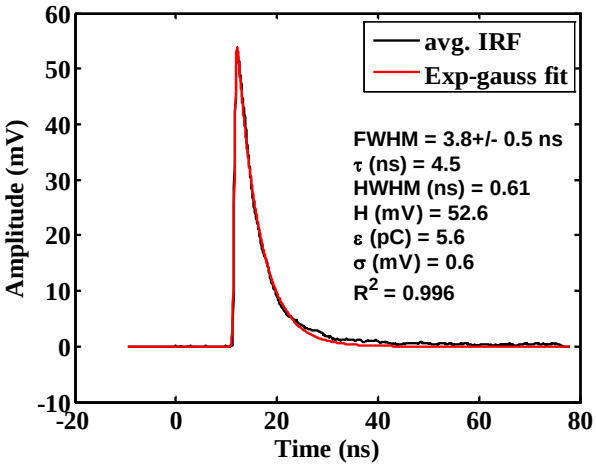

14.4 Data taken with the Photek PMT240 with the Hamamatsu mod-5 in coincidence with the 110-degree SBD

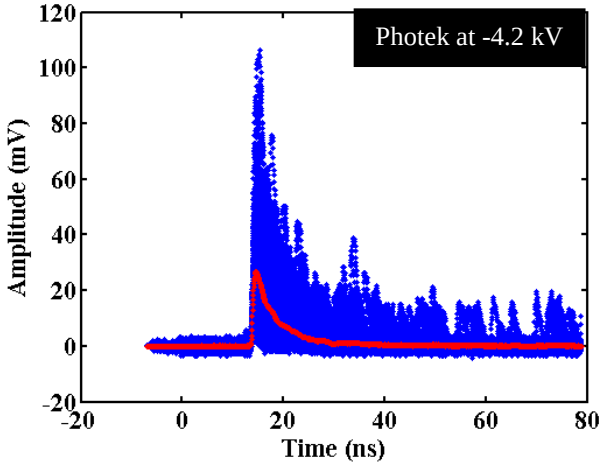

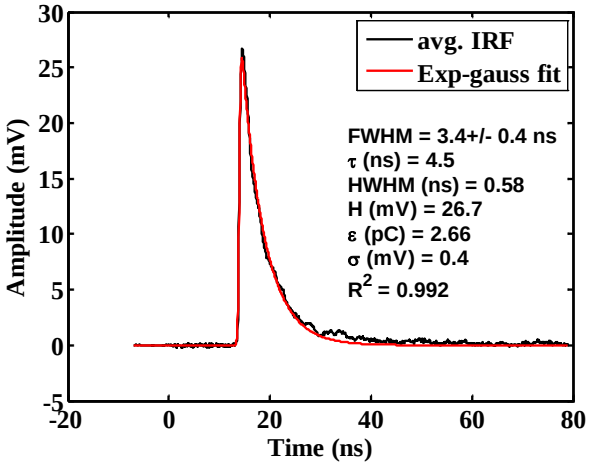

15 Appendix F – Additional Coincidence Data and Throughput Delay Analysis

There are two parameters of interest associated with the coincidence curve: the centroid and the FWHM. The coincidence curve is a measure of the relative time difference of the SBD and NTOF signal and therefore the centroid is the mean difference and the FWHM quantifies the distribution. If the SBD detector is held constant and the NTOF bias is varied, then slight changes are observable in in the mean value of the coincidence peak. Thus, this mean value is a relative measure of the PMT throughput delay as a function of applied voltage. This relationship is shown in Figure 64 for the data acquired with the LMR-600 cable and the RG-223 cable at two different delays. This figure shows that the throughput delay is constant regardless of the cabling used in the data acquisition scheme. The coincidence data used to generate these data are presented in the following sections.

The FWHM observed for the coincidence data does vary as a function of the cabling. The RG223 cabling is a standard 50-ohm cable with a propagation velocity of 0.66c whereas the LMR600 cabling has a propagation velocity of 0.87c. This change in velocities can be observed in the FWHM of the coincidence signal, where the ratio of the FWHM values were equivalent to the ratio of the propagation velocities. This should be the case assuming the particles of interest, the alpha and neutron, arrive at the prospective detectors at the same time.

15.1 Throughput delay comparison of the LMR-600 and RG-223 cabling

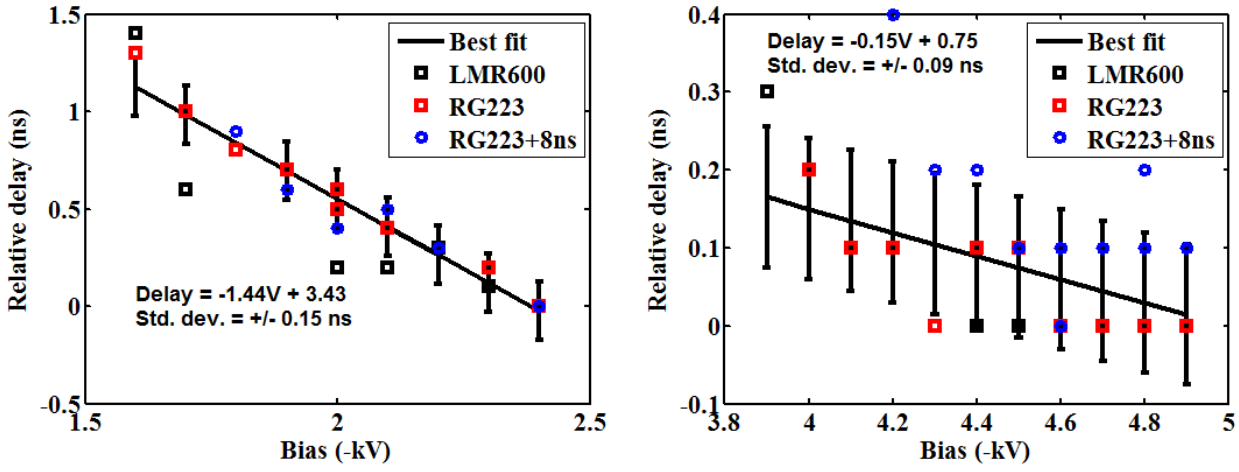

Figure 64 Throughput delays inferred from the data collected with the LMR-600 cable and the RG-223 cable at two different delays. Hamamatsu mod-5 delay shown on the left, Photek PMT240 delay shown on the right.

15.2 Coincidence curves acquired with the RG-223 cabling

15.2.1 Data acquired for the Hamamatsu mod-5 in coincidence with the 110-degree SBD with a 46 ns delay

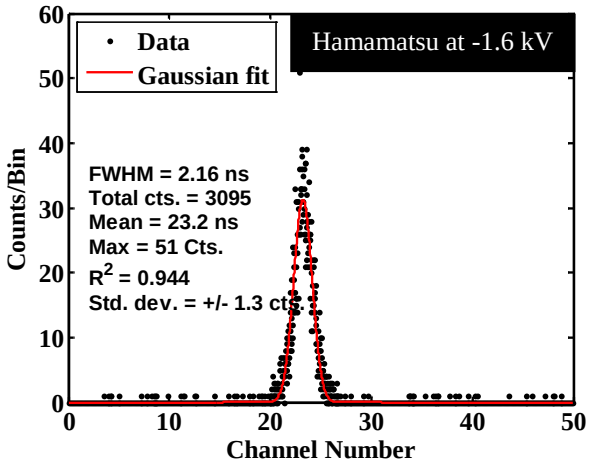

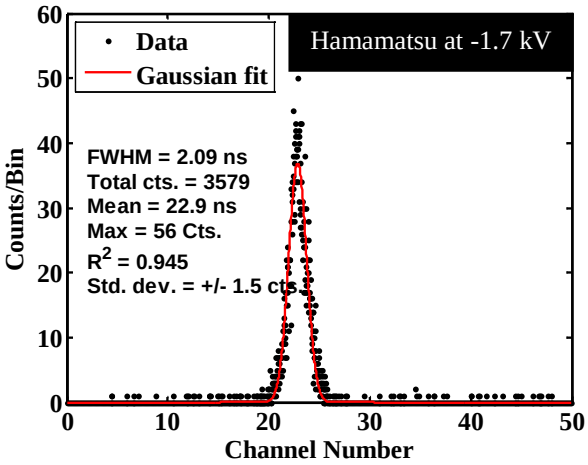

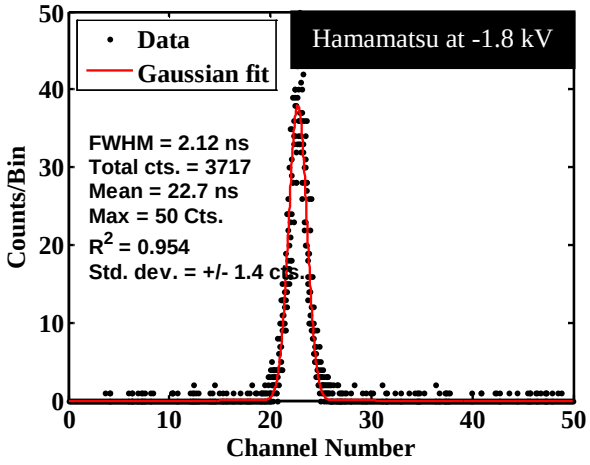

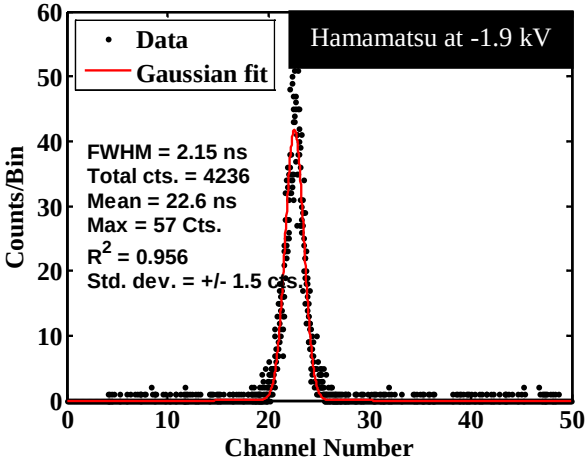

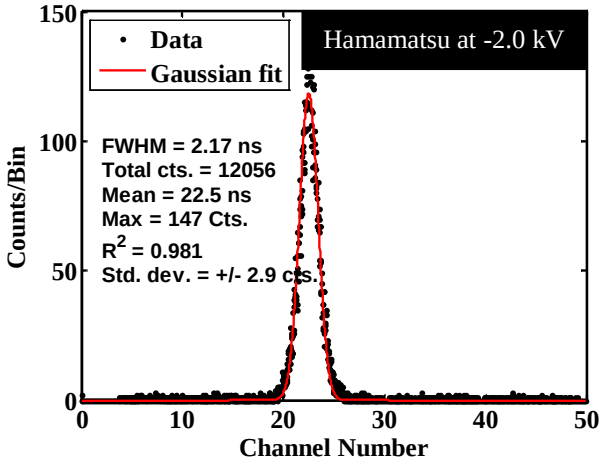

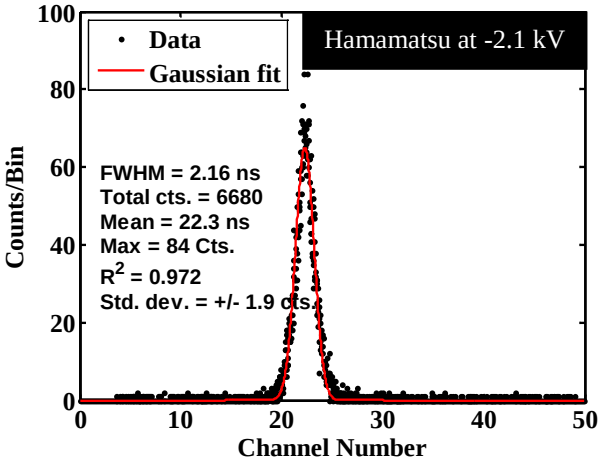

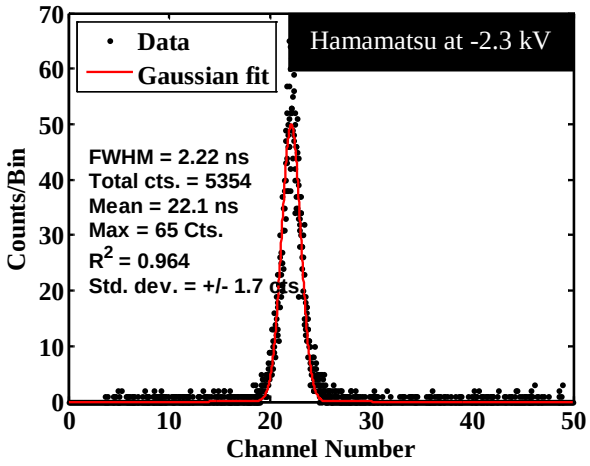

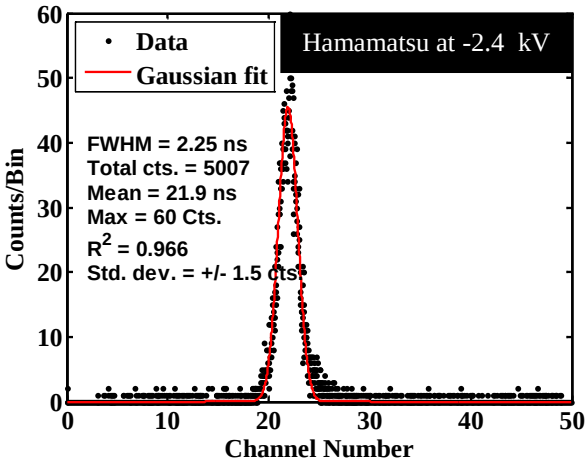

15.2.2 Data acquired for the Hamamatsu mod-5 in coincidence with the 110-degree SBD with a 54 ns delay

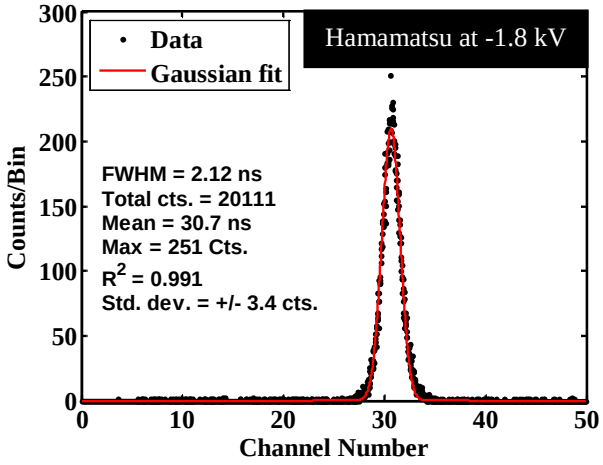

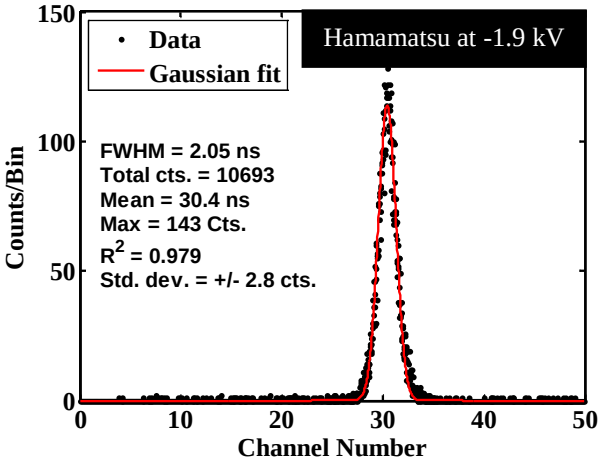

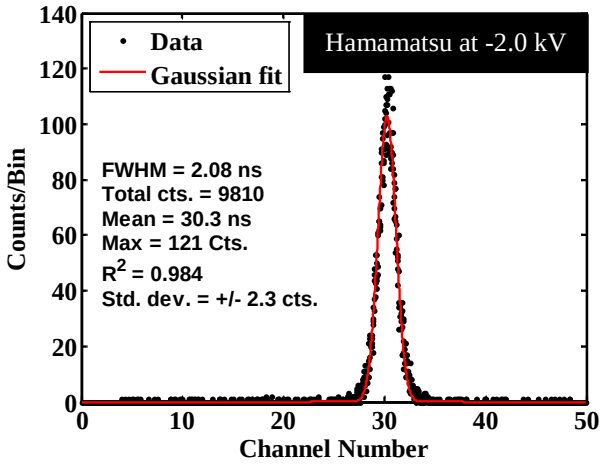

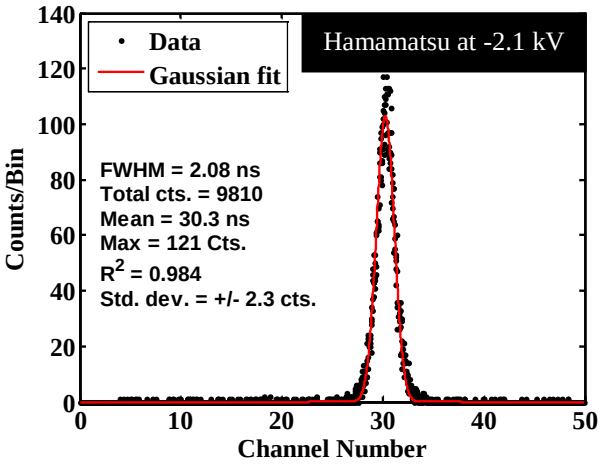

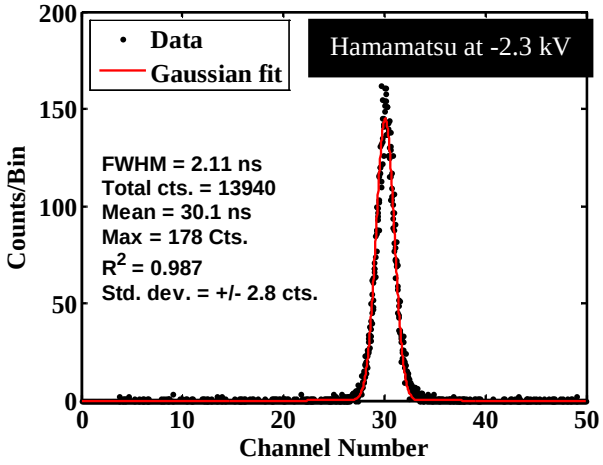

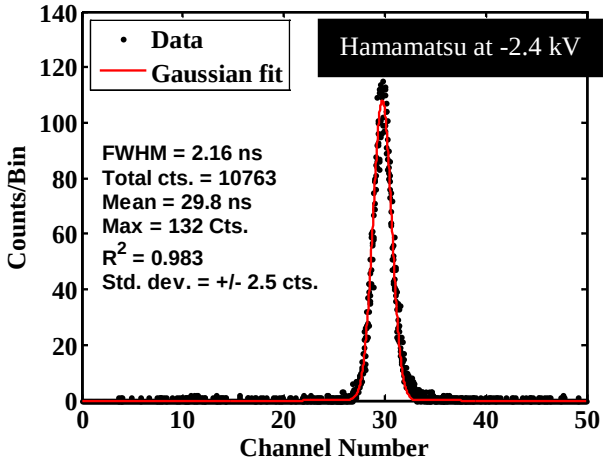

15.2.3 Data acquired for the Photek PMT240 in coincidence with the 110-degree SBD with a 55 ns delay

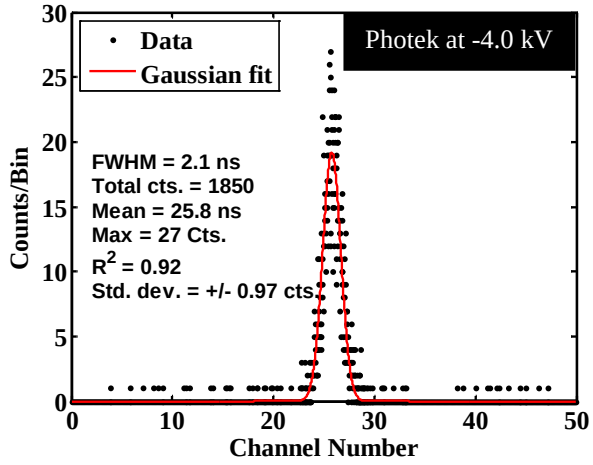

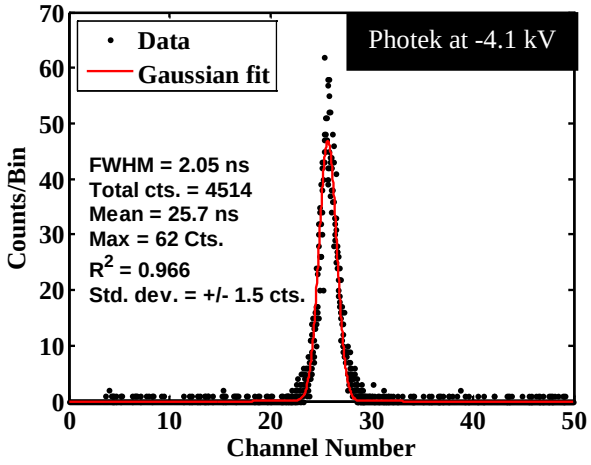

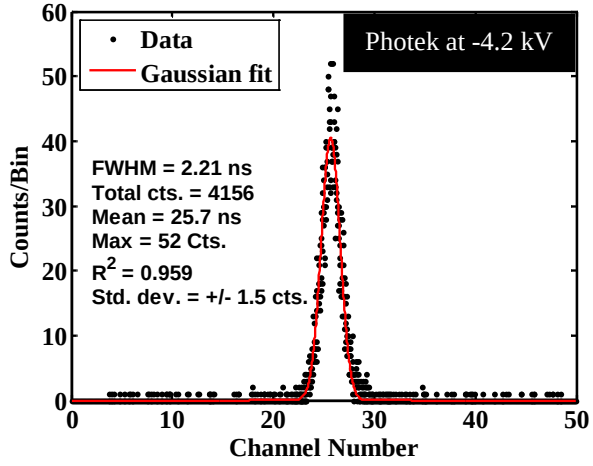

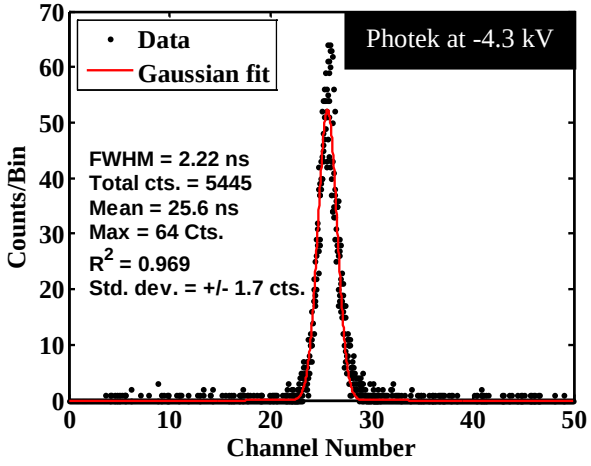

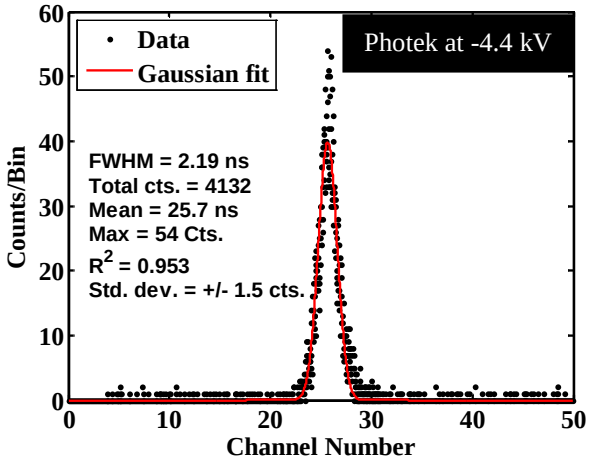

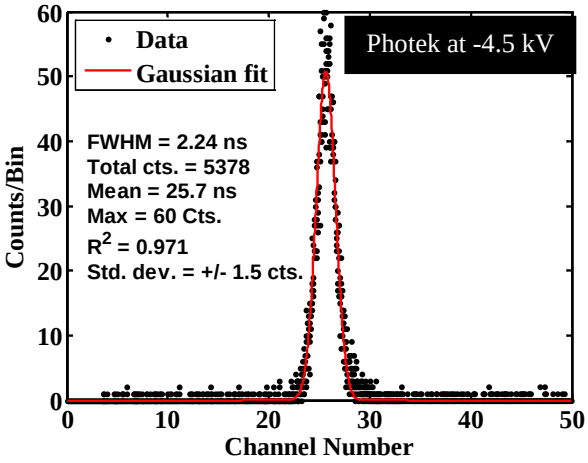

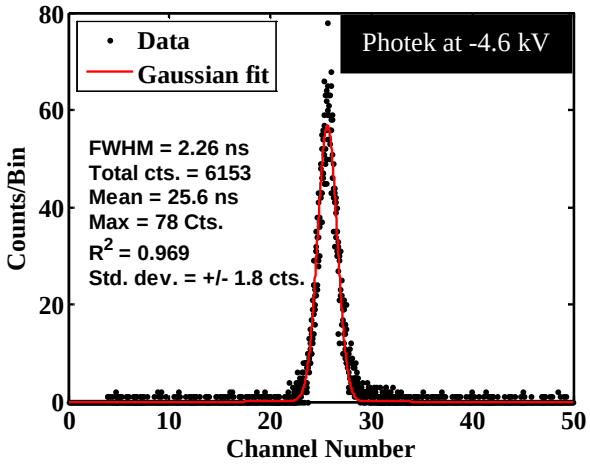

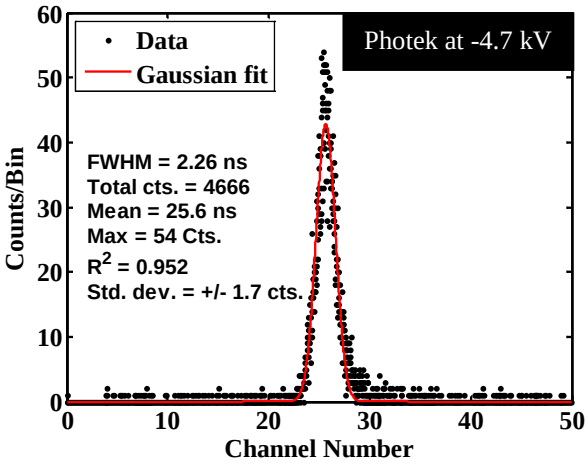

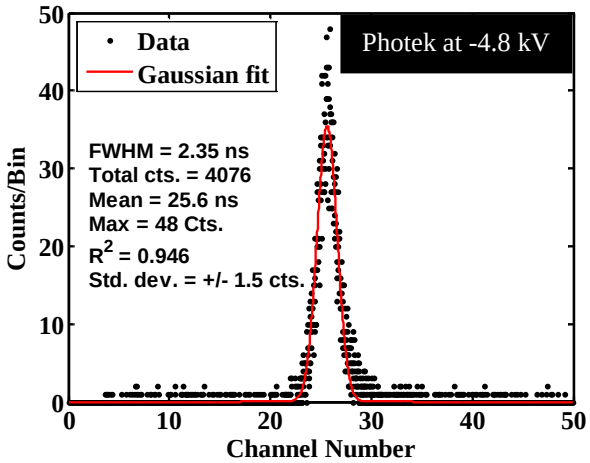

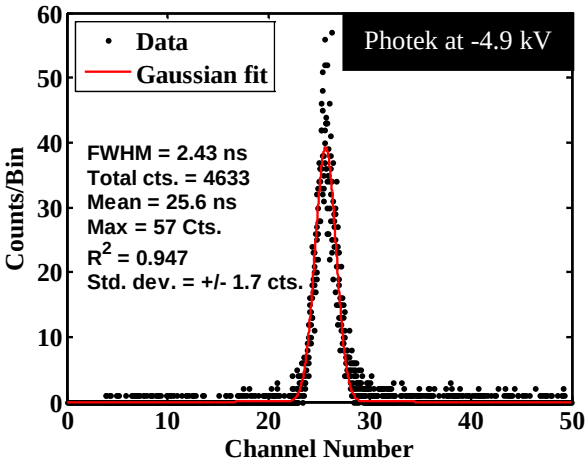

15.2.4 Data acquired for the Photek PMT240 in coincidence with the 110-degree SBD with a 63 ns delay

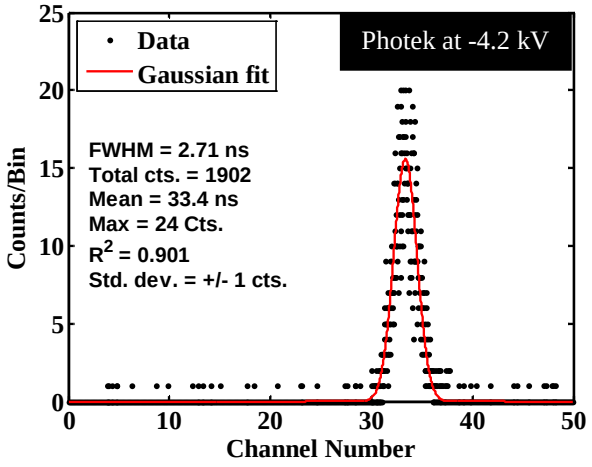

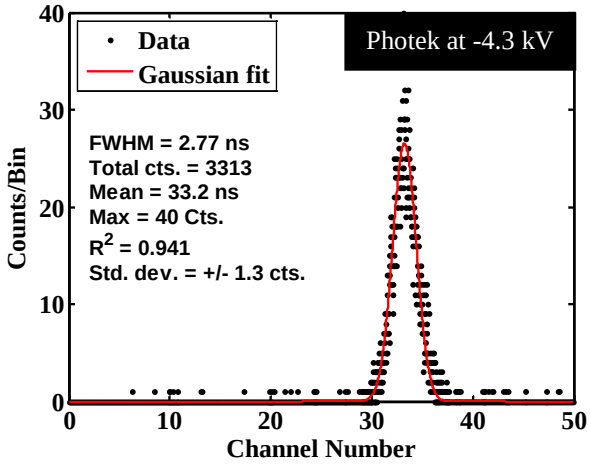

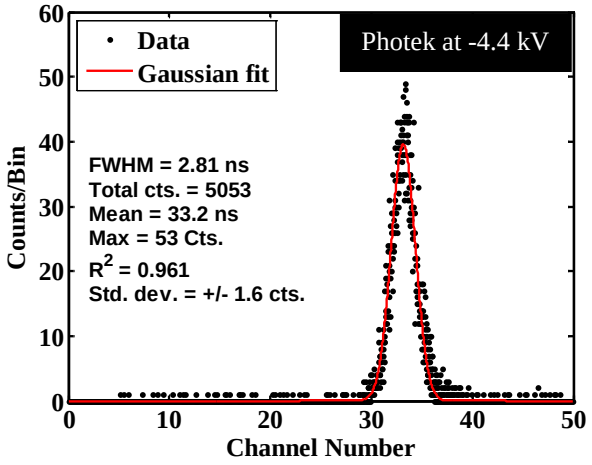

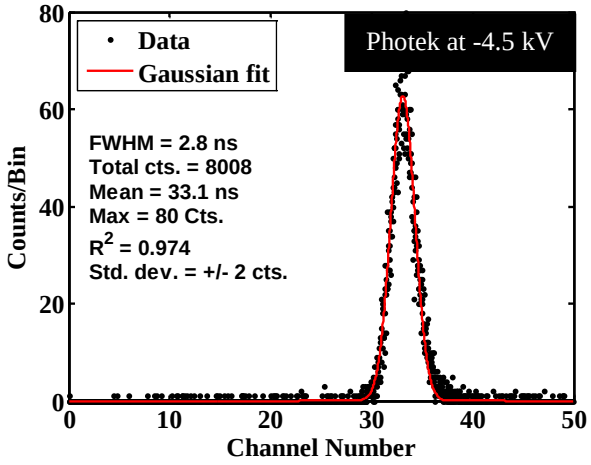

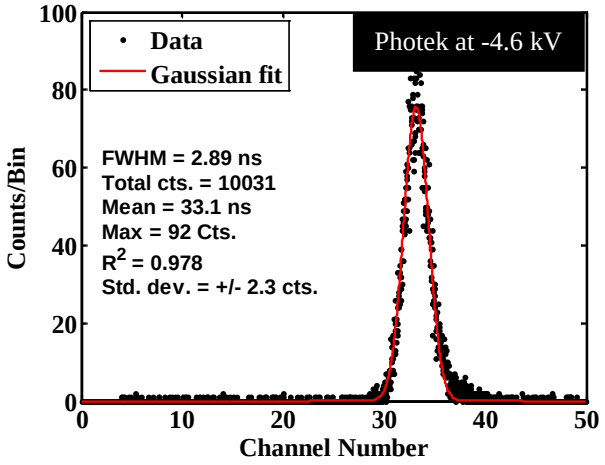

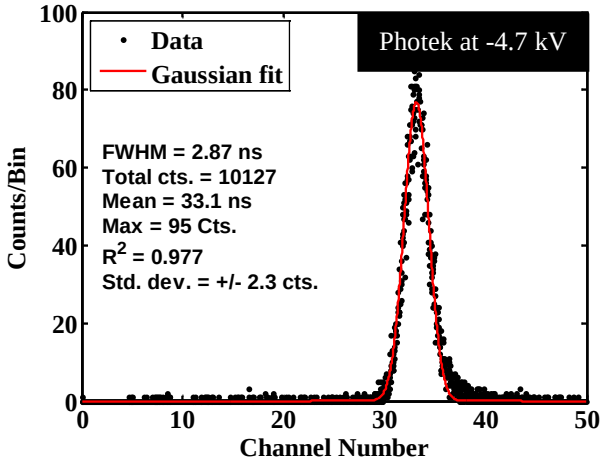

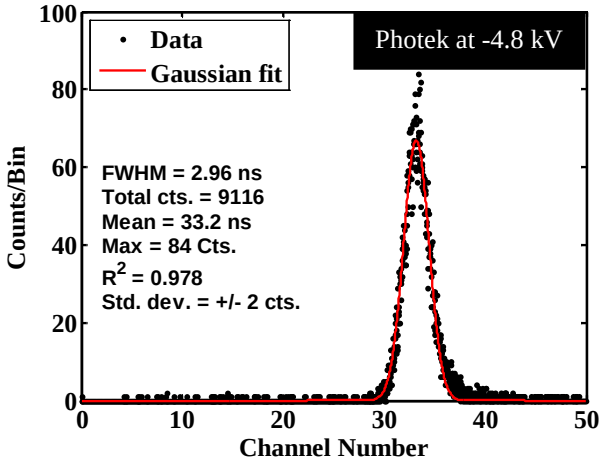

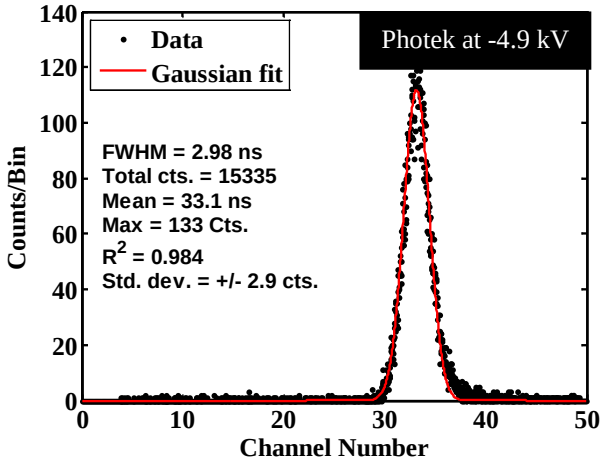

15.3 Coincidence curves acquired with the LMR-600 cabling at a D^+ ion acceleration potential of 175-keV

15.3.1 Data acquired for the Hamamatsu mod-5 in coincidence with the 110-degree SBD with a 54 ns delay

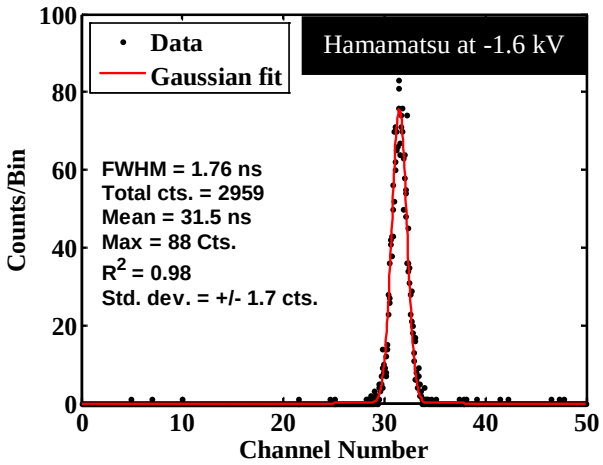

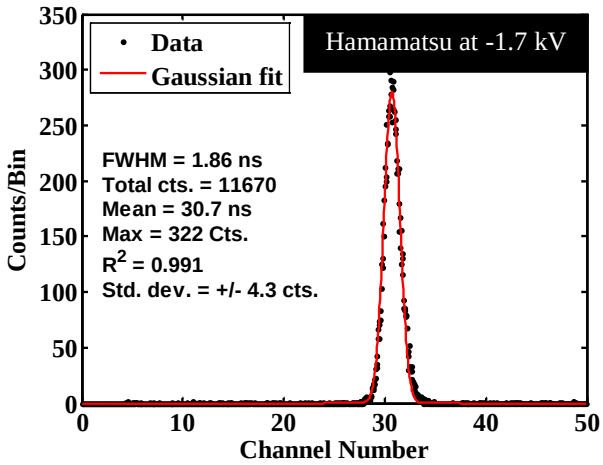

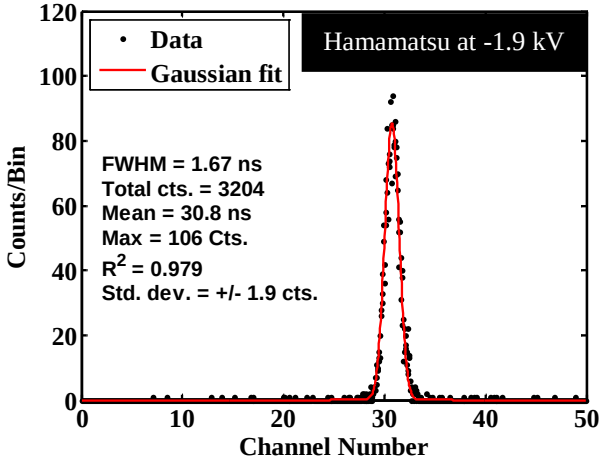

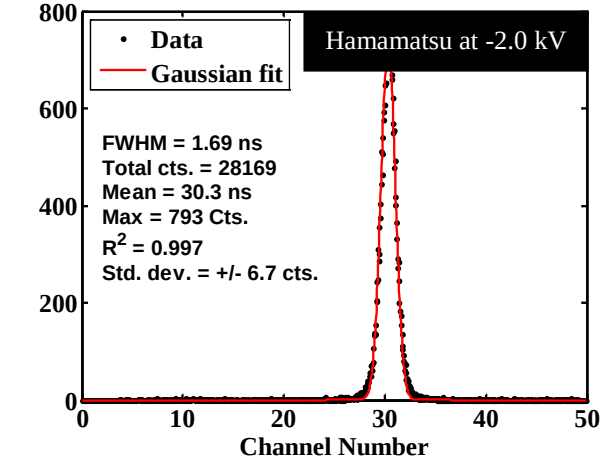

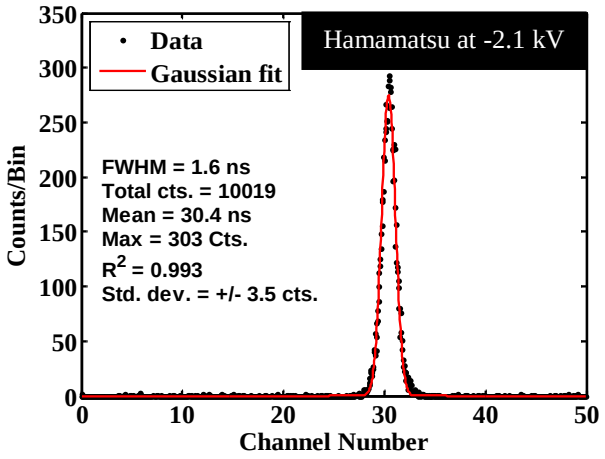

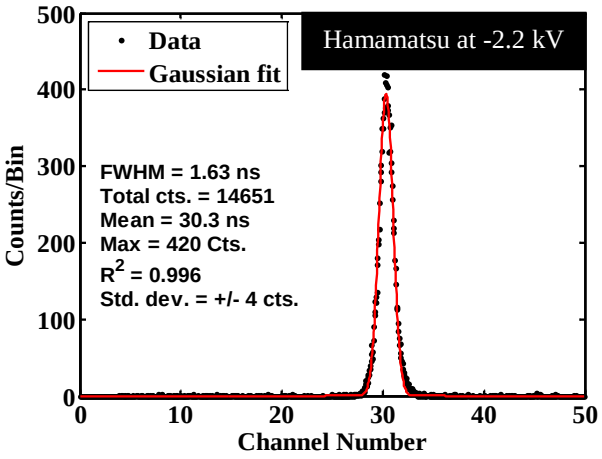

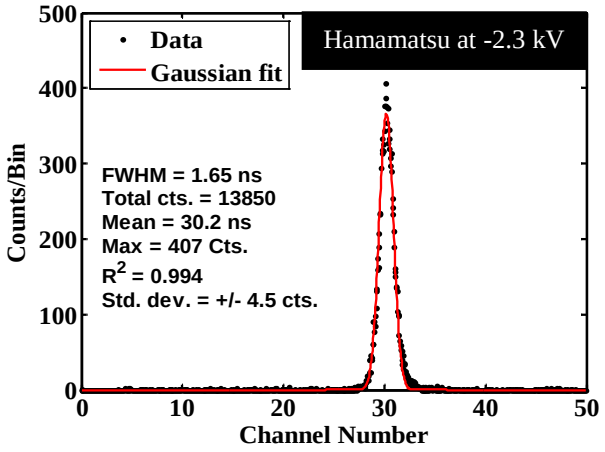

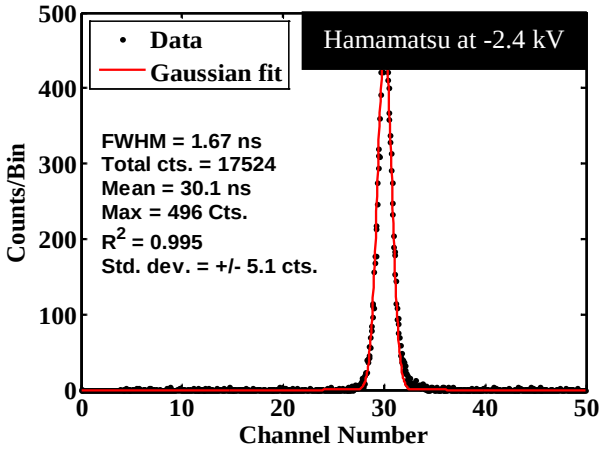

15.3.2 Data acquired for the Photek PMT240 in coincidence with the 110-degree SBD with a 63 ns delay

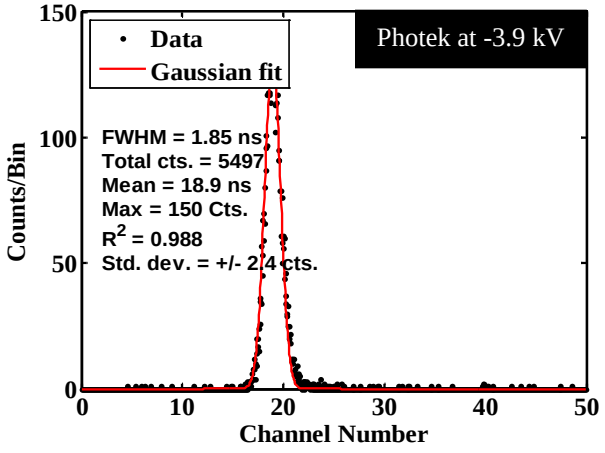

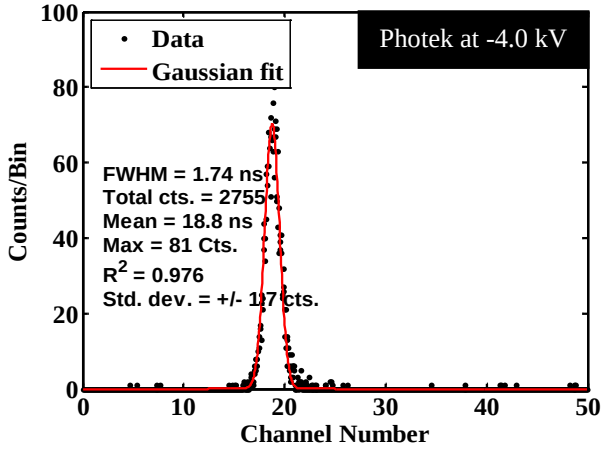

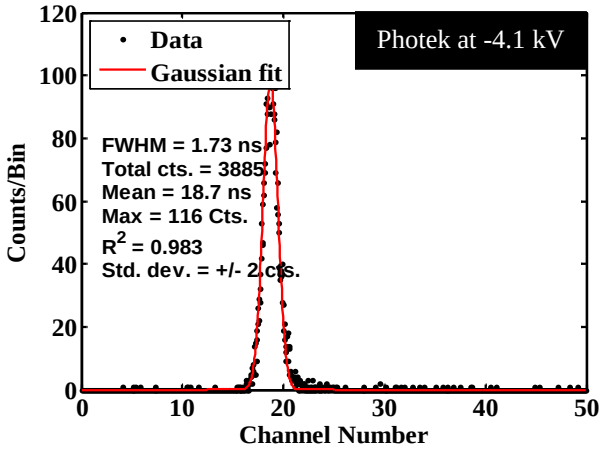

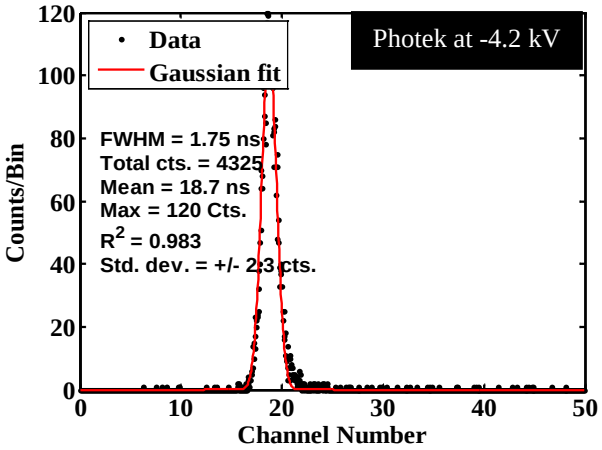

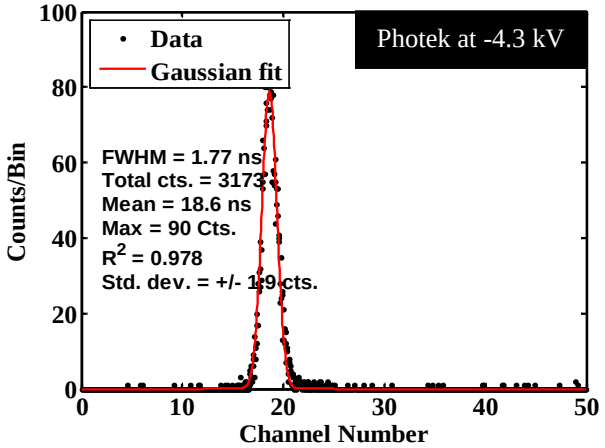

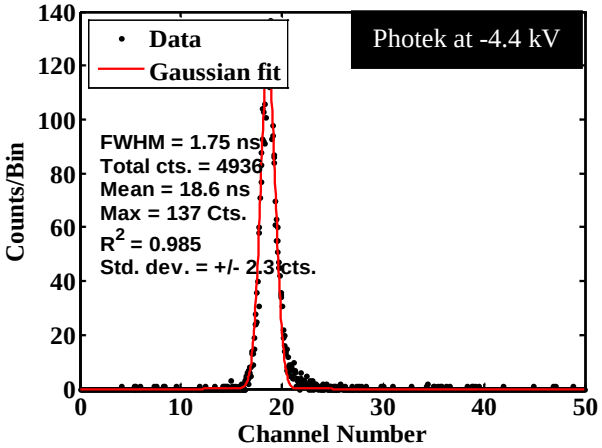

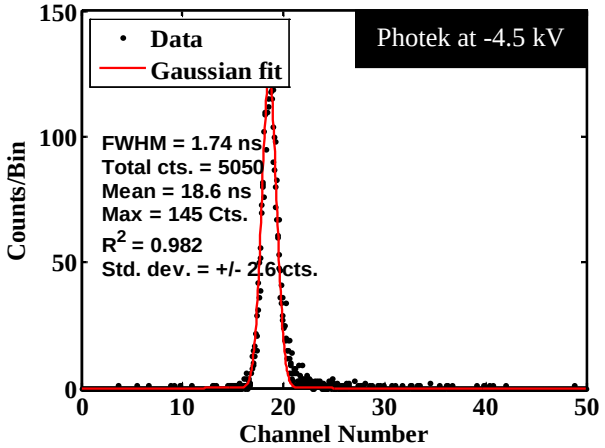

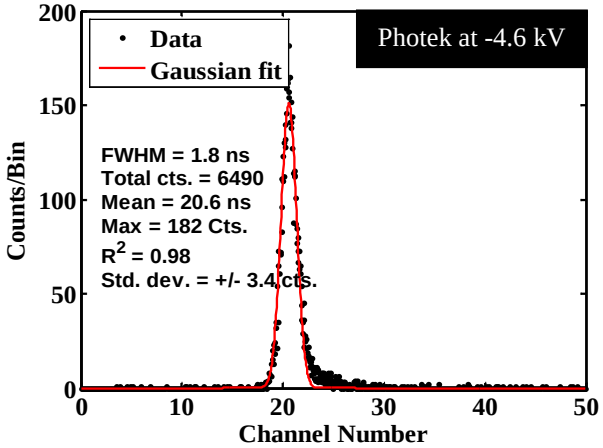

15.4 Coincidence curves acquired with the LMR-600 cabling at a D^+ ion acceleration potential of 50-keV

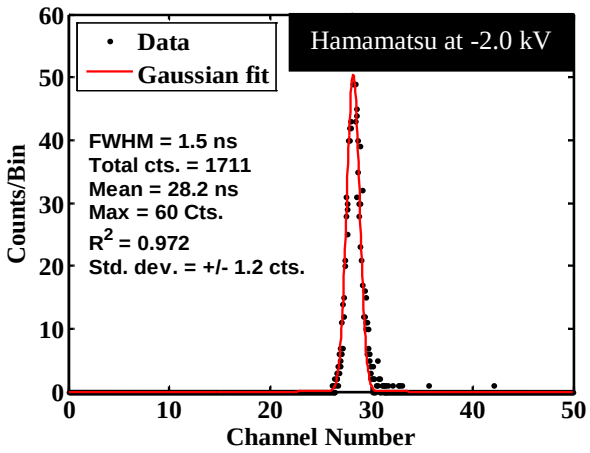

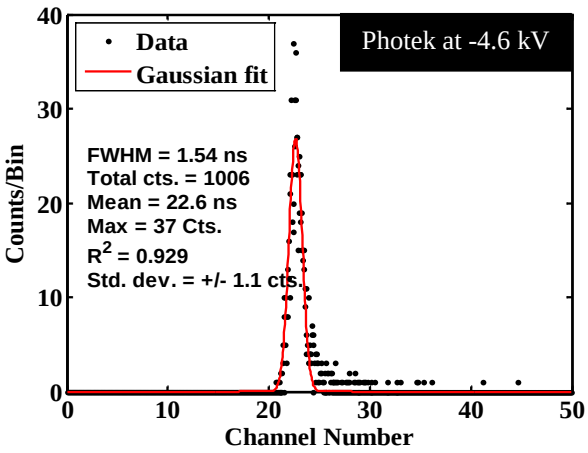

16 Appendix G – Smoothing Technique for Independent Structure Analysis

16.1 Smoothing process for data acquired with the Hamamatsu mod-5 at -2.0 kV

Presented in this section is the smoothing technique implemented to find the centroid location and local maxima prior to fitting the data with a sum of Gaussian functions. For this analysis the raw data was first inverted, time shifted, corrected for baseline offset, and he units were converted from seconds to nanoseconds and volts to millivolts. The results of this process are depicted in Figure 65.

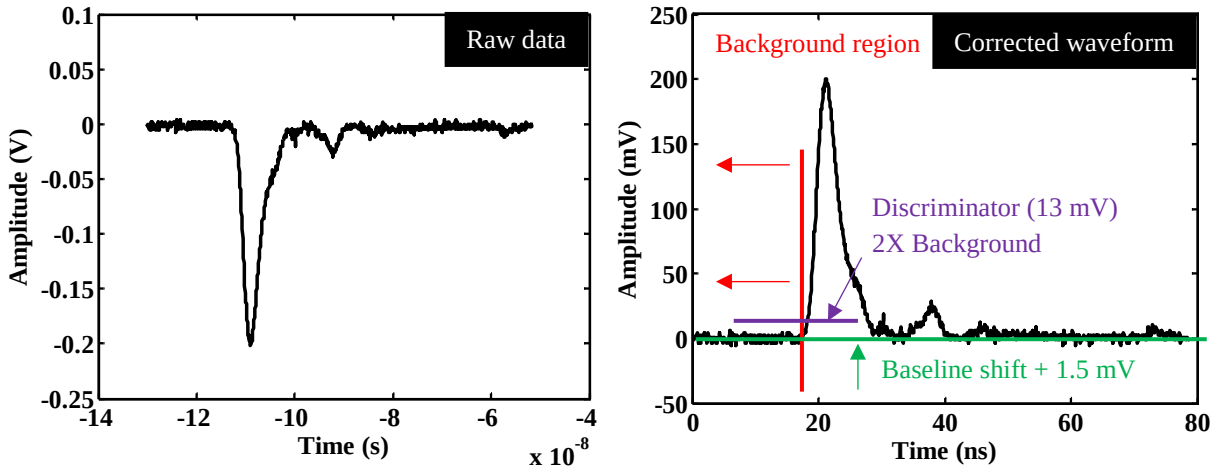

Figure 65 Conversion of raw waveform (left) for analysis. Shown is the corrected waveform (right) after the data has been inverted, time-shifted, corrected for baseline offset, and the units converted to nanoseconds and millivolts.

The data was smoothed by first integrating the data numerically using equation 16-1.

$$Y_i = \frac{(y_{i+1} + y_i)(t_{i+1} + t_i)}{2} \qquad [16-1]$$

The integrated data, Y was then numerically differentiated using equation 16-2, with the adjustable parameter being the timing resolution, Δt. The time-bin resolution was adjusted based on the comparison of the standard deviation of the background region to the standard error of the smoothed to raw data. This process is portrayed graphically in Figure 66.

$$\frac{\partial Y}{\partial t} = \frac{Y_{(i-2)} - 8Y_{(i-1)} + 8Y_{(i+1)} - Y_{(i+2)}}{12\Delta t} \qquad [16-2]$$

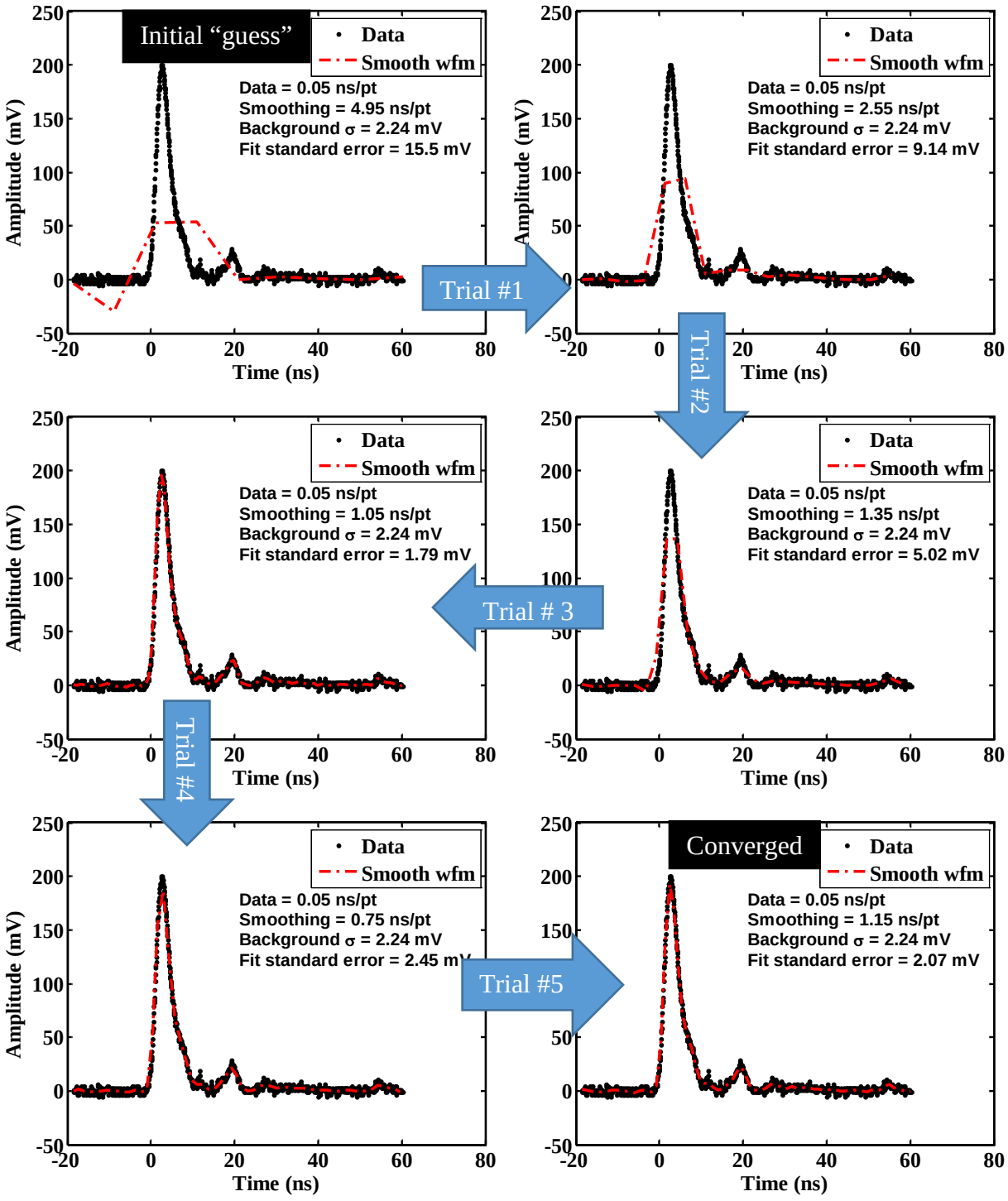

Figure 66 Time-bin resolution adjusted based on convergence criteria

Once the smoothing parameter converged, the second derivative of the integral quantity, Y was found using equation 16-3. The zero crossings of this derivative were found to locate centroid locations and local maxima. The results for this process are shown in Figure 67.

$$\frac{\partial^2 Y}{\partial t^2} = \frac{-Y_{(i-2)} + 16Y_{(i-1)} - 30Y_i + 16Y_{(i+1)} - Y_{(i+2)}}{12\Delta t^2} \qquad [16-3]$$

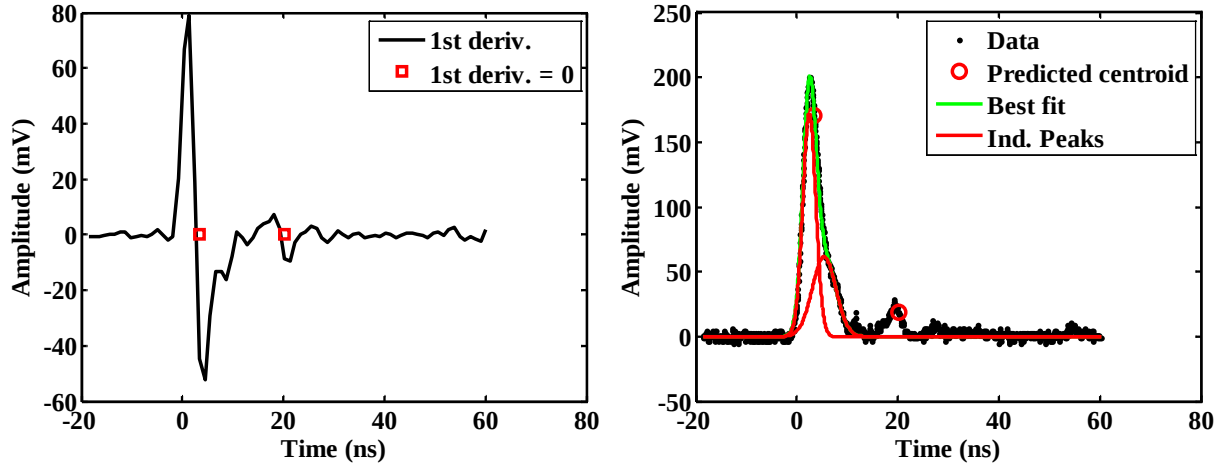

Figure 67 Shown on the left are the second derivative of the integral waveform and where the centroids and local maxima are located. Shown on the right is the non-linear least squares fit to the data using the centroid and local maxima locations.

16.2 Additional Hamamatsu mod-5 waveforms shown with the converged, smoothed waveform

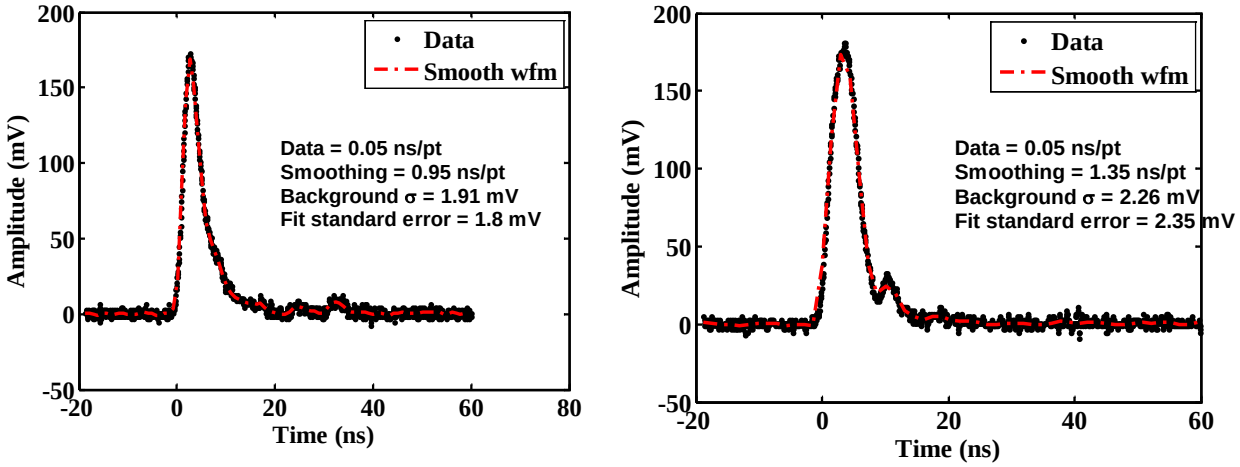

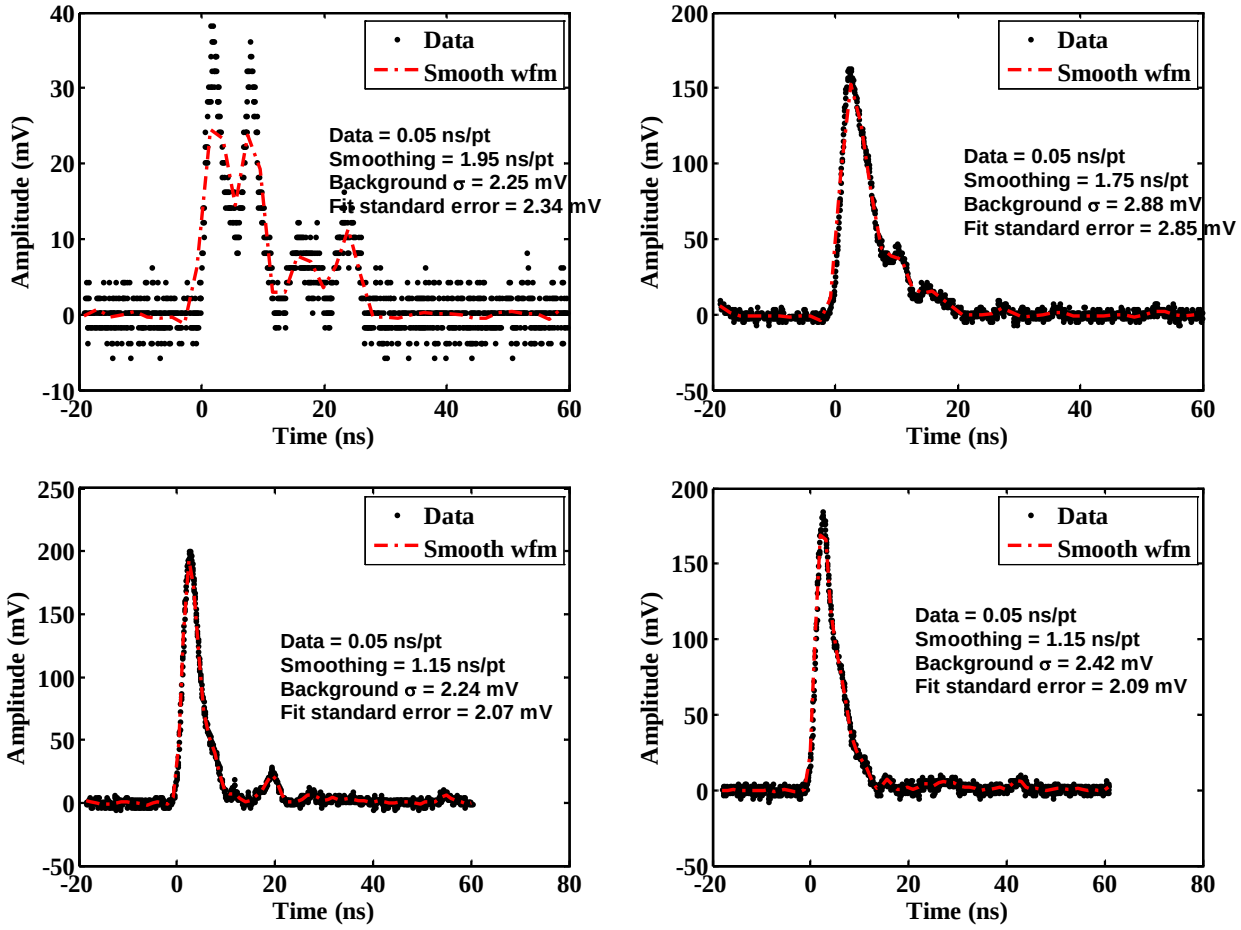

16.3 Photek PMT240 waveforms shown with the converged, smoothed waveform.

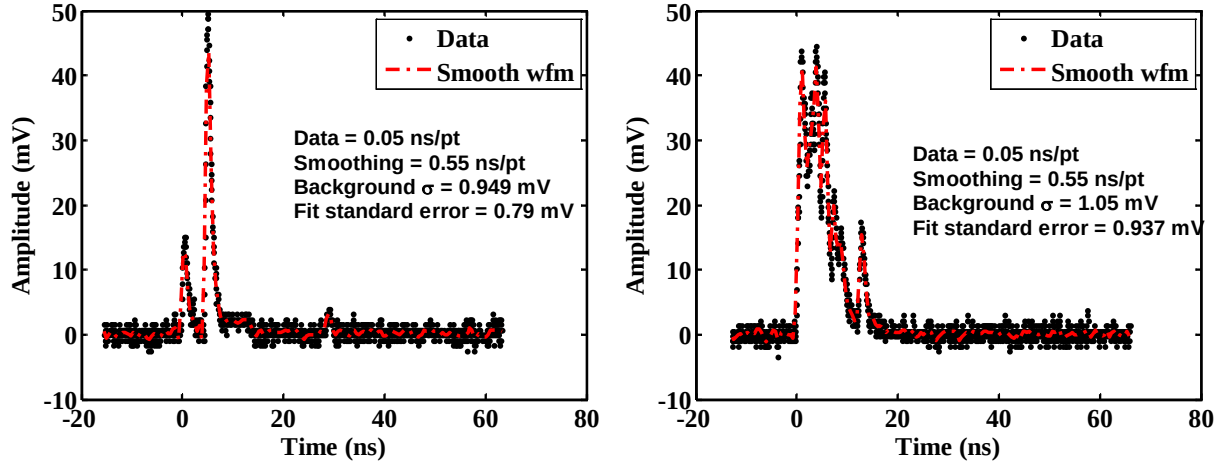

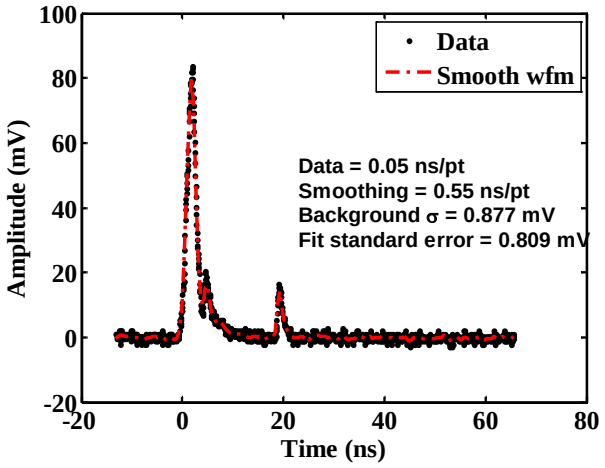

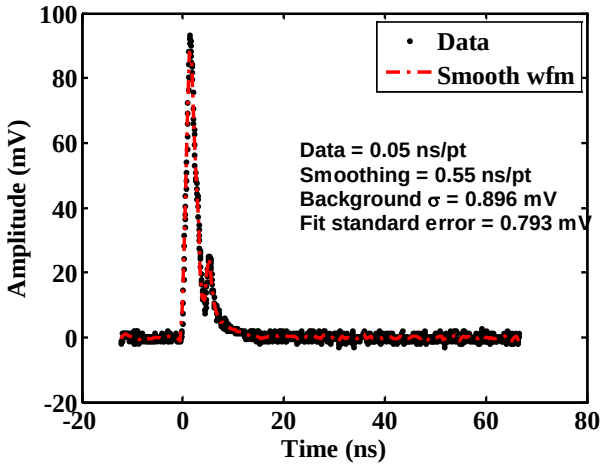

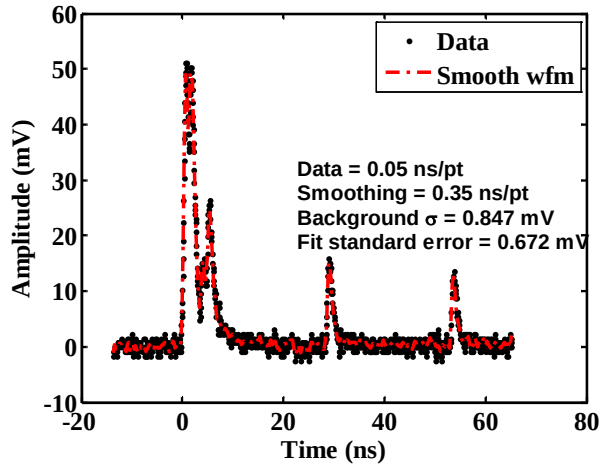

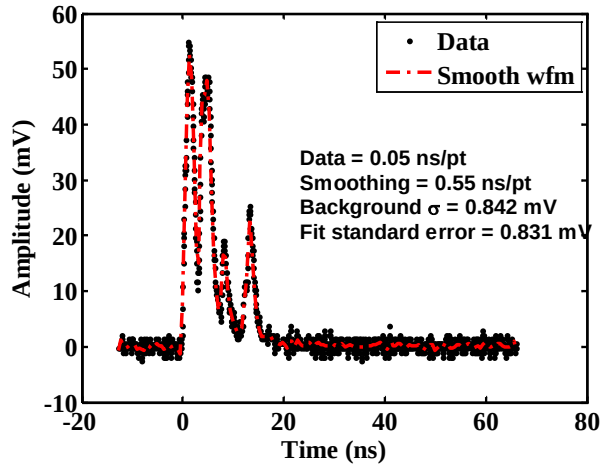

17 Appendix H – Calculated Counting Efficiencies from Light Output Correlation

Coincident Tube	Bias (-kV)	Disc. (mV)	Cts. per incident neutron	Opposing Tube	Bias (-kV)	Calculated disc. (mV)	Calculated Energy (MeV)
Ham	1.7	25	0.019	Pho	3.9	17.32	5.58
Ham	1.8	50	0.010	Pho	4	24.88	5.69
Ham	2	25	0.083	Pho	4.2	27.08	3.94
Ham	2.1	50	0.073	Pho	4.3	23.45	2.50
Ham	2.3	50	0.086	Pho	4.5	20.65	1.37
Pho	3.9	15	0.002	Ham	1.7	25.26	10.13
Pho	4	15	0.006	Ham	1.8	43.52	11.98
Pho	4.1	15	0.012	Ham	1.9	59.98	10.80
Pho	4.2	15	0.019	Ham	2	79.36	8.87
Pho	4.3	25	0.008	Ham	2.1	114.31	10.32
Pho	4.4	25	0.014	Ham	2.2	188.71	12.10
Pho	4.5	25	0.021	Ham	2.3	207.96	7.74
Pho	4.6	15	0.050	Ham	2.4	250.26	7.40

Appendix I –Other data

17.1 Sensitivity as a function of bias inferred from the average IRF analysis

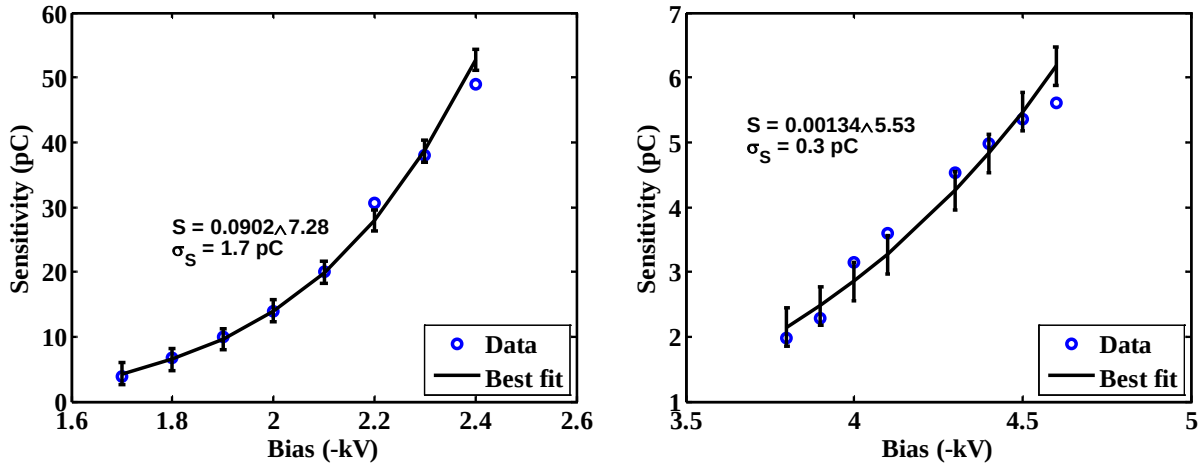

Figure 68 Sensitivity as a function of bias from the average IRF analysis. Shown on the left is the correlation for the Hamamatsu mod-5 tube and on the right is the correlation for the Photek PMT240 tube.

17.2 Normalizing sensitivity (pC) to light-output

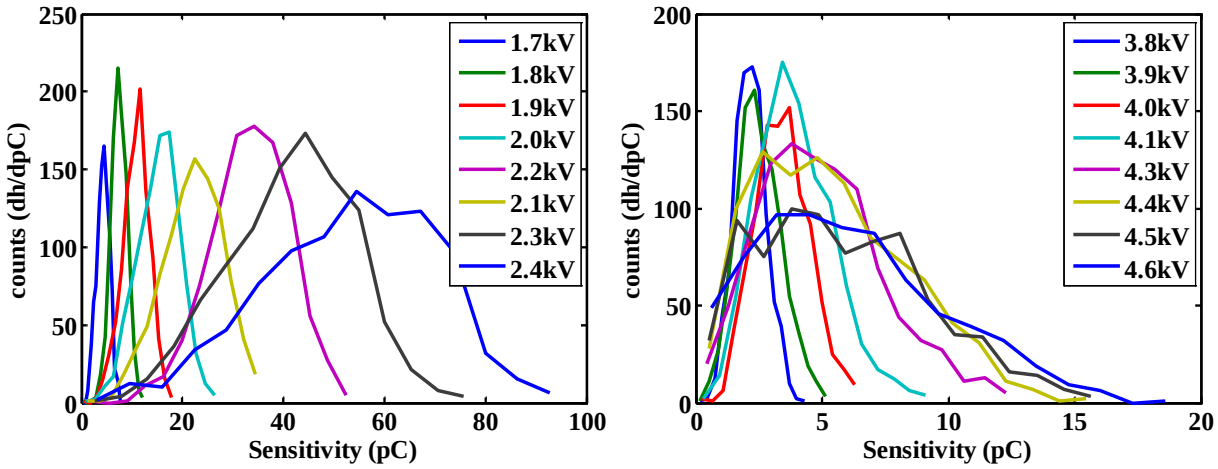

Figure 69 Sensitivity distribution shown as a function of bias for the Hamamatsu tube (left) and the Photek (right)

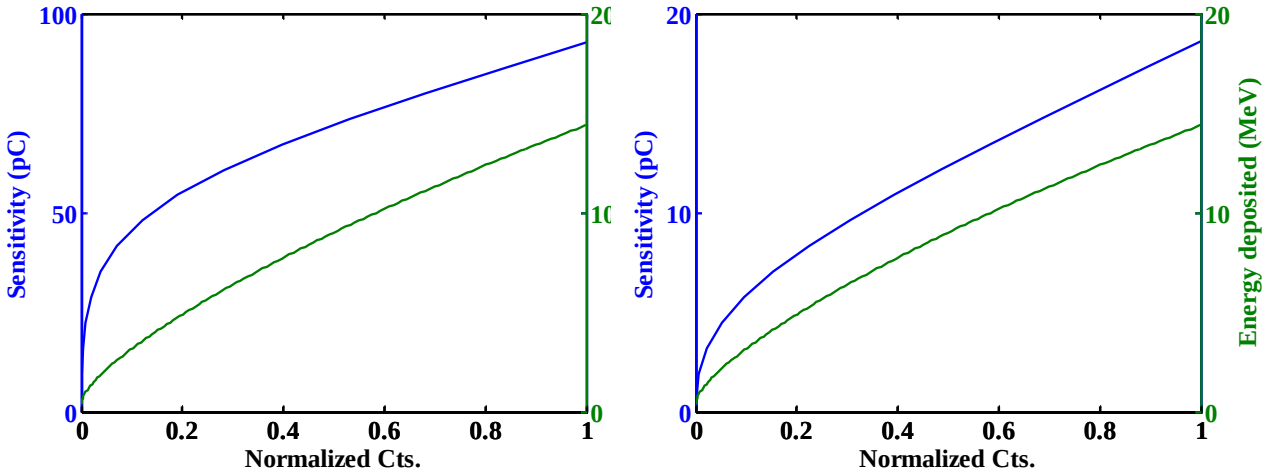

Figure 70 Normalized sensitivity and energy deposition shown for the Hamamatsu at -2.4 kV (left) and the Photek tube at -4.6 kV (right)

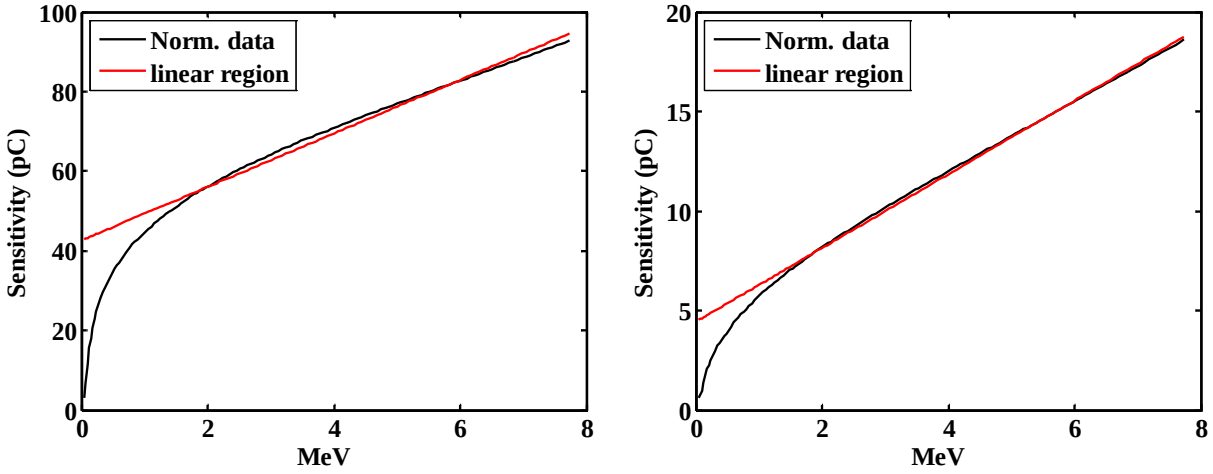

Figure 71 Sensitivity to MeVee correlation derived from the normalization. Shown on the left is the Hamamatsu tube at -2.4 kV and on the right is the Photek tube at -4.6 kV